Validated Loads Prediction Models for Offshore Wind Turbines for Enhanced Component Reliability

Koukoura, Christina; Natarajan, Anand; Branner, Kim

Publication date:
2014

Document Version
Publisher's PDF, also known as Version of record

Validated Loads Prediction Models for Offshore Wind Turbines for Enhanced Component Reliability

DTU Wind Energy PhD Thesis

Christina Koukoura

DTU Wind Energy PhD-0026 (EN)

September 2014

DTU Wind Energy
Department of Wind Energy

Author: Christina Koukoura
Title: Validated Loads Prediction Models for Offshore Wind Turbines for Enhanced Component Reliability
Division: Department of Wind Energy

Abstract:
Accurate prediction of the response of an offshore wind turbine is crucial for the uncertainty reduction and the enhanced reliability of the structures. In the present thesis a 3.6MW pitch regulated-variable speed offshore wind turbine model on a monopile foundation is built in the aero-servo-hydro-elastic tool HAWC2. The model is validated with full scale load measurements. Wind turbulence intensity and wave characteristics are based on site measurements. A flexible soil model is included in the simulations. Discrepancies between measurements and simulations are discussed and the uncertainties are quantified. The support structure net damping is identified from the parameters of an exponential curve fitted to the relative maxima of an impulse response caused by a boat impact. The damping of the model and the full scale wind turbine in normal operation is estimated through the Enhanced Frequency Domain Decomposition method. The importance of the right damping value in the model, with respect to the actual damping of the full scale wind turbine, is stressed for accurate load prediction. The design load case of wind-wave misalignment is also examined. The effect of damping on the side-side fatigue of the structure is investigated. The joint wind-wave distribution and the distribution of the wind-wave misalignment angles are included in the analysis. Variations in the sub-structure/foundation design for material savings considering the higher available damping are examined.

The dissertation is submitted to the Danish Technical University in partial fulfillment of the requirements for the PhD degree from the PhD School DTU Wind Energy. The PhD project was carried out in the years 2011-2014 at the Wind Turbine Section (VIM) of DTU Wind Energy.

Main supervisor: Anand Natarajan, DTU Wind Energy
Co-supervisor: Kim Branner, DTU Wind Energy

Publications

1. C. Koukoura, and A. Natarajan. *"Mitigating the Long term Operating Extreme Load through Active Control."* The Science of Making Torque from Wind, Oldenburg, Germany, 2012

2. C. Koukoura, A. Natarajan, T. Krogh, O.J. Kristensen, *"Offshore Wind Turbine Foundation Model Validation with Wind Farm Measurements and Uncertainty Quantification."* The Twenty-third International Offshore and Polar Engineering Conference. International Society of Offshore and Polar Engineers, Anchorage, USA, 2013.

3. C. Koukoura, A. Natarajan, and A. Vesth. *"Identification of support structure damping of a full scale offshore wind turbine in normal operation."* Submitted to Renewable Energy. Elsevier, 2013

DTU PhD-0026 (EN)
September 2014

ISBN:
xxx-xx-xxxxx-xx-x

Sponsorship:
Danish Energy Agency (2/3)
EUDP project titled,
"Offshore wind turbine reliability through complete loads measurements",
project no. 64010-0123

Copenhagen Cleantech Cluster (CCC), (1/3)

Pages: 182
References: 186
Figures: 112
Tables: 7

Technical University of Denmark
Department of Wind Energy
Frederiksborgvej 399
Building 118
4000 Roskilde
Denmark
Email: kouk@dtu.dk
www.vindenergi.dtu.dk

Summary (English)

To improve the reliability of offshore wind turbines, accurate prediction of their response is required. Therefore, validation of models with site measurements is imperative. In the present thesis a 3.6MW pitch regulated-variable speed offshore wind turbine on a monopile foundation is built in the aero-servo-hydro-elastic code HAWC2. The results are validated with full scale measurements from a 3.6MW Siemens offshore wind turbine installed in the Walney Offshore Wind Farm 1 at the west coast of England. Damping estimation, wind-wave misalignment cases and storm loads are analyzed. The findings are used for the modification of the sub-structure/foundation design for possible material savings.

First, the background of offshore wind engineering, including wind-wave conditions, support structure, blade loading and wind turbine dynamics are presented. Second, a detailed description of the site is given and the metocean conditions are analyzed. The joint wind-wave distribution and the probability of the misalignment angles are estimated. Third, the calibration process of the different components is thoroughly depicted. The turbulence intensity implemented in the simulations is extracted from a nacelle mounted cup-anemometer.

The model setup is based on the downscaled 5MW NREL reference wind turbine. Modifications on the downscaled model to match the actual full-scale wind turbine (mass and natural frequency) are applied. Extreme and mean measured loads from the free wind and the wake sectors, as well as 1Hz equivalent loads are used for the validation of the model. The uncertainties both in the model and the full-scale wind turbine are quantified.

The main contribution of the current thesis is presented in the final three chapters. The support structure net damping is estimated from the impulse response of a boat impact. The first and second modal damping of the system during normal operation both from measurements and simulations are identified with the implementation of the Enhanced Frequency Domain Decomposition technique. The effect of damping on the side-side fatigue of the support structure due to wind-wave misalignment cases is examined. The higher measured net damping is then used in the design process of the sub-structure/foundation for material savings. A detailed ultimate strength, stability strength and fatigue analysis are performed in the baseline and the modified designs to ensure structural integrity of the system.

Summary (Danish)

For at forbedre pålideligheden af havvindmøller, kræves en præcis forudsigelse af deres respons. Det er derfor vigtigt at validere modeller med måledata. I denne afhandling er en 3,6 MW pitch-reguleret havvindmølle med variabel rotorhastighed på et monopæl fundament modelleret i HAWC2 – en aero-servo-hydro-elastisk kode. Resultaterne er valideret med fuldskala målinger fra en 3,6 MW Siemens offshore vindmølle installeret i Walney Havmøllepark 1 ved vestkysten af England. Estimering af dæmpning, tilfælde hvor vind og bølger kommer fra forskellige retninger samt storm belastninger er analyseret. Resultaterne bruges til at ændre designet af sub-struktur / fundament for at opnå potentielle besparelser af materiale.

Først beskrives baggrunden for offshore vind, herunder vind- og bølgeforhold, understøttede struktur, fordeling af belastning over vingerne og vindmøllekomponenternes dynamik. Dernæst er der en detaljeret beskrivelse af testmøllens lokalitet og hydrografi og meteorologi for stedet. Den kombinerede vind og bølge fordeling samt sandsynligheden for forskel mellem vind og bølge retninger er anslået. Endelig er kalibreringsprocessen for de forskellige komponenter grundigt beskrevet. Turbulensintensiteten implementeret i simuleringerne er baseret på anamometer målinger fra nacellen.

Modellen er baseret på en nedskalering af NREL 5 MW reference vindmøllen. Ændringer af den nedskalerede model er foretaget for at matche fuldskala vindmøllen (masse og egen frekvensen). Ekstreme og gennemsnitlige målte belastninger fra fri vind og wake retninger samt 1Hz tilsvarende belastninger anvendes til validering af modellen og usikkerheden kvantificeres.

De vigtigste bidrag i denne afhandling er præsenteret i de sidste tre kapitler. Vindmøllestrukturens netto dæmpning estimeres ud fra impuls-gensvaret fra en båd kollision med vindmøllen. Den første og anden modal dæmpning af systemet under normal drift er identificeret fra både målinger og simuleringer ved hjælp af en forbedret frekvensdomæne dekomposition teknik. Virkningen af dæmpning på side-til-side udmattelse af strukturen i tilfælde hvor vind og bølger kommer fra forskellige retninger undersøges. Den målte netto dæmpning er højere end tidligere brugt og anvendes herefter i designprocessen af sub-struktur / fundament for at opnå besparelser af materiale. En detaljeret analyse af ultimativ brudstyrke, bulingsstyrke og udmattelse udføres for basis designet samt de modificerede designs for at sikre strukturel

integritet af hele systemet.

Acknowledgements

During the three years of this Ph.D. thesis some people have been on my side, supporting me and helping me to carry on. First and foremost, I would like to thank my supervisors Anand Natarajan and Kim Branner for trusting me and giving me the opportunity to be part of this project. My sincere appreciation is going to the head of our section, Thomas Buhl for the support and the guidance throughout these years.

I would also like to thank Allan Vesth for introducing me to the fascinating real world of measurements. Because of his encouragement and the countless hours he spent explaining to me what a wind turbine is, I feel more confident to put into practice everything I learned. My appreciation is extended to Mike Courtney for his invaluable advice during my research.

At this point I would like to thank my friends and colleagues Tomas Hanis and Martin Eder for being so patient with me. Our discussions and their enthusiasm have been the most motivating and constructive inputs to my thesis.

A very big thank you from the bottom of my heart to my family, my mom, my dad and my little sister for always supporting my choices. Your unconditional love has always given me the strength and the courage to continue during the most difficult times. Thank you for teaching me to be brave enough to pursue my dreams and not let anything stand in my way.

Last but definitely not least, I would like to express my deepest gratitude to my "brothers", Angelo, Carlo and Sri for being there for me every single moment, throughout this journey. If what they say is true, that a rich person is not the one with money but the one with real friends, then I am a millionaire, because I have you in my life.

Thank you

Chris

Contents

Summary (English) **v**

Summary (Danish) **vii**

Acknowledgements **ix**

1 Introduction **1**
1.1 Purpose . . . 2
1.2 Thesis Outline . . . 4

2 Environmental Conditions **5**
2.1 Wind Field . . . 5
2.2 Wave Distribution . . . 7
2.3 Soil Model . . . 9

3 Wind Turbine Design **13**
3.1 Support Structure Loading . . . 13
3.2 Blade Loading . . . 17
3.2.1 Wake Effect . . . 19
3.3 Controller . . . 20

4 Damping **23**
4.1 Rayleigh Damping . . . 23
4.2 Aerodynamic Damping . . . 25
4.3 Damping Identification . . . 26
4.3.1 Full Damping Matrix . . . 27
4.3.2 Modal Damping Identification in Time and Frequency Domain . . . 29

5 Site Description **35**
5.1 Metocean Conditions . . . 36
5.1.1 Wind-Wave Joint Distribution . . . 39
5.1.2 Wind-Wave Direction Probability . . . 40

6 Measurements Calibration and Data Processing **45**
6.1 Measurement Calibration . . . 45
6.1.1 Support Structure Calibration . . . 45
6.1.2 Blade Calibration . . . 48
6.1.3 Drivetrain Calibration . . . 50
6.2 Yaw Angle Correction . . . 51
6.3 Data Synchronization . . . 52
6.4 Data Processing . . . 54
6.4.1 Data Availability . . . 54
6.5 Recommendations for Future Measurement Campaigns . . . 55

7 Wind Measurements Calibration **59**
7.1 Nacelle Mounted Cup-anemometer/SCADA . . . 59
7.1.1 Turbulence Intensity . . . 59
7.1.2 Weibull Distribution . . . 62
7.2 LIDAR . . . 65

8 Model Setup **69**
8.1 Support Structure Characteristics . . . 69
8.2 Downscaling Process . . . 70
8.3 Model Damping . . . 72
8.4 HAWC2 Model . . . 73
8.5 Modeling of Ambient Loads . . . 75
8.5.1 Wind Model . . . 76
8.5.2 Wave Kinematics . . . 77
8.5.3 Soil Model . . . 78

9 Model Validation **81**
9.1 Sub-structure/Foundation . . . 82
9.2 Tower . . . 85
9.3 Blades . . . 86
9.4 Validation of Model on the Wake . . . 87

10 Uncertainties **93**
10.1 Calculating Uncertainties . . . 94
10.2 Uncertainty Analysis . . . 95
10.2.1 Measurements Uncertainties . . . 96
10.2.2 Simulation Uncertainties . . . 96

11 Damping Estimation **101**
11.1 Impulse Response . . . 101
11.1.1 Boat Incident-Measurements . . . 102
11.2 Ambient Excitation . . . 105
11.2.1 Enhanced Frequency Domain Decomposition . . . 105

12 Loading under Different Conditions **113**
12.1 Wind-Wave Misalignment . . . 113
12.1.1 Fatigue Analysis/Measurements . . . 114
12.1.2 Fatigue Analysis/Simulations . . . 116
12.1.3 Effect of Damping on Fatigue . . . 117
12.2 Storm . . . 121
12.2.1 Wind and Wave Measurements . . . 121
12.2.2 Storm Loads . . . 123

13 Sub-structure/Foundation Design **125**
13.1 Limit State design . . . 125
13.1.1 Design Load Cases . . . 126
13.1.2 Ultimate Limit State (ULS) . . . 131
13.1.3 Stability Analysis . . . 133
13.1.4 Fatigue Limit State (FLS) . . . 137
13.2 Structural Analysis of the Sub-structure/ Foundation Design . . . 138
13.2.1 Baseline Design . . . 138
13.2.2 Baseline Design-Measured Environmental Conditions . . . 146
13.2.3 Design with Higher Damping . . . 146

14 Conclusions **155**
14.1 Future Work . . . 159

References **160**

A Appendix A **175**
A.1 Wind . . . 175
A.2 Waves . . . 178
A.3 Soil . . . 179

B Appendix B **181**
B.1 Fatigue . . . 181

Chapter 1

Introduction

The increased energy demand and the reduced solutions for the electrification of the planet have stimulated the development and research of renewable energy sources the last years. The commercialization of the wind energy is rising on a very large scale in Europe giving an impetus to the wind energy industry. The higher wind speeds over the sea and the lower visual and acoustic impact turns the interest towards offshore sites. At the same time the challenges due to more severe weather conditions (wind, wave and current loading) are increasing. The European Energy Policy declares 230GW installed cumulative power by 2020, 40GW of which should be installed offshore. The goal for 2030 is 400GW rated power, 150GW of which offshore [1]. The expectation that the offshore wind farms will increase with a mean annual rate of 21.5% per year until 2020, renders important the advanced research and demands for development of more advanced tools in this field. Wind turbines with a rated power of up to 8MW are currently under development. To enhance the reliability of such offshore structures and reduce electricity production cost and maintenance cost, it is essential to update the aero-elastic codes used for the design, the analysis and the optimization of wind turbines.

The reliable prediction of an offshore wind turbine dynamic response depends on the accurate representation of the model (rotor-nacelle assembly, support structure), the realistic environmental conditions and the number of simulations. The modeling of the substructure/foundation is of significant importance due to its influence upon the response of the offshore wind turbine and the variety of excitation frequencies on the support structure (blade passing, waves). The development of simple models for the simulation of the entire system respecting the required accuracy is crucial. The damping has a significant impact on the lifetime and the fatigue of the offshore structure. The wind turbine is often subjected to large deformations, due to wave excitation not only during extreme conditions but also during power production. In the side-side direction where little aerodynamic damping is present, damping that counteracts the strong amplifications of the structure near the resonance region is required, especially when wind-wave misalignment occurs. Detailed guidelines for damp-

ing measurements and estimation techniques is important to be developed. Due to the short duration of measurement campaigns the environmental conditions experienced by the wind turbine are limited, compared to all possible combinations that are likely to occur throughout its whole lifetime. At the same time the amount of simulations required to cover all conditions demands high computational time. For these reasons statistical techniques are implemented to extrapolate long term design loads from limited data.

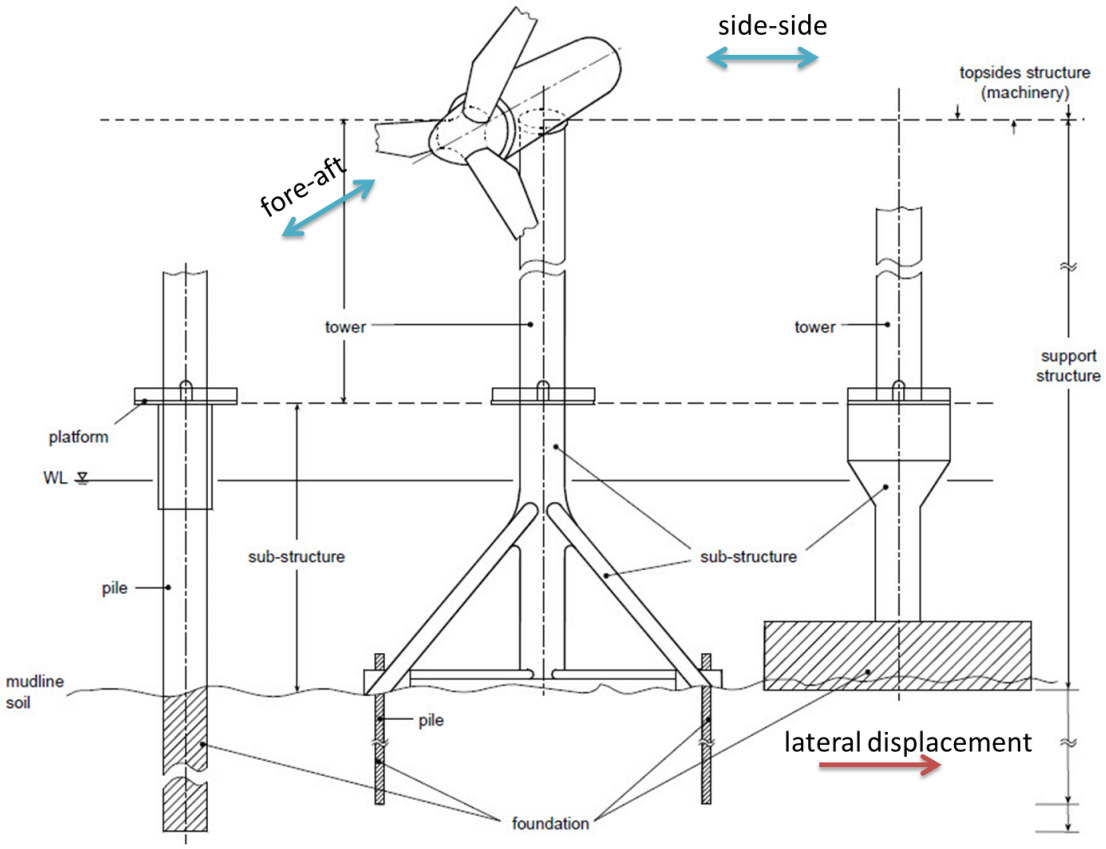

Figure 1.1: Offshore wind turbine. Figure adapted from reference [2].

1.1 Purpose

The development of large offshore structures will require the highest quality of design models that represent accurately the real turbines. The understanding of the environment and the wake effect (effect of the surrounding turbines to the dynamic response and the power production) would be equally important factors. This effort demands accurate design loads prediction of current turbines and validation of model simulations against site measurements in order to improve the structure's design, enhance reliability and reduce maintenance cost.

Validations of offshore wind turbine models with site measurements and damping estimation during normal operation are not very often reported in the literature. For this reason

this project will deal with the validation of loads derived from the in-house developed aero-elastic code HAWC2 [3] with measurements, taken from a fully instrumented 3.6MW Siemens offshore wind turbine in operation, installed in the Walney farm, at the West coast of England (Irish Sea). The damping of the system during normal operation is estimated using the Enhanced Frequency Domain Decomposition (EFDD) technique [4, 5]. Cases of wind-wave misalignment and storms are identified from the environmental measurements for the calculation of fatigue and extreme loads. This information is further used for the prediction of the remaining lifetime and the design of the sub-structure/foundation.

The main aspects covered in this thesis are:

- Model validation with full scale measurements and uncertainty quantification
- Damping of the system during normal operation
- Fatigue loads in wind-wave misalignment
- Extreme loads during storms
- Lifetime prediction and sub-structure/foundation design

More specifically sub-structure/foundation, tower and blade dynamics are thoroughly examined. The target is to understand the loading on the structure under different operational conditions (free wind sector, wake sector, wind-wave misalignment, storm, grid loss, yaw error). Different load cases and wind sectors are investigated to identify the driving factors of the design loads. Fatigue and extreme loads on the structure are calculated considering the joint wind-wave distribution based on site measurements. The Weibull distribution [6] and the JONSWAP spectrum [7] are fitted to the wind and wave data respectively. For the calculation of the hydrodynamic forces the irregular Airy wave theory [8] combined with the wheeler stretching method [9, 10] to account for loads above the mean sea level is applied. The flexibility of the soil is accounted for by implementing the distributed p-y spring model [11].

Great attention is given to the estimation of the system's damping, including aero-, tower-soil- and hydrodynamic- damping. Due to the low aerodynamic damping in the side-side vibration, the fatigue loads on the structure because of wind-wave misalignment are usually driving design factors [11, 12]. Therefore, the effect of damping on the fatigue of the side-side direction due to wave impact is examined. Extreme loads during storms are investigated and extreme environmental conditions are compared with the 1-year and 50-year wind and wave loads proposed in the IEC 61400-3 standards [13]. The results are used for the estimation of the remaining lifetime of the structure and the verification of the lifetime predicted during the design process. The effect of damping on the fatigue of the system is examined. Based on these findings a preliminary sub-structure/foundation design analysis for material savings is performed.

The reliability of the results depends on the uncertainty level of different variables. The wind, wave and soil measurements, the parameters used in the fitted distributions as well as

the derived wind turbine model induce variability in the predicted loads. The range of the loads is connected to the uncertainty introduced by the above mentioned parameters. The simulations' uncertainties are quantified and compared with the measurements' uncertainties to examine the accuracy of the predicted loads.

To conclude, the objective of this work is the reliable prediction of the response of a fixed bottom offshore wind turbine, leading to the improvement of component reliability through accurate lifetime prediction. The findings will be used as a reference for validation of the state of the art models, so that future simulations will reflect reality more accurately, without over- or under estimation of the design loads, avoiding either excessive material or increased maintenance costs.

1.2 Thesis Outline

The organization of this thesis is the following. The first three chapters are dedicated to the literature review of the topics discussed in this work. Chapter 2 describes the wind characteristics, the wave kinematics and the distributions fitted to the wind and wave measurements. In the last section the soil model implemented in the aero-elastic simulations is presented. Chapter 3 is focusing on the components of an offshore wind turbine, namely the support structure, the blades and the controller. In Chapter 4 the dynamics of a vibrating structure with an emphasis on the damping estimation are investigated.

In Chapters 5, 6 and 7 the site and the calibration process are illustrated. More specifically, Chapter 5 deals with the sea climate and the joint wind and wave distribution. Chapter 6 describes in detail the steps followed for the calibration of the different instrumentation used and the problems encountered in measurement campaigns. Chapter 7 is analyzing how the turbulence intensity applied in the simulations is extracted from the wind measurements of a nacelle mounted cup-anemometer.

The procedure for the wind turbine model setup is explained in Chapter 8. The validation of the model with full scale measurements is presented in Chapter 9. Quantification of different types of uncertainties is demonstrated in Chapter 10.

The main contribution of this thesis is presented in the last three chapters. Chapter 11 demonstrates the overall damping of an offshore wind turbine in normal operation, estimated from full scale measurements and compared with the model damping. In Chapter 12 the fatigue of the structure in the case of wind-wave misalignment is examined and extreme loads due to storms and yaw error are presented. The design of the sub-structure/foundation based on the findings of the previous chapters and the effect of the environmental conditions and of the damping on the structure's lifetime are studied in Chapter 13. A conclusion of the findings of the present thesis and recommendations for future work are discussed in the final Chapter 14.

Chapter 2

Environmental Conditions

In this chapter the turbulent wind field and the distribution fitted to the wind data are explained. The wave kinematics, the stretching technique and possible distributions fitted to the wave data are presented. The soil model used in the aero-elastic simulations is also described.

2.1 Wind Field

The wind field around a horizontal axis wind turbine is turbulent, namely non-uniform in space and unsteady in time, mainly due to frictional forces and obstacles (Figure 2.1). Wind shear due to surface friction is always present in atmospheric conditions. Wind speed u_z due to shear is extrapolated at hub height z from measurements at lower heights either using the logarithmic (Equation 2.1a), or the power law (Equation 2.1b), where u_* is the friction velocity , k is the von Karman constant, z_0 is the roughness length, α is the power exponent, u_{zr} is the reference velocity and z_r is the reference height. The presence of the tower affects the airflow, a phenomenon called tower shadow, while the 3P component (3rd harmonic of the rotational speed) has an increased energy in the tower load spectrum, due to the blade passing in front of the tower.

$$u_z = \frac{u_*}{k} ln\left(\frac{z}{z_0}\right), \quad u_z = u_{zr}\left(\frac{z}{z_r}\right)^{\alpha} \tag{2.1}$$

For the analysis of the dynamic response of a wind turbine, stochastic wind fields with a Gaussian turbulence of 10min length are generated, to cover the different environmental

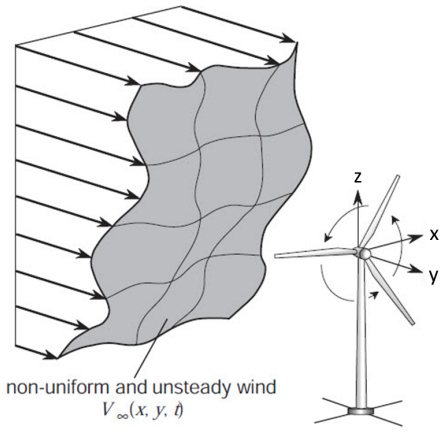

Figure 2.1: Spatial distribution of the wind field upstream of the wind turbine. Figure from reference [14].

conditions that a turbine will operate with during its lifetime. The 10min simulation period is associated with the wind spectrum, where the high frequency side corresponds to the turbulence, as depicted in Figure 2.2 [15].

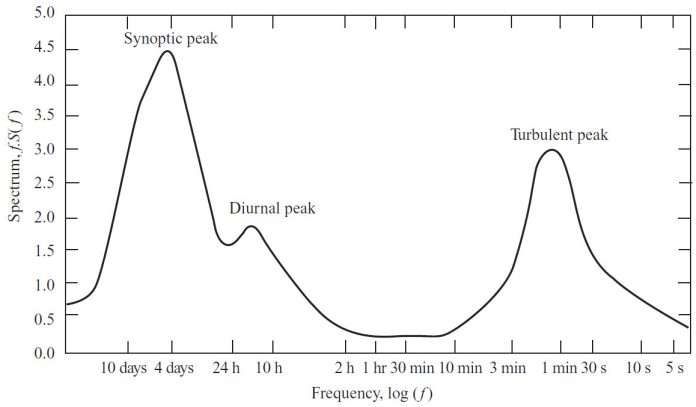

Figure 2.2: Wind spectrum. Figure from reference [15].

The longitudinal turbulence intensity is calculated by the standard deviation of the horizontal wind speed σ_1 at the hub height z_{hub} divided by the mean wind speed U_{hub}. In offshore sites an increase in the turbulence intensity can be observed for higher wind speeds, because of increased surface roughness due to wind induced waves [16].

In reference [6] various wind distributions are presented. The two most commonly used and easiest to apply are the Rayleigh and the Weibull distribution, also proposed by the International Electrotechnical Commission (IEC) standards [17]. Their fitting to the probability density function of the wind is examined through sea wind observations in reference [18]. The equations for the wind distributions are given in Appendix A.

Wind measurements are crucial for the estimation of the wind turbine power performance. With constantly increasing hub height, the traditional mast-mounted cup-anemometer becomes an expensive technique. An alternative to that is the ground-based remote sensing systems. In reference [19] a comparison of the two different available remote sensing instruments, Sodars and LIDARs is presented. Tests performed at the Høvsøre facilities showed good agreement between the wind speed estimation from the mast-mounted cup-anemometer and the remote sensing systems. A fairly new technique for wind measurement is the nacelle mounted LIDAR, facing upstream of the turbine combining in that way the advantages of a nacelle based instrument and those of remote wind speed measurement [20]. A nacelle mounted LIDAR is presented in Figure 2.3.

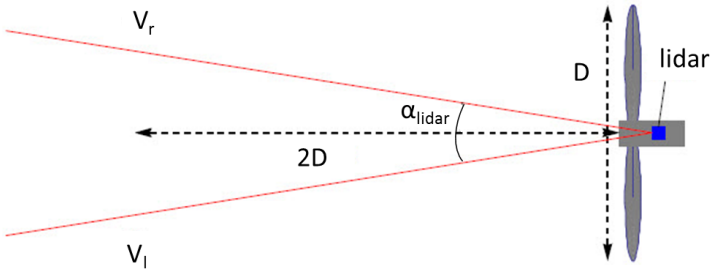

Figure 2.3: Nacelle mounted LIDAR. Figure from [20].

The LIDAR emits a pulsed system that through the Doppler effect measures the wind speed at a distance from 50m up to 300m upstream of the wind turbine. The main assumption of the LIDAR the is a horizontally homogeneous wind speed (no horizontal shear) [21]. The laser sends pulses (approximately 10,000 for each beam) in two lines separated by a horizontal angle a_{lidar} of 30^o. The mean wind speed V_h is computed by the average longitudinal and transverse components V_{long} and V_{trans} respectively, from Equation 2.2, where $V_{long} = \frac{V_l+V_r}{2cos(an)}$ and $V_{trans} = \frac{V_l-V_r}{2sin(an)}$. V_l and V_r are the left-hand and the right-hand laser pulse respectively. Comparison between a nacelle mounted LIDAR and a mast-mounted cup-anemometer showed less scatter and better correlation with the wind in the power curve resulting from the LIDAR [20, 21].

$$V_h = \sqrt{V_{long}^2 + V_{trans}^2} \tag{2.2}$$

2.2 Wave Distribution

Hydrodynamic forces on offshore structures are a major consideration during their design. Measurements performed by the Maritime Research Institute Netherlands (MARIN) and the Energy Research Center of the Netherlands (ECN) proved that breaking waves can induce excessive oscillations and accelerations on the monopile sub-structure of an offshore wind turbine [22]. There are various mechanisms that generate wave motion, but the dominant

and the one applied in aero-elastic codes to account for hydrodynamic forces are the wind generated waves.

Different regular wave theories are reported in the literature to describe the water particle kinematics. The Airy wave theory and Stokes theory are analyzed in reference [23]. Due to the simple implementation of the regular Airy theory, it is widely used in ocean engineering to describe the wave kinematics and dynamics with quite high accuracy. The main representation along with the main characteristics of the regular wave is shown in Appendix A. The waves experienced at any point in the sea are not regular. The irregular waves can be considered as the superposition of an infinite number of regular waves, which are often described by a spectrum that indicates the amount of wave energy at different wave frequencies.

In deep water the wave height follows the Rayleigh distribution [24]. For shallow waters (below 30m) though a more representative combined Rayleigh-Weibull distribution was proposed by Battjes and Groenendijk in reference [25] and tested with wave measurements at three different sites in the German North Sea [26].

Known wave spectra reported in literature are [27]:

- Pierson-Moskowitz
- JONSWAP
- Bretschneider
- DNV Spectrum
- Ochi Spectrum

For North Sea applications the most representative spectra are the Pierson-Moskowitz (Equation A.16) and the JONSWAP (Equation A.17) . The JONSWAP Spectrum is an extension of the Pierson-Moskowitz that gives room for sharper peaks. A comparison between the two spectra is presented in Figure 2.4.

The hydrodynamic forces due to surface elevation are accounted for by applying a stretching method. Stretching techniques reported in the literature are the vertical, the extrapolation and the Wheeler stretching, with the latter being the most commonly used. The Wheeler stretching stretches the water column linearly above the mean sea level. According to the Airy wave theory the horizontal particle velocity is given by the derivative of Equation A.15a multiplied with the scaling factor $E(z)$ calculated by Equation 2.3a, where k_w is the wave number, d the water depth, η the wave surface elevation and z the vertical position. When Wheeler stretching is applied z is substituted by z' (Equation 2.3b) [9, 10].

$$E(z) = \frac{\cosh[k_w(d+z)]}{\sinh(k_w d)}, \quad z' = \frac{z+d}{1+\frac{\eta(t)}{d}} \tag{2.3}$$

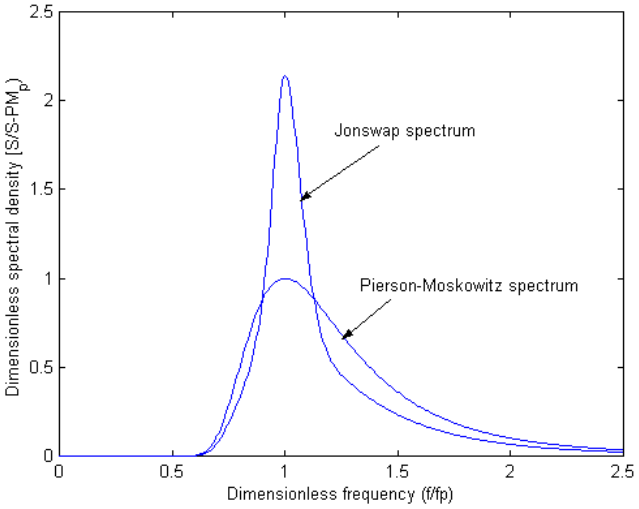

Figure 2.4: JONSWAP vs. Pierson-Moskowitz spectrum. Figure from reference [28].

To predict the response of an offshore wind turbine the joint probability of the wind and waves needs to be estimated. In reference [29] a joint probabilistic model of the mean wind speed, the significant wave height and the spectral peak period is presented. The wind is the governing parameter and the joint model is used to create a contour surface, where the exceedance probability corresponds to 100 year return period. The joint probability density function (PDF) $f_{UH_sT_p}$ of the wind, significant wave height and peak period is given by Equation 2.4, where $f_U(u)$ is the wind PDF, $f_{H_s|U}$ the significant wave height PDF conditional to the wind and $f_{T_P|H_sU}$ the peak period PDF conditional to a given wind and significant wave height.

$$f_{UH_sT_p}(u,h,t) = f_U(u) \cdot f_{H_s|U}(h|u) \cdot f_{T_P|H_sU}(t|h,u) \tag{2.4}$$

For a mean wind speed with a Weibull or a Rayleigh distribution, the conditional distribution of the significant wave height H_s is a 2-parameter Weibull distribution, while for a given combination of mean wind speed and significant wave height the most appropriate distribution for the peak period T_P is a log-normal distribution [29]. In reference [30] the influence of the joint distribution of wind and wave conditions on the support structure loads is examined. A probabilistic method is applied to estimate the long term loads from short-term distributions.

2.3 Soil Model

The importance of an accurate model that accounts for the dynamic soil-pile interaction is often reported in the literature. The pile foundations are designed to sustain both static and cyclic loads. Soil properties, like soil stiffness, cohesion strength and soil plastic resistance have a significant influence on the response of the wind turbine support structure. An investigation

of the effects that the different clay properties have on the support structure is performed in reference [31]. The presented results make clear that the accurate calculation of the support structure's response requires reliable values of the soil properties. In reference [32] the influence of the soil on the wind turbine dynamic response is examined. Two different types of layered soil, drained/un-drained sand and the effect of stratification are tested and their impact on the wind turbine response is quantified. Three different soil-pile interaction models, a) distributed springs model, b) apparent fixity model and c) uncoupled springs model that are usually applied in the aero-elastic codes are presented and validated in reference [33]. For the lateral loading of the monopile the commonly used p-y curve (lateral resistance-deflection), where the soil stiffness is modeled by distributed springs is shown in Figure 2.5a. The elastic soil that supports the wind turbine monopile is discretized with the use of springs distributed along the pile length. The soil spring forces are depth dependent. Based on the DNV guidelines [11] for every deflection y there is a lateral resistance p per unit length of pile according to the type of the soil (sand or clay). For small deflections y, the relation is linear (the deflection of the soil is proportional to the resistance in the soil-pile interaction). The equations used for the generation of the p-y curve can be found in Appendix A.

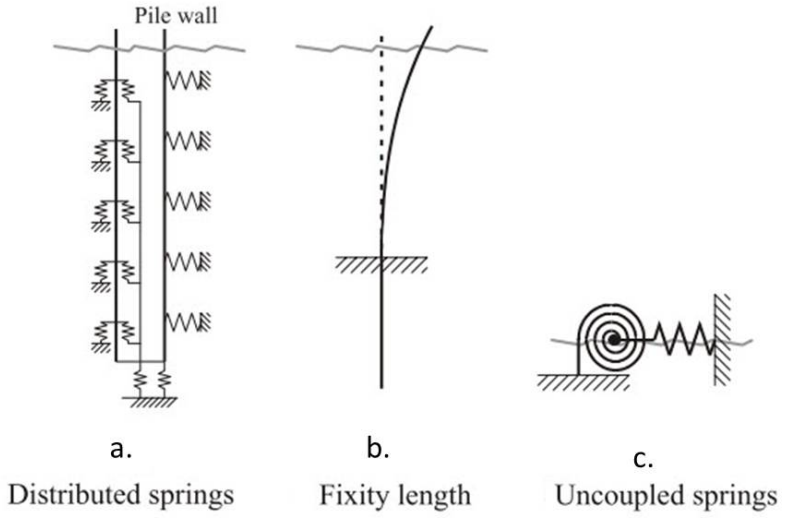

Figure 2.5: Soil-foundation models for pile structures. a) distributed springs, b) effective fixity length c) uncoupled springs. Figure from reference [34].

For the effective fixity length model (Figure 2.5b) the effect of the soil and the true monopile foundation are substituted by a pile with an effective penetration and effective properties below the seabed. The range of the effective length is between 3.3 and 3.7 times the pile diameter [34]. The apparent fixity length L represents the equivalent pile that will result to the same rotation and the same lateral deflection at its free end, under the same moment and shear applied at the mudline on the real pile. The mode shapes and the natural frequencies for the whole system should be the same when applying the apparent fixity model and the higher fidelity p-y model. The main advantage of this method is its simplicity.

In reference [35] a comparison between a fixed base model (rigid connection of the turbine's

support structure to the seabed) and the two flexible models mentioned above is performed, to investigate the influence of the various foundation models on the extreme loads. The results for the flexible models are comparable with the fixed base, but they suggest an increase of 15% on the 20-year accumulated fatigue contrary to the latter, due to their lower stiffness. The power spectra of the loads demonstrated tower resonance peaks at lower frequencies for the flexible foundation. This indicates a great effect on the long-term loads due to foundation modeling.

A study by Zaaijer in [36] showed that the results implementing the effective fixity length model present large variations for different soil conditions, thus increasing the inaccuracies of the natural frequencies. A sensitivity analysis is performed on the models, using the energy distribution, to identify the reasons (measurement uncertainty, aging effects, location) that lead to variations on the dynamic behavior of an offshore wind turbine. The different types of support structures presented in Figure 3.1 display sensitivity in different parameters, like scour, soil and foundation properties [36]. The simulation results were validated with experimental data from two wind farms 'Irene Vorrink' and 'Lely'. Through this study the importance of an accurate and reliable soil profile is pointed out, especially when the depth of the first stiff soil layer affects the dynamic response of the system.

Combined loads from waves and currents are responsible for the development of scour around wind turbine monopiles. The development of scour can modify the natural frequency of the structure, making scour prediction necessary in order to reduce the uncertainties during the dimensioning process. In reference [37] numerical and experimental modeling of scour gave deeper knowledge about its development around the wind turbine structure.

Chapter 3

Wind Turbine Design

In this chapter the different parts of an offshore wind turbine are presented. In the first section the various foundation types and the hydrodynamic loads are described. The fatigue on the blades and the loading due to wake are also explained. The controller characteristics are analyzed in the last section of the chapter.

3.1 Support Structure Loading

The design of the support structure plays an important role in the dynamic response of the offshore wind turbines. Although the offshore oil and gas industry gives an insight into the dynamic behavior of offshore structures, the assessment of offshore wind turbines differs significantly in some aspects. Apart from the wave excitation, the loading on the rotating blades due to the wind introduces at least two more excitation frequencies, the rotational frequency (1P) and the frequency caused by the blades passing in front of the tower (3P). The first natural frequency of oil and gas platforms is higher than the wave excitation. In the case of an offshore wind turbine, the first natural frequency is between the wave and the third harmonic of the rotational frequency. Consequently the challenge for offshore wind turbines is increased due to the requirement that their natural frequency should avoid a) wave excitation and b) blade passing excitation.

Time domain simulations with an increased number of seeds to capture the stochastic behavior of the wind and wave conditions are required both for fatigue and ultimate load analysis. The loading conditions considered for these analysis should cover a wide range of load cases from normal turbulence wind to extreme wind and wave conditions at stand still/idling and during power production. Therefore, the high computational time necessitates the simplest

possible modeling of the sub-structure/foundation that results in accurate prediction of the dynamic behavior of the system.

For shallow water depths the most commonly used sub-structures and foundations reported in literature are (Figure 3.1):

- Monopile
- Tripod
- Suction bucket
- Gravity base

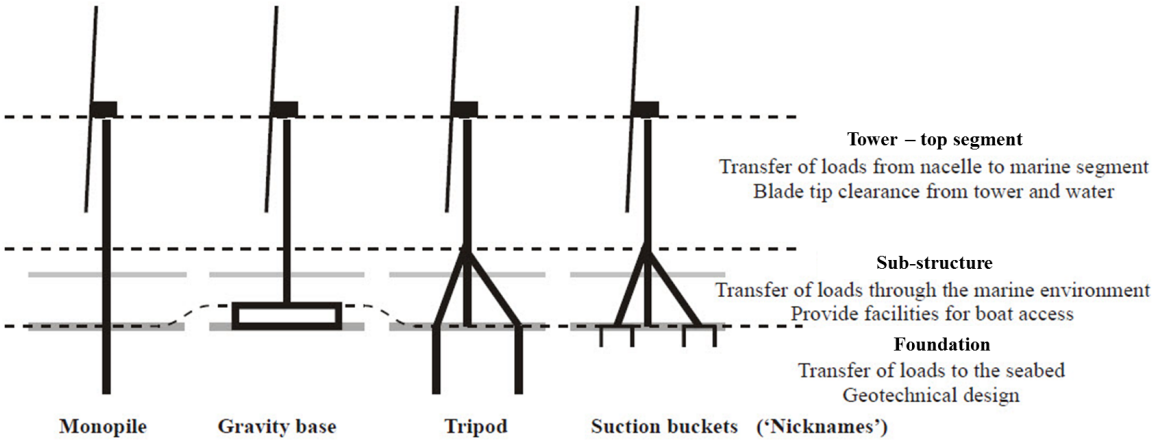

Figure 3.1: Sub-structure and foundation models. Figure adapted from reference [38].

Moving into deeper water, where steadier and stronger wind is provided, different solutions are required. For medium water depths (around 50m) Jacket foundations are installed, while for deep waters the floating concept is the only feasible solution.

In reference [39] a preliminary design of an offshore wind turbine monopile sub-structure is presented. The identification of the structural response to extreme loads and a frequency analysis to ensure that the natural frequencies of the tower do not coincide with the blade passing or the wave excitation are the first steps of the process. The wave height, the wave period and the water depth are used in the Airy linear wave theory to calculate the wave particle velocities and accelerations. These velocities and accelerations are then used as inputs to the Morison's equation (Equation 3.1) to estimate the moments and forces on the monopile. A simple but accurate sub-structure/foundation model is a driving factor in the investigation of the dynamic behavior of offshore wind turbines. As proposed by Zaaijer in [36] the inaccuracies in the prediction of the dynamic response introduced by the support structure modeling can be reduced by implementing simple models and verifying the model accuracy with experimental data.

An extensive comparison between the different foundation concepts for shallow water depths is presented in reference [38]. A 6MW wind turbine with the same tower is considered for the analysis, mounted on the four different support structures presented in Figure 3.1. A study conducted in reference [40] proved that the stress at the upper part of the tower due to hydrodynamic loading may be in the same order of magnitude as below the mean sea level, because of the dynamic behavior of the support structure. Therefore, the calculation of hydrodynamic loading is essential for the design of the support structure of an offshore wind turbine, contrary to the limited impact that it has on the design of the Rotor Nacelle Assembly (RNA). The forces that a pile in water is subjected to are shown in Figure 3.2, where the drag and inertia wave forces are given by Morison's Equation (3.1) and the wind drag force F_w by Equation 3.2. u_w and $\dot{u_w}$ are the wave velocity and acceleration respectively, U is the wind speed, ρ_α and ρ are the air and water density respectively, C_{Dw} is the air drag coefficient and A the cross section area. The first term in the Morison's equation is the drag force (C_D is the drag coefficient) and the second the inertia force ($C_M = C_m + 1$ is the inertia coefficient), which consists of the hydrodynamic mass force and the Froude-Krylov force. The Morison's Equation is valid for a ratio of pile diameter over wave length less than $(D/\lambda) < 0.2$. In the case that this ratio takes higher values, the presence of the pile influences the waves and the diffraction effect should be taken into account. An experimental investigation of the hydrodynamic loads was performed in reference [41].

$$\begin{aligned} F_m &= \frac{1}{2}\rho C_D D u_w |u_w| + \rho C_m A \dot{u_w} + \rho A \dot{u_w} \Rightarrow \\ F_m &= \frac{1}{2}\rho C_D D u_w |u_w| + (C_m + 1)\rho A \dot{u_w} \end{aligned} \tag{3.1}$$

$$F_w = \frac{1}{2}\rho_\alpha C_{Dw} A U^2 \tag{3.2}$$

In the case of an offshore wind turbine mounted on a monopile with diameter 3-5m, installed in shallow water depth the inertia component is dominant [39]. Therefore the valid choice of the inertia coefficient C_M is important for the accurate estimation of the loading on the pile. Common values used for the coefficients in the Morison's Equation are $C_M = 2$ and $C_D = 0.65$ [42].

Although small waves can usually be simulated using the linear airy theory, shallow waters can result in highly non-linear waves. The real wave record depicted in Figure 3.3 shows characteristics that cannot be captured by linear theory, such as sharper crests, flatter troughs and larger amplitudes. In reference [43] recommendations for a different approach of the wave model (distribution and hydrodynamic properties) depending on the type of the foundation are discussed. The different wave models usually applied are:

- Airy linear wave theory (regular and irregular) [8]: simple implementation, with the disadvantage that it cuts off wave peaks and troughs.

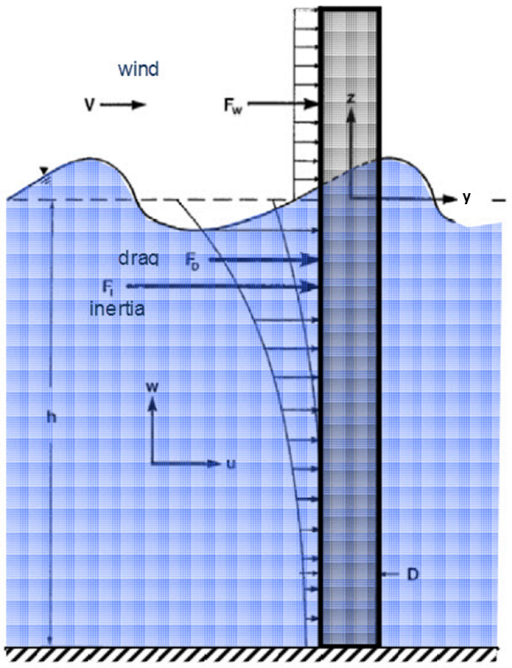

Figure 3.2: Loading on a pile due to wind and waves. Figure adapted from reference [23].

- Wheeler Stretching [44]: the wave kinematics calculated at the mean-water level are stretched up to the true surface, due to water elevation.
- Deans Stream Function [45]: it has replaced most of the cases where regular Airy theory is insufficient.
- Non linear wave theory [46]: More accurate description of the hydrodynamic loads a wind turbine installed in shallow waters is subjected to.

Using the Airy linear theory in shallow waters can result in an underestimation of the lifetime fatigue of the monopiles from 60% to 70%, in contrast to 5% for deeper water. The inappropriate application of the linear Airy theory should also be noted in the case of gravity base structures that suffer from the combination of heave and surge motions [43].

When the wave frequency and its harmonics coincide with the natural frequencies of the structure, the dynamic response of the wind turbine is amplified (resonance). If the ratio between the multiples of the structure's natural frequencies and the wave harmonics is an integer, the wind turbine is moving in phase with the wave when the rising crest reaches the sub-structure and high loads due to dynamic amplifications will occur. Observations proving that theory are presented in reference [43] from an instrumented offshore wind turbine at Blyth. All linear theories underestimate the maximum measured overturning moment, while the non-linear stream function gives a better estimation. Measurements of the fatigue damage for one idling wind turbine and one in operation showed good correlation between the loads and

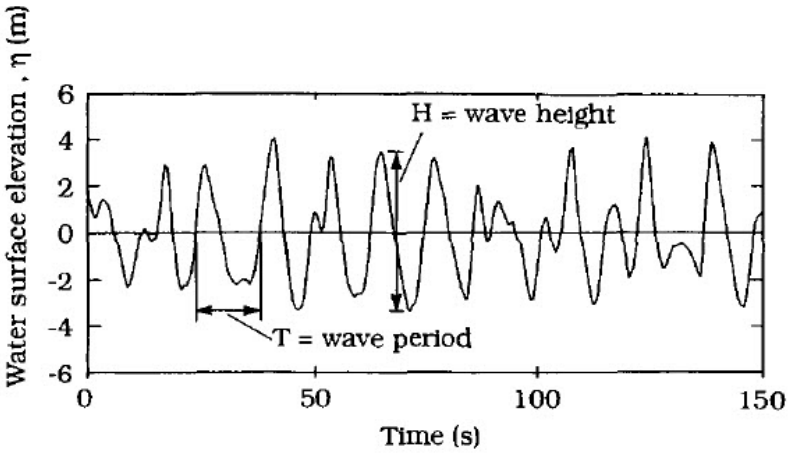

Figure 3.3: Recorded Sea Surface. Figure from reference [7].

the wave height (turbine off) and the loads and the mean wind speed (turbine on), indicating the importance of both wind and wave loads on the design of the support structure.

The narrow band of the support structure natural frequency to avoid resonance with wave excitation and blade passing renders the dynamic behavior of the support structure sensitive to changes in the geometry. As the wind turbines become larger, the natural frequency of the support structure is decreased, moving closer to the part of the wave spectrum with the highest energy content. Its design is driven by the ratio between the diameter and the wall thickness D/t_{th}. Higher values of this ratio result in lighter constructions, increasing though the risk of buckling due to local impacts of waves and ships. Adjustments to the natural frequency of the support structure can be done through variations of this ratio.

3.2 Blade Loading

The aerodynamic loads on the blades are mainly a combination of the turbulent inflow, the yaw misalignment angle, the vertical wind shear and the tower existence. In the case of extreme loads their determination depends upon either extensive simulations or field measurements. In reference [47] a probabilistic approach is used to estimate the long-term loads based on measurements from the Blyth offshore wind farm in the UK. The limited amount of data poses a limitation in the prediction of loading, while simulations can guarantee a wide range of environmental conditions. On the other hand, the field data provide a real representation of the conditions and the dynamic response of the system, contrary to the simulations that depend on how closely the model corresponds to reality. It's always a compensation between accurate representation and available data, that makes the combination of simulations and field measurements crucial for accurate results. What is important in the reliability-based design of wind turbines is the estimation of a long-term load, associated with a given exceedance probability. The loads acting on the offshore wind turbine are very site dependent. For the

Blyth wind farm examined in reference [47], it was observed that the very shallow water and the changes in the mean water level (tidal variations) cause considerable changes in the hydrodynamic loading of the structure, while breaking waves also affect the loading of the support structure.

The response speed of the controller can reduce considerably the extreme loads on the system. Spatial gusts with an extreme time rise are assumed to cause excessive loading on the blades. In reference [48] a gust with extreme time rise is examined. The blade flap moments caused by the gust are not higher than those due to 1P excitation or normal turbulence. Therefore, the blade design of pitch regulated wind turbines based on extreme loading is not governed by spatial gusts with extreme time rise. In the same work a study of the gust shape that might lead to ultimate loads is recommended.

The robustness of the extrapolated loads is analyzed in reference [49], by examining the sample of the extreme loads, identifying only one extreme per 10min simulation to avoid correlations. For the design of the wind turbine apart from the extreme load, the identification of the loads that are happening at the same instant as the primary load is also necessary. Contemporaneous loads obtained from scaling the DLC 1.3 load case time series is suggested in reference [50]. In reference [51] a more advanced technique to obtain the contemporaneous loads corresponding to the extrapolated extreme load is presented, based on the mode of the contemporaneous load distribution.

Loads that might be smaller than the static yield limit of the material can cause failure through cyclic loading (fatigue failure). In reference [52] the reasons that originate the failure in the blades, like abrupt change of thickness, local geometry of stress concentrator and cracks propagation, are examined. The cracks are very often located in the transition area between the root of the blade and the zone of airfoil profile.

The fatigue strength is investigated by performing a fatigue analysis using S-N curves (example of S-N curve shown in Figure 3.4) and applying the Miner's rule to calculate the damage equivalent loads. The S-N curve provides the number of load cycles that the structure can stand without failure, as a function of a constant amplitude cyclic load. The damage caused by a specific load is given by Equation 3.3a and the cumulative damage by Equation 3.3b, where n_i is the applied number of cycles and N_i is the number of cycles that result to failure for a certain load. The number of cycles for a given stress range is calculated with the technique of Rainflow counting. The material is expected to fail for $D_f \geq 1$. The 1Hz equivalent load, associated to a number of equivalent cycles (n_{eq}) equal to the total simulation or measurement time, that leads to the same damage as the summation of all independent loads, is given in Appendix B. In reference [53] the failure probability of different wind turbine components for various m values is estimated.

$$D_i = \frac{n_i}{N_i}, \quad D_f = \sum_{i=1}^{M} \frac{n_i}{N_i} \tag{3.3}$$

Although the fatigue damage in wind turbine blades is due to turbulence, the unsteady

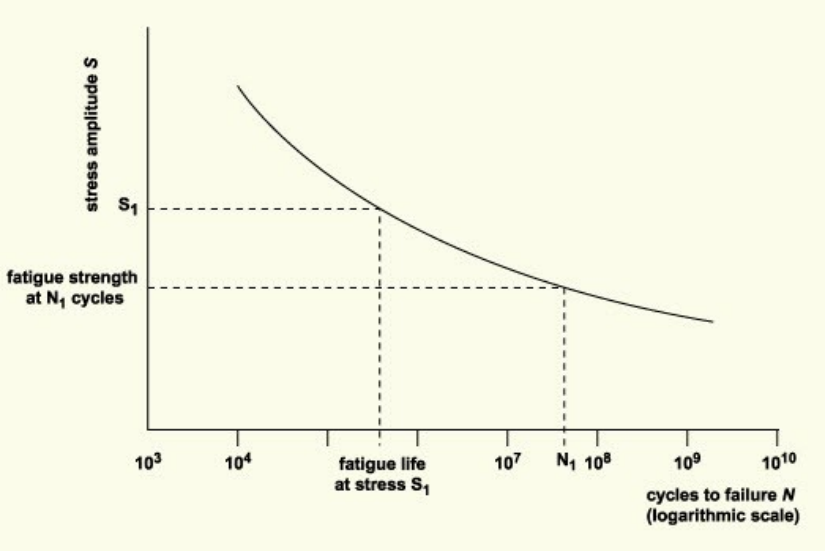

Figure 3.4: Example of an S-N curve.

effects associated with the tower shadow are also examined in reference [14]. One of the main parameters influencing the blade fatigue due to tower shadow is the rotor plane distance from the tower. The stress variation on the blades because of passage from the stagnation zone, created by the tower and depending on its diameter, seems to contribute significantly to blade fatigue loads. The tower shadow does not appear to have an impact on the power production due to limited tower passage time. In reference [54] it was demonstrated that dynamic stall could be caused by tower passage, reducing in that way the aerodynamic damping and increasing the dynamic response. Two methods for calculating the aerodynamic loads connected to the tower shadow, are presented in reference [55]. The substitution of the mono-tower with a tripod is suggested in reference [56] to reduce the cumulative fatigue on the blades. Even though the disturbance of the wind turbine blade is greater because of the three legs, the fatigue damage is lower.

The different wind profiles also have an effect on the fatigue life of wind turbines as reported in reference [57]. Accounting for the atmospheric stability classes, the fatigue damage can change significantly. The logarithmic law used to model the wind shear seems to underestimate the fatigue loads leading to a non-conservative approach.

3.2.1 Wake Effect

Wind turbines placed inside wind farms experience different operating conditions than those on the outside rows. The average mean wind speed is decreased, while the turbulence intensity is increased resulting in greater loads on the structure and lower power production. This increased turbulence intensity can cause a significant reduction in the lifetime of a wind turbine. In order to account for this extra fatigue, simulations with different turbulence models should be performed. A number of wake models are described and compared in reference [58]. Prior

investigations [59, 60] concluded that the effect of the wake on the fatigue loading of a wind turbine is more pronounced for low-turbulence sites, e.g. offshore sites. Therefore the wake effect is required for the design of offshore wind farms.

An effective turbulence intensity I_{eff} (Equation A.4), defined as the constant turbulence intensity resulting in the same material fatigue as variable turbulence from all directions is proposed by the IEC 61400-1 [17] to account for the wake effect of the surrounding turbines. The most well-known model for fatigue analysis under the wake effect was developed by Frandsen [61]. The Frandsen's model, also proposed by the IEC 61400-1 standard [17] to account for the wake effect inside a wind farm, suggests that the wake turbulence is a combination of the ambient turbulence and an added turbulence [62] (Equation A.5). The effective turbulence intensity I_{eff} accounting for ambient turbulence and turbulence generated from the wake effect is used as a primary design parameter.

An investigation based on the Vindeby experiment was performed in reference [63] to examine the wake effects on the fatigue loading of offshore wind turbines. In the wind field analysis the wind speed deficit, the turbulence intensity, the horizontal shear and the turbulence spectrum length were taken into consideration. A good agreement between measurements and simulations with the aero-elastic code HawC was shown. In reference [64] the fatigue was found to be proportional to the wind standard deviation. The decrease in the power production due to the wake effect is estimated through the deficit in the mean wind speed, while the wake loads are predicted using increased turbulence models. In reference [65] a different simulation method is suggested that accounts for a simultaneous analysis of the two mentioned wake effects. The different mechanisms that cause the wake loads, compared to the loads due to increased turbulence intensity are the main reasons for the necessity of such a method. Essential for the prediction of the fatigue due to wake is the accurate representation of the wake region downstream of the wind turbine. In reference [66] an investigation of the wake characteristics is performed through the implementation of a 3D unsteady vortex-panel method, which has been validated with experimental data from the National Renewable Energy Laboratory.

3.3 Controller

The modern wind turbines contain a controller that regulates their performance depending on the wind speed. The aim of the controller is to maximize power production while minimizing the fatigue of the structure, ensuring that no extreme load results from the controller response. The latter can be achieved by avoiding excessive pitch activity and peaks in gearbox torque. The controller guarantees minimum component fatigue loads and optimal power output for wind speeds below rated by optimizing aerodynamic efficiency and rotational speed and constant power production for wind speeds above rated by applying aerodynamic torque within the design limits [67]. The operation is separated in three regions. *Region 2* corresponds to the variable rotational speed operation for optimal power production. In *region 2 1/2* the rotational speed is kept constant to its rated value and the controller is performing a linear adjustment to the generator torque values. *Region 3* corresponds to maintaining the power to rated by pitching the blades [68]. Figure 3.5a presents the three controller regions with re-

spect to the wind speed. For wind speeds above rated the error between the measured and the rated rotor speed is used as a feedback to the controller to regulate the pitch angle and prevent blade stall, maintaining rated power. A simple representation of a Proportional-Integral (PI) controller is shown in Figure 3.5b.

The proportional and integral gains K_P and K_I of the PI controller are given by Equation 3.4 and the gain-correction factor GK that corrects their values for higher wind speeds, due to non-linear characteristics by Equation 3.5 [69], where $I_{Drivetrain}$ is the inertia of the drivetrain given by $I_{Drivetrain} = I_{Rotor} + N_{Gen}^2 I_{Gen}$, ($N_{Gen}$ is the gear ratio I_{Rotor} is the rotor inertia and I_{Gen} is the generator inertia) Ω_0 is the rated rotor speed, $\omega_{\phi n}$ is the natural frequency of the system, ζ_ϕ the damping ratio, θ the pitch angle and $\frac{\partial P}{\partial \theta}$ the sensitivity of aerodynamic power to blade pitch in region 3. The parameter θ_κ is the blade pitch angle at which the pitch sensitivity has doubled from its value at the rated operating point for $\theta = 0$. For a more detailed explanation of the controller operation refer to [69] and [70].

Active control is usually implemented to reduce the loads on the wind turbine. Prior investigations regarding the mitigation of extreme and fatigue loads through active control have also been performed, such as in reference [71]. Methods usually suggested for achieving this are the use of filters to mitigate modal response, sensors at the blade root or the tower top that sense loads, accelerations that are fed to the controller for facilitating individual pitch control and generator torque control in the region when the wind speed is just above rated speed. In reference [72] the twist of the blade to modify the aerodynamic performance that counteracts for the bending due to aerodynamic loading to mitigate the loads, keeping the power production constant, is proposed as a control strategy. In a Sandia report [73], fifteen different devices, like microtabs and active stall strips for active load control are discussed and their potential when implemented on a wind turbine is analyzed. When collective blade pitch control is used and no sensors for load measurement are present, the aim of keeping the power constant at mean wind speeds above rated and mitigating the extreme blade loads simultaneously is achieved through effective control algorithms.

$$K_P(\theta) = \frac{2 I_{Drivetrain} \Omega_0 \zeta_\phi \omega_{\phi n}}{N_{Gear}\left[-\frac{\partial P}{\partial \theta}(\theta = 0)\right]} GK(\theta) \qquad K_I(\theta) = \frac{I_{Drivetrain} \Omega_0 \omega_{\phi n}^2}{N_{Gear}\left[-\frac{\partial P}{\partial \theta}(\theta = 0)\right]} GK(\theta) \tag{3.4}$$

$$GK(\theta) = \frac{1}{1 + \frac{\theta}{\theta_\kappa}} \tag{3.5}$$

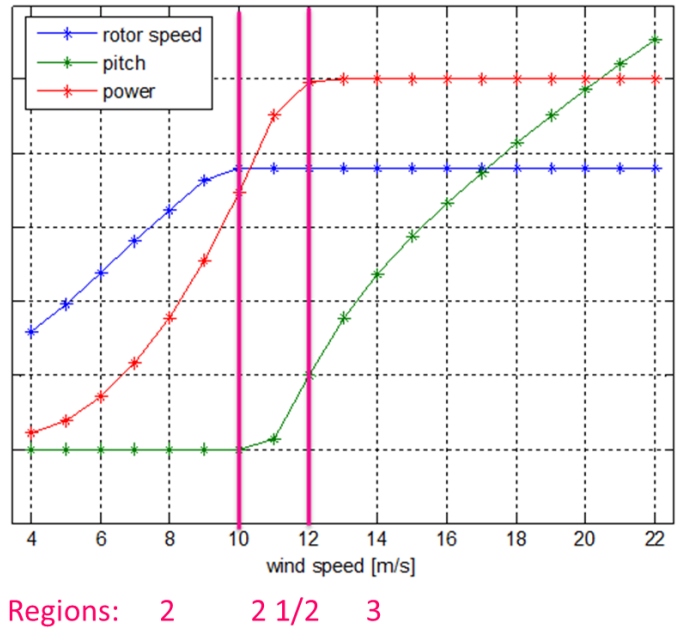

(a) Controller regions on the power curve .

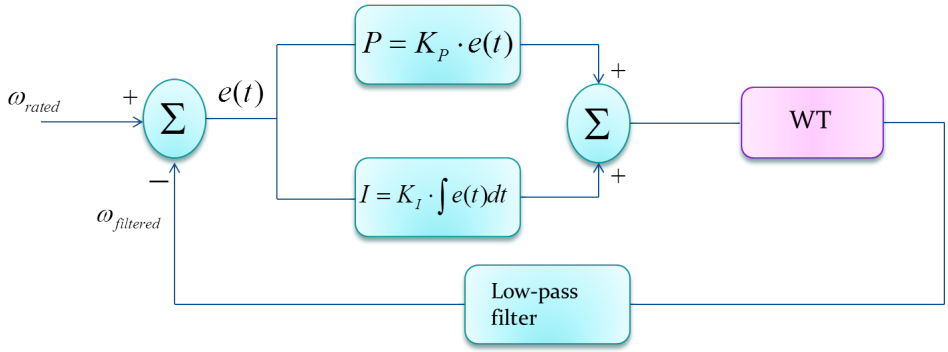

(b) PI controller.

Figure 3.5: Controller regions and PI controller

Chapter 4

Damping

Damping is the dissipation of energy from a structure that is vibrating. Damping is often described as viscous (proportional to velocity), hysteretic (structural damping), and coulomb (due to friction) [74]. The mechanisms and types of damping depend on the characteristics of the structure and the physical processes present at a given situation. Usually they are complicated and any mathematical representation of damping in the equations of motion is only an approximation of the real system. The nature of energy dissipation is most of the times unknown and viscous damping is often used to approximate a non-linear behavior (equivalent viscous damping). In the current chapter various techniques for damping identification are presented.

4.1 Rayleigh Damping

The damping mechanisms in a structure can be highly non-linear. Therefore, classical damping is a mathematically convenient way to represent damping in systems. The damping matrix can be diagonalized by the mode shapes in a similar way as the mass and stiffness matrices, based on the orthogonality of the modes [75]. A classical damping matrix can be constructed if Rayleigh damping is considered, where the damping is mass and stiffness proportional (Equation 4.1). Figure 4.1 presents the mass and stiffness proportional damping along with the Rayleigh damping as a function of the system's frequency. The mass term ζ_m is inversely proportional to the frequency and the stiffness term ζ_k proportional to it.

$$C = \alpha_1 M + \alpha_2 K \tag{4.1}$$

The modal damping ratio ζ_n of a system with Rayleigh damping is given by Equation 4.2, where α_1 and α_2 are the Rayleigh coefficients, and ω_n the natural frequency of the examined mode.

$$\zeta_n = \frac{\alpha_1}{2}\frac{1}{\omega_n} + \frac{\alpha_2}{2}\omega_n \tag{4.2}$$

If the damping ratios of two modes with natural frequencies ω_n and ω_r are assumed equal, they can be used for the calculation of the coefficients α_1 and α_2.

$$\alpha_1 = \zeta\frac{2\omega_n\omega_r}{\omega_n + \omega_r}, \quad \alpha_2 = \zeta\frac{2}{\omega_n + \omega_r} \tag{4.3}$$

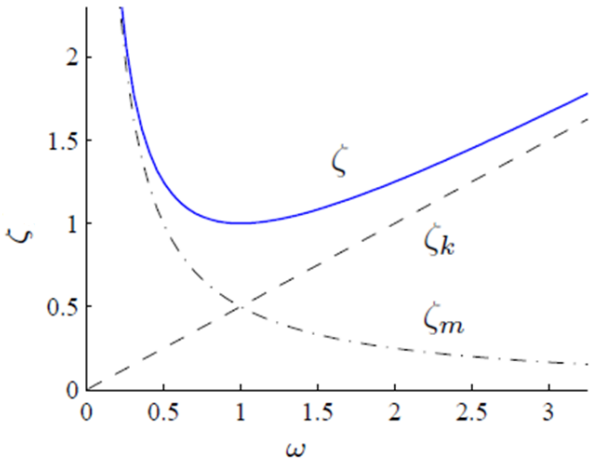

Figure 4.1: Damping ratio with respect to frequency in structures with Rayleigh damping. Figure from reference [76].

A more general expression for classical damping is known as Caughey damping (Equation 4.4), where ν is the number of degrees of freedom in the system.

$$c = \sum_{l=0}^{\nu-1} a_l [M^{-1}K]^l \tag{4.4}$$

Equation 4.4 with only the first two terms reduces to the Rayleigh damping. The modal damping ratio is given by:

$$\zeta_n = \frac{1}{2}\sum_{l=0}^{\nu-1} a_l \omega_n^{2l-1} \tag{4.5}$$

It is often unrealistic to assume that all modes have the same constant damping in order to calculate the Rayleigh coefficients for the whole system. In reference [77] a procedure for the estimation of the coefficients α_1 and α_2 for systems with large degrees of freedom is presented.

The accurate estimation of the damping has a pronounced effect on the load and lifetime prediction as well as on the dynamic response of the system. The total damping of the first bending mode is a combination of aerodynamic, structural, hydrodynamic, soil damping and damping due to damping devices [78, 79]. The additional offshore damping is given by Equation 4.6, where $D_{radiation}$ is the damping from wave creation due to structure vibration, $D_{vis,hydro}$ is the viscous damping due to hydrodynamic drag, D_{steel} is the material damping, D_{soil} is the soil damping due to inner soil friction and D_{damper} the damping from dampers. One of the first attempts to estimate the damping of an offshore structure was made by Cook in reference [80], where the damping of the first fundamental mode of an oil rig is identified. In reference [81] measurements of all sources of damping in an offshore wind turbine at Horns Rev 1 and the Burbo offshore wind farms resulted in a logarithmic decrement δ of about 10% (excluding aerodynamic damping). It was concluded that the available damping is more than what it is used in the simulations. In the same study the case of the side-side aero-elastic damping is examined, and its importance to decrease cross-wind loads due to wind-wave misalignment is pointed out. In reference [82] the estimated logarithmic decrement considering only the additional offshore damping (no aerodynamics included) is 14-15% (2.25% damping ratio).

$$D_{add,offsh} = D_{radiation} + D_{vis,hydro} + D_{steel} + D_{soil} + D_{damper} \tag{4.6}$$

In reference [82] typical values of the individual damping ratios for an offshore wind turbine mounted on a monopile are proposed: steel damping $\zeta_{steel} = 0.19\%$, damping from the passive damping devices on the tower top $\zeta_{tower} = 1.36\%$, hydrodynamic damping $\zeta_{water} = 0.12\%$ and soil damping $\zeta_{soil} = 0.58\%$. The total damping of the system is given by Equation 4.7.

$$\zeta = \zeta_{steel} + \zeta_{tower} + \zeta_{aero} + \zeta_{water} + \zeta_{soil} \tag{4.7}$$

4.2 Aerodynamic Damping

The aerodynamic damping, which consists the greatest part of the total damping during normal operation can reduce significantly the fatigue on the support structure. The basics of aerodynamic damping are presented in Figure 4.2. When the tower is moving forward, the blades see a higher wind speed, reacting with an aerodynamic force that opposes the tower top motion. When the tower is moving backward this aerodynamic force is reduced. In both cases the tower motion is decreased.

The total damping of the blades which is equal to the aerodynamic plus the structural damping can be calculated from the logarithmic decrement δ with the use of Equation 4.8. In

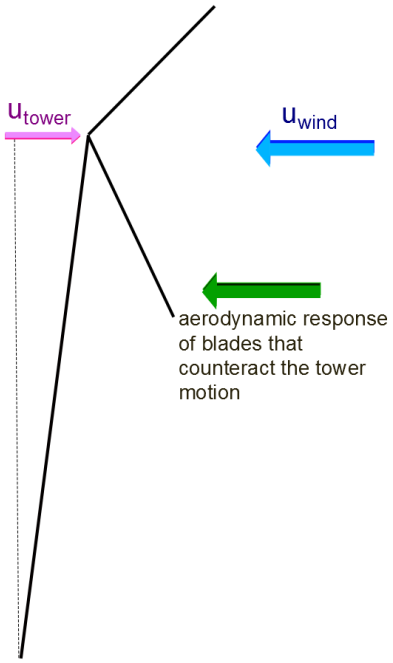

Figure 4.2: Principle of aerodynamic damping

reference [83] different ways of estimating the aerodynamic damping for constant speed and variable speed wind turbines are presented.

$$\xi_{tot} = \xi_{aero} + \xi_{struct} \Rightarrow \xi_{tot} = \frac{\delta}{\sqrt{4\pi^2 + \delta^2}} \tag{4.8}$$

4.3 Damping Identification

There are various ways of estimating the total damping of a system. Figure 4.3 presents schematically the different methods for identifying damping in a vibrating structure. The damping can be extracted either as a modal parameter or as a full damping matrix C. The modal damping identification can be divided into two groups: a) non-parametric methods applied in frequency domain and b) parametric methods implemented in time domain [84]. In reference [85] a comparison of four different system identification methods (Peak-picking, Polyreference LSCE, Stochastic Subspace method and prediction error) emphasizing on the advantages of each technique is presented. In reference [86] a survey of viscous damping identification techniques for the estimation of the full damping matrix is demonstrated. These methods can be separated into two categories: a) damping identification from modal testing or b) from response measurements. Most of the techniques are extensively applied to large civil engineering structures.

For large structures like wind turbines forced excitation can be difficult and expensive.

Therefore, the available ambient excitation is used to measure the response and derive the system characteristics, a technique called Operational Modal Analysis (OMA). Due to no requirement of excitation equipment the OMA is a cheaper technique. The results correspond to realistic levels of vibration and not artificial ones generated by shakers. Based on recorded time series (output) of the system response and assuming that the ambient excitation is random in time and space (stochastic) like wind and waves, the modal parameters and dynamic characteristics of the whole system can be extracted. This process is also called Stochastic System Identification. The great potential of operational modal analysis in wind turbines was firstly presented in references [87, 88, 89]. Different applications of Experimental and Operational Modal Analysis are discussed in references [90, 91, 92]. For a more detailed explanation of modal analysis the reader is addressed to references [93, 76, 94, 90].

4.3.1 Full Damping Matrix

The full damping matrix of a structure provides information about the spatial distribution of the damping. Due to the unknown nature of damping it is usually convenient to assume viscous damping in the system that allows the implementation of modal analysis. Viscous damping though is not the only linear damping model that can be implemented in a vibrating structure. In reference [95] a more general damping model within the linear range is introduced.

In general the modal damping matrix is not diagonal, since there is no physical reason why a system should be viscously damped. However, for lightly damped structures the damping matrix is assumed to uncouple with the mode-shapes.

In reference [95] the nature of proportional damping is analyzed and the condition that the system matrices should satisfy so that classical modes (modes that diagonalize the mass, stiffness and damping matrices) appear in viscously damped systems is presented. An approach for the appropriate selection of the Rayleigh coefficients is suggested in reference [96]. The reasons for unrealistically high damping forces that appear under certain conditions, when Rayleigh damping is used, are discussed in reference [97].

The nature of the damping in a structure affects the mode shapes. Non-viscouly damped systems have both elastic modes, that appear in complex conjugate pairs and non-viscous modes that are not oscillatory in nature. Viscously damped systems have only elastic modes. If the viscous damping is proportional, the modes are real. The nature of modes are presented schematically in Figure 4.4.

For the identification of the full viscous damping matrix of multiple-degrees of freedom systems various techniques have been developed. The first group of methods, as mentioned in the beginning of Section 4.3 includes the estimation of modal parameters (natural frequencies, damping ratios and mode shapes) from transfer functions determined by modal testing, where a damping matrix is fitted to the measured data. In reference [98] an iterative method of the inverse eigenvalue problem for all damping matrices, where the mass matrix is known and the eigenvalues are experimentally obtained, is presented. Incomplete experimental data and an a priori knowledge of the mass and stiffness matrices are used in reference [99] to identify

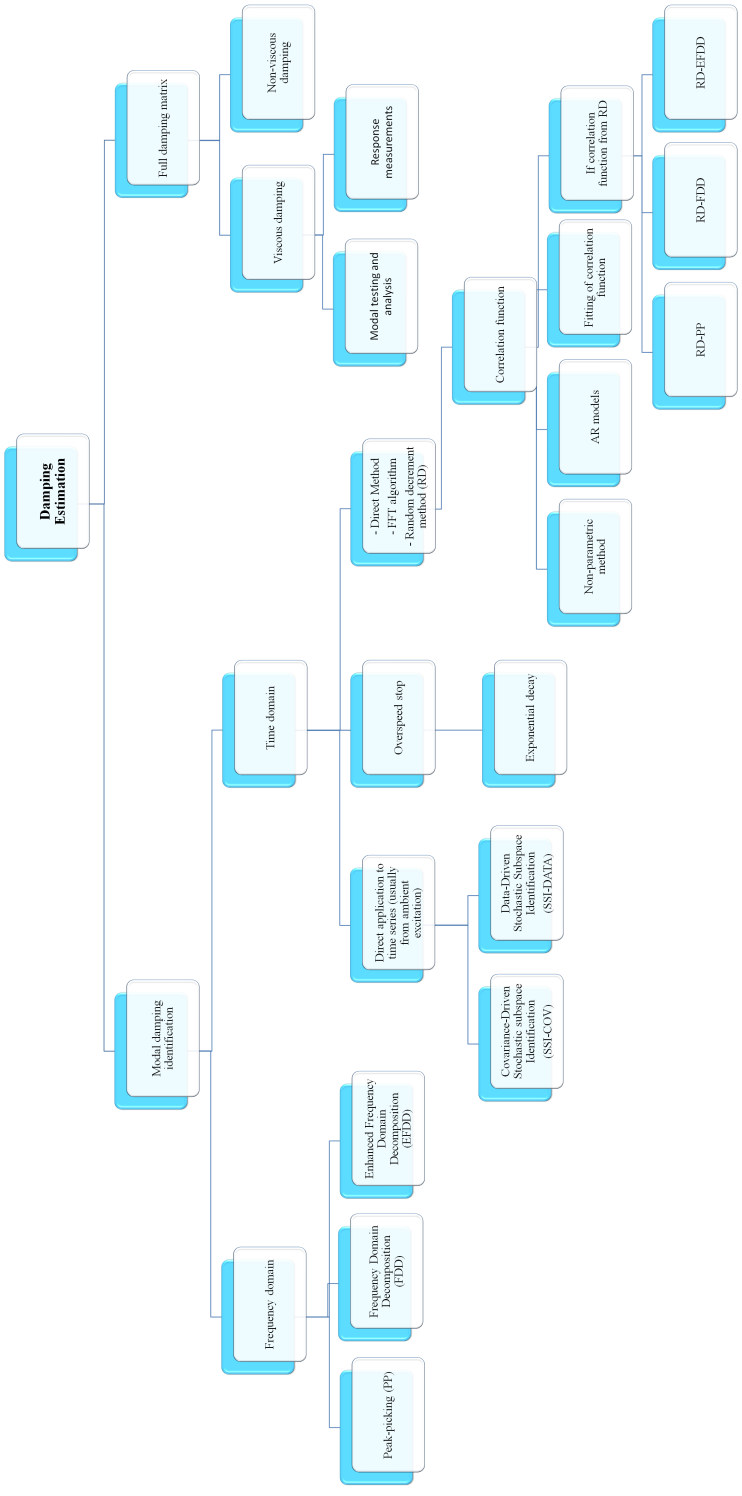

Figure 4.3: Schematic representation of different methods for damping identification

the damping matrix. An inverse vibrational problem is discussed in reference [100] where the form of the damping matrix is defined by the user beforehand. The identification of a non-proportional viscous damping matrix of light damped structure with the use of an incomplete set of eigenmodes and natural frequencies and no a priori knowledge of the mass and stiffness matrix is studied in reference [101]. The second group consists of methods that are fitting equations of motions to the data. A time-domain approach was investigated in reference [102] to identify mass, stiffness and damping matrices from measurements with high levels of noise. Frequency response data of a structure decomposed into linear combinations are used in reference [103] to estimate the damping matrix when the mass and stiffness matrices are known. A frequency domain method is discussed in reference [104] for identification of all system matrices, where the damping matrix is estimated separately.

The assumption of viscous damping in a non-viscously damped system does not always result in an accurate representation of the damping behavior. Therefore, different methods for the identification of non-viscous damping have been developed. Considering a hysteretic material damping model the loss factor of the n-th mode was calculated in reference [105]. In reference [106] a material damping parameter estimation method, based on frequency response functions and elastic modes determined by a finite element model is proposed. Experimentally identified complex modes and natural frequencies are used along with the mass matrix to identify the damping by an exponential relaxation function in reference [107].

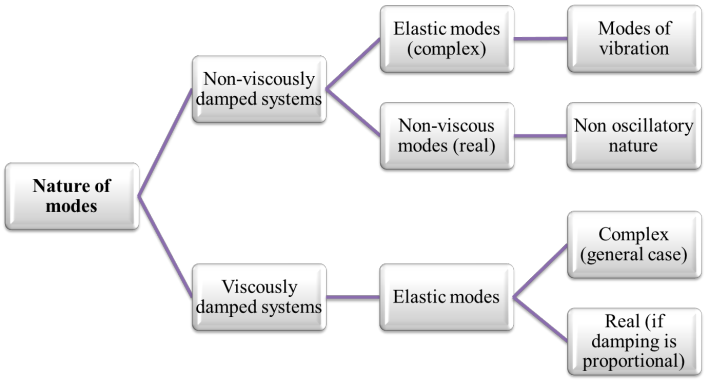

Figure 4.4: Nature of modes depending on the type of damping

4.3.2 Modal Damping Identification in Time and Frequency Domain

In the frequency domain the most common method known as Peak-Picking (PP) was thoroughly analyzed and implemented by Felber in reference [108]. This approach is based on the construction of averaged normalized power spectral density functions (ANPSD) by performing a Discrete Fourier Transformation to the data. The resonance peaks of the spectrum corresponding to the vibration modes are the identified natural frequencies of the system. At these frequencies the coherence function of two signals measured at the same time has a value close to 1. Peaks present in the spectrum due to harmonics should be excluded from the identification process, since they don't correspond to vibration modes. The method itself does

not provide an estimation for the damping and therefore it is combined with the half-power bandwidth method to identify the damping ratio as proposed in reference [109]. Equation 4.9 gives the damping ratio from the half-power bandwidth method, where Q is called the quality factor and is defined as $Q = \frac{f_n}{\Delta f}$. f_n is the natural frequency of each specific mode and Δf is the half power bandwidth, namely the bandwidth where the vibration has power greater than half of the power at the natural frequency. The relation for the half-power bandwidth is determined from the frequency response transfer function as indicated in references [110]. However, the assumptions of independently excited modes and the error in the damping estimation of higher modes should be kept in mind when analyzing the results. In references [111, 112] the accuracy of the half-power bandwidth method is examined and the differences, when it is applied to the acceleration and the displacement frequency response curves are pointed out. In the same studies a third order correction is proposed in order to reduce the damping estimation error. A different approach in the frequency domain is proposed by Bricker et. al in [113, 114] where the Frequency Domain Decomposition (FDD) method is introduced. A Singular Value Decomposition (SVD) is applied to the power spectral density function matrix and the spectral response is decomposed into a set of single degree of freedom (SDOF) systems, each of them corresponding to the contribution of the different modes at every frequency. In that way closely spaced modes can be identified quite accurately. In a specific frequency the dominant mode appears at the first singular value spectrum. An improvement of this method called Enhanced Frequency Domain Decomposition (EFDD) is presented in references [4, 5]. The auto spectral densities of the SDOF systems are based on the modal assurance criterion (MAC) value between the singular vectors at the resonance peak and the frequency lines around the peak. The auto spectral density functions are transformed back to time domain using the inverse Fast Fourier transformation resulting in auto correlation functions for each mode. The damping ratios are estimated from the exponent of a curve fitted to the relative maxima of these functions. The potential of the EFDD method is shown in reference [115], where the technique is applied to a wind turbine blade for modal parameter identification. The advantage of the last two techniques is the identification of close modes even in the case of high noise in the signal. Although, closely spaced modes can be more accurately identified compared to the Peak-Picking method, their identification can be still difficult in cases with a high number of modes present in the response. Harmonics due to rotating parts in wind turbines can be easily identified with the frequency domain decomposition techniques, due to a peak being present at all SVDs at a specific frequency, indicating that this is not a vibration mode.

$$|Q|_{max} \approx \frac{1}{2\zeta} \Rightarrow 2\zeta = \frac{f_2 - f_1}{f_n} \tag{4.9}$$

In the time domain the different methods can either be directly applied to the response time series, or to correlation functions. Impulse response is widely used in wind turbines to accurately identify the damping ratios. An exponential curve is fitted to the relative maxima of the decay response and an estimation of the damping is obtained by the exponent of the fitted function. The main limitation of this method is the assumption of the contribution of a single mode to the decay. This assumption can be close to reality for well separated modes, but in the case of offshore wind turbines, where the first two modes of the system (fore-aft and

side-side of the tower) are usually closely spaced, it can give erroneous results for the damping. Correlation functions are a different representation of the time series. Three techniques for estimating the correlation function are presented in reference [116], the direct method, the Fast Fourier Transform (FFT) technique and the Random Decrement (RD) technique.

The direct method is the simplest but slowest technique. The Fast Fourier Transform (FFT) is faster but provides biased estimates. The correlation function is estimated by applying an inverse FFT to the spectrum. A technique to obtain unbiased results is presented in reference [116]. The Random Decrement (RD) method is based on averaging N segments of the time series with one of them satisfying a triggering condition. A detailed analysis of the Random Decrement method and a theoretical explanation that the RD is a correlation function is presented in reference [117]. By fitting an exponential curve to the maxima of the auto-correlation function, the damping ratio can be estimated from the parameters of the fitted expression. An application of the method in the frequency domain is presented in reference [109], where the advantages due to noise reduction and the avoiding of leakage are also pointed out. When the estimation of the correlation function from the Random Decrement technique is combined with the three frequency domain methods mentioned before, the resulting identification methods are the RD-PP, RD-FDD and RD-EFDD. Direct application to the time series response is allowed by using stochastic subspace identification techniques like Covariance-Driven Stochastic Identification (SSI-COV) or Data-Driven Stochastic Identification (SSI-DATA) methods.

In references [22, 79, 118] the method of obtaining the damping ratios directly from vibrations of the tower under ambient excitation is analyzed and compared with the commonly used overspeed stop. The two different processes showed good agreement. The data for the tests are obtained from an offshore wind turbine in the Belgian North Sea. In the case of overspeed stop an exponential function is fitted to the maxima of the decaying time series, in order to calculate the damping ratio. In the beginning of the decay the thrust excites the tower mainly in the wind direction, but towards the end both modes, fore-aft and side-to-side, contribute to the motion. Analysis in the frequency domain is also investigated by applying a Fast Fourier Transformation (FFT) to the decaying oscillation. Similar results were obtained with the ambient excitation, making this method more appealing due to its less harmful nature towards the system. In the time domain an exponential curve was fitted to the relative maxima of the auto-correlation function of the tower acceleration. In reference [74] three different non-parametric damping estimation techniques were applied to structures under ambient excitation, the time domain approach using Data Correlation, the time-frequency analysis via Wavelet Transform and the Frequency Domain Decomposition. The definition of proportional damping and the extraction of the modal frequency and modal damping from the complex eigenvalues is discussed.

In reference [82] the measured acceleration of the tower in the fore-aft and the side-side direction is used to estimate the total system damping of the first bending mode. A tendency of decreased damping with increased wind speed was observed, mainly due to higher acceleration levels for higher wind speeds. Experimental results agree quite well with the numerical simulations when using a simple linear viscous damping model. In the same study an attempt to estimate the soil stiffness using the $p-y$ method (Winkler type approach) is presented. "Rotor stops" and fitting of theoretical energy spectra to measured response were

used in reference [119] for estimation of the first modal damping of offshore wind turbines on a monopile foundation. Accelerometers for the measurement of the vibration decay of twelve 'rotor-stop' tests were also used in reference [120], where the damping is both identified in the frequency and the time domain. A difference observed in the displacements of the first two modes, allowed the investigation of the influence that the soil-pile interaction has on the vibrations of the wind turbine. In reference [121] the natural frequency and the damping ratio are estimated with two different methods, an Experimental Modal Analysis and an Operational Modal Analysis. In the latter technique the modal parameters are extracted from output-only measurements. The potential of output-only techniques was also demonstrated in [122], even in the case of closely spaced modes. Two identification methods, the Enhanced Frequency Domain Decomposition (EFDD) and the Covariance driven Stochastic Subspace Identification (SSI-COV) were compared with a free decay test.

Direct application to the response time series for estimation of the modal parameters is done through various System Identification techniques. Subspace System Identification (SSI) methods are extensively used to provide a good estimation of the system's parameters from operational modal analysis. The reason for the designation 'subspace' is that the system matrices are retreived as subspaces of projected data matrices [123]. Often reported in the literature [124, 125, 126, 127], a System Identification Method (SI) is applied to estimate damping from structures excited by deterministic or stochastic loads. The (SI) method has been extensively tested and applied to various vibration problems, like offshore structures and bridges. In reference [127] the System Identification method based on the covariance block Hankel matrix (CBHM) is thoroughly analyzed, by examining both simulated and measured response data of a deep-water offshore platform. This work was further investigated in [128] and extended to recover full structural system matrices of structures under ambient excitation. In references [129, 130] a data-driven stochastic subspace method (SSI) was introduced. An overview of subspace system identification techniques, categorized as realization based and direct methods is given in reference [131]. SSI methods provide reliable state-space models from measured data. The states are estimated either directly from the input-output with the use of principal angles and directions between the past and future output data or by the formation of covariance matrices. The advantage of the former approach is the avoidance of the covariance matrix and thus the elimination of the squared propagation of error and noise from the covariance estimation. The state sequences can be considered as the output of an extended Kalman filter. Then the system matrices are derived by solving a least squares problem. Three different subspace algorithms, the 'Canonical Variate Analysis' (CVA), the 'Multi-variable Output-Error State space' (MOESP) and the 'Numerical algorithm for Subspace State Space System Identification' (N4SID) are mentioned in reference [132] and their similarities under a unified theorem are pointed out. In all three algorithms the system order and the extended observability matrix are determined from the observed input-output data. The only variation between them is introduced by the choice of different weighting matrices.

In the classical approach the system matrices are derived before the states, but in reference [129] it was illustrated that an algorithm based on principal angles and directions to estimate the states before the system matrices provides more accurate results. Figure 4.5 presents the difference between the two techniques. In reference [130] the effectiveness of two N4SID algorithms for combined deterministic-stochastic systems is analyzed. In reference [133] only past reference outputs are used in the identification procedure, reducing the computation time.

The eigenfrequencies, damping ratios and modes are estimated quite accurately compared to the classical SSI approach. Measured input-output data without strong excitation and increased noise may lead to failure of the system identification algorithm. In references [134, 135] prior information about the system is included into the subspace method to improve the quality of the model.

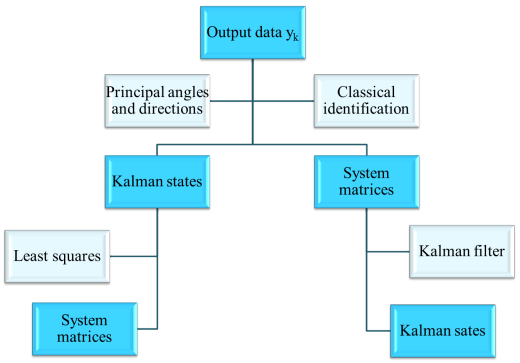

Figure 4.5: Classical identification technique vs. approach based on principal angles and directions (adapted from reference [129]).

A comparison between the two different identification methods, Covariance Block Hankel Matrix (CBHM) and data-driven Subspace System Identification (SSI), was conducted in reference [136]. The damping estimates given by the latter appear to be more consistent and reliable and the method is better suited for the determination of dynamic properties of structures under stochastic loading. The two different techniques are also compared in reference [137]. The modal parameters and system matrices were more accurately determined and less scattered when applying the data-driven subspace method. In reference [124] an SSI method for estimation of the wind turbine damping is compared with excitation of the system by a harmonic force at its natural frequency. The excitation of a pure mode was not possible with the second method, thus resulting in a damping not equal to the real one. The advantage of the SSI method of no required knowledge of the structural characteristics of the turbine and the estimation of modal parameters for modes with almost identical natural frequencies was demonstrated. However, it should be taken into consideration during the post-processing of the results, that the P-harmonics are determined as modes due to their significance in the aerodynamic forces. A large amount of data (long time series) is required for an accurate identification algorithm. The effect of the time length in the quality of the results is pointed out in reference [122]. For a detailed analysis of the System Identification Theory the reader is addressed to reference [138].

In table 4.1 the different methods for damping estimation with their advantages and disadvantages are presented. Very often the selection of a method is a trade-off between simplicity and accuracy. The most appropriate technique depends on each application and usually methods are combined. The main assumption present in all techniques is that the considered modes to be identified are sufficiently excited, otherwise they cannot be observed.

The identification methods of output-only data provide accurate results under certain assumptions both for the system itself and the nature of the input excitation. The system

Table 4.1: Pros and Cons of damping estimation methods

	Advantages	Disadvantages
PP	• easy implementation • fast method	• harmonics identified as modes • no obvious peaks from very damped modes • no identification of closely spaced modes
FDD/EFDD	• identification of closely spaced modes even when noise is present in the signal • identification of weakly excited modes • indication of harmonics	• Biased estimates of spectral density functions
Exponential Decay	• easy implementation	• assumption of seperate mode excitation • no identification of closely spaced modes • system handled as SDOF
Correlation function	• smaller amount of data • faster identification process	• assumption of seperate mode excitation • dependency on time length • information will be lost due to data compression • system handled as SDOF
SSI-COV	• operate directly on time series • no a-priori knowledge of the structure • identification of closely spaced modes • with one identification run receive all considered modes of the system	• harmonics identified as modes • error propagation due to covariance estimation • long time series required • complicated method • requires longer computational time
SSI-DATA	• operate directly on time series • no a-priori knowledge of the structure • identification of closely spaced modes • with one identification run receive all considered modes of the system	• harmonics identified as modes • long time series required • complicated method • requires longer computational time

is supposed to be linear time invariant and the excitation white noise. The input forces are uncorrelated and distributed over the entire structure. However, the harmonics of the rotating parts, can coincide or be close with one of the natural frequencies of the system resulting in a high energy in the spectrum and causing the identification to fail. The time invariance assumption is also violated by the rotation of the rotor around its axis (azimuth position), the blade pitch angle depending on the operational conditions and the rotation of the nacelle around the tower axis (yaw angle). To deal with the last two problems, periods where these angles don't change significantly should be chosen for the identification procedure. For the azimuth position a Coleman transformation is proposed in reference [139] to avoid the time dependencies. The limits of OMA in wind turbines are presented in reference [140]. In order to deal with these problems the OMA methods need to be improved. Some solutions are presented in references [141, 142, 143, 144], where different techniques of identifying and removing the effect of the harmonics are discussed. A more recent method to deal with these problems is presented in reference [145]. For the separation of the harmonics from the real structural modes various methods are proposed in reference [144]. A technique based on Kurtosis to eliminate the harmonics using the EFDD method is suggested in reference [5].

Chapter 5

Site Description

A 3.6MW Siemens pitch regulated-variable speed offshore wind turbine installed in the Walney Offshore Wind farm 1 (Figure 5.1), located at the west coast of England, 15km from the shore (Irish Sea) has been fully instrumented for load measurements. The turbine is mounted on a monopile structure at a water depth of 27m. The mean wind speed at 80m above the mean sea level (hub height) is 9.6m/s. Wind and waves in the site appear to have a misalignment of 10^o. Turbine yaw angles, blade pitch angles, rotational speed and power production are also obtained as a ten minutes average from the SCADA data. The instrumentation of the sub-structure/foundation consists of 44 strain gauges located at 11 heights along the pilesand, the monopile and the transition piece. 4 gauges are mounted at each height, placed one across each other at 90^o connecting half bridges for the measurement of the bending moments. Strain gauges and accelerometers are installed at 3 different heights throughout the whole length of the tower (4 gauges per height) and 2 inclinometers at the tower bottom. 4 strain gauges are placed on the shaft for the measurement of the bending and yaw moments. 4 strain gauges are mounted 1m from the blade root along each blade (12 gauges in total), for the measurement of the out-of-plane and in-plane moments on the blade. The time series of the low speed and high speed shafts rotational speed, the azimuth, the pitch and the yaw angles are also measured. The measurement rate of the sub-structure/foundation is 20Hz and of the tower, the shaft and the blades 35Hz. The SCADA data from the instrumented and the surrounding wind turbines are obtained by DONG Energy.

The site measurements for the wind are nacelle anemometer readings from a cup-anemometer installed behind the rotor and from a nacelle mounted LIDAR. The metocean data (surface elevation, directional spectrum, significant wave height and peak period) are provided by a buoy installed close to the instrumented wind turbine. On site measurements about the soil characteristics are also available.

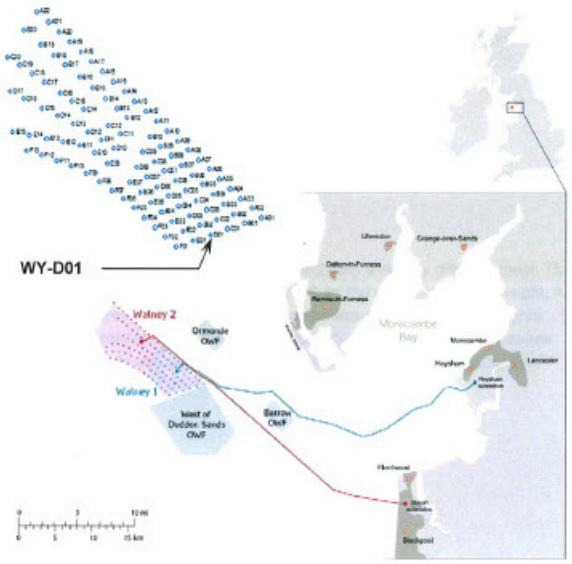

Figure 5.1: Outline of Walney Offshore Wind farm 1 (DONG Energy).

5.1 Metocean Conditions

A buoy installed close to the wind turbine on the site is measuring the surface elevation and the wave direction in a time interval of 30 minutes. The time series of the surface elevation are used to estimate the wave properties, like the wave spectrum, the significant wave height H_s and the peak period T_p. Figure 5.2a presents H_s and T_p measured by the buoy as a function of the mean wind speed and Figure 5.2b depicts the metocean conditions used during the design process (provided by DONG Energy). A Fast Fourier Transformation (FFT) to the measured data results in the wave spectrum, from where the peak frequency f_0 can be identified as the frequency that corresponds to the maximum wave energy.

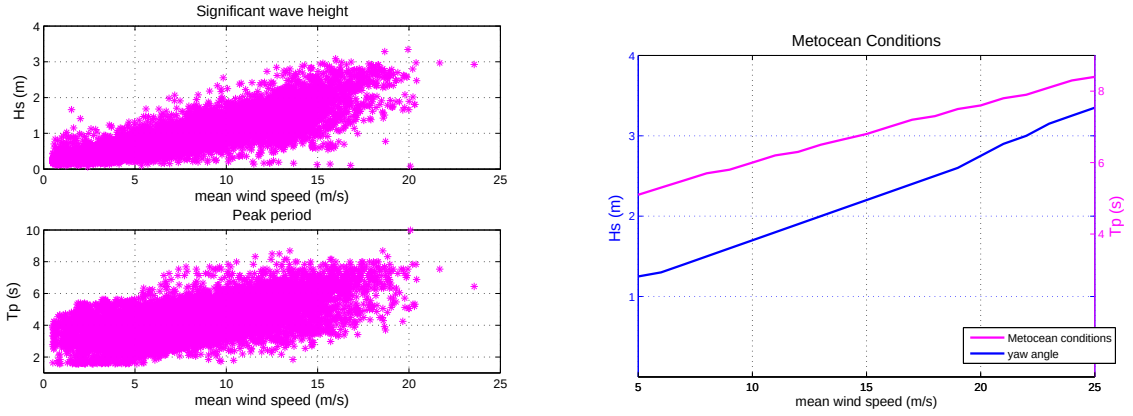

(a) **(b)**

Figure 5.2: a) Significant wave height and peak period from site measurements as a function of the mean wind speed. b) Metocean conditions used in the design process.

The spectral moment of the wave m_w and the width parameter of the wave spectrum ϵ are given by Equation 5.1. When $\epsilon > 0.6$ the spectrum is considered broad band. The significant wave height H_s, defined as the average of the highest one-third of all waves, can be expressed by Equation 5.2, where $m_{w,0}$ is the zeroth moment. For narrow banded wave spectra, the probability density function of the wave heights is approximated by a Rayleigh distribution (Equation 5.3), where $H_{rms} = \bar{H^2}$. Based on site measurements the mean width parameter is equal to $\epsilon = 0.52$. Therefore, the wave spectra are narrow banded and can be represented by a Rayleigh distribution.

$$m_{w,i} = \int_0^\infty f^n S_n \mathrm{d}f, \quad \epsilon^2 = 1 - \frac{m_{w,2}^2}{m_{w,0} m_{w,4}} \tag{5.1}$$

$$H_s = 4\sqrt{m_{w,0}} \tag{5.2}$$

$$p(H) = \frac{2H}{H_{rms}^2} exp\left(-\frac{H^2}{H_{rms}^2}\right) \tag{5.3}$$

The wave period is defined as the time interval between the successive zero-upcrossings of the surface elevation. The different wave periods are given by Equation 5.4, where T_p denotes the peak period, T_{mean} the mean period and T_s the significant wave period. Due to an integration error, performed by the buoy system to the measured accelerations, the obtained peak period has erroneous values. Therefore, the calculated T_p from equation 5.4a has been used for further analysis of the wave data.

$$T_p = \frac{1}{f_0}, \quad T_{mean} = \frac{m_{w,0}}{m_{w,1}}, \quad T_s = 0.92 T_p \tag{5.4}$$

After the calculation of the peak period T_p and the significant wave height H_s, the γ parameter of the JONSWAP spectrum can be estimated from Equation A.20. The buoy also measures the velocity and the direction of the current every 0.8m from the surface to the seabed, giving a very high velocity when the measurement reaches the seabed. The position that gives this erroneous value is the water depth and it is used as an indication of the tidal change. Figure 5.3 presents the variations in the water depth over a period of 2 months.

Due to very low current velocities, the influence of the current can be neglected in fatigue analysis [53]. For the ultimate strength analysis the currents should be considered in the simulations. Therefore, the relation between the current velocity and the water depth is estimated through site measurements. The current profile can be approximated by a power law (Equation 5.5), where U_0 is the current velocity at mean water level, d is the water depth and z is the depth below the mean water level. From Figure 5.4 it can be observed that the

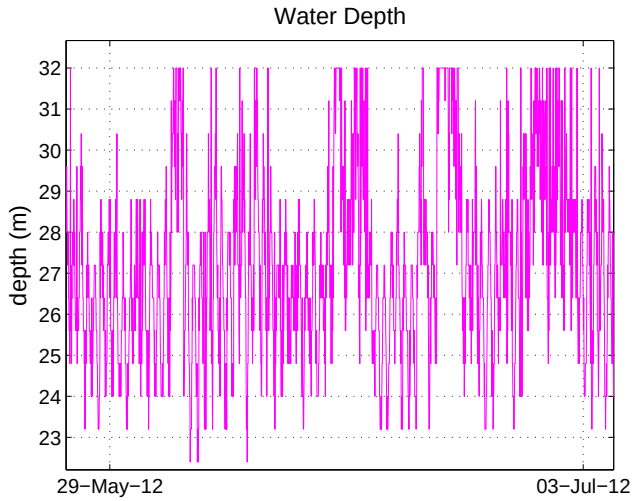

Figure 5.3: Tidal changes on the side. Mean water depth is 26m.

current profile can be better approximated by a power law with $\alpha = 4$.

$$U_{cur}(z) = U_0 \left(1 + \frac{z}{d}\right)^{\alpha} \tag{5.5}$$

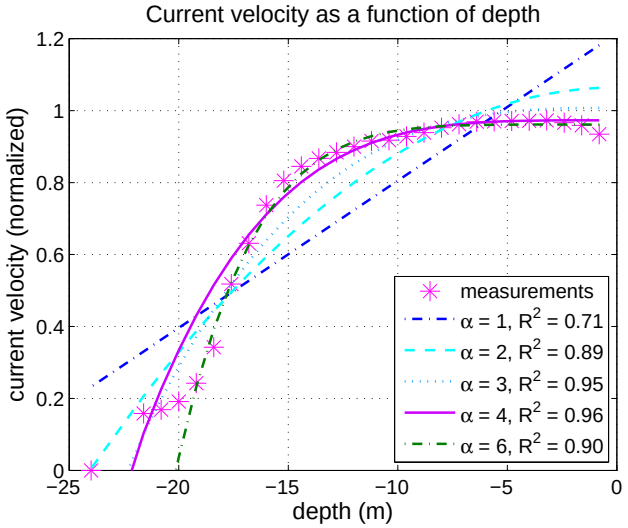

Figure 5.4: Current profile as a function of water depth.

A 2-parameter Weibull distribution is suggested as the conditional distribution of the significant wave height for a given wind speed [29]. The measured wind speed is separated in bins of 1m/s and the Weibull scale and shape parameters α_w and β_w for the wave heights within each group are estimated. Figure 5.5 depicts the Weibull Probability Density Function (PDF) distribution of the significant wave height for different wind bins.

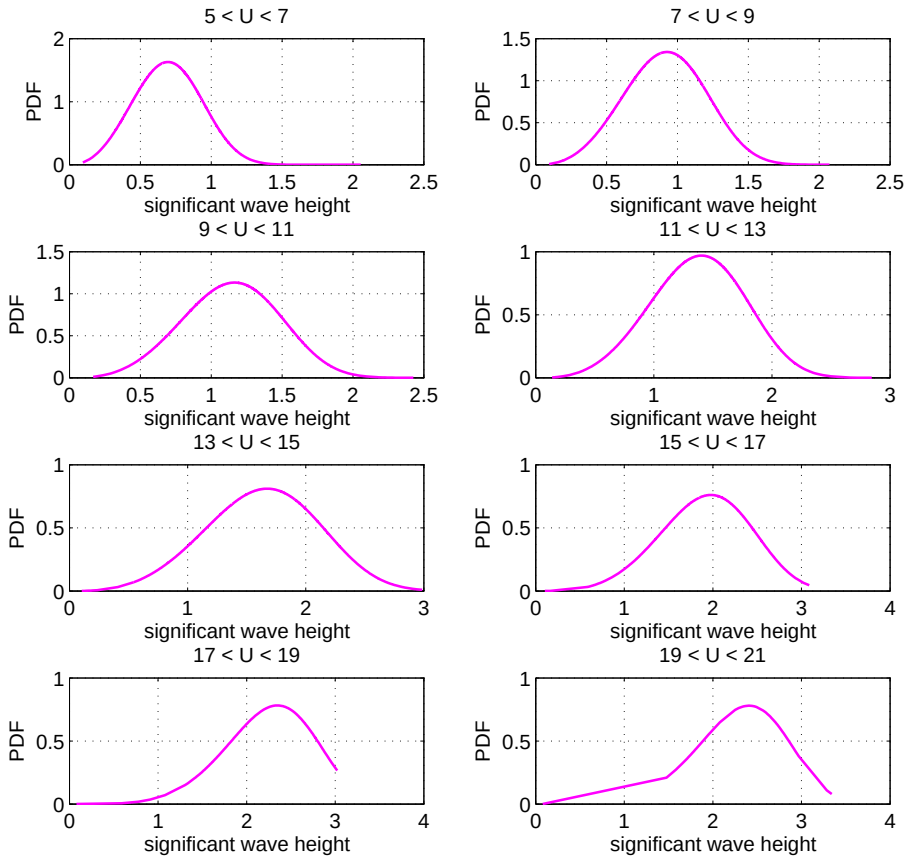

Figure 5.5: Weibull probability density function of the significant wave heights for the different wind speed bins, based on measurements (conditional wave probability).

5.1.1 Wind-Wave Joint Distribution

For the calculation of the joint wind-wave distribution, the 10min mean wind speed U is separated in bins of 2m/s in such a way that the bin for $U = 6 - 8m/s$ covers all the wind speeds in the interval $6 \leq U < 8$. The significant wave height H_s is separated in bins of 0.5m. For the generation of the contour surface of the local joint wind-wave probability density function, shown in Figure 5.6, 6 months of measurements have been used. Due to limited data availability, in Figure 5.6 the average wind speed on the site appears to be 8m/s. This is lower than the expected mean wind speed for the Walney site. The wind turbine D01 is 80% of the time in the wake, so the apparent average wind speed was expected to be lower. Another reason for the discrepancy between the expected site conditions and the estimated wind from the joint wind-wave distribution, is due to the short measurement period of six months, which might not be representative of the site (wind index). The uncertainty of the measurement period should be considered in a more detailed analysis. The probability of each combination of wind speed and significant wave height for the joint distribution (Figure 5.6),

was then based on the number of observations in each bin (Equation 5.6), where the index i represents the wind bins, the index j the wave bins and N the number of observations.

$$p_{i,j} = \frac{n_{i,j}}{\sum_{i=1}^{9}\sum_{j=1}^{8} N_{i,j}} \tag{5.6}$$

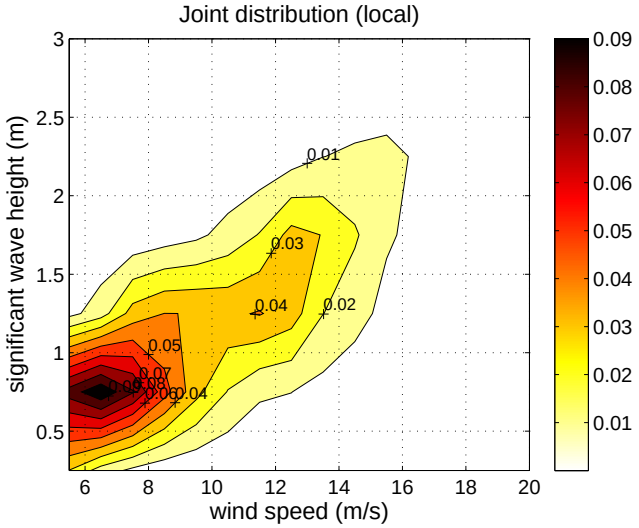

Figure 5.6: Contour surface of the local joint distribution based on 6 months of measurements. Significant wave height versus wind speed.

As an alternative method of estimating the joint wind-wave distribution, the fitted conditional wave height distribution is combined with the fitted wind speed distribution. The wind distribution is based on measurements from the wake sector, since the wind turbine is mostly on the wake. Figure 5.7 presents the contour surface of the fitted joint wind-wave distribution. Using this methodology, the average wind speed is 9m/s. The time weighting used for the estimation of the lifetime accumulated fatigue are calculated from this fitted joint wind-wave probability multiplied with the hours obtained from the free wind Weibull distribution ($hours_{free\_wind}$, Equation 5.7). The reduced mean wind speed, seen by the wind turbine due to the wake, should not be considered in the analysis, as the Sten Frandsen model was used for the estimation of the effective turbulence intensity [17]. 90% availability of the wind turbine due to maintenance is considered in the calculation of the operating hours.

$$life\_hours = P_{H_s|U} \cdot P_U \cdot hours_{free\_wind} \tag{5.7}$$

5.1.2 Wind-Wave Direction Probability

The uncertainty on the wave direction measured by the buoy is identified by comparing the mean wave direction with the peak wave direction (i.e. the direction that results in the

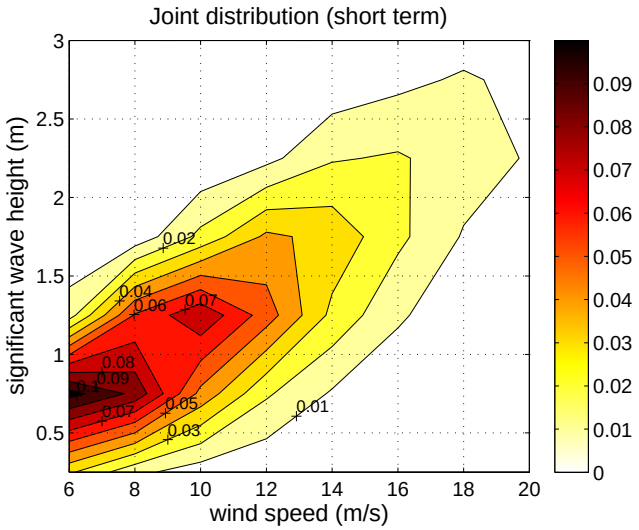

Figure 5.7: Fitted wind-wave distribution. Significant wave height versus wind speed.

highest energy from the directional spectrum). Figure 5.8 compares the peak and the mean wave direction measurements from the buoy; on the y axis is the mean wave direction, while the peak direction is presented on the x axis. It seems that there are no multi directional sea states from the swell contributions, which could cause differences between the mean and peak wave directions. Therefore the mean wave direction is a good estimate of the wave direction, with an uncertainty of $\pm 30^o$ (93% confidence interval). For the construction of the wind and wave roses shown in Figure 5.9 the directions are separated in 12 bins of 30^o each.

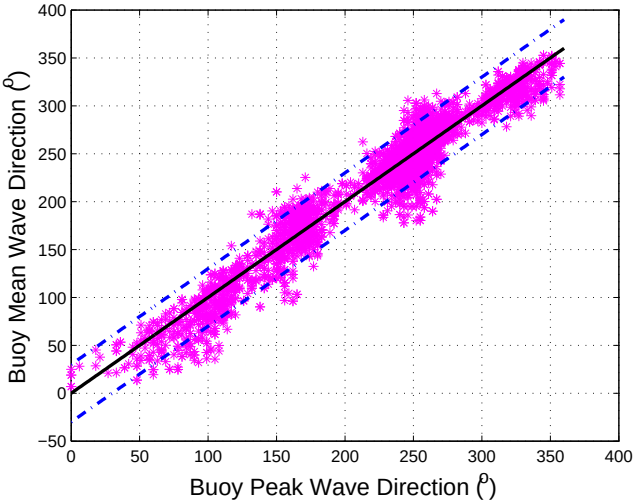

Figure 5.8: Confidence interval of 93% of the mean wave direction measured by the buoy.

The mean yaw angle provided by the SCADA data indicating the wind direction and the mean wave direction from the buoy are compared to identify cases of wind-wave misalignment. Figure 5.10 depicts the misalignment of the wind and the waves on the site.

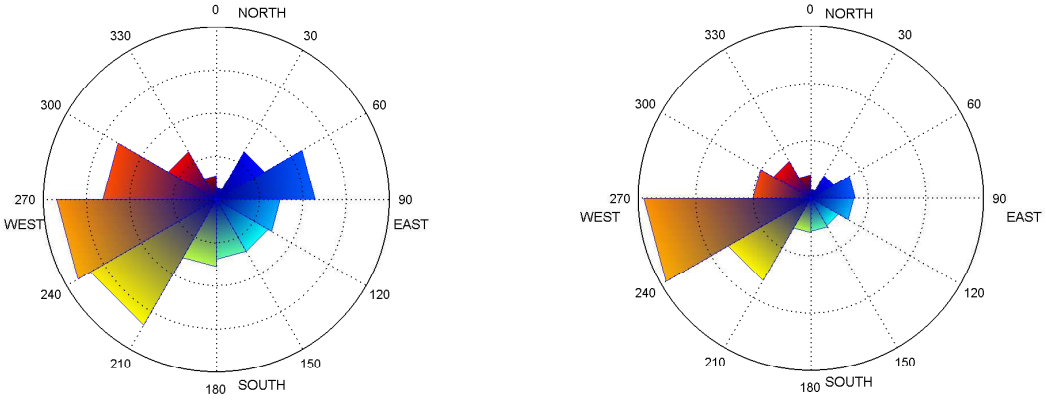

(a) Wind rose. **(b)** Wave rose.

Figure 5.9: Wind and wave roses with bins of 30^o.

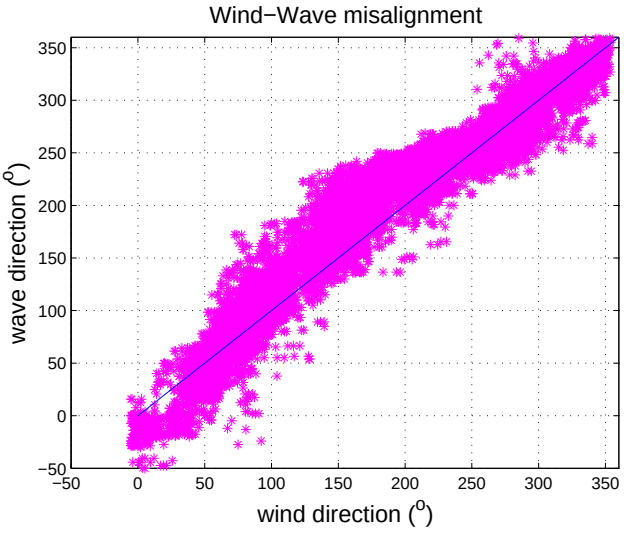

Figure 5.10: Wind-wave misalignment in the site.

Based on the wind and wave direction roses, it was found that a kernel distribution described by Equation 5.8 best fits the data, where n is the sample size, $K(\bullet)$ the kernel function, h the bandwidth and x the wind or wave direction (angle). From the mode of the two distributions (Figures 5.11a, 5.11b) it can be observed that the main wind and wave directions have a difference of 10^o. The same can be seen from the mean value of the normal distribution fitted to the wind-wave misalignment data (Figure 5.11c). The fitting of distributions to the measured data was examined through the histogram, since no specific distribution is suggested for fitting in the direction data.

$$PDF_{ker} = \frac{1}{nh} \sum_{i=1}^{n} K\left(\frac{x - x_i}{h}\right) \tag{5.8}$$

The misalignment angles are separated in bins of 10^o from the minimum to the maximum observed angle for a specific mean wind speed and significant wave height combination. The cumulative distribution function (CDF) is then used to calculate the probability of occurrence of each misalignment angle. Table 5.1 presents the probability of occurrence of nine wind speeds and sea states along with the misalignment probability between the wind and wave directions based on six months of measurements. The probability of occurrence of misalignment angles larger than $|\pm 50|$ is very small and therefore not presented in the table. For all the wind speeds the misalignment of -10^o has the highest probability of occurrence. It can also be observed that as the wind speed increases the misalignment probability decreases. This is because the waves are mainly generated by the wind, especially in sheltered areas like the Irish sea. So the wind-wave correlation at high wind speeds is higher and the probability that the waves are aligned with the wind larger, due to fully developed sea states.

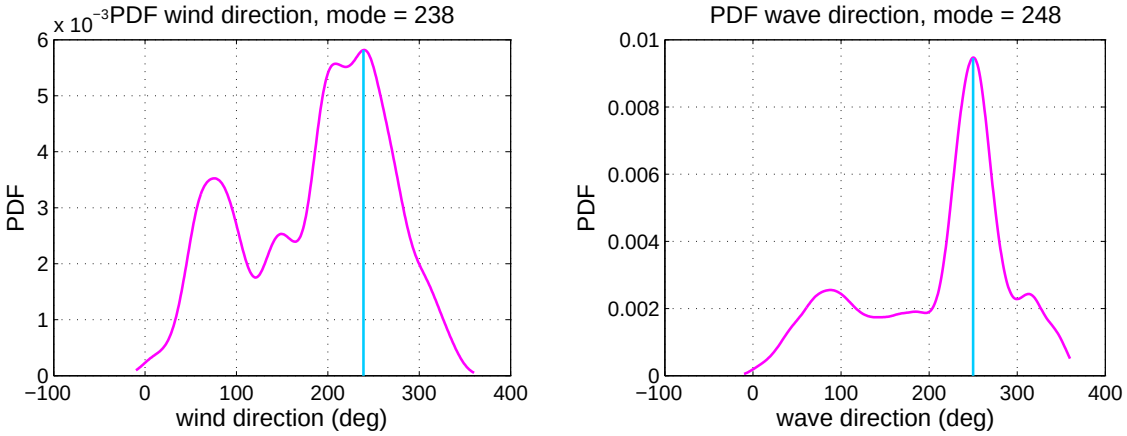

(a) Kernel distribution fitted to the wind direction. **(b)** Kernel distribution fitted to the wave direction.

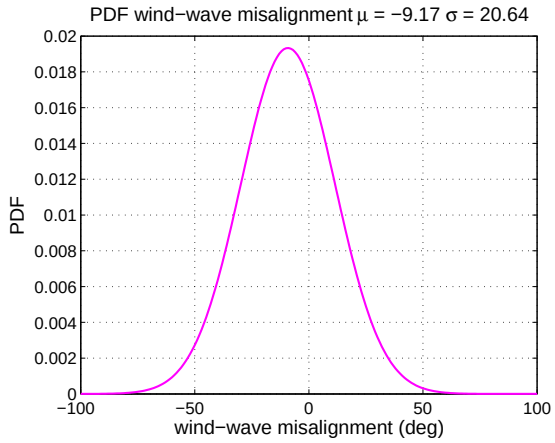

(c) Normal distribution fitted to the wind-wave misalignment.

Figure 5.11: Wind and wave direction distributions.

U (m/s)	H_s (m)	$p_{i,j}$	-50^o	-40^o	-30^o	-20^o	-10^o	0^o	10^o	20^o	30^o	40^o	50^o
6	0.75	0.183	0.031	0.070	0.125	0.175	0.195	0.167	0.112	0.062	0.026	0.008	0.002
8	0.75	0.135	0.029	0.072	0.133	0.190	0.206	0.170	0.107	0.051	0.019	0.005	0.001
8	1.25	0.074	0.014	0.048	0.105	0.171	0.209	0.194	0.134	0.070	0.025	0.008	0.000
10	1.25	0.078	0.023	0.057	0.109	0.165	0.194	0.180	0.130	0.069	0.032	0.008	0.002
12	1.25	0.075	0.006	0.025	0.074	0.153	0.223	0.220	0.161	0.083	0.031	0.006	0.000
12	1.75	0.054	0.009	0.033	0.086	0.161	0.216	0.210	0.148	0.073	0.025	0.008	0.000
14	1.75	0.051	0.043	0.077	0.111	0.143	0.155	0.144	0.116	0.077	0.044	0.017	0.008
16	2.25	0.021	0.046	0.099	0.141	0.162	0.166	0.128	0.081	0.037	0.013	0.000	0.002
18	2.75	0.009	0.033	0.065	0.116	0.148	0.173	0.153	0.113	0.065	0.000	0.000	0.000

Table 5.1: Probability of occurrence of nine wind-significant wave height combinations along with the observed misalignment between their directions. The mean wind speed, significant wave height and misalignment angles represent the center of each bin.

Chapter 6

Measurements Calibration and Data Processing

Before the post-processing of the measurements a calibration of the raw data from the strain gauges is required. Each time series corresponds to 10min measurement. The sub-structure/ foundation measurements are converted from voltage to strains and provided by DONG Energy, while the rest of the wind turbine load signal is received in voltage. The calibration of the different components is gravity based, where either the nacelle is slowly rotated 360^o around the yaw axis, or the rotor is rotated 360^o, providing in both cases a sinusoidal curve seen by the strain gauges.

6.1 Measurement Calibration

6.1.1 Support Structure Calibration

Figure 6.1 presents the coordinate system of the support structure used for the measurements' calibration, along with the nacelle center of gravity (CoG). The moment induced by the nacelle weight is defined as negative. The subscript T denotes tower.

Sub-structure/Foundation

Four strain gauges are installed per height placed one across each other at $150^o - 330^o$ for the measurement of the North-South and $60^o - 240^o$ for the East-West bending (Figure 6.2a). In the same figure the sign of the moments from the coordinate system definition is also depicted. Due to imbalances in the bridge circuit, the output data from the acquisition device ϵ_{out} always includes an offset ϵ_{offset}. The offset is calculated by performing a yaw test,

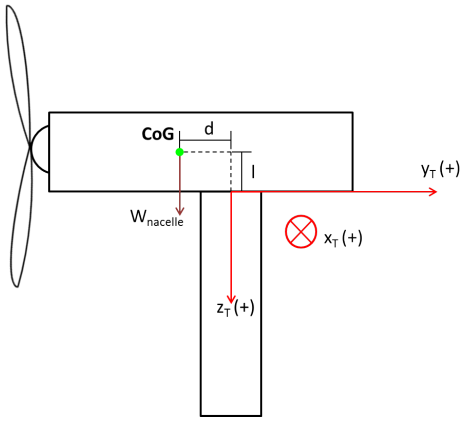

Figure 6.1: Support structure coordinate system.

where the Rotor-Nacelle Assembly (RNA) is rotated 360 degrees around its vertical axis. The weight of the rotor and the nacelle creates a moment (expected moment), captured by the strain gauges during the yaw test as a sinusoidal curve. Figure 6.2b presents an example of the strain signal versus the yaw angle. The difference of the mean value of the sinusoidal curve from zero is the offset of each strain gauge. The bending strain ϵ_B is given by Equation 6.1:

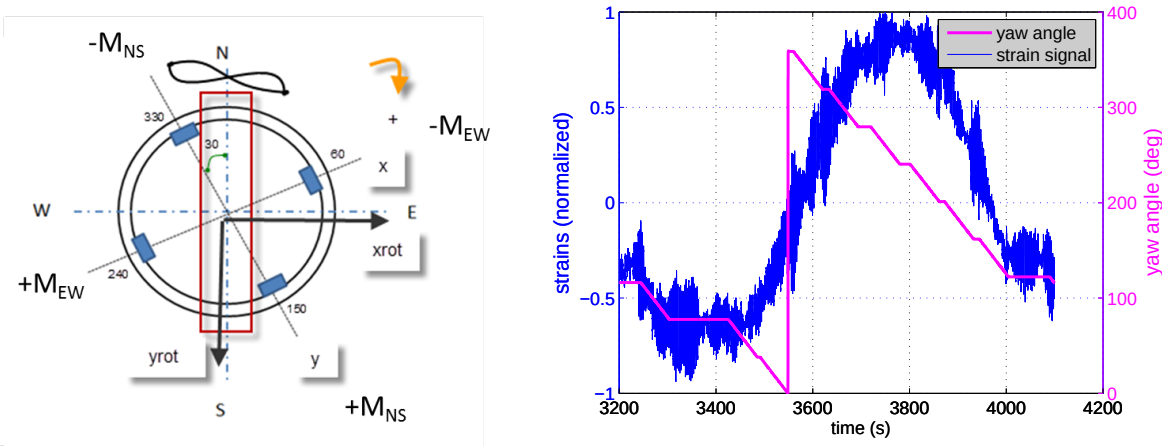

(a) Strain gauges for bending strain measurements (support structure).

(b) Normalized strain signal versus yaw angle during yaw test.

Figure 6.2: Strain gauges on the support structure.

$$\epsilon_B = \epsilon_{out} - \epsilon_{offset} \tag{6.1}$$

The bending strain is transformed to bending moment M_B through Equation 6.2, where EI is the bending modulus of the support structure ($E = 210(GPa)$) and R is the outer

radius of the monopile where the strain gauges are mounted.

$$M_B = \frac{EI}{R}\epsilon_B \tag{6.2}$$

The calculated bending moment is transformed to the rotating system that follows the wind turbine (Equation 6.3), providing the pure fore-aft and side side moments, where a is the angle between the strain gauge position and the bridge north 30^o and yaw is the yaw angle at each time step.

$$\begin{aligned} M_{x,rot} &= M_x \cos(a - yaw) - M_y \sin(a - yaw) \\ M_{y,rot} &= M_x \sin(a - yaw) + M_y \cos(a - yaw) \end{aligned} \tag{6.3}$$

Tower

For the tower strain gauges the calibration is similar, but the data is obtained already in full bridges (in voltage) instead of independent strains. The range of the sinusoidal curve captured during the yaw test is equal to twice the expected moment due to the nacelle weight. This allows the gain of the bridge to be estimated as shown in Equation 6.4a. The bridge offset is the mean value of the sinusoidal curve, calculated by Equation 6.4b. $min(V)$ denotes the minimum strain value in voltage observed during the test, $Mass_{nacelle}$ is the mass of the nacelle, g is the acceleration due to gravity, d is the distance of the nacelle center of gravity (CoG) from the tower axis and $range(V)$ is the range of the sinusoidal curve in voltage. The transformation to the rotating system is performed through Equation 6.3.

$$gain = \frac{2 \cdot M_{nacelle} \cdot g \cdot d}{range(V)}, \quad offset = -M_{nacelle} \cdot g \cdot d - gain \cdot min \tag{6.4}$$

The transfer function from the electrical signal to the moment is given by Equation 6.5.

$$M_B(kNm) = gain \cdot M(V) + offset \tag{6.5}$$

The signal during the yaw test, obtained from two sets of strain gauges mounted at the transition piece, one by DONG Energy and one by DTU with 1cm height difference between them has been used for the verification of the instrumentation's calibration on the tower and the sub-structure. During the first tower calibration using Equations 6.4 and 6.5 a difference with a factor of 2 has been observed between the two signals. Due to the uncertainty introduced in the tower calibration by the nacelle center of gravity d, it was decided to trust the results from the theoretical calibration of the sub-structure (Equation 6.2). Therefore, the gain and offset for the tower strain gauges were re-calculated based on the moment range captured by the strain gauges on the transition piece. Even though the signal at that position is more

noisy than the tower top, the geometry of the structure only at the transition piece was known to us. Figure 6.3 presents the two signals in bending moments as a function of the yaw angle, normalized with the maximum observed by the DTU instrumentation. The range that corresponds to twice the expected moment due to the rotor weight seems to agree satisfactorily between the two systems.

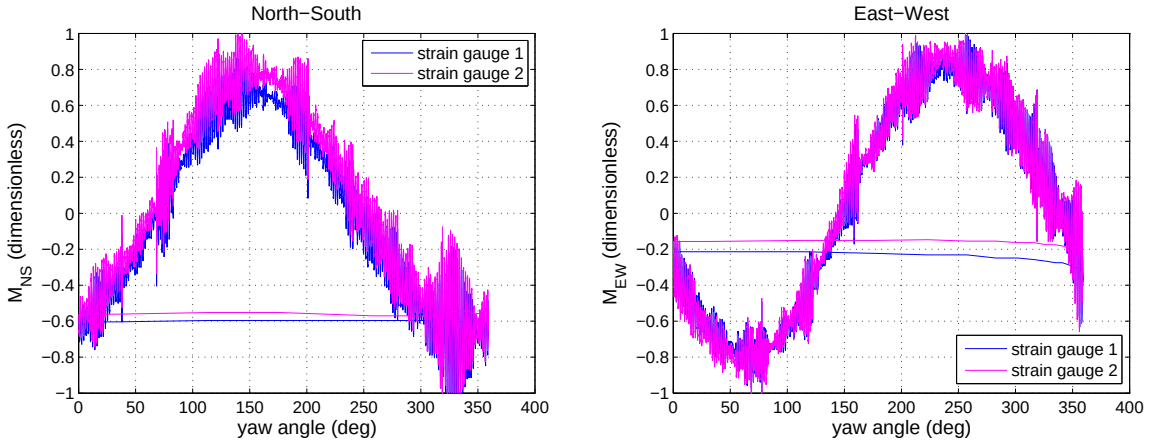

(a) Bending moment in the North-South direction observed during the yaw test from the two sets of strain gauges on the transition piece. Normalized with the maximum from strain gauge 2.

(b) Bending moment in the East-West direction observed during the yaw test from the two sets of strain gauges on the transition piece. Normalized with the maximum from train gauge 2.

Figure 6.3: Comparison of signal captured during the yaw test by the two sets of strain gauges on the transition piece.

6.1.2 Blade Calibration

Along each blade 4 strain gauges are mounted 1m from the root, for the measurement of the flapwise and edgewise moments on the blade root (Figure 6.4a). The calibration of the blade strain gauges is gravity based (Low Speed Idle LSI). Two tests were performed where the rotor was slowly rotated 360^o. The first test with pitch angle 0^o is used for the calibration of the edgewise moment and the second with pitch angle 90^o for the calibration of the flapwise moment. The resulting signal (in voltage) is a sinusoidal curve presented in Figure 6.4b, where the weight load is taken equal to unity.

The gain is the ratio between the load range, which is twice the expected moment at the strain gauge position because of the blade weight and the range in voltage (Equation 6.6). The offset is the distance of the mean value of the sinusoidal curve from 0.

$$gain = 2\frac{M_{blade} \cdot g \cdot d}{max(V) - min(V)} \tag{6.6}$$

To obtain the pure out-of-plane and in-plane moments a transformation to the fixed co-

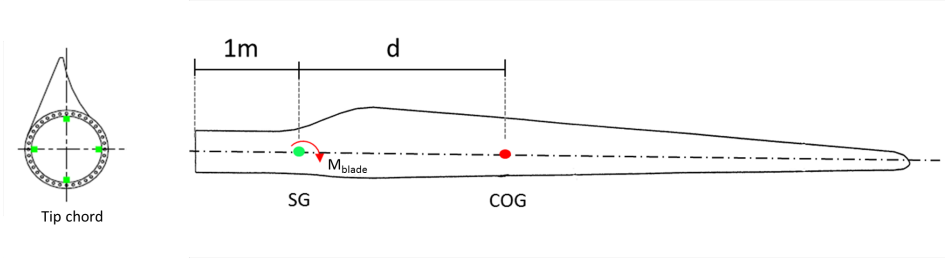

(a) Strain gauge mounting on the blade and moment around the gauge because of the blade weight.

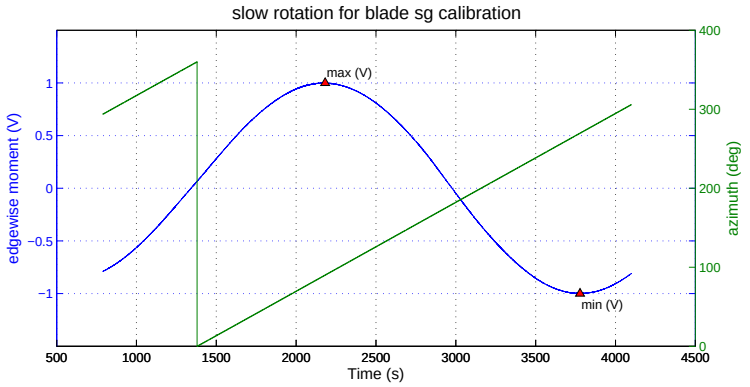

(b) Strain gauge signal mounted close to the blade root during rotor slow rotation test for calibration.

Figure 6.4: Strain gauges on the blade root.

ordinate system of the hub is required (Equation 6.7), where α_t is the offset between the tip chord and the strain gauge bridges and θ is the blade pitch angle at each time step. The accurate calculation of the offset α_t is not always possible on the site. During the calibration of the blade moments, several values of α_t should be tested, until the profile of the in-plane root bending moment as a function of the mean wind speed follows the shape of the power curve.

$$\begin{aligned} M_{out-of-plane} &= M_{flap}\cos(\alpha_t - \theta) - M_{edge}\sin(\alpha_t - \theta) \\ M_{in-plane} &= M_{flap}\sin(\alpha_t - \theta) + M_{edge}\cos(\alpha_t - \theta) \end{aligned} \tag{6.7}$$

During the blade strain gauge calibration some limitations need to be taken into consideration and the results should be examined with caution. Even though the blade is pitched either at 0^o or 90^o the crosstalk causes a deformation in the perpendicular plane and the strain gauges on that plane are no longer on the neutral axis, rendering difficult the excitation of the modes independently during the calibration test. Furthermore, the calibration of the blade strain gauges is performed in an ideal condition of low wind speed, where the real loading due to aerodynamic forces during operation is not taken into account. An uncertainty is also introduced due to misalignment between the tip chord and the strain gauge bridges.

6.1.3 Drivetrain Calibration

The drivetrain strain-gauge calibration is also gravity based, where the rotor was slowly rotated 360^o as happened in the case of the blades. Two strain gauges are mounted at 0^o-180^o to measure the tilt moment and two at 90^o-270^o for the yaw moment. The torsion signal is not reliable due to the curved geometry of the shaft where the strain gauges are installed. Figure 6.5a illustrates the nacelle and the rotor coordinate systems as seen from above, where the subscripts N and R denote nacelle and rotor respectively. Figure 6.5b presents how the signs of the moments are changing during the drivetrain rotation, based on the definition of the coordinate system.

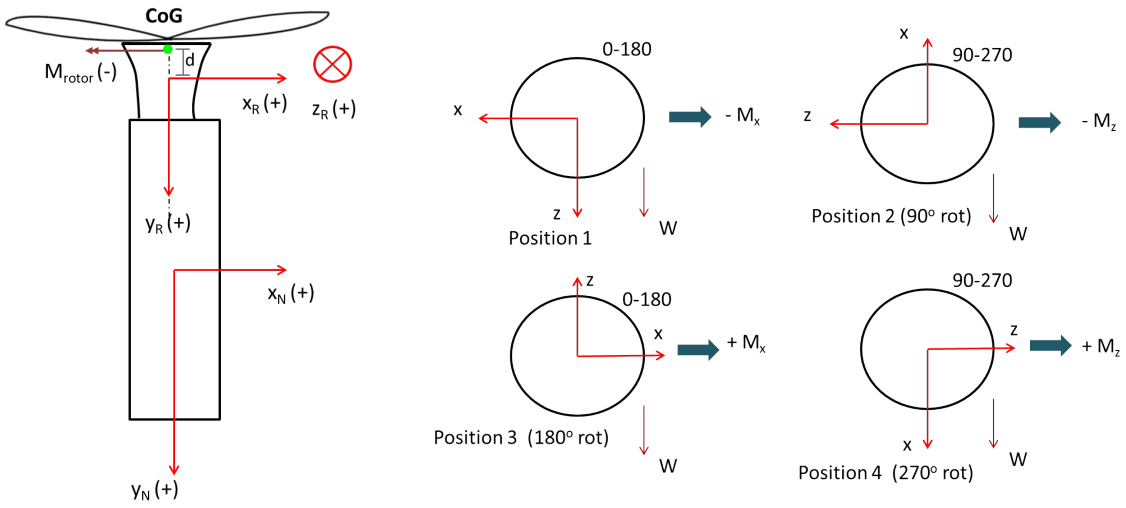

(a) Nacelle coordinate system. **(b)** Drivetrain orientation.

Figure 6.5: Nacelle coordinate system and drivetrain orientation.

The strain gauges capture a sinusoidal signal due to the moment induced by the weight of the rotor. The transfer function to the moments is given as before from Equation 6.5 and the gain from Equation 6.4a, where the mass of the rotor M_{rotor} instead of the nacelle is used. The offset is the distance of the mean value of the sinusoidal curve from 0. To obtain the pure tilt and yaw moments on the drivetrain a transformation of the coordinate system is required (Equation 6.8), where α_d is the offset from the definition of the 0 azimuth angle and az is the azimuth angle at each time step.

$$\begin{aligned} M_{tilt} &= M_{0-180}\cos(\alpha_d - az) - M_{90-270}\sin(\alpha_d - az) \\ M_{yaw} &= M_{0-180}\sin(\alpha_d - az) + M_{90-270}\cos(\alpha_d - az) \end{aligned} \tag{6.8}$$

To examine the correctness of the calibrated data, some signals from different components are plotted together. Figures 6.6a and 6.6b present the tilt moment of the shaft along with the fore-aft moment on the tower top and the yaw moment of the shaft along with the tower

top torsion respectively. The values are normalized with the maximum shaft moment of each signal. The signals agree satisfactorily, where the differences are attributed to the position of the tower strain gauges a few meters below the yaw bearing.

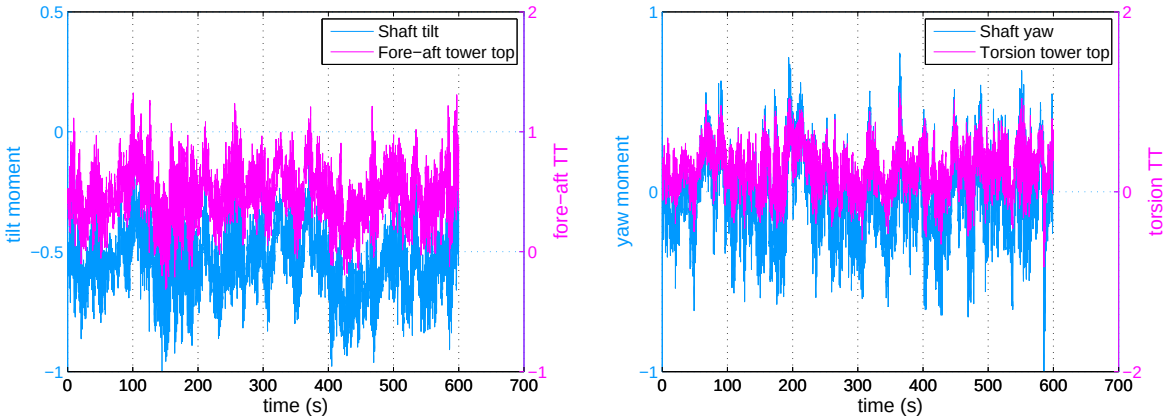

(a) Shaft tilt and tower top fore-aft moments.

(b) Shaft yaw and tower top torsion.

Figure 6.6: Shaft and tower top signal comparison, normalized with the maximum shaft moment.

For the calibration of the sub-structure/foundation instrumentation MATLAB scripts were written to read the .asc files obtained from the wind farm, calibrate the strains to moments, resample to 35Hz to obtain equal sampling rate as the rest of the structure instrumentation and transform the fixed to the rotating coordinate system. The results were saved in MATLAB structures for every 10min measurements. The calibration of the strain gauges mounted in the rest of the structure was performed using the in-house developed software EASY. The calibrated results are stored in files, for every 10min measurement. In the names of both file formats the date of the measurement is included for a more convenient selection of the same time series from all the measuring systems.

6.2 Yaw Angle Correction

A difference in the measured yaw position between D01 and the surrounding wind turbines is depicted in Figure 6.7a. This difference seems to be constant throughout the whole period and it is likely due to an error in the calibration of the yaw positions with the North orientation. Taking D01 as the reference wind turbine the error in the yaw measurement from the surrounding wind turbines can be calculated as $yaw_{diff} = yaw - yaw_{D01}$. The distribution of error between the other wind turbines and D01 indicates that there is a constant offset between the turbines and therefore the median of the distribution is chosen as a representation of the error (internal communication with DONG Energy). The yaw angle of D01 is also corrected for the North orientation based on the position of the strain gauges. The final formula for the correct yaw signal is given by Equation 6.9. Figure 6.7b shows the measured yaw angles after

the applied correction.

$$yaw_{corrected} = yaw_{measured} - \Delta\theta_{D01,median} - \Delta\theta_{D01,North} \tag{6.9}$$

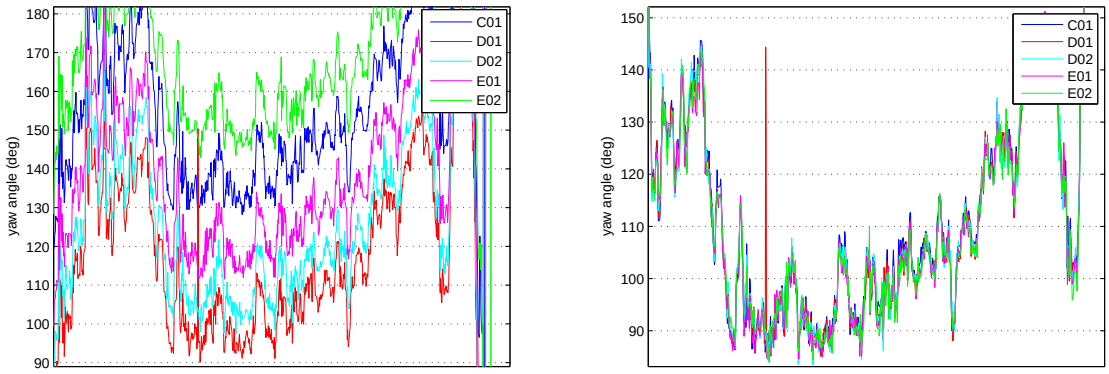

(a) Yaw angle of the instrumented wind turbine D01 and the surrounding ones as provided by the SCADA system.

(b) Corrected yaw angle of D01 and the surrounding wind turbines.

Figure 6.7: Yaw angles of the wind turbines before and after correction.

6.3 Data Synchronization

A problem usually encountered in measurement campaigns is the synchronization of the different measurement systems. In the fully instrumented wind turbine D01 there are four measurement systems, a) the sub-structure/foundation instrumentation by DONG Energy, b) the wind turbine instrumentation by DTU, c) the data acquisition (SCADA) system and d) the nacelle mounted LIDAR. A time lag is observed between all of them. In order to specify the difference in the time stamps, the yaw test performed for the strain gauge calibration on the 10^{th} of January 2013 has been used. The signal is clear rendering it easy to observe the difference in the overlap of the time series. The two sets of strain gauges mounted at the transition piece have been used for the synchronization of the DONG and DTU systems. The estimated time difference was found to be 50min (DTU measurement is preceding). The sub-structure/foundation system is set to the UTC and the time stamp specifies the end of the 10min measurement, while the DTU system is set to the CET and the time stamp specifies the beginning of the measurement. None of the systems has daylight saving. Figure 6.8 depicts the time lag in the two signals.

The same yaw test was used for the synchronization of the SCADA with the DTU system. The SCADA data are stored with time stamps in CET and CEST for summer time. Figure 6.9 shows the two measured yaw signals. During winter time there is no time lag, but since the

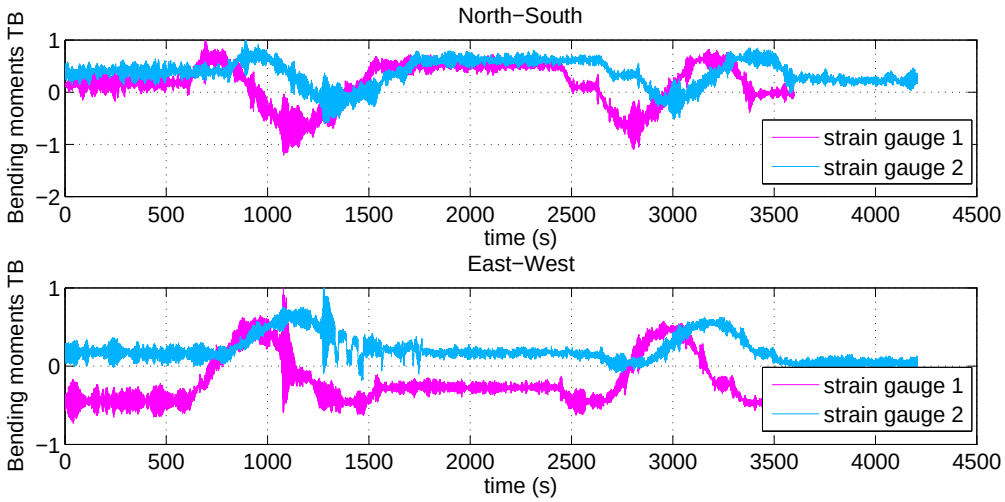

Figure 6.8: Time difference between the DTU and the foundation measuring systems by comparison of the measured strains during the yaw test.

SCADA system has daylight saving, during summer time there is an hour difference between the two systems.

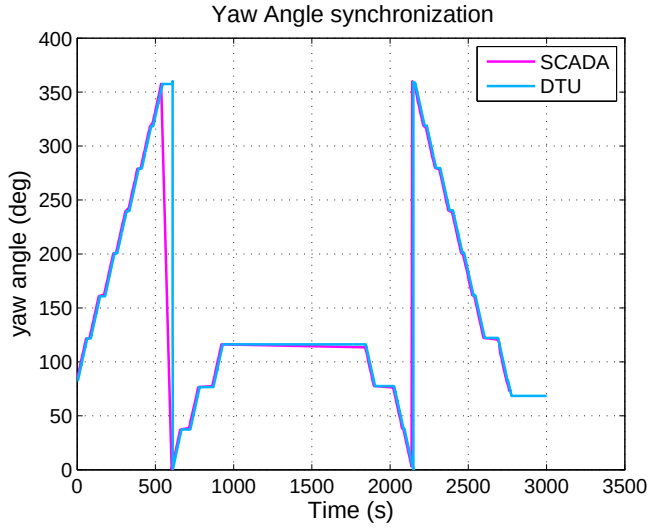

Figure 6.9: Time difference between the DTU and the SCADA systems by comparison of the measured yaw angle during the yaw test.

For the synchronization of the nacelle mounted LIDAR the mean values of the 10min mean wind speed over a period of time measured by the DTU nacelle cup-anemometer and the LIDAR are plotted against each other. A time lag of 1-hour, where the LIDAR is following, has been observed (Figure 6.10).

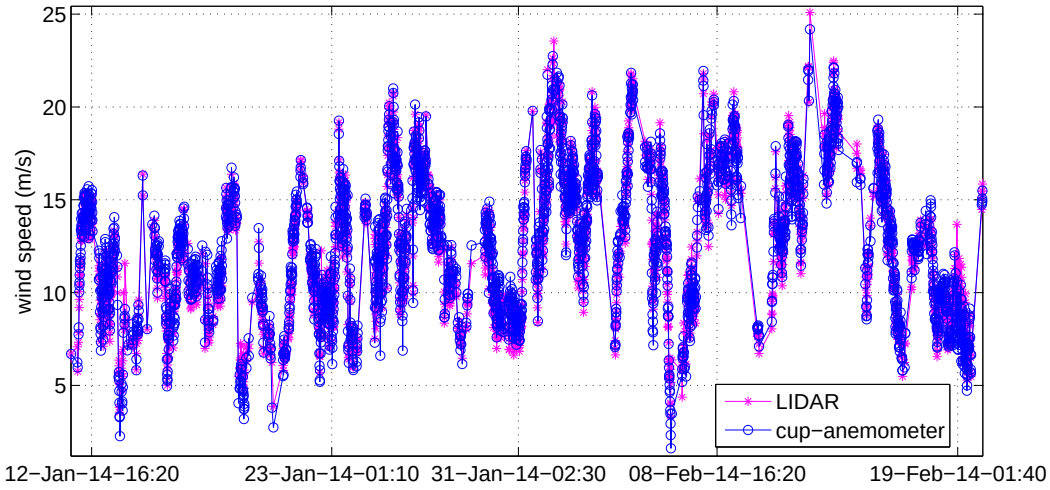

Figure 6.10: Synchronization of the 10min mean wind speed measured by the LIDAR and the nacelle cup-anemometer.

6.4 Data Processing

For the post-processing of the calibrated measurements MATLAB scripts were developed to read the data, based on the measurement date included in each file name. An example of the support structure load profiles when the wind turbine is in operation and is facing free wind, is presented in Figure 6.11, where the fore-aft and the side-side bending moments along the tower and the sub-structure/foundation are depicted. The values are normalized with the maximum load appeared at the tower bottom and they correspond to six months of measurements.

6.4.1 Data Availability

During the measurement campaign, the operation of the different instrumentation has not been constant. The main systems used are the data acquisition system (SCADA), the instrumentation of D01, the sub-structure/foundation instrumentation, the nacelle mounted LIDAR and the wave buoy. Due to a gearbox failure the wind turbine was down for 9 months (January-September 2013). However the data obtained during this period can be used for the analysis of the response in stand-still conditions. Figure 6.12 presents the data time-line for the whole period. The main problem experienced is the lack of data overlap.

6.5 Recommendations for Future Measurement Campaigns

During this measurement campaign several lessons have been learned from the different problems encountered. Therefore, a few recommendations about future campaigns are presented.

- Before the beginning of the measuring period the synchronization of the different instrumentation systems should be ensured. Erroneous data interpretation might be due to comparison of different time periods.
- Yaw and low speed idle (LSI) tests should be performed more often, for the accurate calibration of the strain gauges due to drifts in the mean values mainly because of changes in the temperature.
- The overlap of the different measuring systems should be ensured at least once during winter and summer, in order to examine different environmental conditions.
- The theoretical calibration based on the dimensions of the structure should be trusted more than the calibration based on the expected moment from the rotor weight, due to the uncertainties introduced by the estimation of the nacelle center of gravity.
- The battery of a wave buoy should be replaced immediately, when it reaches the minimum voltage threshold, not only due to a pause on the measurements but also because of the risk of equipment loss.
- Cases of boat impacts on the sub-structure should be recorded for further analysis, for the estimation of the net damping.

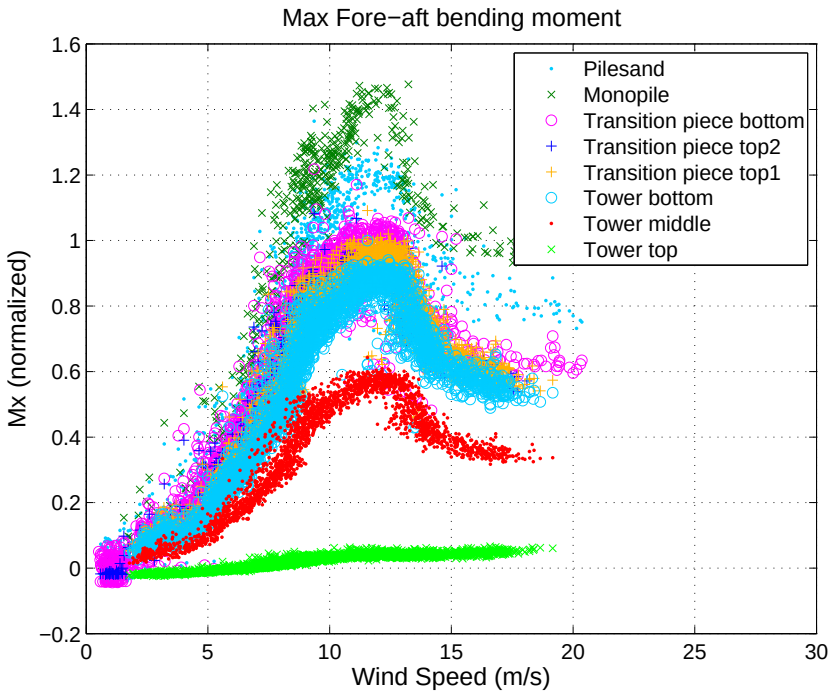

(a) Fore-aft bending moment clouds along the tower and the sub-structure/foundation, normalized with the maximum load appeared at the tower bottom.

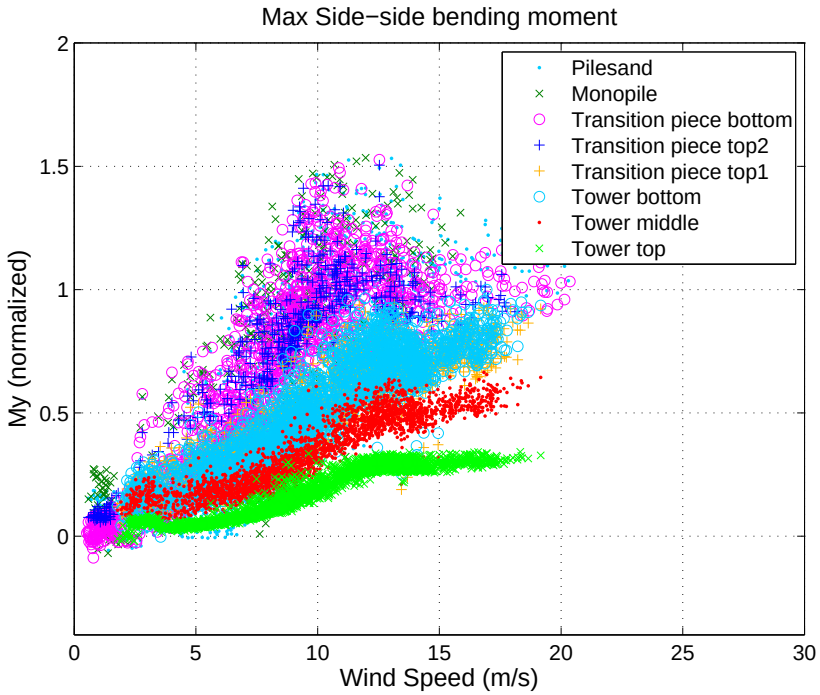

(b) Side-side bending moment clouds along the tower and the sub-structure/foundation, normalized with the maximum load appeared at the tower bottom.

Figure 6.11: Profiles of support structure bending moments.

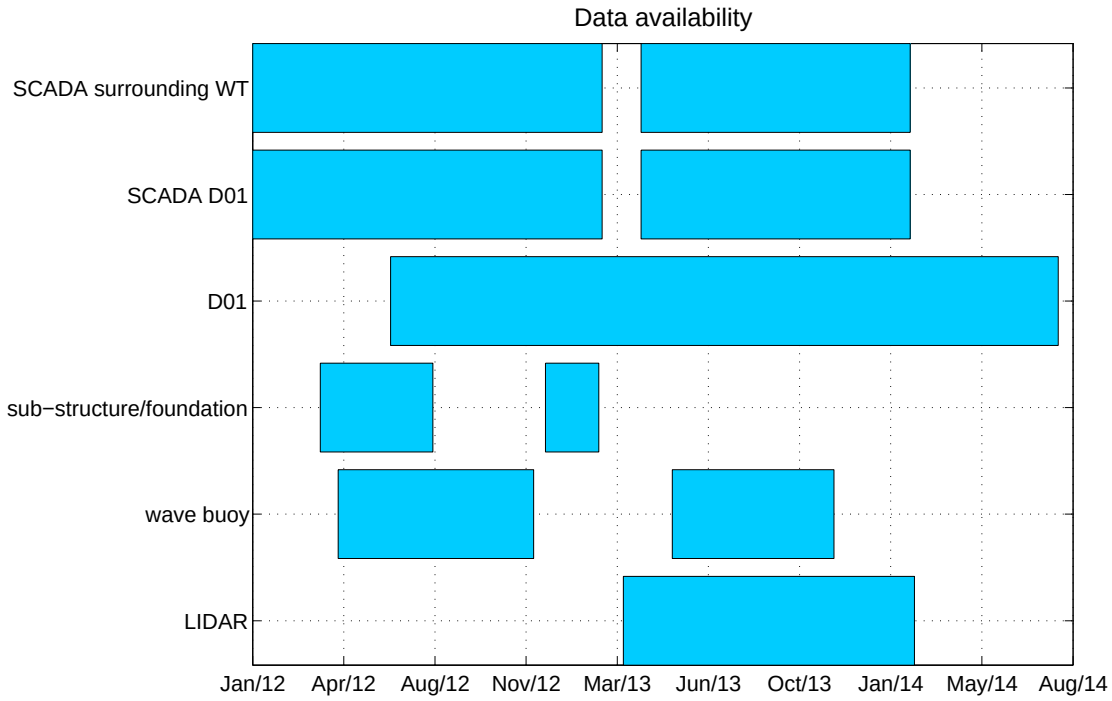

Figure 6.12: Data time-line for the whole measurement period. The hatched entries show data availability.

Chapter 7

Wind Measurements Calibration

Wind speed on the site is measured by three different systems, a) the SCADA system of the wind turbine, b) two nacelle mounted cup-anemometers and c) a nacelle LIDAR all measuring wind speed time series. In this chapter the wind data from all the different systems are analyzed and compared for a better overview of the wind conditions. Both sectors of free wind and wake are examined. The turbulence intensity provided as an input to the aero-elastic software and the Weibull probability density function used in the fatigue analysis of the structure are estimated. 1 year of measurements are used for the analysis.

7.1 Nacelle Mounted Cup-anemometer/SCADA

The nacelle mounted cup-anemometer was calibrated externally and installed on the wind turbine nacelle by DTU. A second cup-anemometer was calibrated and installed by Siemens wind power. Figure 7.1 presents the mean wind speed measured by the SCADA system of the fully instrumented wind turbine D01 during 2012. Throughout the whole year the wind turbine was in operation. The average wind speed on the site is 9.6m/s and the main wind direction is 260^o. D01 is in the free wind sector when the yaw angle is between 130^o and 170^o.

7.1.1 Turbulence Intensity

7.1.1.1 Free Wind

The longitudinal turbulence intensity (TI) is equal to the standard deviation of the horizontal wind speed at the hub height divided by the mean wind speed. Scatter data both from the

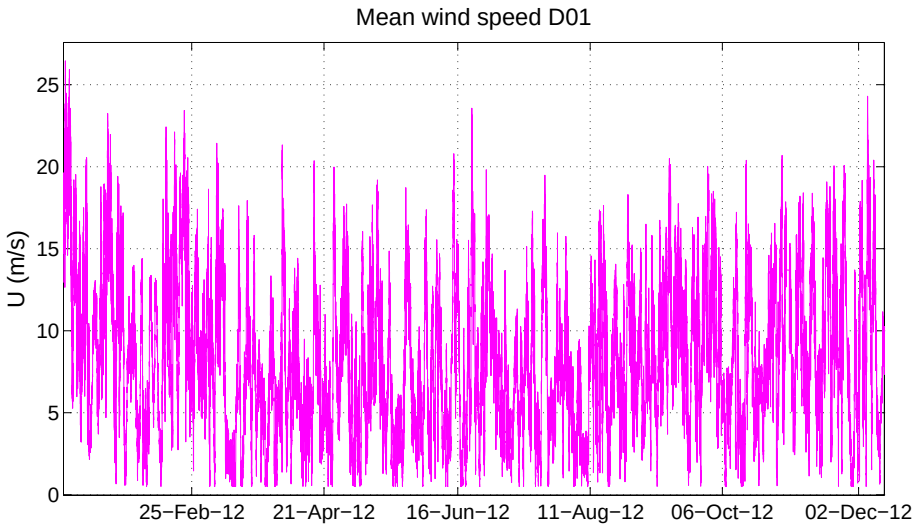

Figure 7.1: Mean wind speed measurements from the SCADA system of D01, for 2012.

SCADA system and the nacelle mounted cup-anemometer have been used for the calculation of TI. The wind was separated in bins of 1m/s and the 90^{th} percentile of the TI in each bin is calculated (free wind sector). An exponential curve of the form $y = a \cdot e^{bx} + c \cdot e^{dx}$ is fitted to this data to obtain the turbulence intensity as a function of the mean wind speed. Figure 7.2 presents the scatter TI data in the free wind sector from the SCADA system along with the two fitted curves (SCADA and cup-anemometer) and the TI proposed by the IEC 61400-1 standard [17], for wind turbine class B ($I_{ref} = 0.14$). The standard deviation for offshore conditions according to the standards is given by Equation A.1.

As it can be noticed in the operational region there is a difference of 30-40 % between the TI estimated from the measurements of the SCADA data and from the DTU cup-anemometer. This discrepancy is attributed to the conservative cup-anemometer readings, due to the wake effect of the rotor. Figure 7.3 displays the wind power spectrum obtained from a Fast Fourier Transformation to the DTU nacelle cup-anemometer time series. The influence of the rotor on the wake flow is portrayed by the spikes at 3P and 6P. The wind measurements provided by the SCADA system are derived by the Siemens nacelle cup-anemometer. The calibration of the nacelle mounted cup-anemometer by Siemens was performed in Høvsøre, based on 3 months of measurements. A transfer function between the nacelle and the mast cup-anemometer readings was derived.

To investigate the effect of the conservative cup-anemometer readings on the wind turbine response, the blade and tower load spectra from the simulations are compared with the measurements for each mean wind speed. Figure 7.4 (y axis in logarithmic scale, x axis omitted) depicts the difference in the load spectra energy for $U = 15m/s$. Assuming that the difference is only a result of the higher turbulence present in the simulations, various correction factors for the TI have been tested for each mean wind speed, until the load spectra match. The green dotted line presents the simulations with the measured turbulence intensity from the cup-anemometer, the light blue dashed line the simulations including the correction factors

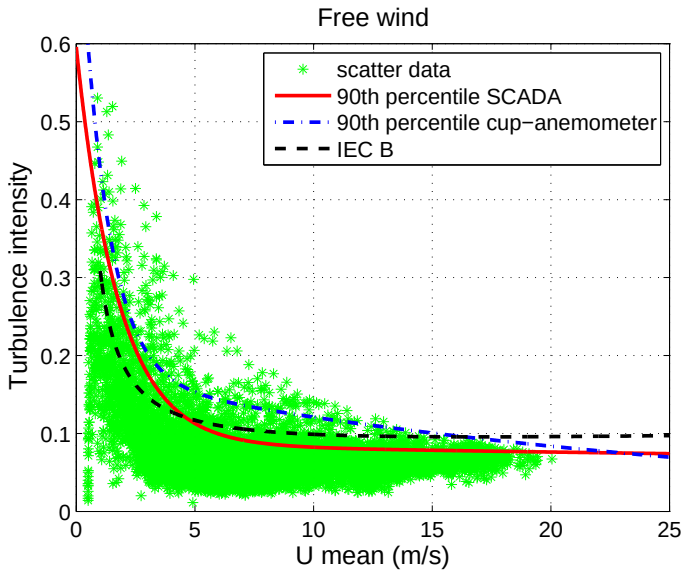

Figure 7.2: Turbulence intensity for the free wind sector, based on 1 year measurements. Scatter data from SCADA system (green points), IEC class B (dashed black line), exponential fitting to the 90^{th} percentile of the scatter data provided by the SCADA system (solid red line) and by the DTU nacelle cup anemometer (dash-dot blue line).

for the TI and the pink solid line the measurements. The vertical lines correspond to the harmonics of the rotational speed. The agreement in the load spectra between measurements and simulations is better when a correction has applied to the cup-anemometer readings. Figure 7.5 illustrates the fitted curve to the scatter turbulence intensity data from the SCADA system along with the corrected TI from the nacelle cup-anemometer. There are small differences (less than 10%) in the values provided by the two curves. Even though the limitations of the wind measurements from both systems are known, the turbulence intensity provided by either of them is used in the following simulations, being the only available wind data. Comparison of measurements and simulations should still be analyzed with caution, as possible discrepancies can be due to different wind conditions between them.

7.1.1.2 Wake

To account for the wake effect from different directions an effective turbulence intensity I_{eff} (Equation A.4) is proposed in the IEC 61400-1 standards [17]. Instead of the recommended uniform distribution, the wind rose was used for the estimation of the probability of the wind direction. The yaw angles are separated in bins of 1^o and the probability of each bin is calculated from the Cumulative Density Function (CDF) of the distribution fitted to the wind direction data (Section 5.1.2). D01 is installed on the outside row of the wind farm and sees free wind in the South-East direction. These yaw angles are excluded from the calculation of the effective turbulence intensity. The effective TI estimated from the wind speed measurements is shown in Figure 7.6 and compared with the free wind TI and the effective TI using uniform

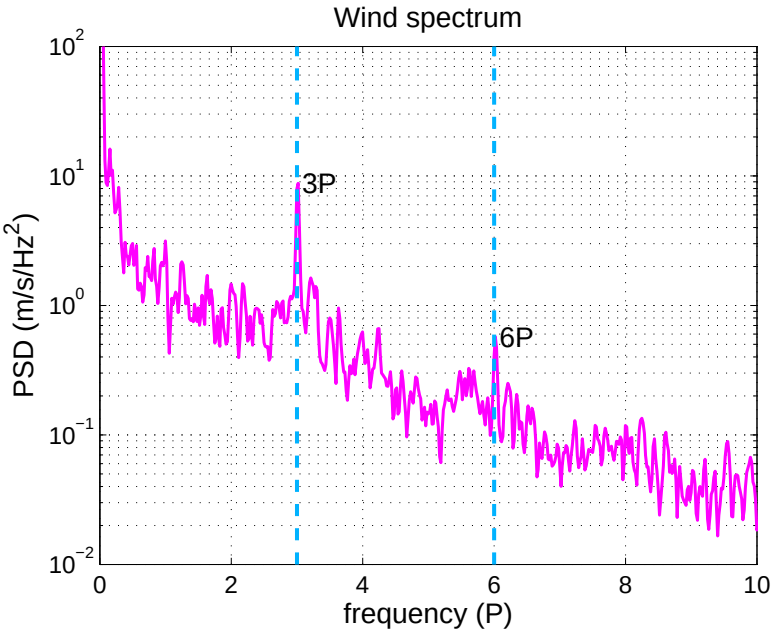

Figure 7.3: Wind spectrum obtained from the DTU nacelle cup anemometer. The y axis is on a logarithmic scale and the frequencies are normalized with the rated rotational speed. The vertical lines correspond to the harmonics of the rotational speed.

PDF for the wind direction. As proposed in reference [62] the Wöhler exponent m of the most sensitive material should be used. Here $m = 12$. The difference between the I_{eff} using uniform PDF and the I_{eff} based on measurements at different wake sectors is up to 10%. The I_{eff} accounting for the wind direction probability is more representative of the site and therefore it will be used in the simulations for the analysis of the wind turbine response on the wake.

7.1.2 Weibull Distribution

The 10min mean wind speed measurements from the free wind sector provided by the SCADA system of the instrumented wind turbine D01 and the surrounding turbines C01, D02, E01, E02, were used in Equation A.8 to calculate the Weibull probability density function of the wind speed. Based on that and assuming 25 years of lifetime, the hours of each mean wind speed can be estimated for the fatigue analysis of the system ($hours_{free\_wind} = 25 \cdot 365 \cdot 24 \cdot PDF_{weibul}$). Figure 7.7 presents the PDF of the wind speed for all the turbines.

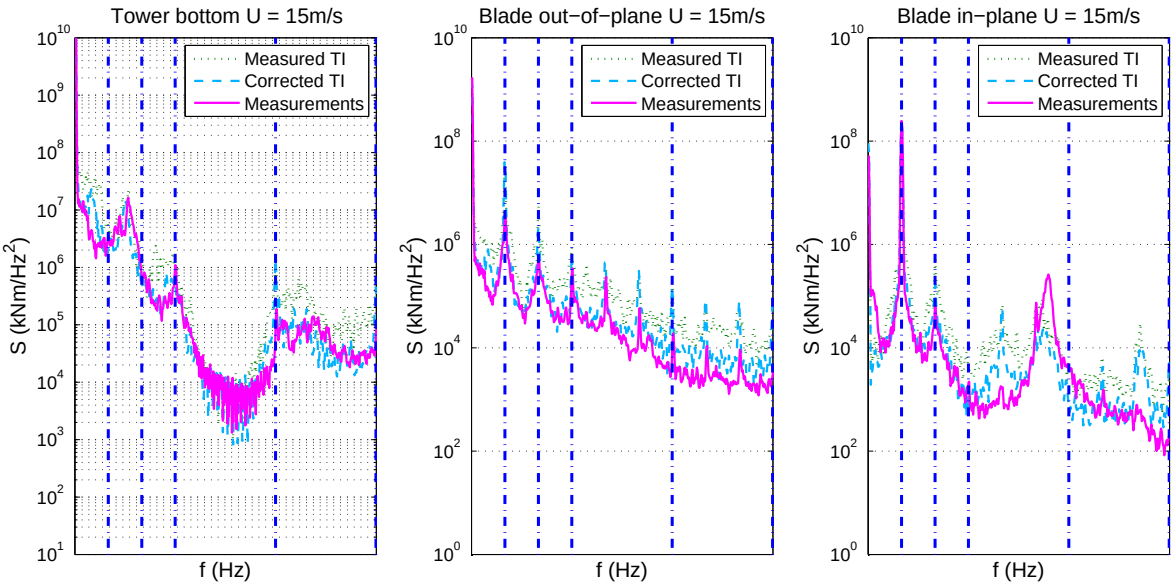

Figure 7.4: Load spectra of the tower bottom, the out-of-plane and the in-plane blade root bending moments for $U = 15m/s$. Comparison between measurements (solid line) and simulations for two different TI values, measured TI (dotted line) and corrected TI (dashed line). The x axis has been omitted and the vertical lines show the harmonics of the rotational speed.

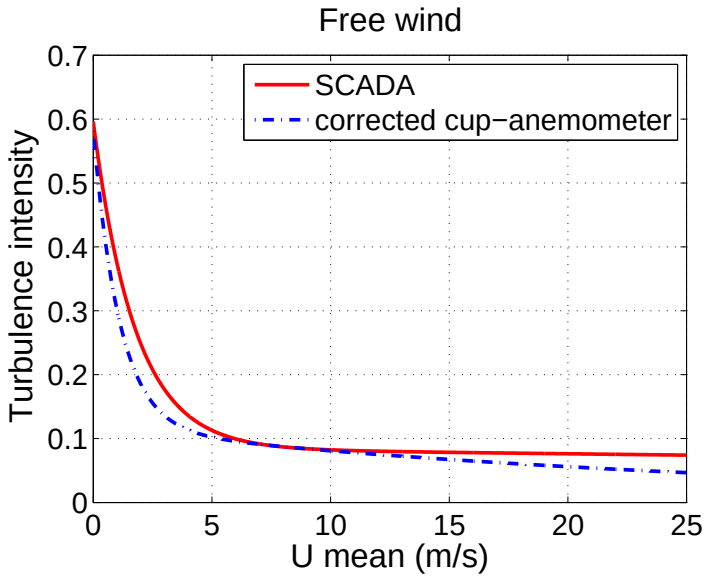

Figure 7.5: Comparison of turbulence intensity provided by the SCADA system and the corrected cup-anemometer measurements.

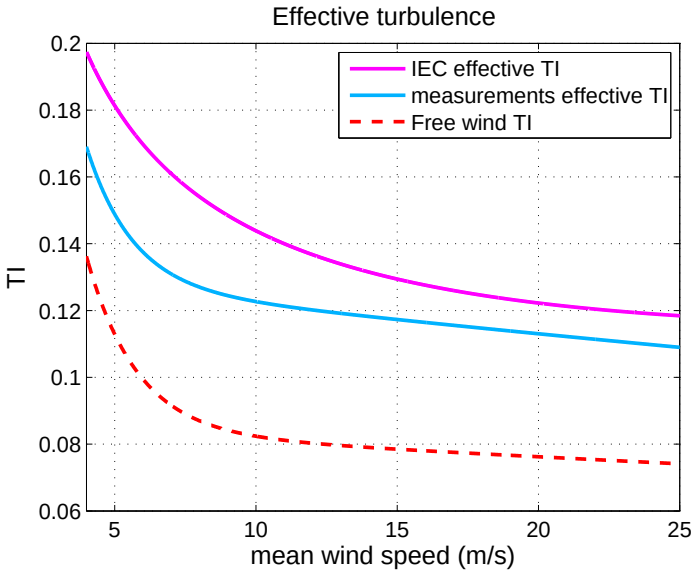

Figure 7.6: Effective turbulence intensity from the measurements using the wind rose (blue solid line) and from the standards using uniform wind direction (pink solid line). The red dashed line represents the free wind TI.

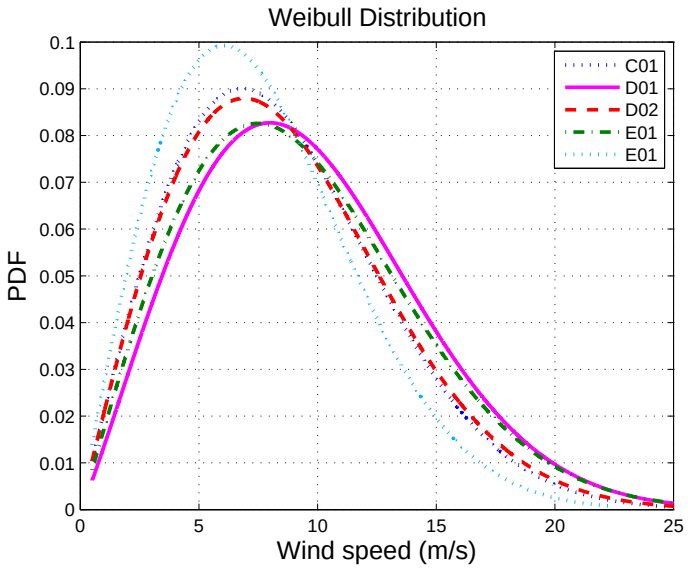

Figure 7.7: Wind probability distribution function, Weibull, based on 1 year SCADA measurements for the instrumented and the surrounding wind turbines.

7.2 LIDAR

A nacelle mounted LIDAR is installed on the wind turbine, to measure the upstream wind flow. The operation of a LIDAR is described in Section 2.1. The wind speed measured by the two beams is combined by Equation 2.2 to construct the wind seen by the turbine.

The nacelle mounted LIDAR senses the wind speed over a volume defined by the two beams. This characteristic does not allow enough resolution for small turbulence structures, which results in an underestimation of the wind speed standard deviation and thus an underestimation of the turbulence intensity [146]. Around the area of small yaw error ($\pm 15^o$) the ratio of the wind speed standard deviation from the LIDAR over the standard deviation from the cup-anemometer is close to 0.8, but as the wind direction deviates more from the LIDAR axis the ratio increases drastically. Therefore, the turbulence intensity estimation from the nacelle LIDAR should be examined carefully keeping in mind the sensitivity of the measurements to the wind direction relative to the LIDAR axis.

Figure 7.8 presents the correlation between the mean wind speed measured by the nacelle cup-anemometer and the LIDAR when the wind turbine is in operation. Figure 7.8a shows the mean wind speed from the 10min time series constructed by the instantaneous beam measurement and Figure 7.8b illustrates the wind speed calculated from the combination of the mean of each beam. Higher spread is observed when the wind speed is obtained from the instantaneous beam measurements. In the case that the 10min mean wind speed is calculated from the time series, where the horizontal wind speed is computed at each time step from the instantaneous measurement of the radial wind speeds, overestimation of the mean wind speed is expected. The horizontal shear or a local gust visible from one of the beams results in an erroneously high transverse component, which is translated to a yaw error. For this reason it is recommended that the mean wind speed is obtained by first calculating the mean radial speeds of each beam Vl and Vr and then applying Equation 2.2 [21].

The correlation of the wind speed from the two instrumentation for different wind sectors is depicted in Figure 7.9. In the free wind sector the agreement is satisfactory, while the spread is higher in the wake. Cases where the wind speed is partially in the wake, result in a larger deviation of the radial wind speed measured by the two beams. This introduces an error in the wind speed estimation as the main LIDAR assumption of homogeneous horizontal wind is violated.

An empirical method to estimate the turbulence intensity from the LIDAR readings is proposed in reference [21]. The turbulence intensity estimated from the radial wind speed of each beam is combined through Equation 7.1, where TI_l and TI_r are the turbulence intensity of each beam, defined as the standard deviation of the radial wind speed of the laser beam over the beam's mean wind speed. The TI estimated from the two beams is expected to be the same, due to the assumption of homogeneous horizontal wind speed. The violation of this assumption in the wake sector, renders the estimation of the turbulence intensity from the

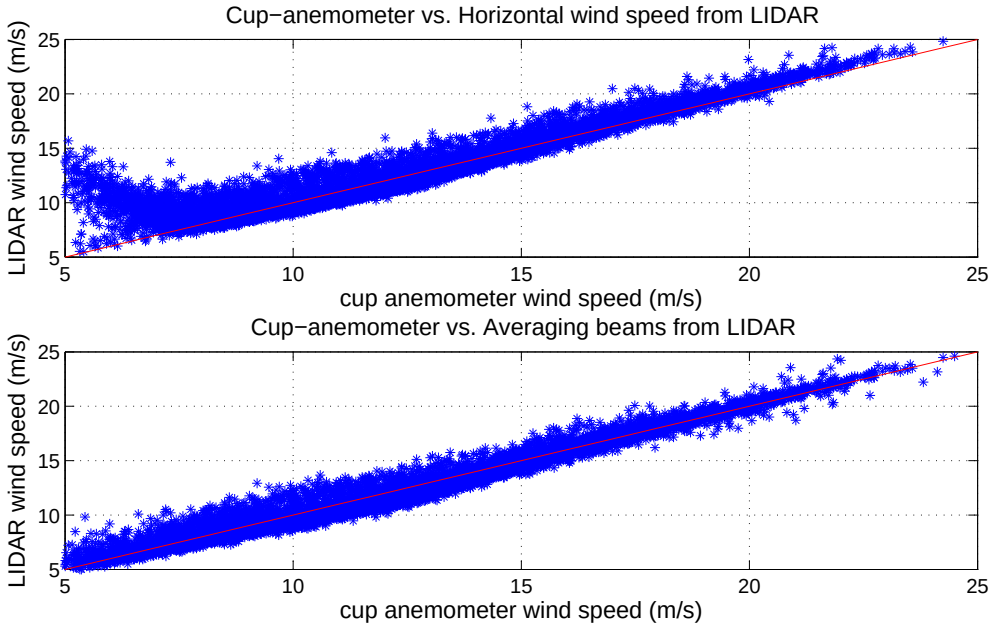

Figure 7.8: a) Correlation between the 10min mean wind speed by the nacelle LIDAR compared with the nacelle cup-anemometer. b) Correlation between the 10min mean wind speed by averaging the radial wind speed of the beams compared with the nacelle cup-anemometer.

LIDAR in the wake not reliable.

$$TI_{lidar} = \frac{TI_l + TI_r}{2} \tag{7.1}$$

Figure 7.10 presents the correlation between the turbulence intensity estimated by the nacelle cup-anemometer and the LIDAR in the free wind sector. An overestimation of the TI by the cup-anemometer can be observed, due to the rotor wake effect. However, TI measurements from nacelle mounted instruments should always be considered with caution. In order to build up confidence in the turbulence intensity estimation from a LIDAR, the measurements should be validated against a mast cup-anemometer.

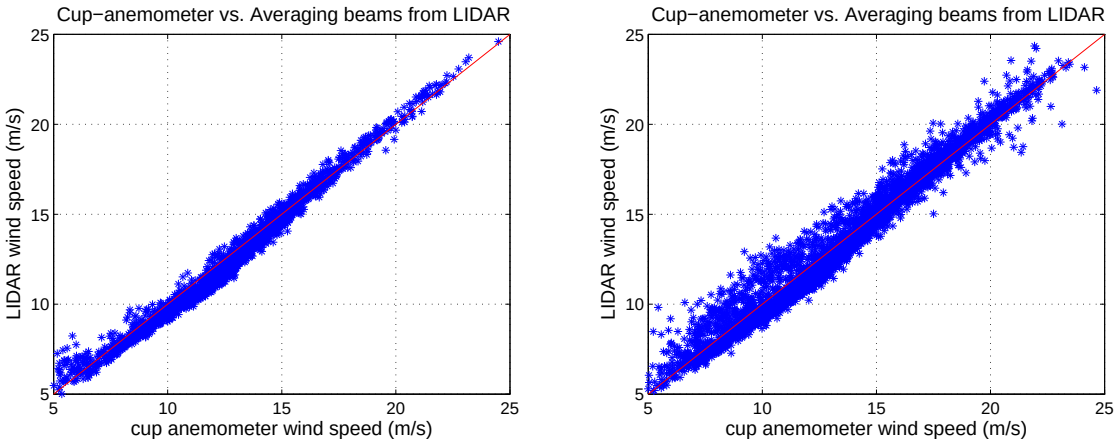

(a) Mean wind speed correlation between the LIDAR and the nacelle cup-anemometer in the free wind sector.

(b) Mean wind speed correlation between the LIDAR and the nacelle cup-anemometer in the wake sector.

Figure 7.9: Correlation between the LIDAR and the cup-anemometer for different wind sectors.

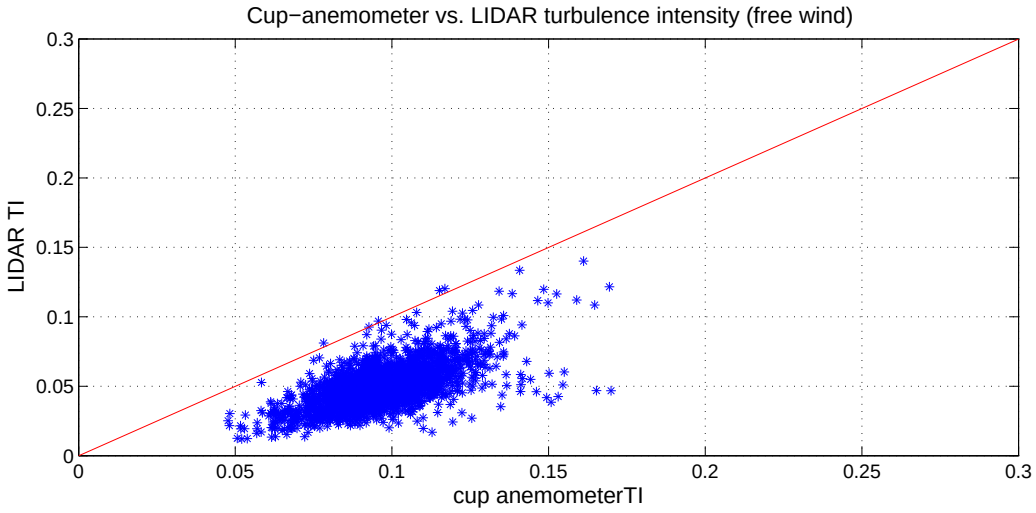

Figure 7.10: Turbulence intensity estimated by the LIDAR and the nacelle cup anemometer for the free wind sector.

Chapter 8

Model Setup

In this section a detailed description of the process followed to build the wind turbine model is presented. The wind-wave distributions and the soil model given as inputs to the software are also described. The aero-elastic software HAWC2 [3] developed at DTU is used for the simulations. The code is based on a multi-body formulation, where each body is a Timoshenko beam with six degrees of freedom for each node. The different bodies are connected with constraints equations. The response of a horizontal axis wind turbine under aerodynamic, hydrodynamic and soil loads is calculated in the time domain. The Newmark-beta method is used for the solution of the equations. The 3 bladed 3.6MW pitch regulated-variable speed offshore wind turbine model is developed as a multi-body finite element beam model. For the modeling of the support structure (tower, sub-structure and foundation) the drawings from DONG Energy have been employed. The blade is built based on information provided by Siemens wind power and on the downscaled blade geometry and aerodynamics of the NREL 5MW wind turbine [147]. Table 8.1 presents the gross properties for the 3.6MW wind turbine model.

8.1 Support Structure Characteristics

The distributed tower properties are based on the information from Siemens wind power. The tower has a height of 62m. For the calculation of the bending stiffness the Young's and the shear modulus are taken equal to 210 GPa and 80.8 GPa respectively.

The transition piece has a constant diameter of 5m and a length of 24m. The monopile has a linearly tapered diameter from the end of the transition piece to the seabed. The submerged pile has a constant diameter of 6m and a penetration length of 23m. The geometrical

Description	Value
Rated Power	3.6MW
Rotor type, position	3-bladed, upwind
Power Regulation	variable speed, collective pitch
Rotor diameter	107m
Blade length	52m
Cut-in, rated, cut out wind speed	4m/s, 13.5m/s, 25m/s
Cut-in, rated rotor speed	5rpm, 13rpm
Hub height (above LAT)	83.5m
Water depth	27m
Tower top mass	234.5tons
Shaft tilt, coning	5^o, 2.5^o

Table 8.1: Gross properties for the 3.6MW Siemens wind turbine

characteristics of the substructure were provided by DONG Energy. The depth on the site is 27m. The Young's and shear modulus are taken equal to the tower values.

8.2 Downscaling Process

The initial blade model has been built up in reference [148] based on the similarity rules for wind turbine up-scaling developed by Chaviaropoulos in [147]. Geometric similarity rules were applied to the geometric, structural and aerodynamic properties of the NREL 5MW reference wind turbine [68] to obtain the 3.6MW blade. The initial blade model characteristics were tuned to match the blade mass, natural frequencies and center of gravity based on the information provided by Siemens wind power. Respecting the shape of the downscaled mass distribution, mass has been moved along the blade model to make the center of gravity coincide with the one from the real blade. The bending stiffness has been accordingly modified to match the blade natural frequencies with the ones provided by the manufacturer.

The scaling factor SF (Equation 8.1), defined as the square root of the ratio of the rated power of the considered wind turbines, was used in the downscaling process.

$$SF = \sqrt{\frac{P_{rated,3.6MW}}{P_{rated,5MW}}} = 0.849 \tag{8.1}$$

Each characteristic of the downscaled blade is calculated from Equation 8.2, where the exponent n depends on the considered property. The values for n can be found in reference [147]. The thickness of the blade is given by the relation $t = \delta c$, where δ is the relative thickness and c the chord of the blade. The spar cap was chosen to be $0.3c$ at the blade root and $0.5c$ at the tip, with linearly changing intermediate values. The Young's modulus was taken equal to 22 GPa for the first 3.5m from the root, and equal to 16.7 GPa for the rest of

Blade Natural Frequencies	Percentage difference
1^{st} flapwise bending	0.13%
1^{st} edgewise bending	0.9%
2^{nd} flapwise bending	3.38%
2^{nd} edgewise bending	15.14%

Table 8.2: Difference in the natural frequencies between modeled and real blade

the blade. Table 8.2 presents the difference in the natural frequencies between the downscaled model and the actual blade.

$$Downscaled = Reference \cdot SF^n \tag{8.2}$$

In Figure 8.1 the thrust curve provided by the manufacturer is compared with the thrust obtained by a HAWC2 simulation, normalized with the maximum given thrust. The two curves seem to agree well. Discrepancies in the maximum thrust are attributed to the different control strategies around rated wind speed.

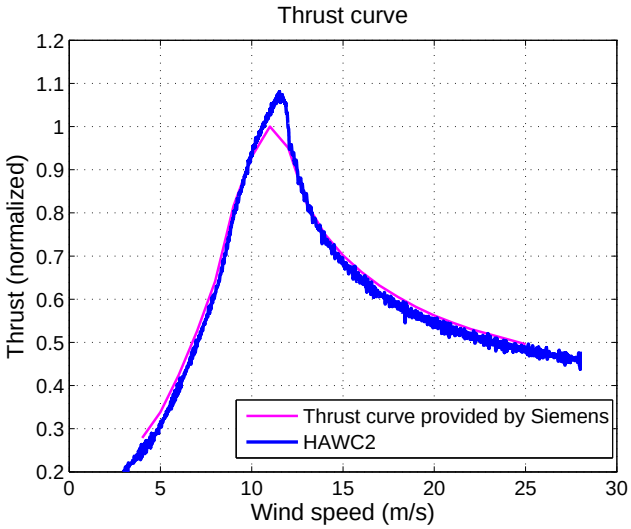

Figure 8.1: Thrust curve provided by the manufacturer compared with the HAWC2 blade model, normalized with the maximum given thrust.

The blade tip-tower clearance of the undeformed blade is $11m$ taking into account the 5^o tilt of the nacelle and the 2.5^o coning angle of the blade. The maximum blade tip deflection for the design case DLC 1.3 should not exceed 67% of the clearance of the undeformed blade, which corresponds to a maximum acceptable tip deflection of $7.4m$. 10min simulations with 12 turbulence seeds per mean wind speed were performed in HAWC2 and the maximum tip deflection was calculated for an azimuth angle range of $\pm 15^o$ in front of the tower. Figure 8.2 presents the blade tip deflection for all three blades for each mean wind speed. The maximum deflection is observed around rated wind speed and it does not exceed the maximum acceptable value.

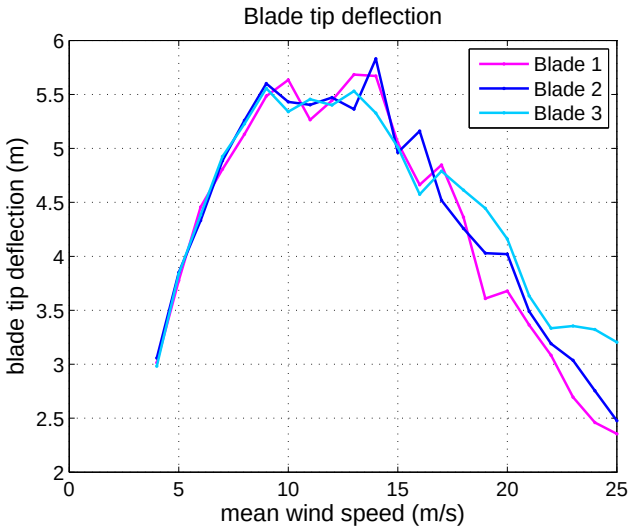

Figure 8.2: Maximum tip deflection for all three blades for each mean wind speed.

8.3 Model Damping

The damping of the structure is tuned to match the measured damping in stand still from the boat impact, analyzed in Section 11.1.1. In the HAWC2 model the damping is applied as a Rayleigh stiffness proportional damping. For the estimation of the additional offshore damping in the 3.6MW model wind turbine an impulse is applied in the side-side direction for various Rayleigh coefficients, until the model damping matches the measured one (trial and error). A tower damper is not included in the simulations. A Rayleigh damping factor multiplying the linear stiffness coefficients is used to obtain the soil damping coefficients. Simulations were performed with 2m/s mean wind speed, blade pitch angle 82^o, flexible soil and waves with significant wave height 0.41m. The damping was estimated by fitting an exponential function to the relative maxima of the tower top acceleration time series.

Figure 8.3a shows the tower top acceleration in the fore-aft and side-side direction in four separate time instants after the impulse was applied. The assumption of separate mode excitation is satisfied. Figure 8.3b presents the envelope of the decaying time series in the side-side direction and the fitted exponential function. The estimated damping ratio is $\zeta = 0.019$ which corresponds to a logarithmic decrement of $\delta = 12.4\%$.

To verify the result for the additional offshore damping estimated from the impulse response, another simulation with ambient excitation was performed in HAWC2. The mean wind speed was 4m/s, the blades were pitched at 82^o, and the significant wave height was 0.41m. Figure 8.4a depicts the motion seen from above in the two directions (fore-aft and side-side), where the main excitation seems to be in the fore-aft direction. When using the vibrations resulting from ambient excitation, the damping ratios can be estimated in a similar way as from the decaying time series, through the parameters of a fitted exponential curve to the relative maxima of the auto-correlation function of the tower top acceleration [149]. The separate mode excitation assumption is satisfied due to the presence of vibration only in the

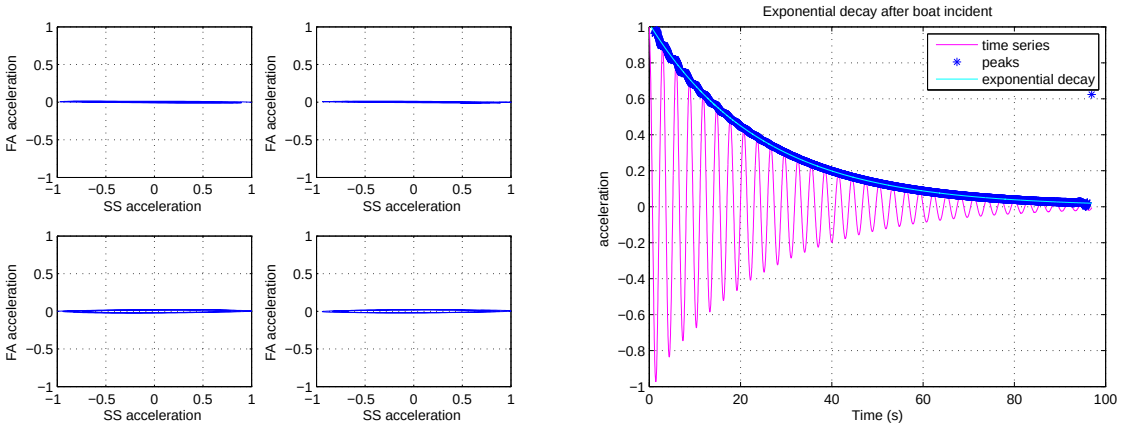

(a) Tower top motion at four different moments after the application of the impulse (normalized with the maximum side-side acceleration).

(b) Impulse response of tower top acceleration in the side-side direction (simulations, normalized with the maximum side-side acceleration).

Figure 8.3: Tower top accelerations and exponential decay after the application of an impulse to the structure in the side-side direction (normalized).

fore-aft direction, so the system can be handled as a Single Degree of Freedom (SDOF). Taking the inverse Fast Fourier Transform of the power spectral density of the tower top acceleration signal in the direction of the wind flow gives the auto-correlation function shown in Figure 8.4b (normalized auto-correlation). In the same figure the fitted exponential curve to the relative maxima is also presented. The obtained damping ratio is $\zeta = 0.015$. The lower value compared to the impulse response applied in the side-side direction is due to the pitch angle of the blades (82^o) that introduces some aerodynamic damping in the side-side direction, an observation also made from the measurements (Section 11.1.1).

8.4 HAWC2 Model

The different sections provided as inputs to HAWC2 are the Structure, the Orientation, the Constraints, the Soil, the Wind, the Hydrodynamic, the Control and the Output Section. In the first three sections the wind turbine model is built up. The soil, the wind and the hydrodynamic sections include the parameters defining the different operational conditions. In the control section the controller actions are declared. In the output section the sensors over the wind turbine are specified, in order to obtain the simulation results.

A schematic picture of the complete HAWC2 model is presented in Figure 8.5. The tower top mass is equal to the mass of the nacelle plus the hub and the blades: $tt_{mass} = M_{nacelle} + 3 \cdot M_{blade} + M_{hub}$. The nacelle mass is modeled as a concentrated mass on the tower top with a corresponding inertia (Equation 8.3). The inertia of the nacelle about the yaw axis I_{yaw} and the location of the center of gravity r are based on the downscaled values of the 5MW reference wind turbine. The nacelle center of mass is located 1.61m downwind of the yaw axis and 1.48m above the yaw bearing.

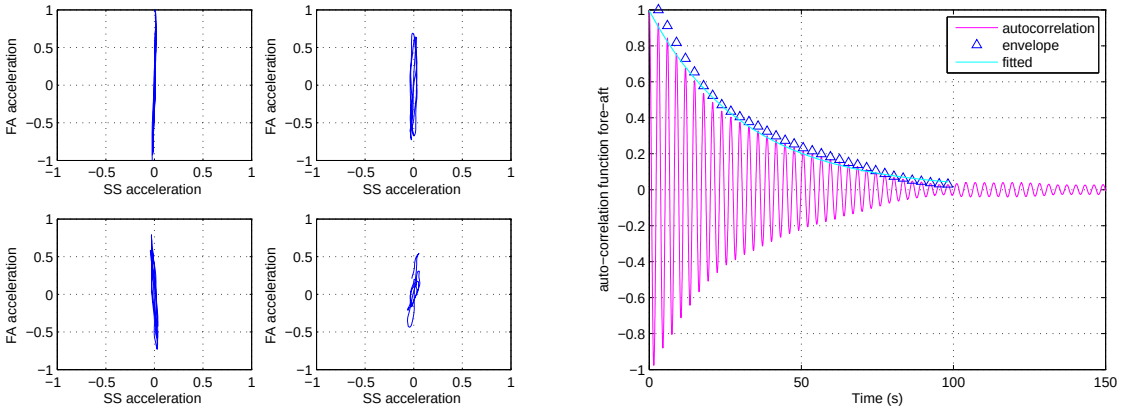

(a) Motion seen from above in fore-aft and side-side direction during ambient excitation (normalized with the maximum fore-aft acceleration).

(b) Normalized auto-correlation function of the fore-aft tower top acceleration (simulations).

Figure 8.4: Tower top accelerations and auto-correlation function of tower top acceleration. Simulation with 4m/s mean wind speed.

Mode nr.	Mode Name	Percentage difference
1	1^{st} tower fore-aft	0.19%
2	1^{st} tower side-side	0.9%
3	1^{st} yawing flap (asymmetric)	4.53%
4	1^{st} tilting flap	2.69%
5	1^{st} symmetric flap	0.86%
6	1^{st} edge symmetric + tilt	3.33%
7	1^{st} edge asymmetric + yaw	4.42%

Table 8.3: Difference in the natural frequencies between model and real wind turbine

$$I_{necelle} = I_{yaw} - r^2 M_{nacelle} \tag{8.3}$$

The dynamics of the drivetrain are not modeled in HAWC2, instead an equivalent inertia of the generator about the slow speed shaft is implemented to account for it. The inertia of the generator is given by $N^2 \cdot I_{gen,HSS}$. The electrical efficiency of the generator was taken to be 90% and the gear box ratio $N = 1 : 119$.

Tables 8.3 and 8.4 depict the differences observed between the model characteristics and the real turbine. The frequencies of the coupled structure match well the requirements. The properties of the blade and the support structure match the natural frequencies, the total mass and center of gravity given by the manufacturer. The maximum acceptable tip deflection in front of the tower during operation is below the required threshold. The model characteristics seem to be within acceptable limits and the wind turbine model reasonably represents the actual wind turbine on site. Therefore, the simulation results can be considered comparable.

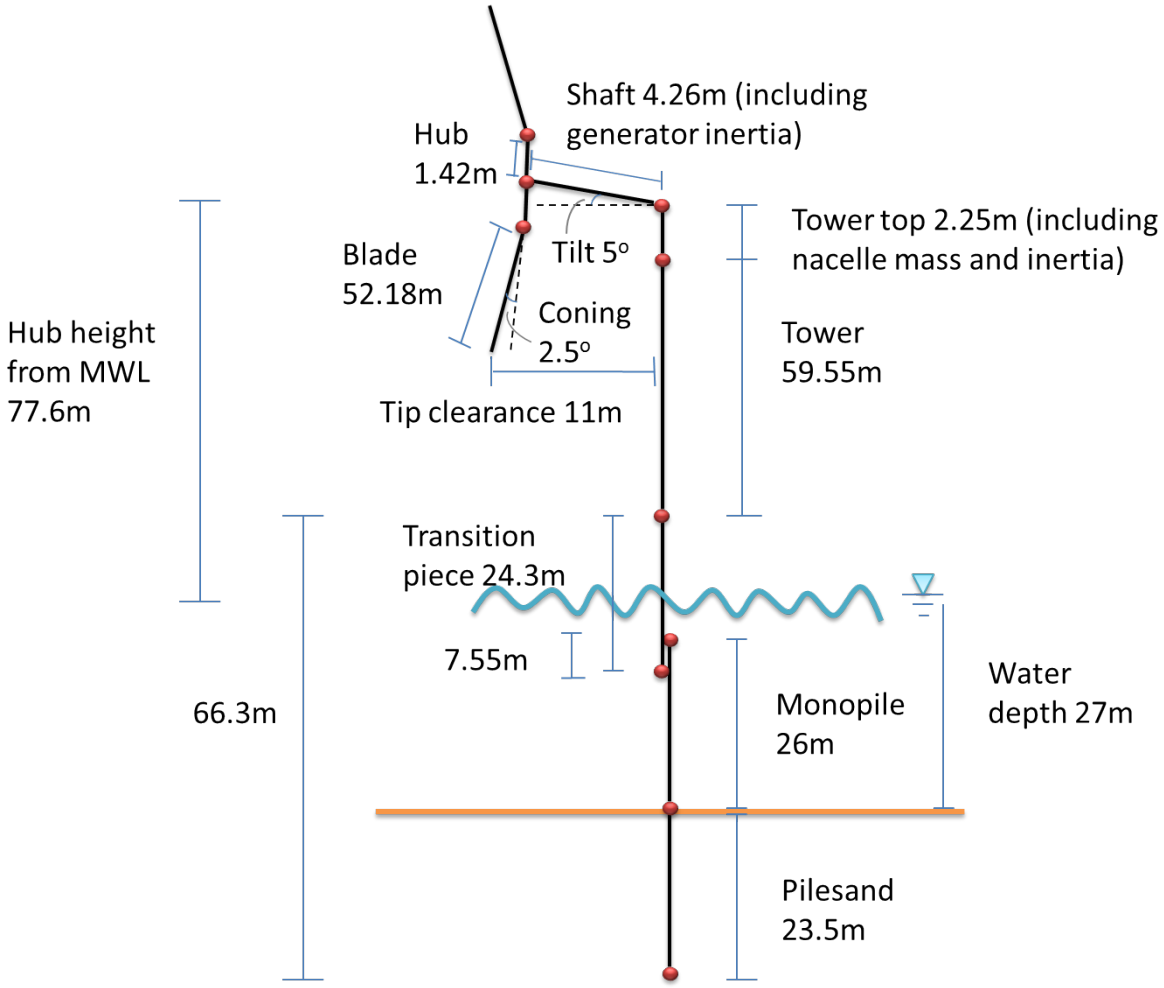

Figure 8.5: HAWC2 model.

The variable speed and collective blade pitch control of the wind turbine is modeled through a proportional integral-controller (PI) developed in DTU [70], performed through different DLLs (Dynamic Link Library) defined in the controller section. For the verification of the controller behavior, the mean pitch angle, the mean rotational speed as a function of the mean wind speed and the power curve resulting from the simulations is matched against the measurements and the power curve provided by the manufacturer (Figure 8.6).

8.5 Modeling of Ambient Loads

In the following sections the modeling of the ambient loads in HAWC2 is explained. The wind inflow data, irregular wave characteristics and soil properties have been measured in the site and have been imported in the simulations.

Mass characteristics	Percentage difference
Blade mass	0.16%
Blade center of gravity	0.08%
Tower top mass	0.24%

Table 8.4: Difference in the mass properties between model and real wind turbine

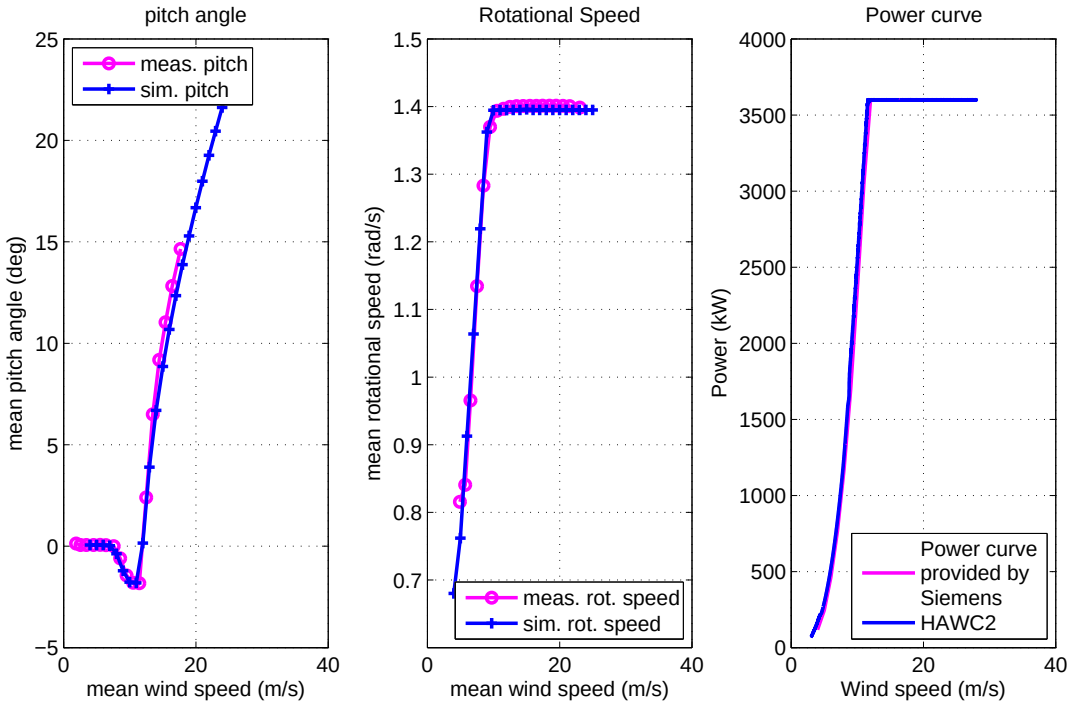

Figure 8.6: Verification of controller behavior.

8.5.1 Wind Model

The Blade Element Momentum theory (BEM) is implemented in HAWC2 for the calculation of the aerodynamic loads, extended to include dynamic inflow, dynamic stall, skew inflow and shear effects on the induction. The airfoil lift and drag coefficients (C_l , C_d respectively), the chord and the relative thickness distribution are given as inputs to the software. The wind section is specified by the deterministic part of the wind that consists of the mean wind speed, linear trends and ramp ups if desired. The stochastic part of the wind is based on the Mann turbulence model. The shear can either be constant, linear, follow the logarithmic or the power law. In the current simulations the power law is used with a shear exponent $\alpha = 0.2$ (Equation 2.1b). The tower shadow effect that influences the wind in the region close to the tower, is taken into account in the simulations.

Mean wind speed measurements of 1 year from the site obtained from the SCADA system (Section 7.1.2) are used to fit a Weibull distribution to the data. The scale and shape

parameters are $\alpha_w = 10.69m/s$ and $\beta_w = 1.98$ respectively. The shape parameter β_w is obtained by solving iteratively Equation A.10 [6]. After estimating the shape parameter β_w the scale parameter α_w is given by Equation A.11. The resulting Weibull probability distribution function is shown in Figure 8.7a and is given by Equation A.8.

Figure 8.7b presents the scattered wind turbulence intensity obtained from wind speed measurements, along with the fitted exponential curve, which is applied in the aero-elastic simulations. The simulation of the wind turbulence is then made based on the Mann wind turbulence model as described in [17]. The air density used in the simulations is equal to $\rho_\alpha = 1.225kg/m^3$.

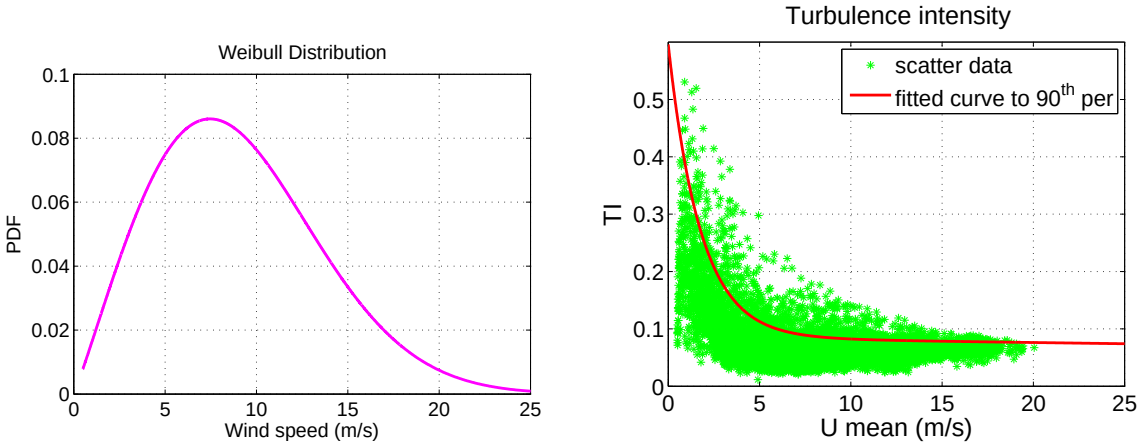

(a) Wind probability distribution function, Weibull, based on 1 year measurements.

(b) Scattered turbulence conditions for free wind sector, fitted curve based on the 90^{th} percentile of the TI (solid line) and IEC A (dashed line).

Figure 8.7: Wind turbulence scatter data from the nacelle mounted cup-anemometer and Weibul distribution.

8.5.2 Wave Kinematics

For the calculation of hydrodynamic forces the irregular linear wave theory combined with the wheeler stretching method to account for loads above the mean sea level is implemented in the aero-elastic code. The hydrodynamic loads are based on the Morison's equation (Equation 8.4). The Morison's equation is valid for piles with diameter D much smaller that the wave length λ. When this assumption is not satisfied, the presence of the pile influences the waves and the hydrodynamic loads, calling for a diffraction correction.

$$F_m = \frac{1}{2}\rho_w C_D(u_w - u_s)|u_w - u_s| + \rho_w C_M \frac{\pi D^2}{4}(\dot{u}_w - \dot{u}_s) \tag{8.4}$$

u_w is the fluid velocity, $\dot{u}_w$ the fluid acceleration, u_s the structure's vibration velocity, $\dot{u}_s$the structure's vibration acceleration, ρ_w the water density equal to $1027kg/m^2$ and D the

pile diameter. The first part of the equation constitutes the drag force F_D with the drag coefficient C_D and the second the inertia force F_M with the inertia coefficient C_M. In the inertia coefficient the contribution from both the hydrodynamic mass force and the Froude-Krylov force is included. For piles with diameter 3-5m installed at water depths of 5-25m the inertia component is dominant based on the calculation of the Keulegan-Carpenter number KC [39, 150].

According to the design rules, typical values for the coefficients of a vertical cylinder are $C_M = 2$ and $C_D = 0.65$. The Christchurch Bay experiment [42], relevant in this case, as it deals with random waves, resulted in a value of 2 for the C_M and in a range of 0.65-1.05 for the C_D accounting for marine growth. In this study the inertia and drag coefficients are selected equal to 2 and 1 respectively. Different wave direction with respect to the wind and currents can also be used in the simulations.

Two different wave spectra can be implemented in HAWC2. In the present work the JONSWAP spectrum (Equation A.17) is fitted to the wave elevation, measured by a buoy installed near to the offshore wind turbine (Figure 8.8). Time series of surface elevation and directional spectrum are measured by the buoy, providing a view of the sea state every 30min. The γ parameter of the spectrum is given by Equation A.20 [11]. The parameters of the fitted spectrum are given as inputs to the HAWC2 simulations (hydrodynamics section), for the generation of the wave field. The significant wave height and the peak period follow the trend shown in Figure 5.2a. The wave kinematics are provided through a DLL interface.

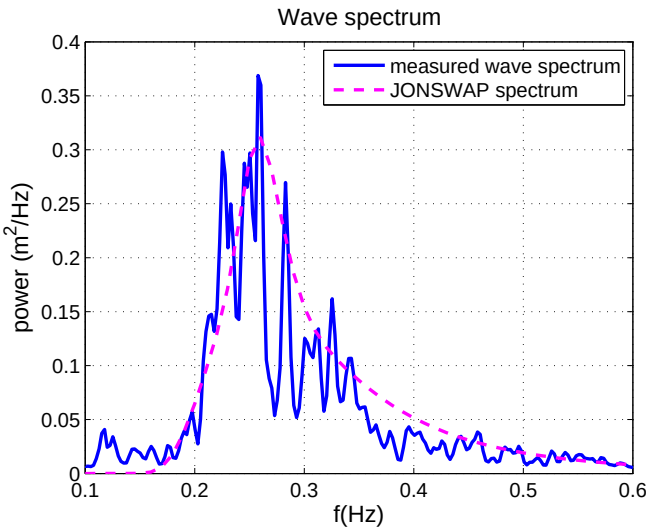

Figure 8.8: JONSWAP spectrum fitted to the wave data measured by the buoy.

8.5.3 Soil Model

In the following simulations, for the lateral loading of the monopile, the commonly used p-y curve (lateral resistance-deflection) is employed, where the soil stiffness is modeled by distributed nonlinear springs along the subsoil portion of the support structure, as shown

in Figure A.2. The soil characteristics used in the simulations are based on geotechnical measurements (Figure 8.9a). The p-y curve can be generated from Equation A.21 for sand and Equations A.23 and A.24 for clay, using the measured submerged unit weight γ' and friction angle ϕ. Figure 8.9b presents the p-y curve for three different soil depths in the site.

The pile penetrates the first two soil layers of clay and sand based on the site measurements. The soil properties in terms of friction angle and effective unit weight within the same layer are varying. A p-y matrix at 1m spacing along the pile calculated from the above characteristics is given as input to HAWC2 in the soil section.

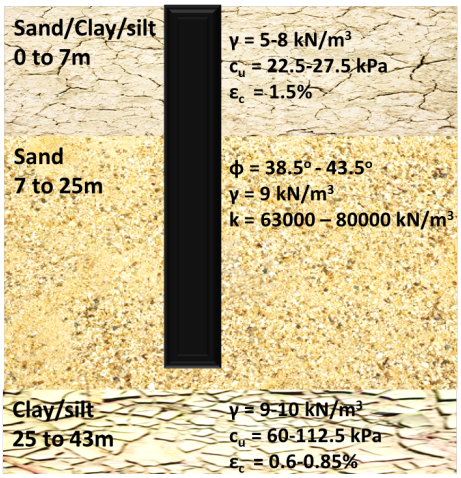

(a) Soil profile on the site.

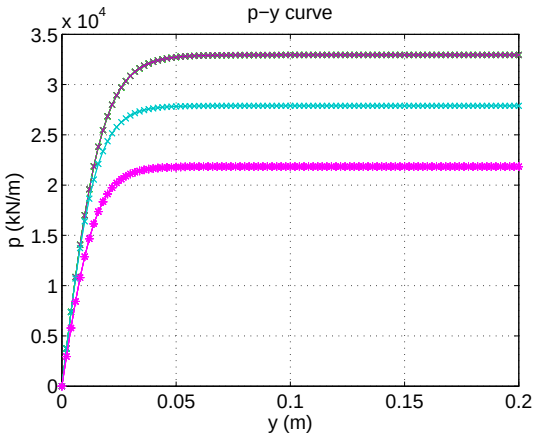

(b) Soil model, p-y curve for different depth values.

Figure 8.9: Soil profile and p-y curve.

Chapter 9

Model Validation

Accurate design loads prediction of offshore wind turbines from model simulations is required for component reliability. Therefore, validation of design tools with measurements from operational wind farms is essential. Validation of a general model has been reported in reference [151], where a variable speed wind turbine model was developed and a qualitative comparison with available measurements was performed to prove the accuracy of the derived results. In references [65, 66] simulation methods for wind turbines in wake were validated with measurements from the Tjæreborg wind farm and with experimental data from the National Renewable Energy Laboratory. Prior validation of aero-elastic codes for offshore applications has been made to a limited extent, such as a comparison of the modeled loads with measurements for the offshore wind farm at Blyth, as performed by van der Tempel in reference [152]. The frequency domain method applied to estimate the fatigue loads is compared with measurements. A comparison and verification of the aero-elastic codes for offshore wind turbines developed by universities and companies world wide is presented in references [153, 154]. The aero-elastic code HAWC2 and the dynamic wake meander model for loads and power production were validated in reference [155] by comparing simulation results from HAWC2 and full-scale measurements from the Dutch Egmond aan Zee wind farm. The comparison was performed in terms of statistics and 1Hz equivalent loads, both for free and wake sector. The loads on the wind turbine and the power production with respect to the wind direction were also examined, where power drops were observed for directions with 7D and 11D separation from the neighboring turbines. Validation of support structure models was performed in reference [36], where the simulation results were compared with experimental data from the two wind farms 'Irene Vorrink' and 'Lely'.

In this chapter the validation of the wind turbine model is performed with full scale measurements. The extreme and mean loads as well as the 1Hz equivalent load of the substructure/foundation, the tower and the blades are presented separately for the validation of the different components.

9.1 Sub-structure/Foundation

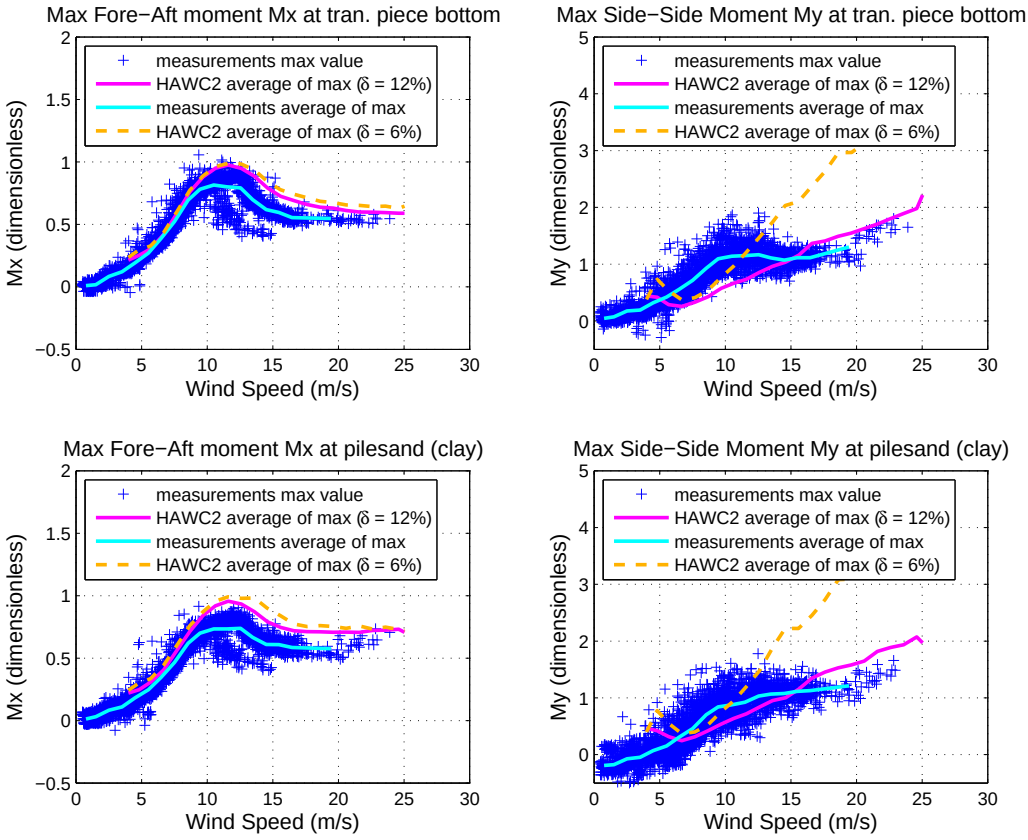

Figure 9.1: Maximum values of the bending moments from measurements and HAWC2 simulations at the sub-structure/foundation normalized with the simulation maximum value at the rated wind speed (free wind sector). The scatter data (blue crosses) present the measured extreme bending moments. The solid lines denote the average of the extreme values both from measurements (cyan line) and simulations (average of 12 extremes from 12x10 min per mean wind speed).

A comparison of the extreme values of the bending moments at two different positions along the substructure between measurements and simulations is presented in Figure 9.1. The displayed data are normalized with the simulations' maximum value at the rated wind speed. 10min simulations were performed in HAWC2 with 12 different turbulent seeds per mean wind speed for load case DLC 1.1. Two different damping values (structural, hydrodynamic, soil damping) were used in the simulations $\delta = 6\%$ and $\delta = 12\%$, as estimated from the boat impact (Section 11.1), to examine the importance of the accurate damping value for reliable load prediction. The damping in the model is tuned by applying an impulse as described in section 8.3. The average value of the extreme loads both from measurements (light blue line) and simulations (pink line, average value of the 12 extremes from the 12x10min simulations per mean wind

speed) are presented. The measurements' average curve is obtained by separating the wind in bins of 1m/s and calculating the average of the extreme values in each bin.

The profile of the simulations seems to follow satisfactorily the measurements. The simulated loads in the fore-aft direction follow the envelope of the measured bending moments. The increased side-side loads in the measurements in the area around the rated wind speed could be due to switching between the controller regions. Discrepancies are mainly attributed to differences in the blade profiles and aerodynamics, limitations of the wind speed readings and uncertainties in the soil modeling. Lower simulated side-side bending moment M_y at wind speeds below rated are due to differences in the edgewise stiffness of the blades in the model from the actual turbine. The reasonably good agreement between measurements and simulations in the average of the extreme loads in the side-side direction verifies the importance of sufficient damping in the model for accurate load prediction. The higher damping in this direction makes the loads more stable for wind speeds above rated, while for lower damping values the extreme simulated load are significantly higher compared to measurements. In the fore-aft direction the aerodynamic damping is dominant and the influence of the additional offshore damping not so apparent. Differences in the aerodynamic characteristics of the blades between model and turbine are more influential factors and are responsible for the discrepancies in the loads estimation in the fore-aft vibration mode.

A comparison of the mean values of the bending moments at the transition piece are presented in Figure 9.2. The data are normalized with the simulations' maximum value at the rated wind speed.

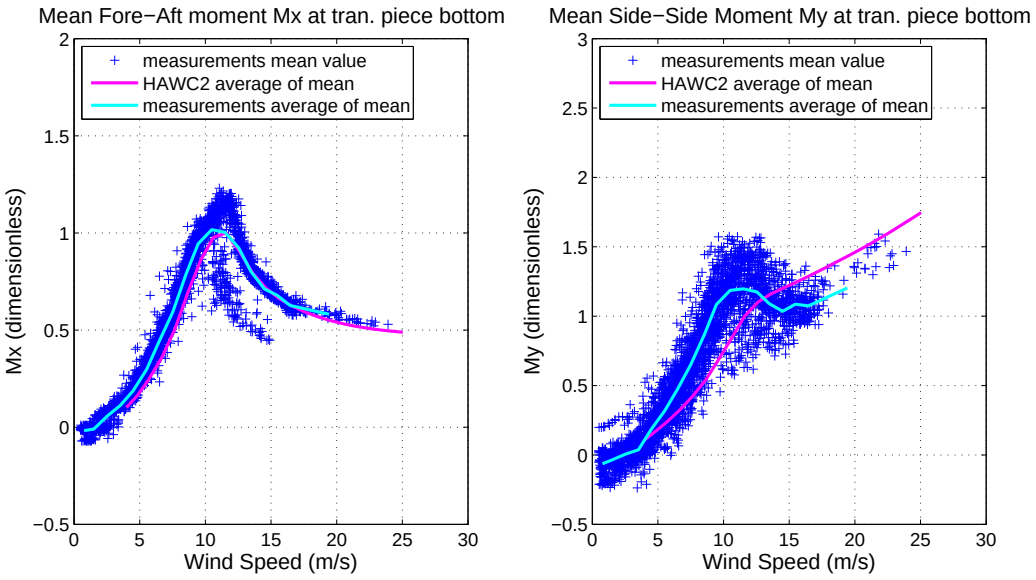

Figure 9.2: Mean values of the bending moments from measurements and HAWC2 simulations at the sub-structure normalized with the simulation maximum value at the rated wind speed (free wind sector).

Figure 9.3 presents the moment distribution in the fore-aft direction along the pilesand and the displacement in the longitudinal and lateral direction for $U = 15m/s$ from the simulations.

The data are normalized with the maximum of the curve that represents the maximum values.

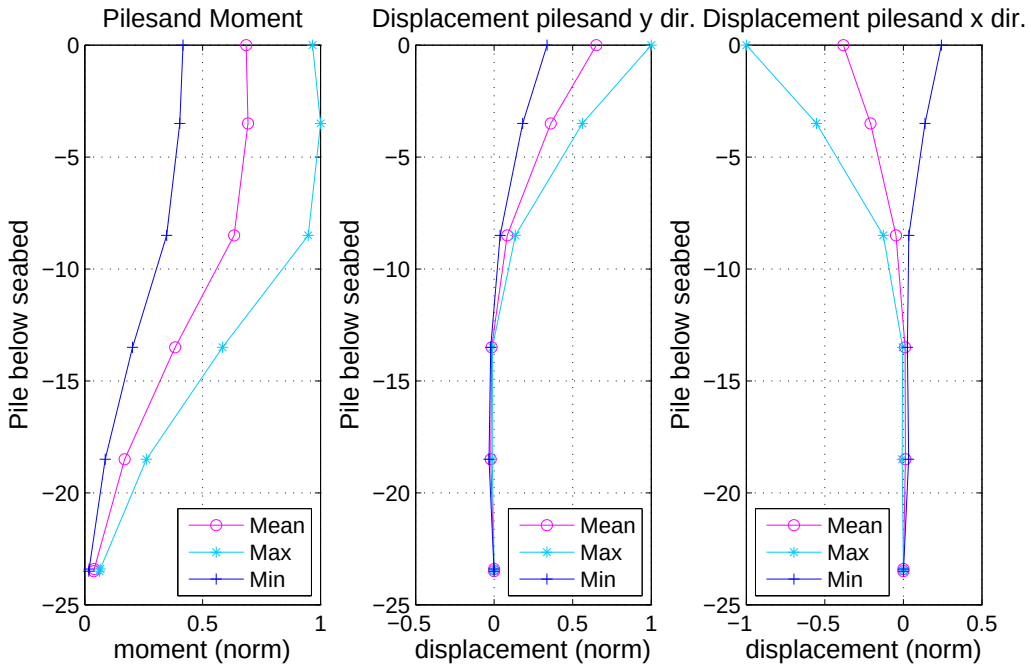

Figure 9.3: Moment in the fore-aft direction and displacement distribution along the pilesand at 15m/s from simulations, normalized with the maximum value of the max curve.

The 1Hz damage equivalent loads are computed for the fore-aft and side-side moments ($m = 4$ for steel structures). Figure 9.4 presents the 1Hz damage equivalent load from the HAWC2 simulations as compared with the measurements, at the bottom of the transition piece and at the pile sand near the clay surface, normalized with the simulated fatigue load at rated wind speed. The peak that appears at that wind speed in the fore-aft moment at the transition piece could be attributed to the switching in the controller regions as discussed earlier. For all wind speeds the damage equivalent loads both of the fore-aft bending moment M_x and the side-side moment M_y resulting from the HAWC2 simulations show reasonable agreement with the site measurements. Higher simulated fatigue in the fore-aft direction is also due to conservative turbulence intensity values. The higher discrepancies in the fatigue of the pilesand are due to the uncertainties in the soil model. Differences in the spring stiffness distribution and the actual soil properties are responsible for the discrepancies in the pilesand moment distribution and thus the extreme and fatigue loads. For the calculation of the measurement's fatigue all wind-wave misalignment sectors are considered, while for all the simulations the waves are aligned with the wind. The wind-wave misalignment affects mainly the loading in the side-side direction. For this reason the simulations' fatigue in that direction appears to be lower. This topic will be discussed in Chapter 12.

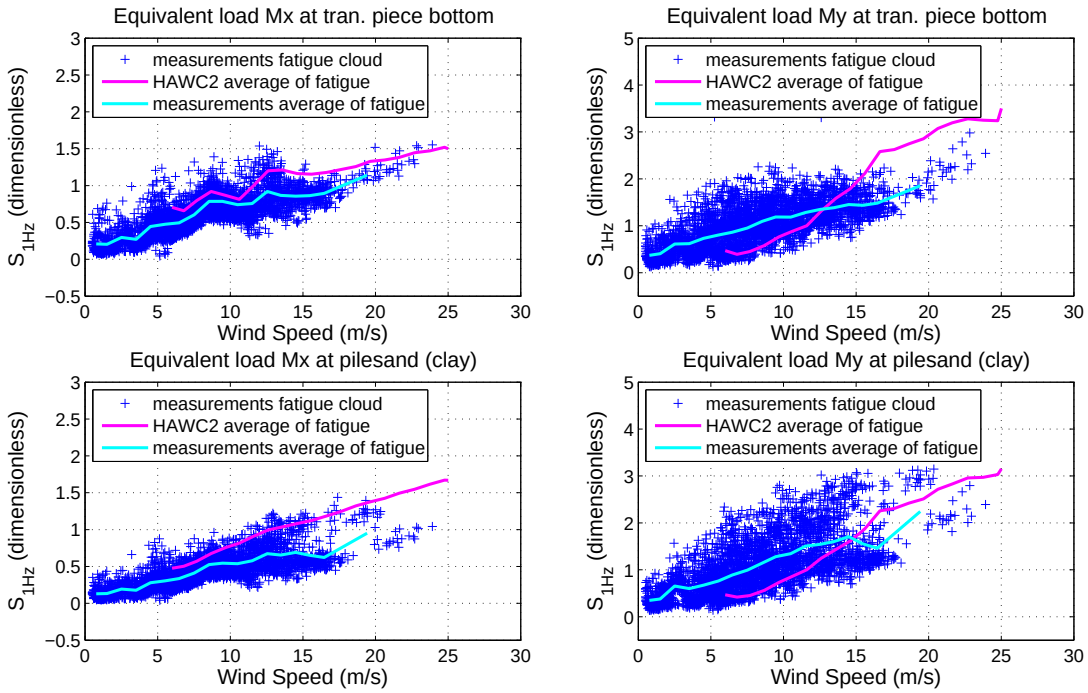

Figure 9.4: 1Hz equivalent load from HAWC2 simulations compared with the site measurements, against the wind speed (free wind speed). Values are normalized with the simulations fatigue load at rated wind speed.

9.2 Tower

A comparison of the extreme values of the fore-aft and the side-side bending moments at the tower top and tower bottom is shown in Figure 9.5. The data are normalized with the simulations' maximum at rated wind speed. Figure 9.6 presents the comparison of the mean values of the bending moments at the tower bottom. The profile of the simulations follow satisfactorily the measurements. The negative values of the fore-aft bending moment at the tower top for low wind speeds is due to the negative defined bending moment from the rotor weight.

The 1Hz damage equivalent loads are computed for the fore-aft and side-side moments ($m = 4$ for steel structures) at the tower top and tower bottom. Figure 9.7 shows the damage equivalent load from the HAWC2 simulations as compared with the measurements, at the bottom of the tower. The presented data are normalized with the simulation maximum value at the rated wind speed. The agreement in the fore-aft direction is satisfactory. Discrepancies in the side-side direction are always attributed to the differences in the edgewise stiffness of the blades and the uncertainties in the soil model. In the fatigue estimated from the measurements the cases of wind-wave misalignment are also included, but not taken into consideration in the simulations presented here.

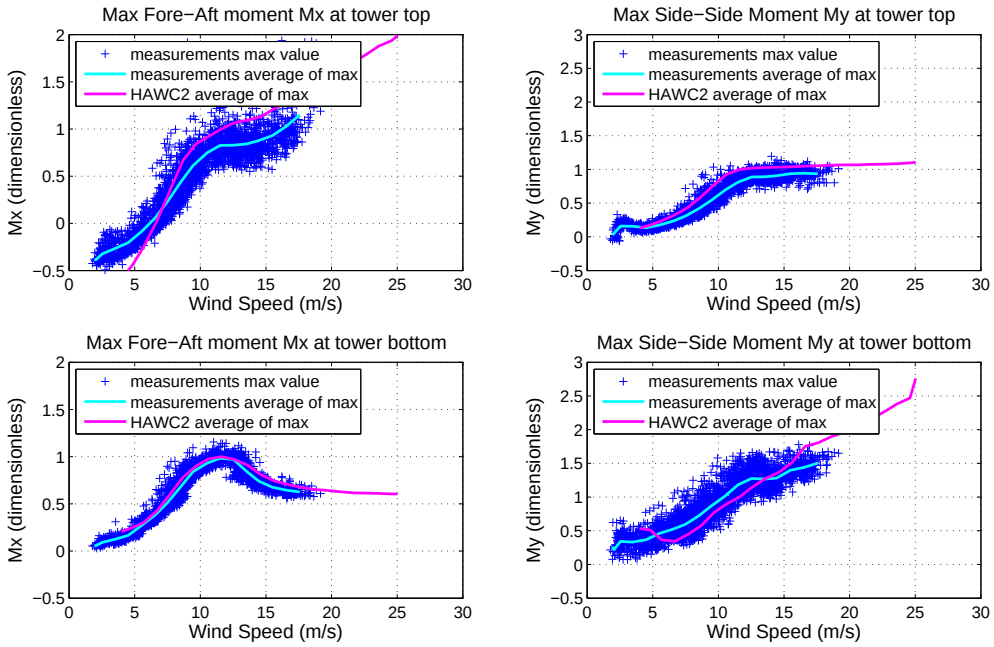

Figure 9.5: Maximum values of the bending moments from measurements and HAWC2 simulations at the tower bottom normalized with the simulation maximum value at the rated wind speed (free wind sector). The blue crosses correspond to each 10min measurement, the cyan line to the average of the measurements' max values and the pink line to the average of the simulations' max values.

9.3 Blades

A comparison of the in-plane and out-of-plane blade root bending moments between measurements and simulations is presented in Figures 9.8 and 9.9. Keeping in mind the fact that the only available information about the actual blade are the first four natural frequencies, the mass and the center of gravity and that the model setup is based on the downscale of a conceptual blade, the simulation profiles follow satisfactorily the measurements. The presented data are normalized with the simulations' maximum bending moment at the rated wind speed. The discrepancies observed in the in-plane moment are due to differences in the edgewise stiffness of the blades. Quite accurate tuning of the flapwise frequencies (Table 8.2) and the high contribution of the aerodynamic damping results in a better agreement of the extreme out-of-plane root bending moment between measurements and simulations. However, differences in the aerodynamic characteristics of the blades between the model and the actual turbine are responsible for the discrepancies in that direction, which is also visible in the higher simulated fore-aft bending moment of the support structure.

The comparison of the 1Hz equivalent load of the in-plane and the out-of-plane blade root bending moments between measurements and simulations is presented in Figure 9.10. The Wöhler exponent m is equal to 12. The relatively good agreement in the fatigue of the in-plane

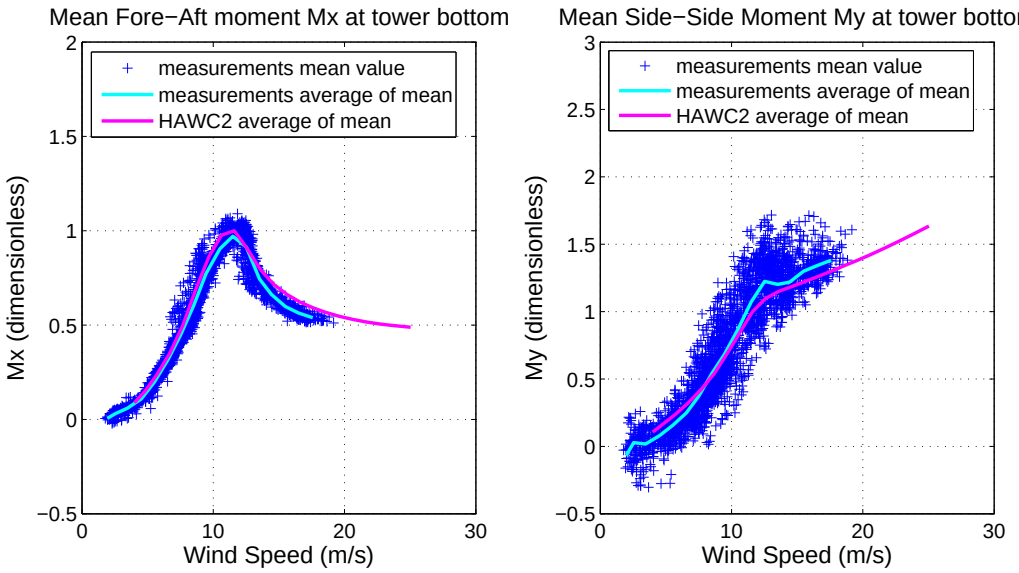

Figure 9.6: Mean values of the bending moments from measurements and HAWC2 simulations at the tower normalized with the simulation maximum value at the rated wind speed (free wind sector). The blue crosses correspond to each 10min measurement, the cyan line to the average of the measurements' mean values and the pink line to the average of the simulations' mean values.

moment proves that the model blade mass and the rotational speed are similar to the actual values. Variations in the aerodynamics of the airfoils, conservative turbulence intensity and different controller tuning are mainly responsible for the discrepancies in the fatigue of the out-of-plane root bending moment.

9.4 Validation of Model on the Wake

Figures 9.11 to 9.16 present the comparison of measurements and simulations in the wake sector for the different components. The calculated effective turbulence I_{eff} applied in the simulations to account for the wake effect is described in Section 7.1.1.2. The simulated extreme bending moments and 1Hz equivalent loads from the wake sector on the substructure/foundation, the tower and the blades are compared with site measurements. The profiles seem to follow satisfactorily the measurements. Discrepancies are due to differences in the blade aerodynamics, blade stiffness distribution and soil modeling uncertainties as discussed earlier.

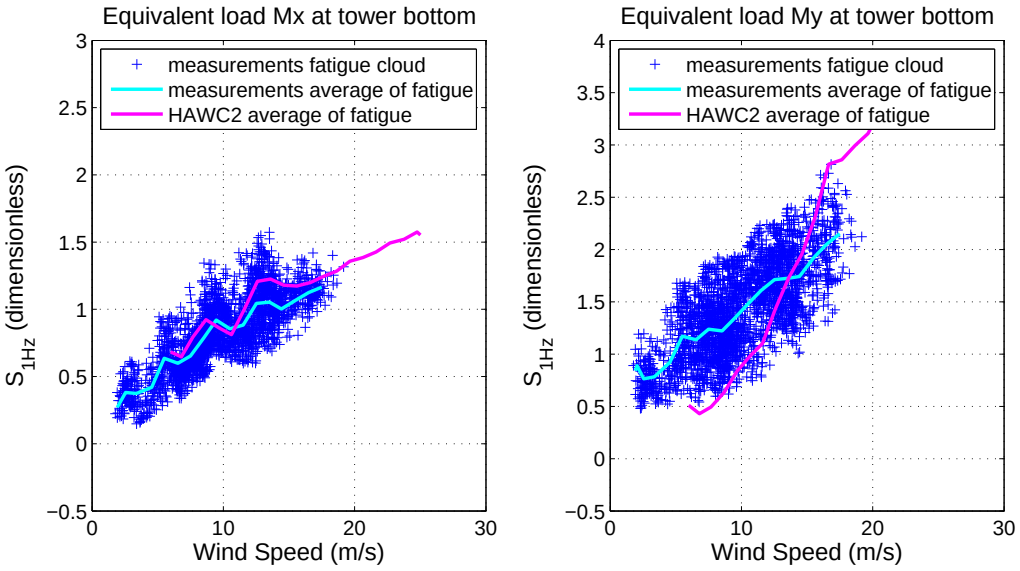

Figure 9.7: 1Hz equivalent load from measurements and HAWC2 simulations at the tower bottom normalized with the simulation maximum value at the rated wind speed (free wind sector). The blue crosses correspond to the 1Hz equivalent load of each 10min measurement, the cyan line to the average of the measurements' fatigue and the pink line to the average of the simulations' fatigue.

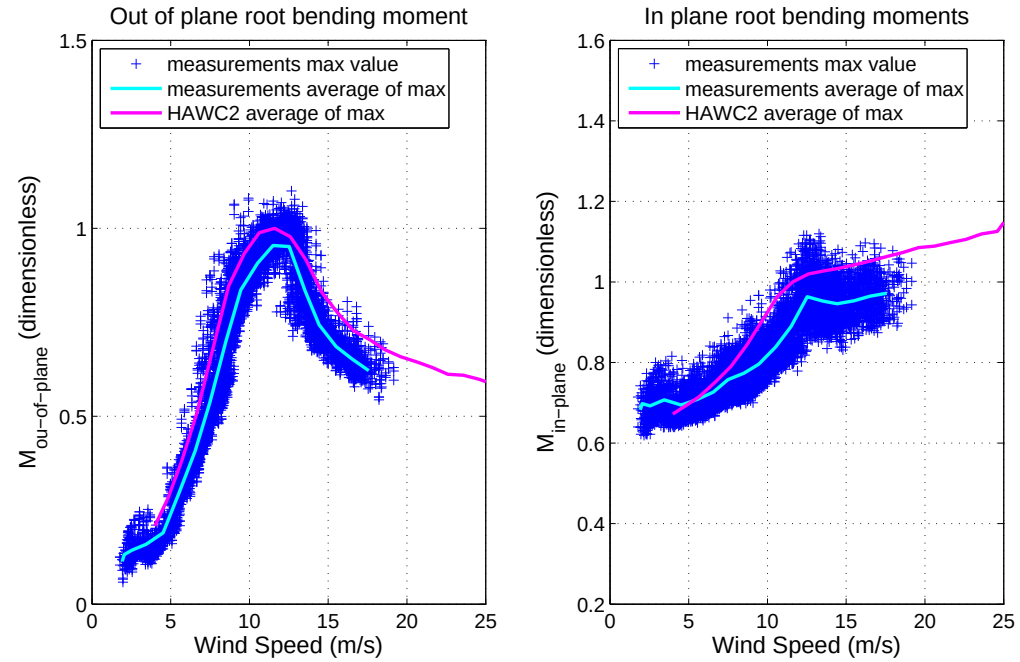

Figure 9.8: Maximum values of the in plane and out of plane blade root bending moments of all three blades from measurements and HAWC2 simulations normalized with the simulation maximum value at the rated wind speed (free wind sector).

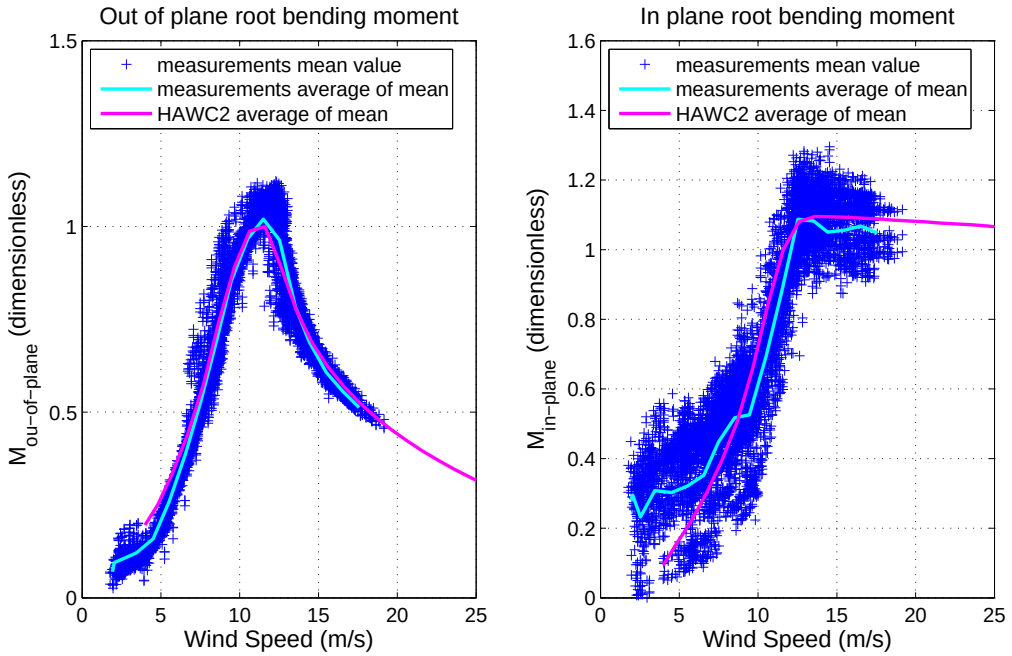

Figure 9.9: Mean values of the in plane and out of plane root bending moments of all three blades from measurements and HAWC2 simulations normalized with the simulation maximum value at the rated wind speed (free wind sector).

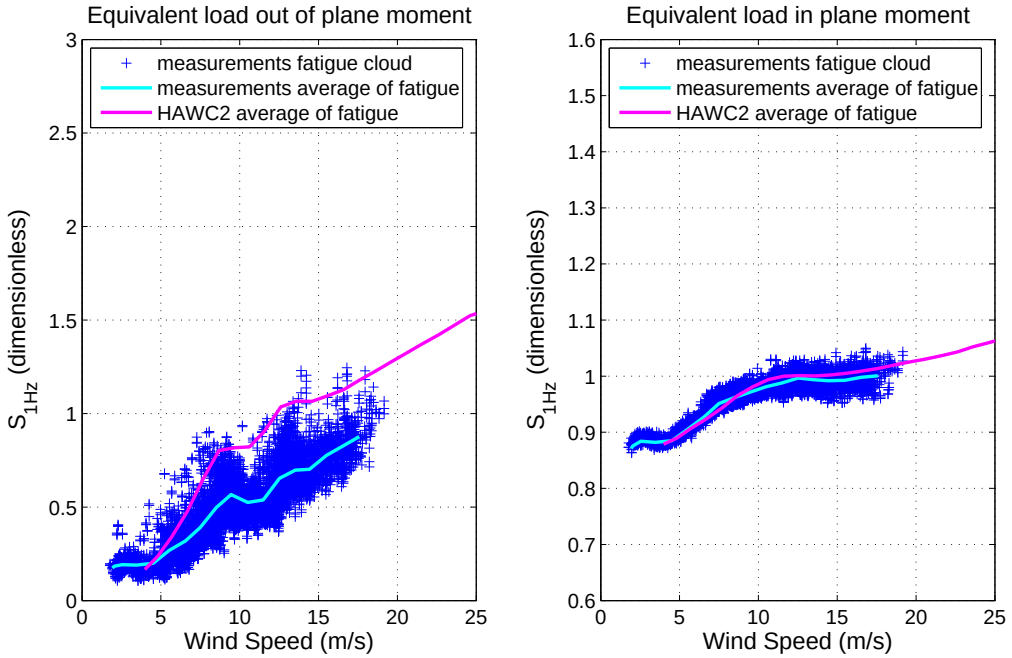

Figure 9.10: 1Hz equivalent load of the in plane and out of plane root bending moments of all three blades from measurements and HAWC2 simulations normalized with the simulation maximum value at the rated wind speed (free wind sector).

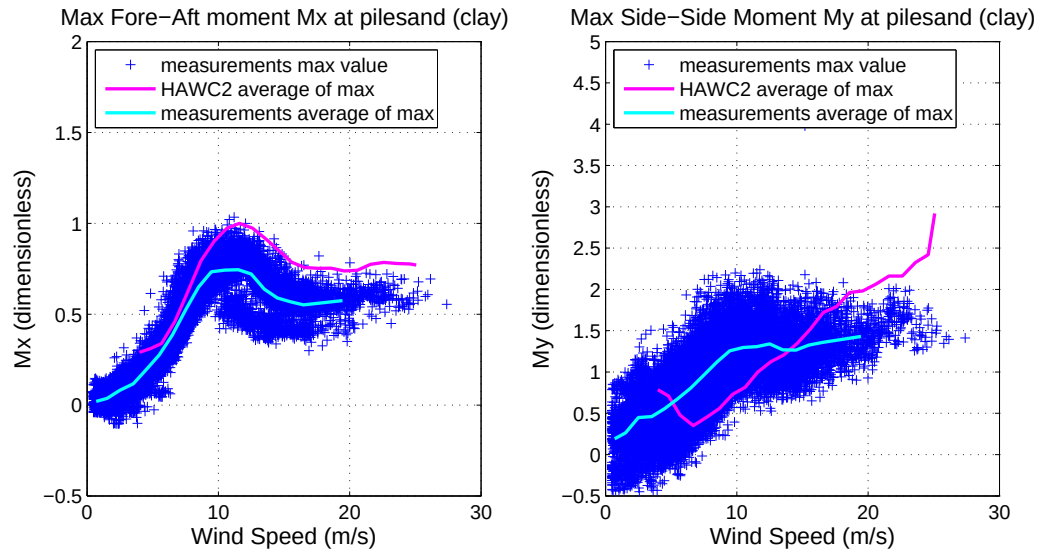

Figure 9.11: Maximum values of the bending moments from measurements and HAWC2 simulations at the foundation normalized with the simulation maximum value at the rated wind speed (wake sector).

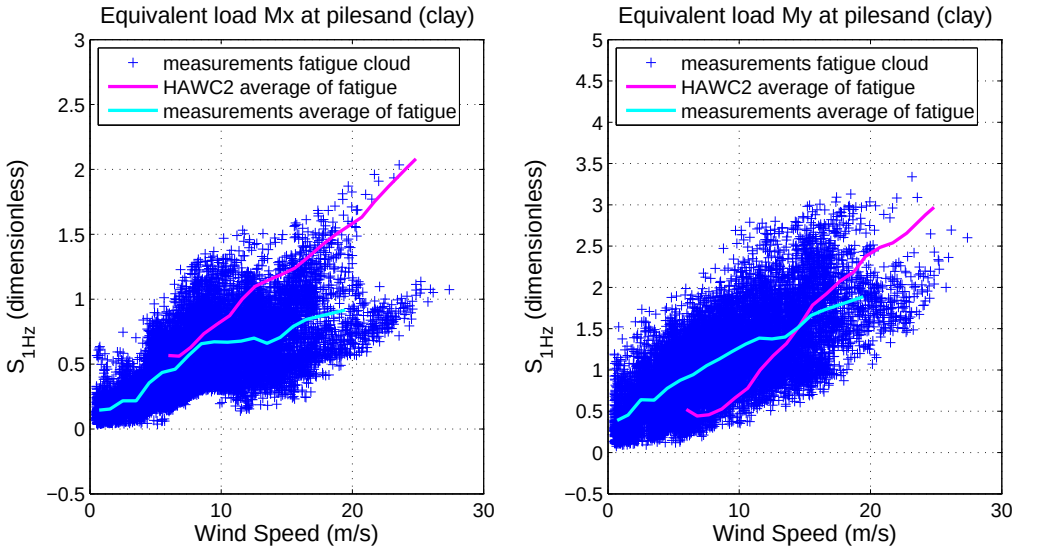

Figure 9.12: 1Hz equivalent of the bending moments from measurements and HAWC2 simulations at the foundation normalized with the simulation maximum value at the rated wind speed (wake sector).

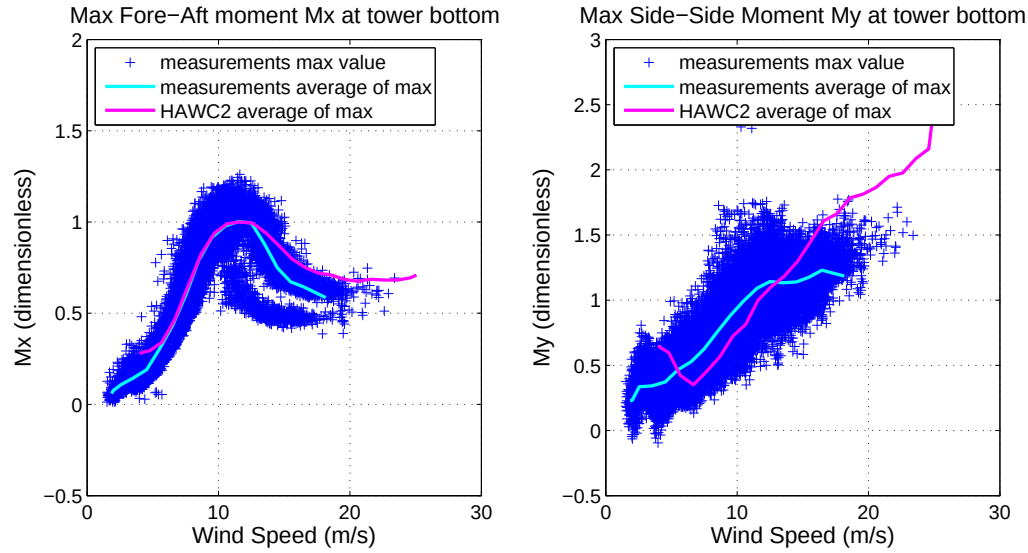

Figure 9.13: Maximum values of the bending moments from measurements and HAWC2 simulations at the tower normalized with the simulation maximum value at the rated wind speed (wake sector).

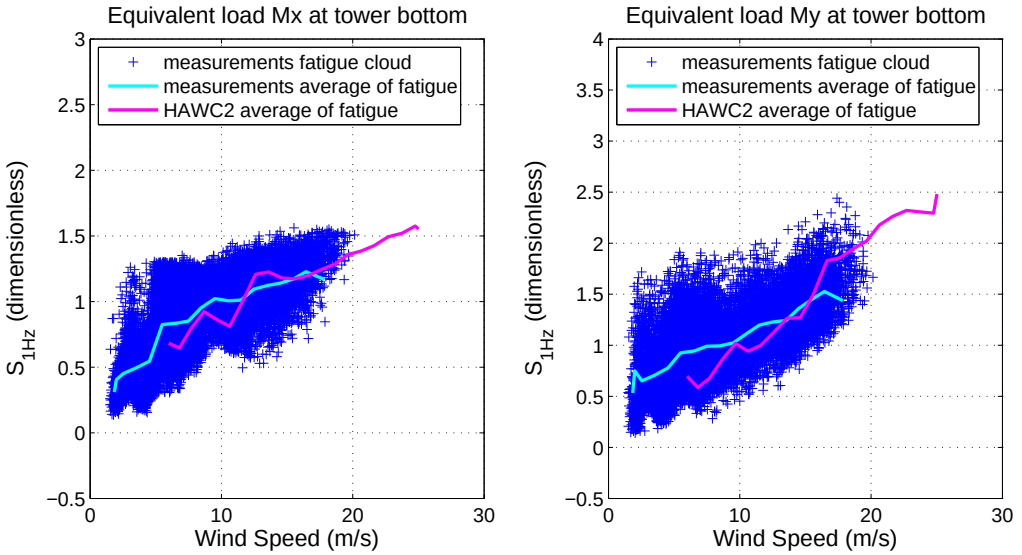

Figure 9.14: 1Hz equivalent of the bending moments from measurements and HAWC2 simulations at the tower normalized with the simulation maximum value at the rated wind speed (wake sector).

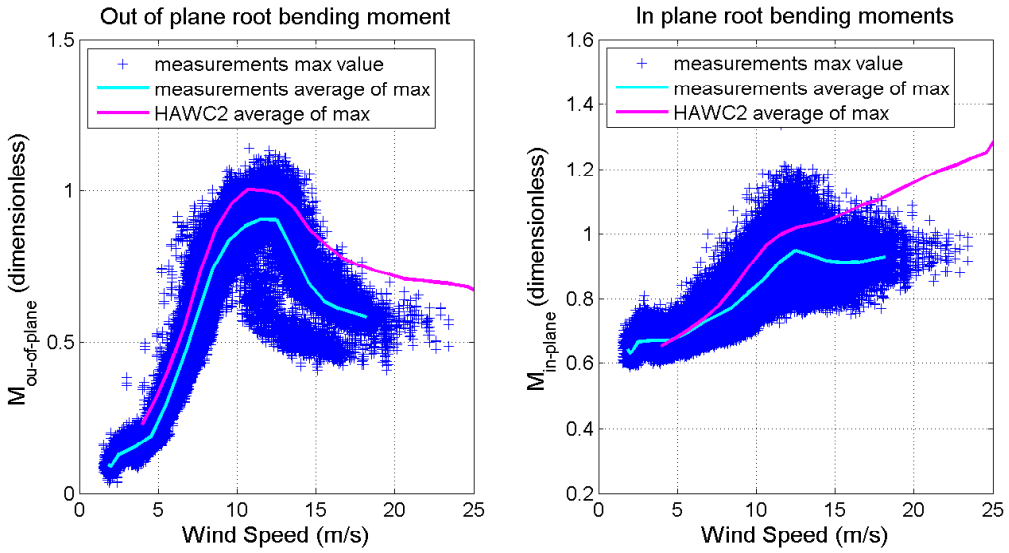

Figure 9.15: Maximum values of the in plane and out of plane root bending moments of all three blades from measurements and HAWC2 simulations normalized with the simulation maximum value at the rated wind speed (wake sector).

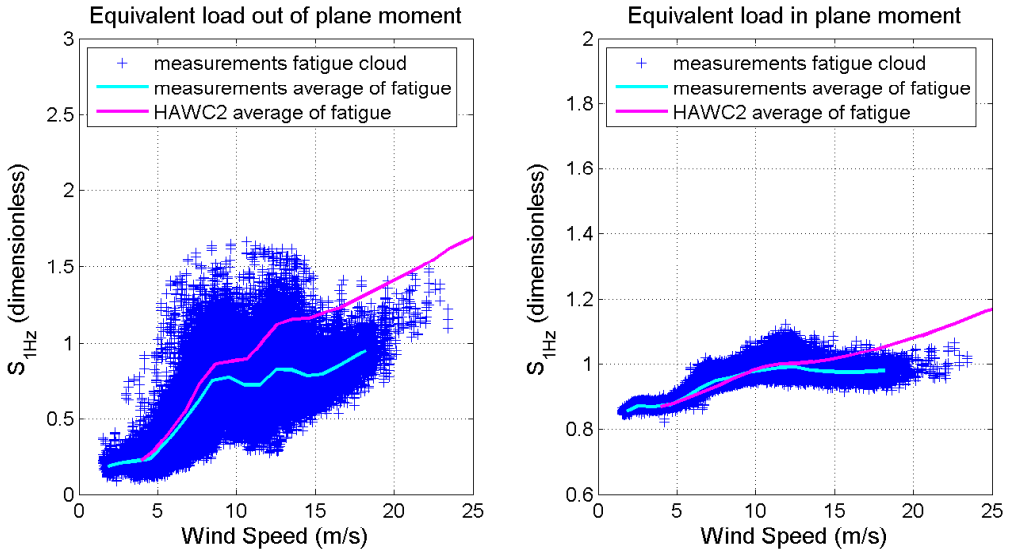

Figure 9.16: 1Hz equivalent load of the in plane and out of plane root bending moments of all three blades from measurements and HAWC2 simulations normalized with the simulation maximum value at the rated wind speed (wake sector).

Chapter 10

Uncertainties

Measurements or simulations no matter how carefully they are designed and completed, they are always subject to errors. It is crucial for the reliability of the predicted wind turbine response to quantify the uncertainties of the system. Model loads validation is a challenging task, since it involves uncertainties in the soil properties (soil stiffness and damping), in the wind and wave model, as well as in the modelling of the coupled wind turbine dynamics. The uncertainties examined in model validation can be of three types: wind turbine model (software modeling), physical (soil stiffness, wind and wave model), measurement (equipment limitations) and statistical uncertainties. *Model uncertainties* refer to the approximations made during the design of the simulation models as well as to the distribution of the stochastic variables. *Physical uncertainties* contain the uncertainties of the physical parameters, like the mean wind speed or the significant wave height. *Measurements uncertainties* are related to the quality of the equipment. *Statistical uncertainties* refer to the amount of data available. Reference is made to [156] and [157], where the uncertainty quantification for modal test data is analyzed, based on the sources of uncertainties that are random and with bias. Random errors are categorized as Type A uncertainties that can be evaluated directly from measurements, while systematic and bias errors as Type B that are estimated by other means [158]. Bias errors are constant over a measurement campaign assuming that the same equipment is used. They are usually the result of an error during the calibration process and their uncertainty is based on experience.

In references [30] and [47] the bootstrap method is applied to specify the uncertainty on the predicted loads due to limited amount of field measurements. By estimating the standard uncertainty (defined as the standard deviation over the square root of the number of observations) of the various parameters contributing to the wind turbine loading, it is possible to quantify their variability and hence their effect on the range of the predicted design loads.

The uncertainty in wind measurements and wind energy production estimation is thor-

oughly analyzed in reference [159]. If the Weibull distribution is used for the wind resource, the wind uncertainty is equal to the uncertainty of the estimated parameters α_w and β_w. The wind resource uncertainty is divided into four categories: wind speed uncertainty which is connected to errors in the anemometers, long-term resource uncertainty due to specific duration of measurements that might not represent the environmental conditions experienced through the lifetime of the wind turbine, wind resource variability uncertainties and site assessment uncertainties like shear extrapolation techniques applied to a specific location. An overall uncertainty of the wind speed measured by a mast cup-anemometer in the range of 3%-13% (of the measured U) is estimated by Brower in [160]. In reference [159] the use of wind measurement devices like LIDAR or SODAR is suggested for the reduction of the uncertainty in the wind speed estimation, mainly due to elimination of errors introduced by shear models extrapolation or tower and wake effects.

The standard deterministic wind turbine assessment described in the IEC standards [17] is compared with a probabilistic approach in reference [161]. In the probabilistic method the uncertainties, expressed as coefficients of variation (COV), related to the wind data are accounted for and used for the evaluation of the reliability of the wind turbine. The uncertainties are considered as stochastic variables with probability distributions and they include uncertainties connected to the wind (quality and quantity of wind measurements), the model, the physical uncertainties and other sources like turbine malfunctions.

10.1 Calculating Uncertainties

The uncertainty referred in the current work is defined as the dispersion of the values around an estimated mean [158]. The procedure of uncertainty quantification is thoroughly described in reference [162] and is summarized in this section. Firstly, all sources of uncertainties have to be identified and their standard uncertainty should be estimated. Assuming that several independent observations have been made for each variable x_i, the standard uncertainty u_{x_i} is given as the ratio between the estimate of the standard deviation s_{x_i} and the square root of the number of observations N (Equation 10.1). In case that no data are available, the value of the standard uncertainty is based on scientific experience. A list of uncertainty parameters that should be taken into account in the uncertainty quantification of measurements is given in IEC 61400-12 [163].

$$u_{x_i} = \frac{s_{x_i}}{\sqrt{N}} \tag{10.1}$$

The accuracy of the estimation of the mean and the standard deviation of the random variable x_i depends on the amount of samples. The difference between the actual standard deviation σ_{x_i} and its estimate s_{x_i} is given through the Student's parameter t. Assuming that the variable x_i is normally distributed the corrected standard uncertainty is given by Equation 10.2. Considering a confidence level of 95% and a system with infinite number of degrees of

freedom the value of $t = 2$ [164, 165].

$$u_{x_i} = \frac{t \cdot s_{x_i}}{\sqrt{N}} \tag{10.2}$$

The contribution of each variable to the standard uncertainty of the output/measurement is given through the sensitivity factor c_{x_i}, which is associated with the partial derivative of the mathematical expression of the output/measurement f as a function of the different variables (Equation 10.3). In the case of correlated input variables, their covariance should be also included in the calculation of the uncertainty. If it is omitted, an erroneous evaluation of the standard uncertainty of the measurement is possible.

$$c_{x_i} = \frac{\partial f}{\partial x_i} \tag{10.3}$$

The overall uncertainty is a combination of the uncertainties of the variables, accounting for their sensitivity factors c_{x_i} and their correlation coefficients $r(x_i, x_j)$. Equation 10.4 gives the combined standard uncertainty, where n is the number of variables contributing to the overall uncertainty of the measurement/output. [162, 165].

$$u_c = \sqrt{\sum_{i=1}^{n} c_{x_i}^2 u_{x_i}^2 + 2 \sum_{i=1}^{n-1} \sum_{j=i+1}^{n} c_{x_i} c_{x_j} u_{x_i} u_{x_j} r(x_i, x_j)} \tag{10.4}$$

Even though u_c is used to quantify the uncertainty of a measurement, it is often recommended that this uncertainty is expanded to cover a large variation of the possible values observed [164, 165]. The expanded uncertainty U_c is obtained by multiplying the combined standard uncertainty with a coverage factor k (Equation 10.5). For an infinite number of degrees of freedom and a confidence level of 95% k is equal to 2 [162].

$$U_c = k \cdot u_c \tag{10.5}$$

10.2 Uncertainty Analysis

A detailed uncertainty analysis should list all sources of uncertainties, the standard uncertainty of each variable and their method of evaluation [162]. An uncertainty analysis is performed both in the measured and the simulated response following the steps described in the previous section. The analysis is carried out assuming a confidence level of 95%.

10.2.1 Measurements Uncertainties

The main parameters contributing to the loading of the structure and whose uncertainties are propagated to the measurement are the wind speed, the wave velocity and the soil properties. The wave and the soil uncertainties are not considered, as no information is known about the uncertainty of the wave buoy and the soil properties measurements. Since the tolerance of the different instrumentation systems (category B uncertainty) are not provided by the manufacturer, typical values suggested in IEC 61400-12[163] are implemented. The standard uncertainty of the measurement (category A) is obtained directly from Equation 10.1 multiplied with the coverage factor to gain the expanded uncertainty U_c. The combined measurement uncertainty, accounting for the uncertainty in the wind measurement, is given by Equation 10.4 with correlation coefficient equal to $r(x_i, x_j) = 0$.

The sensitivity factor c_{x_i} corresponding to the contribution of the wind uncertainty to the overall measured fore-aft bending moment uncertainty is calculated from the derivative of the thrust force ($T = 1/2\rho_a C_T A U^2$). For the quantification of the uncertainty of the side-side bending moment the torque uncertainty (combined standard uncertainty of the uncertainty in the power and the rotational speed measurements $M_t = P/\omega$) instead of the wind uncertainty is estimated.

Figures 10.1 to 10.3 depict the measured average of the bending moments per mean wind speed on the blade root, the tower and the sub-structure/foundation. In the same figures the error bars indicating the expanded uncertainty U_c of each measurement are also presented. The wind is separated in bins of 1m/s and the mean of each 10min time series is calculated. The standard deviation of the means and the number of observations in every bin are used for the calculation of the standard uncertainty. The measurement standard uncertainty is combined with the wind and the torque uncertainty for the estimation of the overall uncertainty of the measured bending moments. The expanded uncertainty of the sub-structure/foundation is between 100-500kNm while for the tower and the blades between 20-150kNm and 5-30kNm respectively. The reason for this difference is the shorter measurement period of the sub-structure/foundation moments. For higher wind speeds the uncertainty is larger due to higher data dispersion and less observations. The presented data are normalized with the maximum value of each curve.

10.2.2 Simulation Uncertainties

The overall uncertainty in the load prediction can be from different sources, like the simulation model or the representation of the environmental conditions. The model uncertainties are not quantified in the present study, as the model parameters remain constant. The uncertainty of the simulated load values, is herein estimated as the standard uncertainty, given by Equation 10.1 multiplied with the coverage factor for the estimation of the expanded uncertainty. A more detailed analysis of the uncertainties accounting for all variables will require the application of more advanced probabilistic methods like the Monte Carlo technique.

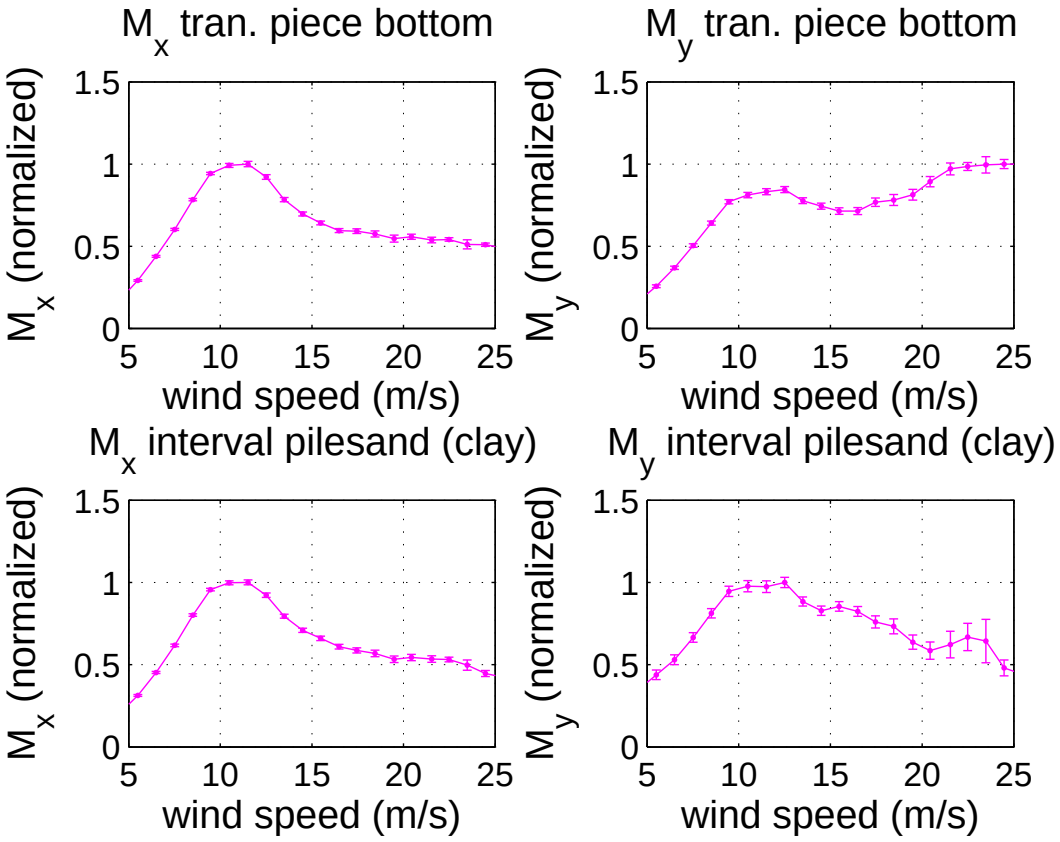

Figure 10.1: Average measured fore-aft and side-side bending moment at the bottom of the transition piece and at the pilesand with the corresponding error bars per mean wind speed. Data normalized with the maximum value of each curve.

Figures 10.4 to 10.6 present the average values of the simulated bending moments (solid blue line) as a function of the mean wind speed and their upper and lower boundaries given from the uncertainty analysis (dashed light blue lines). In the same graph the average of the measured bending moments along with their error bars are also depicted. The highest discrepancies are observed in the sub-structure/foundation loads. For wind speeds below rated the average fore-aft measured moment at the tower bottom is accurately simulated, being always within the simulation uncertainties. Differences in the side-side bending moment of the support structure are due to different control strategies and uncertainties in the soil model. The commonly used p-y curve is not representative of the actual soil-pile interaction and more advanced models (ex. 3D FEM models) should be implemented in the simulations. In the case that the soil modeling uncertainties are included in the analysis, the overall uncertainty is expected to increase, due to the significant influence of the soil properties upon the response of the structure. The measured out of plane root bending moment is within the uncertainties of the simulated loads for all wind speeds, while the discrepancies in the in plane root bending moment are due to model uncertainties (unknown blade stiffness distribution).

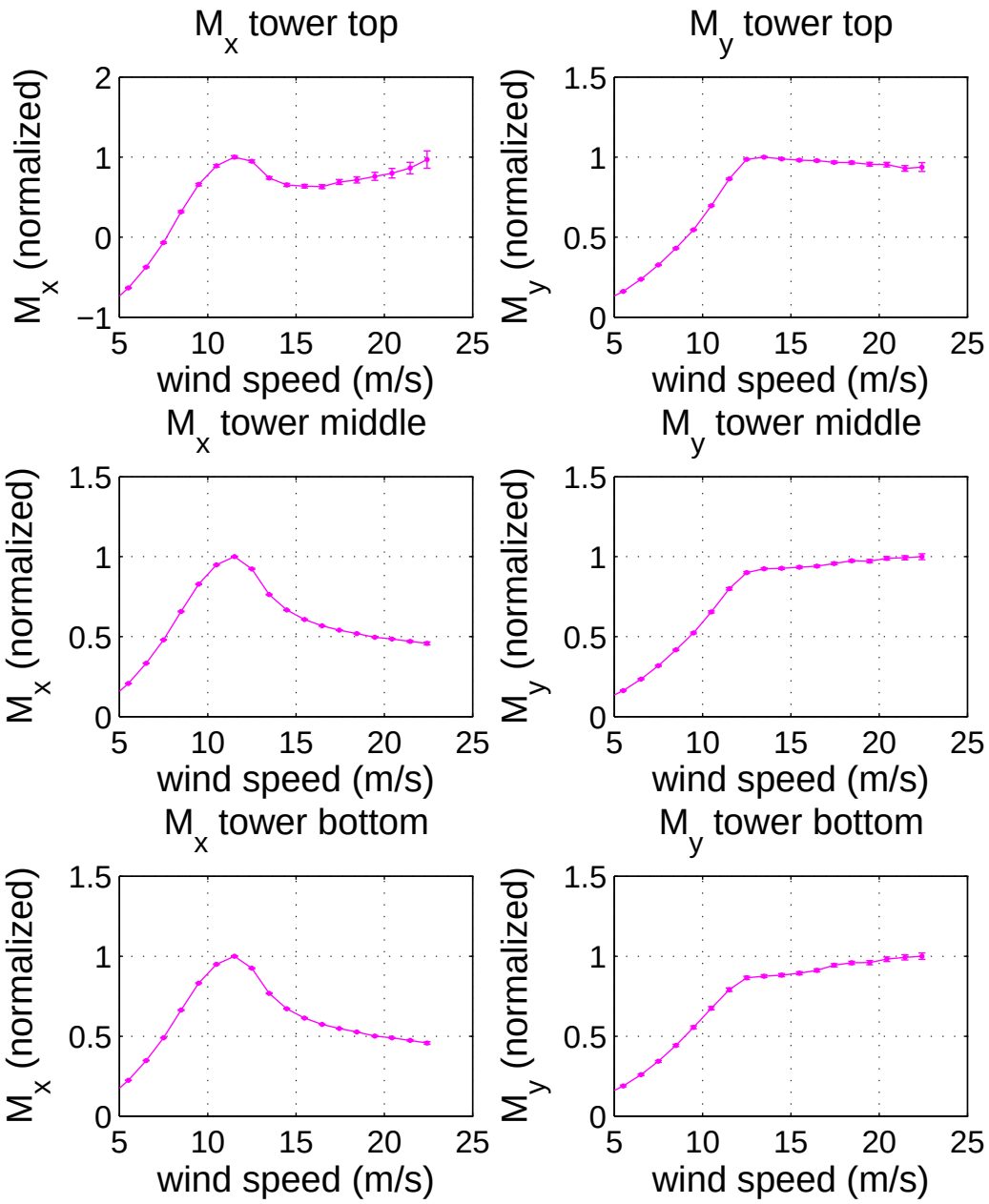

Figure 10.2: Average measured fore-aft and side-side bending moment along the tower with the corresponding error bars per mean wind speed. Data normalized with the maximum value of each curve.

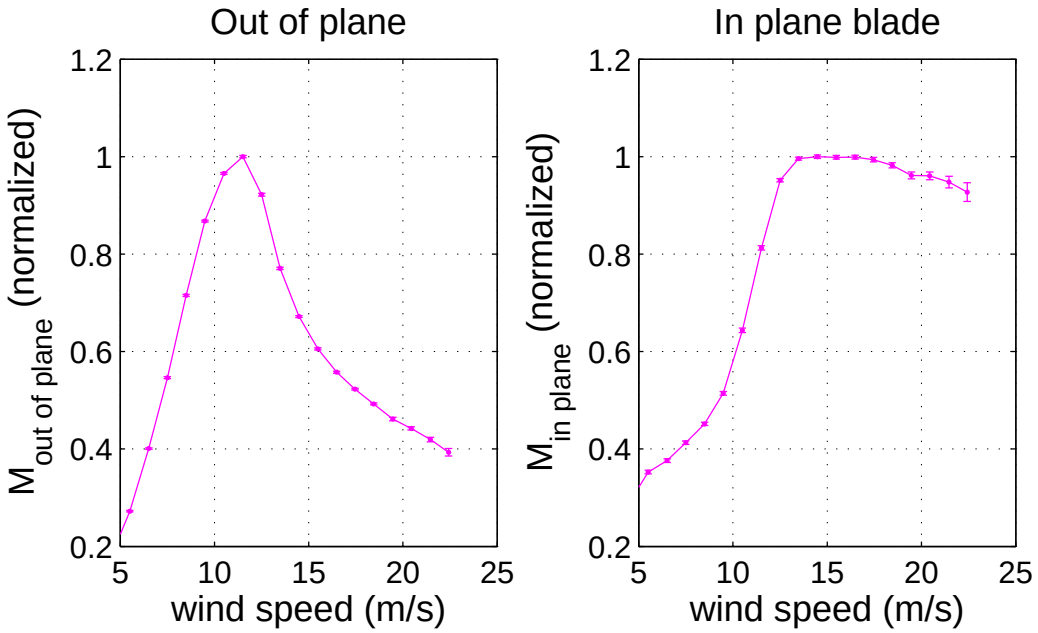

Figure 10.3: Average measured out of plane and in plane blade root bending moment with the corresponding error bars per mean wind speed. Data normalized with the maximum value of each curve.

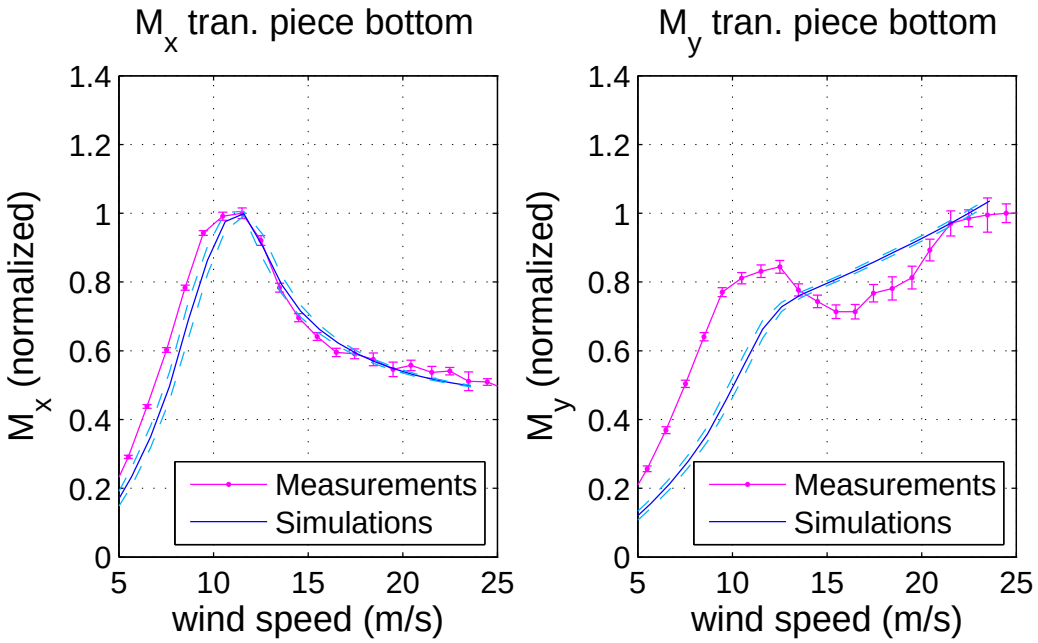

Figure 10.4: Comparison of the average fore-aft and side-side bending moment at the bottom of the transition piece between measurements and simulations along with the simulations' uncertainty limits. Data normalized with the maximum measured value of each curve. The dashed lines correspond to the simulations' standard uncertainties.

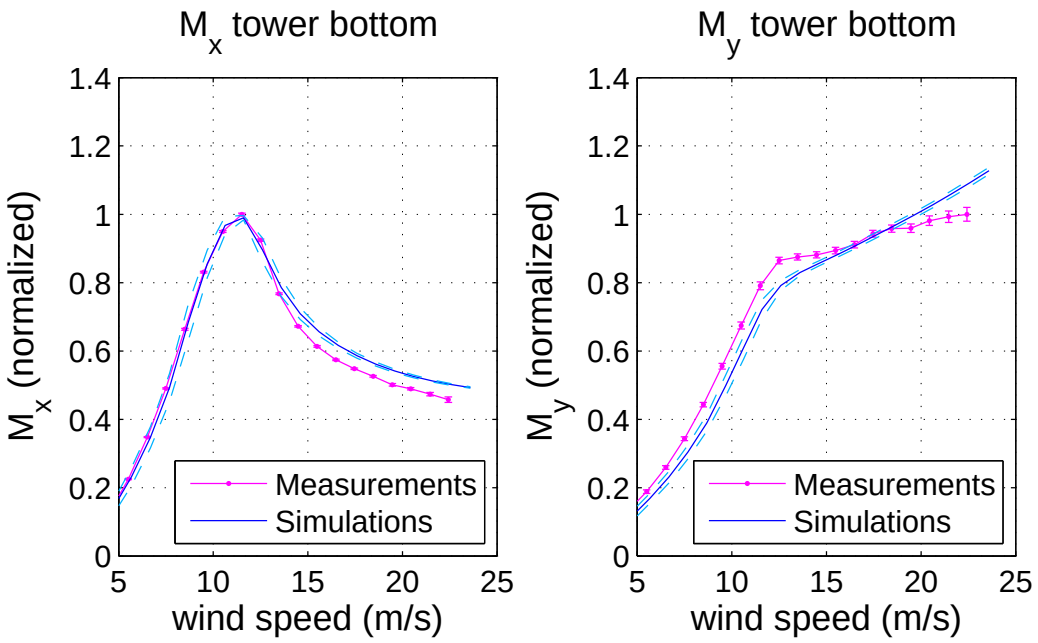

Figure 10.5: Comparison of the average fore-aft and side-side bending moment at the tower bottom between measurements and simulations along with the simulations' uncertainty limits. Data normalized with the maximum measured value of each curve. The dashed lines correspond to the simulations' standard uncertainties.

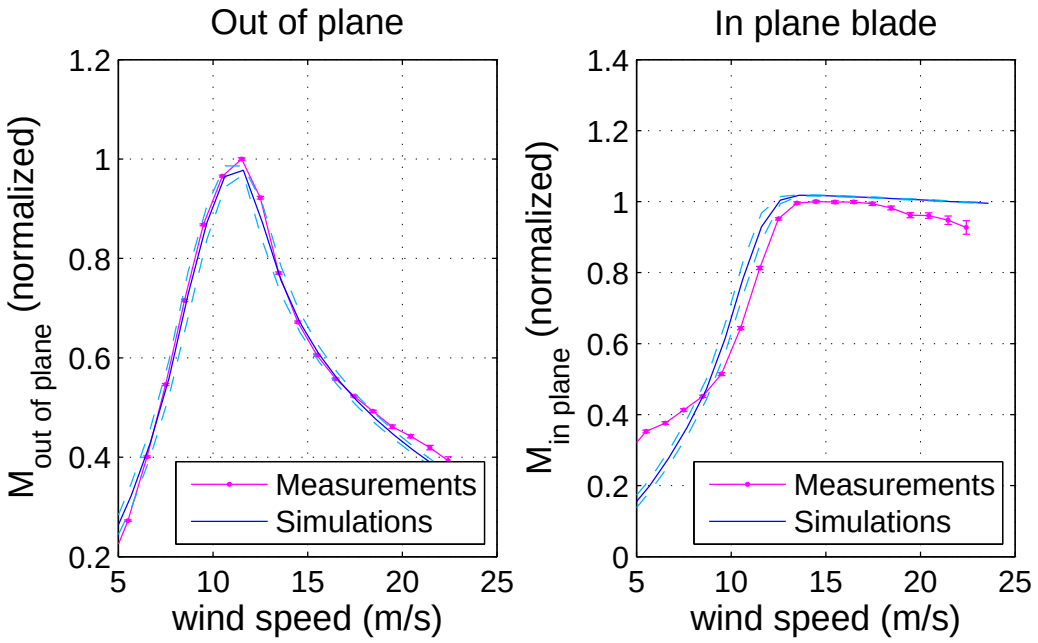

Figure 10.6: Comparison of the average out of plane and in plane blade root bending moment between measurements and simulations along with the simulations' uncertainty limits. Data normalized with the maximum measured value of each curve. The dashed lines correspond to the simulations' standard uncertainties.

Chapter 11

Damping Estimation

In this section the net damping of the structure is estimated from a boat impact. The damping under normal operation is identified both from measurements and simulations. The reliable load prediction is influenced by the accurate damping value in the model. In cases of wind-wave misalignment, where the side-side vibration is highly excited and low aerodynamic damping is present, the magnitude of the vibrations is mostly dominated by the additional offshore damping. It has often been reported in the literature that the real available damping is higher than what is used in the models. In the following sections a comparison between damping estimation from measurements and simulations is presented and its influence in the loading of the structure is analyzed.

11.1 Impulse Response

The additional damping of the structure is identified with the following three methods. a) An exponential curve is fitted to the relative maxima of the decaying response of the tower top acceleration after the application of an impulse and the logarithmic decrement is estimated from the exponent of the function. b) The half-power bandwidth method is also applied to the data in the frequency domain to obtain another estimate of the damping. c) The damping ratio is identified from the slope of a linear curve fitted to the envelope of the auto-correlation function of the tower top acceleration under ambient excitation.

11.1.1 Boat Incident-Measurements

During a yaw test, where the nacelle is swept slowly 360^o around the tower axis for the calibration of the support structure strain gauges, a boat accidentally hit the tower once, acting as an impulse to the turbine. The mean wind speed during the incident was 2.5m/s and the blades were pitched out to 82^o. The rotation of the nacelle was sufficiently slow (0.42rad/min) to assume a quasi stationary response with no interaction with the yawing dynamics. The logarithmic decrement in tower top accelerations can be estimated from the measured time series either by fitting an exponential curve to the relative maxima (time-domain approach, exponential curve of the form $x = Ae^{-\zeta\omega t}$) or with the use of the half-power bandwidth method (frequency-domain approach).

The fitting of an exponential function to the relative maxima of the decaying time series for the extraction of the damping ratios from the function parameters, assumes the contribution of a single mode. This may be accurate when the damping is small and the modes are well separated, but when this assumption is not satisfied the damping estimates can be wrong [122]. Figures 11.1a and 11.1b present the tower top acceleration in the fore-aft and side-side direction at the beginning and at the end of the incident. It can be observed that the boat impact excites only the side-side vibration mode, as the boat landing is aligned with the lateral strain gauges, while the fore-aft vibration is due to wind and waves as the level of acceleration is not decreasing with time.

Figure 11.1d presents the decay in the side-side direction and the fitted exponential function to the relative maxima, derived from the nonlinear least squares method. The exponential curve has the form $Ae^{-2\pi f\cdot\zeta\cdot t}$ and since the natural frequency can be easily estimated from the period of the decaying time series, the damping ratio can be extracted from the exponent of the fitted function. The identified critical damping ratio is $\zeta = 0.019$, which corresponds to a logarithmic decrement $\delta = 12.2\%$ and it's in agreement with the values proposed in references [81, 82]. The result is also in agreement with the overall damping of the first mode found in reference [118] from a measurement campaign at the Belwind wind farm. The higher damping value estimated in the present work is due to the tower damper that is not active in reference [118].

A decaying response is not observed in the time series of the fore-aft acceleration, due to the aligned boat with the side-side strain gauges, when it impacts the tower. The turbine is under ambient excitation in the fore-aft vibration mode, as the only forces acting in the longitudinal direction are the wind and the waves. Therefore, the auto-correlation function of the measured tower top acceleration, which gives the same decay with the time, is computed [149]. An estimation of the auto-correlation function $R_{XX}(\tau)$ of a stochastic, ergodic process $x(t)$ with limited data is given by Equation 11.1, where T is the finite time that the time series is known. As the time series are known over a limited amount of time, to ensure positive time lags the upper limit of the integral is equal to $T - \tau$.

$$R_{XX}(\tau) = \frac{1}{T-\tau}\int_0^{T-\tau} x(t+\tau)x(t)\mathrm{d}t, \quad \tau \in [0;T] \tag{11.1}$$

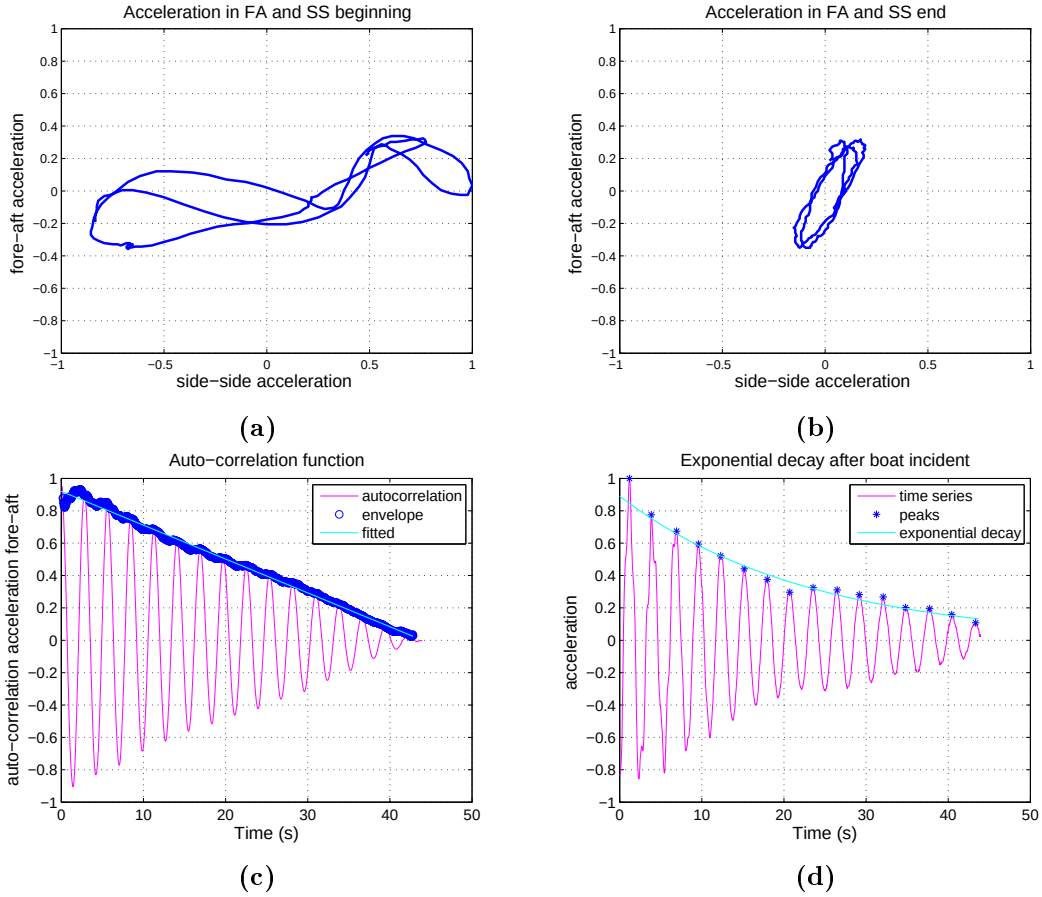

Figure 11.1: a) Tower top motion seen from above for the first 5s after the boat impacts the tower (normalized with the maximum side-side acceleration at the beginning of the impulse) b) Tower top motion seen from above for the last 7s of the incident (normalized with the maximum side-side acceleration at the beginning of the impulse). c) Normalized auto-correlation function of fore-aft acceleration after the boat impact. The lags, where the auto-correlation function is obtained, are divided with the sampling rate of $F_s = 35$Hz to provide time. d) Exponential decay of side-side vibration after the boat impact (normalized with the maximum acceleration).

Taking the inverse Fourier transform of the power spectral density of the tower top acceleration signal in the fore-aft direction yields the auto-correlation function. A linear curve is fitted to the envelope of the function (Figure 11.1c) and a logarithmic decrement of $\delta = 11.5\%$ is then extracted from its slope. The slightly higher damping value in the side-side vibration is due to the pitch angle of the blades (82^o) that introduces a small aerodynamic damping in that direction [140]. The identified damping of the first mode obtained from the auto-correlation function is then compared with the estimated value from the exponential curve fitted to the relative maxima of the decaying response. In Section 11.2 the auto-correlation function will be used for damping estimation in normal operation.

The time series of the tower top acceleration are transformed to the frequency domain through a Fast Fourier Transformation. Figure 11.2 presents the power spectral density (PSD) of the support structure acceleration based on strain gauge measurements at different heights. The tower top acceleration in the side-side direction is used for the estimation of the damping from the half-power bandwidth method. Observing the frequency f_n with maximum power P_{max} and the two frequencies f_1 and f_2 where the power is $P_{max}/2$, the damping can be estimated by Equation 11.2 [75]. The identified damping ratio is $\zeta = 0.018$, which is slightly lower compared to the exponential function fit. The accuracy of this method depends on the window length, the resolution and the overlap of the FFT, giving a biased estimation for the damping.

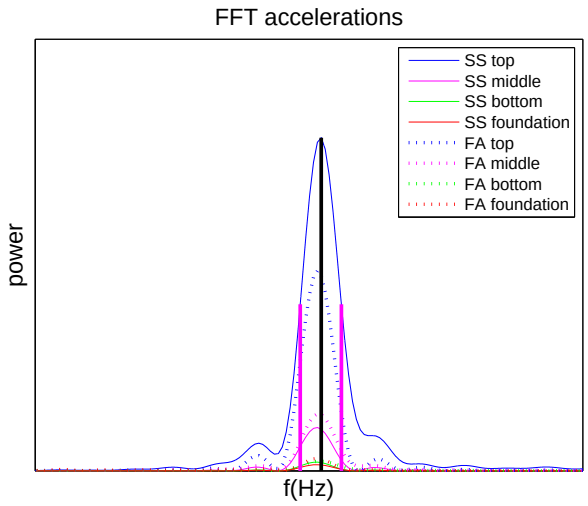

Figure 11.2: Power spectra of fore-aft and side-side acceleration time series at four heights along the support structure. Qualitative representation. The vertical lines denote the frequencies where the power is equal to P_{max} and $P_{max}/2$.

$$2\zeta = \frac{1}{Q} = \frac{f_2 - f_1}{f_n} \tag{11.2}$$

11.2 Ambient Excitation

The measured response of a wind turbine under normal operation is further analyzed to verify the support structure damping. The main advantage of ambient excitation is that the identified modal parameters correspond to real levels of vibration. Cases with aligned wind and wave directions are examined. In the following sections the damping is estimated from the logarithmic decrement of the auto-correlation of the tower top accelerations, based on the Frequency Domain Decomposition (FDD) technique. The method was chosen for its simplicity and fast application. It can deal with closely spaced modes and it does not require the assumption of separate excitation.

11.2.1 Enhanced Frequency Domain Decomposition

The Enhanced Frequency Domain Decomposition (EFDD) is an output only identification technique for the estimation of the modal parameters of a vibrating structure. Based on the measured response of the wind turbine and assuming that the loading is unknown the modal characteristics are estimated.

The Power Spectral Density (PSD) matrix $G_y(f)$ of the measured signal (tower top acceleration in this case), is given by:

$$G_y(f) = [H_f(f)]^*[G_x(f)][H(f)]^T \tag{11.3}$$

$G_x(f)$ is the input PSD matrix and $H(f)$ is the Frequency Response Function (FRF) matrix. The superscripts $\bullet^T$ and $\bullet^*$ denote transpose and complex conjugate respectively. By writing the FRF in a typical partial fraction form, using the Heaviside partial fraction theorem and assuming that the input is stochastic with a zero mean white noise distribution ($G_x(f) = C$), Equation 11.4 is obtained for the output PSD, where $k \in Sub(f)$ is the set of modes that contribute to this frequency, ψ_k is the mode shape, d_k is the scaling factor, λ_k the pole and ω the damped natural frequency of the k^{th} mode. For a more detailed explanation of the process refer to references [113, 115].

$$G_y(f) = \sum_{k \in Sub(f)} \frac{d_k \psi_k \psi_k^T}{j\omega - \lambda_k} + \frac{d_k^* \psi_k^* \psi_k^{*T}}{j\omega - \lambda_k^*} \tag{11.4}$$

At each discrete frequency, the final spectral density matrix is decomposed into singular values and vectors (Singular Value Decomposition SVD Equation 11.5). Under the assumption of small damping it was shown in reference [113] that the singular values of the spectral density matrix are auto spectral density functions of SDOF systems that have the same frequency and

damping as the modes of the examined structure.

$$G_y(f) = U_i \Sigma_i U_i^T \tag{11.5}$$

The matrix U_i is an orthogonal matrix ($UU^* = U^*U = I$, U^* is the conjugate transpose of U) containing the singular vectors u_{ij} (Equation 11.6) and Σ_i is a diagonal matrix with non-negative entries holding the singular values s_{ij} (Equation 11.7). Thus, at a specific frequency, the contribution of each mode to the total response becomes evident and the system is decomposed to Single Degree of Freedom auto-spectral density functions. The dominant mode in each frequency appears at the first singular value. An estimate of the mode shape is the first singular vector $\psi_s = u_{i1}$ that corresponds to a peak in the spectrum given by the maximum singular value. The auto power spectral density function for each mode is then identified around this peak by estimating the MAC (modal assurance criterion) of the mode shape estimate ϕ_s with the singular values for the frequencies around the peak.

$$U = [\{u_1\} \quad \{u_2\} \quad \{u_3\} \quad \cdots \quad \{u_j\}] \tag{11.6}$$

$$\Sigma = \begin{bmatrix} s_{11} & 0 & 0 & \cdots & 0 \\ 0 & s_{22} & 0 & \cdots & 0 \\ 0 & 0 & s_{33} & \cdots & 0 \\ \vdots & \vdots & \vdots & \vdots & \vdots \\ 0 & 0 & 0 & \cdots & s_{jj} \end{bmatrix} \tag{11.7}$$

The Modal Assurance Criterion (MAC) is a statistical factor used to indicate consistency between mode shapes [166]. It takes values from 0 to 1, with 1 showing that the mode shapes represent the same shape and 0 when the mode shapes are linearly independent (orthogonal) [167]. For complex modes MAC is given by Equation 11.8.

$$MAC = \frac{|\{\phi_s\}^T \{\phi_x\}^*|^2}{(\{\phi_s\}^T \{\phi_s\}^*)\,(\{\phi_x\}^T \{\phi_x\}^*)} \tag{11.8}$$

ϕ_s is the mode shape estimate corresponding to the peak of the auto power spectral density function at a specific frequency (max singular value) and ϕ_x are the mode shape estimates for the frequency lines around the peak. As long as the MAC of ϕ_s with a singular vector is close to 1, the corresponding singular value belongs to the auto-spectral density function of this mode. If the MAC drops below a certain limit (rejection level), as defined by the user, the spectral density function is terminated at the last identified singular value. The lower the chosen MAC limit is, the more singular values will be included in the SDOF Bell function (Figure 11.3). The rejection level should be selected in such a way that will give a good representation of the Bell function around the chosen peak without including any noise.

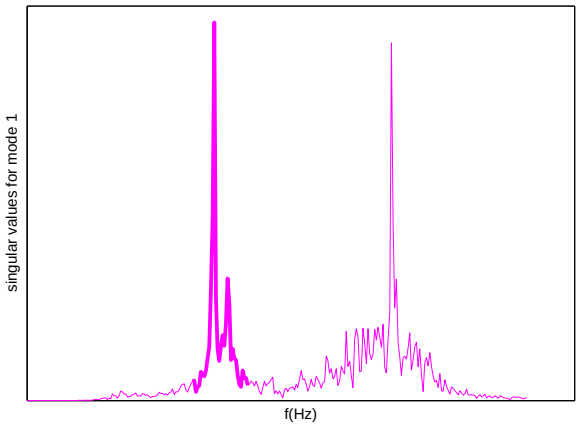

Figure 11.3: Bell Function of singular value spectrum. The thick line denotes the part of the spectrum that takes part in the identification process of the first mode. The second peak corresponds to a harmonic.

The Single Degree of Freedom auto-spectral density functions are transferred back to the time domain through an inverse FFT (using the complex conjugate of each entry), resulting in auto-correlation functions for each mode. The logarithmic decrement δ is given by Equation 11.9 through observation of all the extremes r_k of the correlation function [4].

$$\delta = \frac{2}{k} ln \left(\frac{r_0}{|r_k|} \right) \tag{11.9}$$

r_0 is the initial value of the auto-correlation function and r_k the k^{th} value. The first positive peak occurs at the time instant $t = 0$ and every interval $t = 2\pi/\omega_d$, where ω_d is the damped natural frequency.

Considering the ratio of the height of the first peak of the auto-correlation function with an arbitrary peak later in time, the solution to the equation of motion for an under-damped single degree of freedom system, is derived. Taking the natural logarithm on both sides of the equation, the expression for the k^{th} logarithmic decrement is given by Equation 11.11.

$$\left(\frac{r_0}{r_k} \right)^2 = \left(\frac{r_0 cos(0)}{r_0 e^{-\zeta \omega_n 2\pi k/\omega_d}} \right)^2 = (e^{\zeta \omega_n 2\pi k/\omega_d})^2 \tag{11.10}$$

$$\delta_k = 2ln \left(\frac{r_0}{r_k} \right) = 2 \frac{2\pi k\zeta}{\sqrt{1-\zeta^2}} \overset{small damping}{\Rightarrow} \delta_k \simeq 2\pi k\zeta \tag{11.11}$$

By fitting a linear curve to the data, the regression coefficient gives the slope of the line, which corresponds to the damping ratio ζ. The natural frequencies are identified from the

peaks of the singular values of the decomposed spectral density matrix.

The accelerations of the support structure at 4 different heights were used as inputs to the frequency domain decomposition technique to estimate the natural frequency and the damping ratio of the first fore-aft and side-side vibration modes of the system. Figure 11.4a shows the singular values of the decomposed spectral density matrix. Peaks present at more than one singular values indicate harmonics. Figure 11.6 presents the auto-correlation function corresponding to the time domain free decay, obtained through the inverse FFT to the auto-power spectral density function (first singular value).

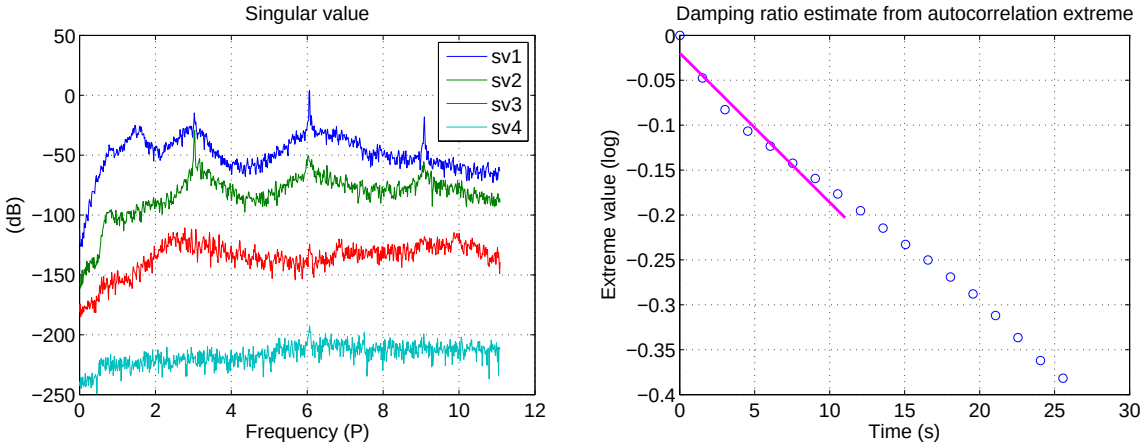

(a) (b)

Figure 11.4: a) Singular values of the decomposed spectral density matrix. The x axis is scaled with the rated rotational speed to show the 3P, 6P and 9P inputs. b) Envelope of auto-correlation function in logarithmic scale and linear fit for damping ratio estimation.

Figure 11.4b shows the linear regression to the logarithmic envelope of the auto-correlation function, the slope of which gives the damping ratio of this mode.

11.2.1.1 Measurements

The Enhanced Frequency Domain Decomposition technique was applied in the measured accelerations of the tower. The MAC rejection limit used for the identification of the auto-power spectral density matrix is 0.9. The data used for the modal parameters' identification are from the measurement period of July 2012, where the maximum observed mean wind speed was 19m/s. The results for the fore-aft and side-side modal damping identified from the measured response of the wind turbine are presented in Figure 11.5. The case of aligned wind and waves is examined. The mean damping of the fore-aft tower mode is approximately $\delta = 65\%$ with a standard deviation of 8.1% (Figure 11.5a). During operation this mode is dominated by the aerodynamic damping. The mean damping in the side-side direction derived from the tower top accelerations is $\delta = 30\%$ with a standard deviation of 6.7% (Figure 11.5b). An increase of the damping ratio in the side-side direction for higher wind speeds is due to control

actions and the aerodynamic damping introduced from the blade pitching. In this direction the parameters influencing the modal damping are the soil-pile interaction, the tower damper, the tidal variation and the wind speed. [119].

The uncertainty levels of the estimated damping per mean wind speed are presented as error bars in Figure 11.5. The standard uncertainty u_{x_i} is the ratio between the estimate of the standard deviation s_{x_i} and the square root of the number of observations N. For higher wind speeds due to the lower number of observations the uncertainty of the damping estimation is increased.

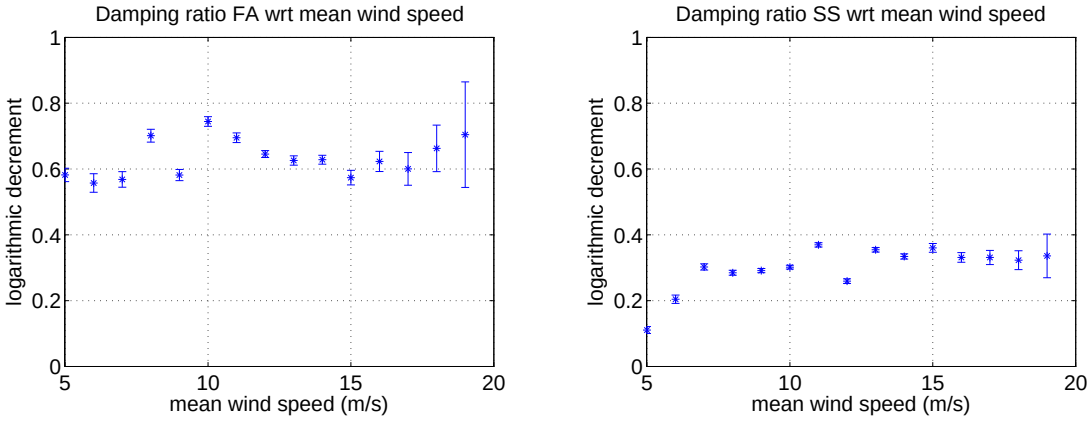

(a) **(b)**

Figure 11.5: a) Logarithmic decrement of the fore-aft vibration mode with respect to the mean wind speed obtained from the measured tower top accelerations along with the error bars. b) Logarithmic decrement of the side-side vibration mode with respect to the mean wind speed obtained from the measured tower top accelerations along with the error bars.

Due to the close natural frequencies of the fore-aft and side-side modes, which results in energy being transferred from the highest to the lowest damped mode [124, 122], the absence of aerodynamics in the latter and the presence of the harmonics, the side-side vibration is more excited introducing a beating phenomenon and a longer decay in the auto-correlation (Figure 11.6b). The fore-aft vibration is dominated by the aerodynamic damping during operation, rendering the auto-correlation function smoother and the damping estimation more accurate (Figure 11.6a).

11.2.1.2 HAWC2 Simulations

The Enhanced Frequency Decomposition method was applied to the simulation results for all mean wind speeds and the natural frequencies and logarithmic decrements as a function of the wind speed are presented in Figure 11.7. Results both from measurements and simulations are presented and discrepancies are discussed. The environmental conditions used in the simulations are the same with the measured ones. Each simulation is half an hour of time series and was performed with the aero-elastic code HAWC2 using turbulent wind field and

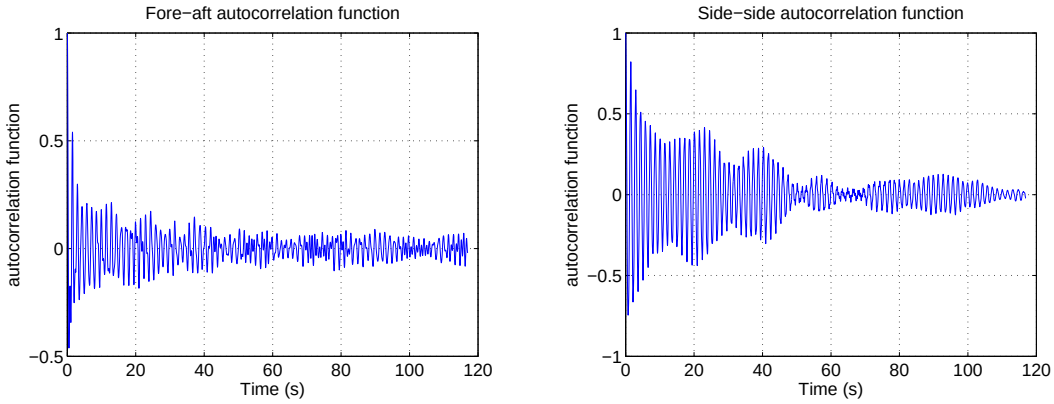

(a) **(b)**

Figure 11.6: a) Normalized auto-correlation function Fore-Aft direction. b) Normalized auto-correlation function Side-Side direction.

irregular waves. The MAC rejection limit used for the identification of the auto-power spectral density matrix is 0.95.

The results for the fore-aft and side-side natural frequency and modal damping obtained from measurements are presented in Figure 11.7 along with the modal parameters from the simulations. Figures 11.7a and 11.7c present a qualitative comparison of the natural frequencies of the first two modes for all mean wind speeds showing their percentage change from standstill. The estimated frequencies show small variation with the wind speed. Larger variations in the frequency estimation of the first mode (tower fore-aft) are attributed to the more noisy acceleration signal in this direction due to wave impact. Figures 11.7b and 11.7d show the damping obtained from measurements and simulations. As depicted from Figure 11.7b in the fore-aft vibration mode there is a good agreement between the estimated damping from the measurements and the simulations, after the model was tuned to the standstill frequencies and damping of the real turbine. On the side-side direction though the discrepancies are higher for wind speeds above rated. A tower damper is not implemented in the model and therefore its influence cannot be accurately investigated in the current simulations. Further inadequate modeling of the soil damping and the tidal variation may be responsible for this difference [119]. The discrepancies in the damping estimation of the second mode (side-side vibration) need to be further investigated.

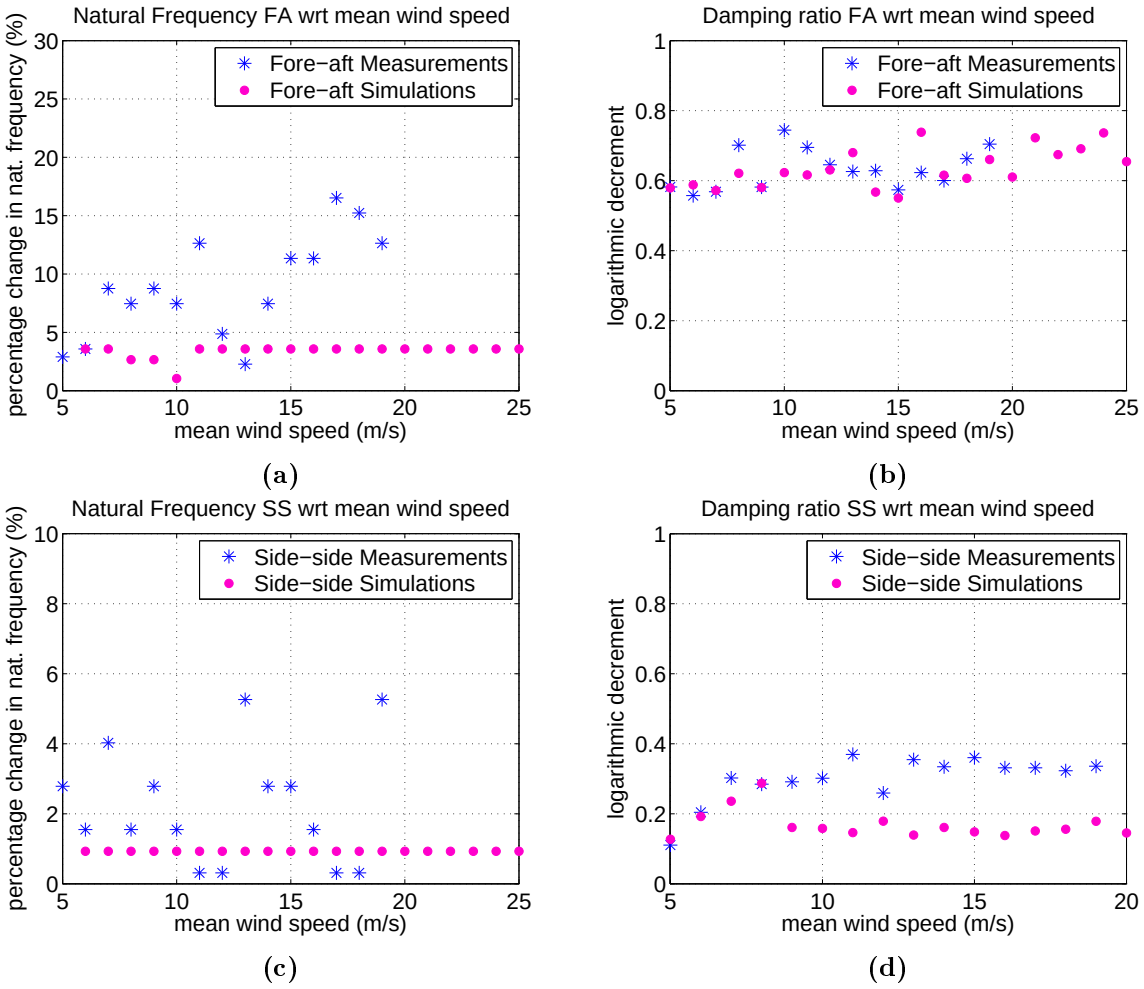

Figure 11.7: a) Change in the natural frequency of the fore-aft vibration mode from the standstill, measurements vs. simulations. b) Logarithmic decrement of the fore-aft vibration mode with respect to the mean wind speed, measurements vs. simulations. c) Change in the natural frequency of the side-side vibration mode from the standstill, measurements vs. simulations. d) Logarithmic decrement of the side-side vibration mode with respect to the mean wind speed, measurements vs. simulations.

Figure 11.8 presents the overall damping of the first two modes in normal operation, estimated with the Enhanced Frequency Domain Decomposition method. Three different values of the additional offshore damping have been used in the simulations, by changing the Rayleigh coefficients in the model and applying an impulse to estimate the additional offshore damping from the decaying response. The stars in the figure correspond to the tuned damping from the boat incident ($\delta = 12\%$), the circles to the additional offshore damping of $\delta = 6\%$ (value usually implemented in the simulations) and the crosses to 15% higher damping than the tuned ($\delta = 13.8\%$). It can be observed that the lower additional offshore damping, often used in the simulations ($\delta = 6\%$), results in much lower overall damping in both directions. However, as was shown in Section 11.2 [168], the damping in the real structure was found to be higher.

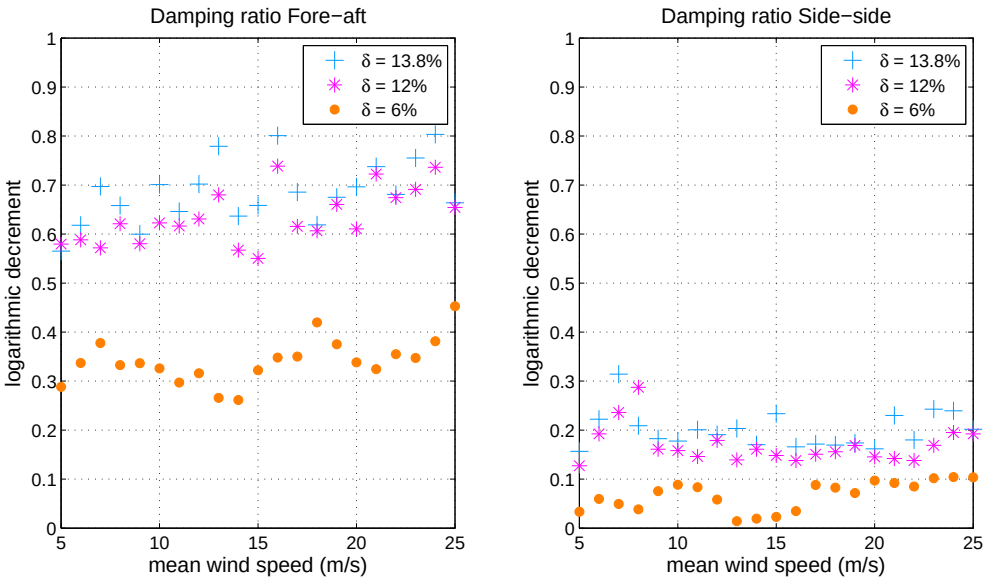

Figure 11.8: Overall damping in normal operation from simulations using the enhanced frequency domain decomposition method. Three different additional offshore damping values are examined (stars correspond to $\delta = 12\%$, circles to $\delta = 6\%$ and crosses to $\delta = 13.8\%$).

Chapter 12

Loading under Different Conditions

The dynamic response of an offshore wind turbine in the case of wind-wave misalignment is examined in the first section of this chapter. The accumulated fatigue accounting for the joint wind-wave probability is estimated and the effect of damping on the side-side fatigue is investigated. The loading on the system during a storm with the presence of a yaw error is analyzed in the second section.

12.1 Wind-Wave Misalignment

Side-side fatigue at the support structure due to wave loading misaligned with the wind can become a significant design factor, because of the low aerodynamic damping experienced in this direction. According to reference [11] the misalignment between the wind and wave directions should be included in the design if misalignment conditions are present in the site of installation. The over-dimensionalization of the substructure due to high estimated fatigue loading might result in a non-economically feasible design. In reference [81] the case of the side aero-elastic damping is examined, and its importance to decrease side-side loads due to wind-wave misalignment is stressed.

The effect of misalignment angles on the fatigue of the structure is examined in reference [12]. A study conducted by Fisher et al. in [169] considering all load cases described in reference [13] and misalignment angles from $0^o - 360^o$ demonstrated the importance of wave directionality during the design process. The bending moment in the fore-aft direction is 30% higher in the case of waves perpendicular to the wind, while the side-side loading is 5 times larger compared to the case of aligned wind and waves. In reference [46] the equivalent loads and fatigue damage at the tower and monopile bottom were examined for different cases of wind-wave misalignment considering both linear and non-linear waves. The effect of

misalignment on the fatigue, including the probability density function of misalignment angles has been investigated in reference [170]. For a misalignment distribution with a peak close to 0^o the fatigue damage in the tower bottom was increased by 3.6% between the misaligned and the collinear cases. For the case where the highest probability of occurrence is for an angle of 60^o the increase in the fatigue damage is up to 15%. An increase in the fatigue damage accumulation due to waves perpendicular to the wind direction is also reported in reference [171], where a non-linear irregular wave model is implemented in the analysis.

In this section the target is to investigate the sensitivity of the side-side fatigue loading to the different misalignment angles, for various values of the damping available on the system. In the analysis the misalignment distribution is considered.

12.1.1 Fatigue Analysis/Measurements

The equivalent fatigue load corresponds to the cyclic load that if applied n_{eq} times in the structure, it will result in the same damage as the variable load fluctuations experienced over the lifetime of the wind turbine [53]. The measured time series binned as described in Section 5.1.1, were combined to calculate the 1Hz equivalent load (Equation 12.1) for each mean wind speed-significant wave height combination. N_i are the number of cycles for a given stress range S_i, in all measured time series. m is the Wöhler exponent equal to 4 in the present study for the steel components, $h_{i,j}$ is the total measurement time of each bin in seconds and n is the number of stress range bins.

$$S_{1Hz} = \left(\frac{\sum_{i=1}^{n} N_i S_i^m}{h_{i,j}} \right)^{(1/m)} \tag{12.1}$$

Figure 12.1a presents the 1Hz equivalent load for the cross-wind fatigue at the tower bottom as a function of the mean wind speed. The different lines correspond to the different significant wave heights and the values are normalized with the maximum load for $U = 14m/s$. The equivalent load has the tendency of increasing with the wind speed and the wave height. Taking into account the joint wind-wave distribution, the fatigue damage contribution D_f of each bin, to the lifetime fatigue of the wind turbine support structure is estimated. Under the assumption of linear cumulative damage, the fatigue damage accumulation is given by Equation 12.2, where $N_{tot,i}$ are the number of cycles to failure for a given stress S_i and α is the intercept of the S-N curve with the log N axis [172]. The result with respect to the mean wind speed is presented in Figure 12.1b. The different curves illustrate the different significant wave heights. It can be observed that the greatest contribution to the lifetime fatigue is not due to the most severe cases but due to bins with higher probability of occurrence, even though the wind and wave conditions are milder. This observation demonstrates the importance of the joint wind-wave distribution in the calculation of the fatigue of the structure and indicates that it is not only the severeness of the operating conditions that contribute to the fatigue

but their probability of occurrence as well.

$$D_f = \sum_{i=1}^{n} \frac{N_i}{N_{tot,i}} = \frac{1}{\alpha} \sum_{i=1}^{n} \frac{N_i}{S_i^m} \tag{12.2}$$

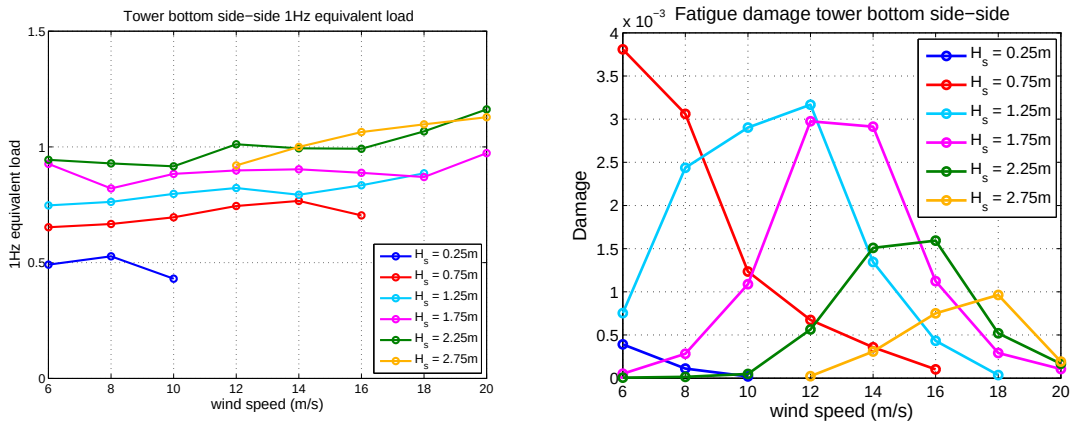

(a) 1Hz equivalent load for the cross-wind fatigue at the tower bottom, normalized with the maximum equivalent load for $U = 14m/s$.

(b) Relative damage based on the probability of occurrence of each wind-wave bin for the side-side fatigue at the tower bottom.

Figure 12.1: 1Hz equivalent load and relative damage at the tower bottom in the side-side direction.

12.1.1.1 Fatigue Analysis for Various Misalignment Sectors (Measurements)

In order to examine the effect of the misalignment angles on the fatigue of the structure, the equivalent load for different misalignment sectors within each wind-wave bin is calculated. The misalignment angles are separated in bins of 10^o is such a way that the bin for $mis\_ang = (-15^o) - (-5^o)$ covers all the misalignment angles in the interval $-15 \leq mis\_ang < -5$. The 1Hz equivalent load for each misalignment sector is calculated by Equation 12.3, where $h_{misal,mes}$ are the measured hours of a specific misalignment sector. The relative damage is estimated accounting for the probability density function of each misalignment angle as was shown in Section 5.1.2. The loads as a function of the misalignment angle are presented in Figure 12.2. The 1Hz equivalent loads are normalized with 0^o misalignment. The 1Hz equivalent load has a small tendency to increase with the increased absolute value of the misalignment angle. However, the trend is not clear and the side-side 1Hz equivalent load does not appear to have a high sensitivity to the wind-wave misalignment for the combinations of wind speed and wave heights presented in 12.2.

Considering the probability density function of the misalignment angles and using it as a weight to calculate the relative damage of every misalignment angle to the lifetime fatigue of the wind turbine support structure (Equation 12.2), it can be observed that the highest

damage contribution is given for the misalignment angle with the highest probability, namely -10^o.

$$S_{1Hz,misal} = \left(\frac{\sum_{i=1}^{n} N_i S_i^m}{h_{misal,mes}} \right)^{(1/m)} \tag{12.3}$$

In the same figure the uncertainty level of the 1Hz load are also presented as error bars. The standard uncertainty u_{x_i} is the ratio between the estimate of the standard deviation s_{x_i} and the square root of the number of observations N (Equation 10.1). For large misalignment angles due to the lower number of observations the uncertainty of the equivalent load is increased.

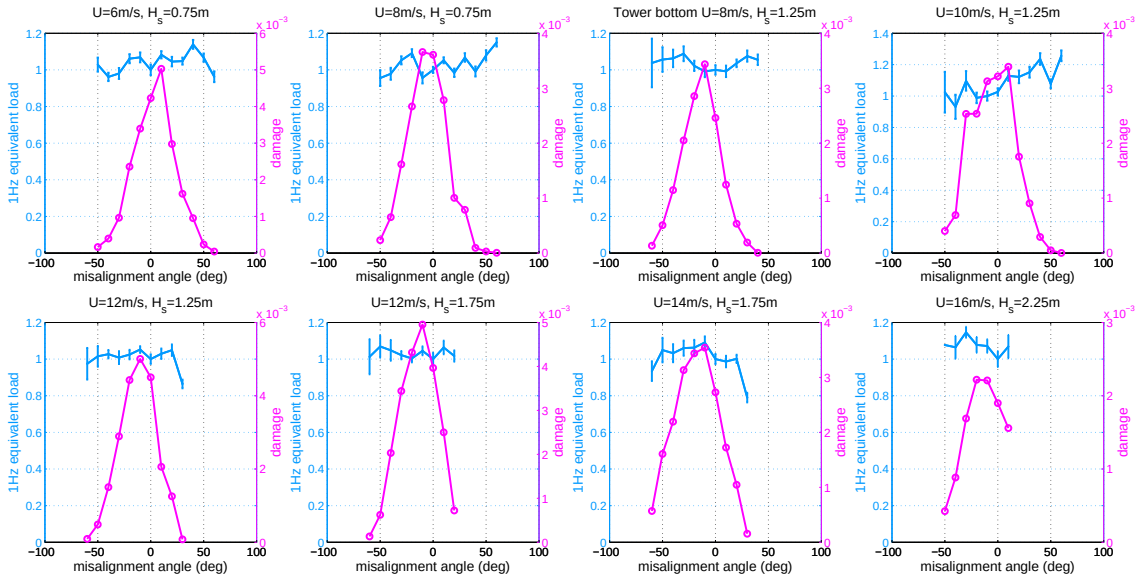

Figure 12.2: 1Hz equivalent load and relative damage contribution to the side-side fatigue at the tower bottom based on the probability of occurrence of different misalignment sectors for various wind-wave combinations (measurements). The values are normalized with the equivalent load at 0^o misalignment. The error bars on the 1Hz equivalent load represent the uncertainty of the estimation.

12.1.2 Fatigue Analysis/Simulations

The lifetime equivalent load is based on the joint wind-wave distribution calculated from the measurements (Equation 5.7), scaled to a lifetime of 25 years. Figure 12.3 presents the 1Hz equivalent load and the relative damage of each bin to the fatigue of the structure with respect to the mean wind speed both for simulations and measurements (dashed lines correspond to simulations and solid to measurements). For each of the 46 mean wind speed-significant

wave height combinations 12 turbulence seeds of 600s and 11 misalignment angles were used in HAWC2, which resulted in a total of 6072 simulations. The illustrated 1Hz equivalent load data are normalized with the simulation maximum equivalent load for $U = 14m/s$. The simulated equivalent loads seem to follow satisfactorily the measurements. Discrepancies are mainly attributed to differences in the blade aerodynamics and uncertainties in the soil modeling.

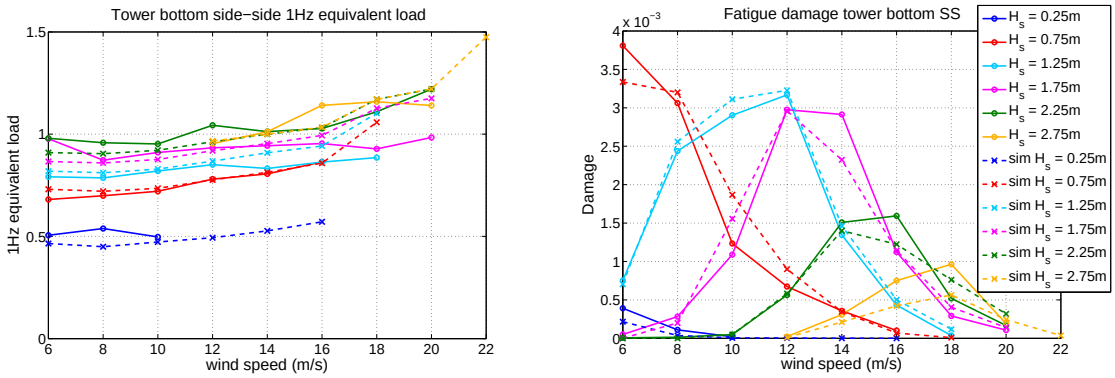

(a) Comparison of 1Hz equivalent load for the side-side fatigue at the tower bottom. (measurements vs. simulations). The values are normalized with the simulations maximum equivalent load for $U = 14m/s$.

(b) Relative damage based on the probability of occurrence of each wind-wave bin for the side-side fatigue at the tower bottom (measurements vs. simulations).

Figure 12.3: 1Hz equivalent load and relative damage at the tower bottom in the side-side direction, based on the joint wind-wave distribution (measurements vs. simulations)

The accumulated fatigue load for the whole lifetime of the structure (25 years) is calculated both for measurements and simulations. Figure 12.4 presents the accumulated fatigue damage at the tower bottom in the fore-aft and side-side directions. The illustrated data are normalized with the simulated load. The agreement between measurements and simulations is satisfactory. The higher simulated accumulated fatigue is due to the lower damping present in the simulations as was shown in reference [168].

12.1.3 Effect of Damping on Fatigue

Figure 12.5 presents the accumulated fatigue load for four different damping values and different wind-wave conditions. The illustrated data are normalized with the fatigue from the model tuned to the measured damping of $\delta = 12\%$ (reference model). In the fore-aft direction the different damping values have small impact on the fatigue. When the additional offshore damping is half of the measured ($\delta = 6\%$) the accumulated fatigue is up to 6% higher than the reference model. However, in the side-side direction, due to the little aerodynamic damping, the effect of the additional offshore damping is more pronounced. For differences in the damping of $\pm 15\%$, the change in the fatigue is up to 17%. But for the lowest damping value, the fatigue in the side-side direction is up to 86% higher than the reference model.

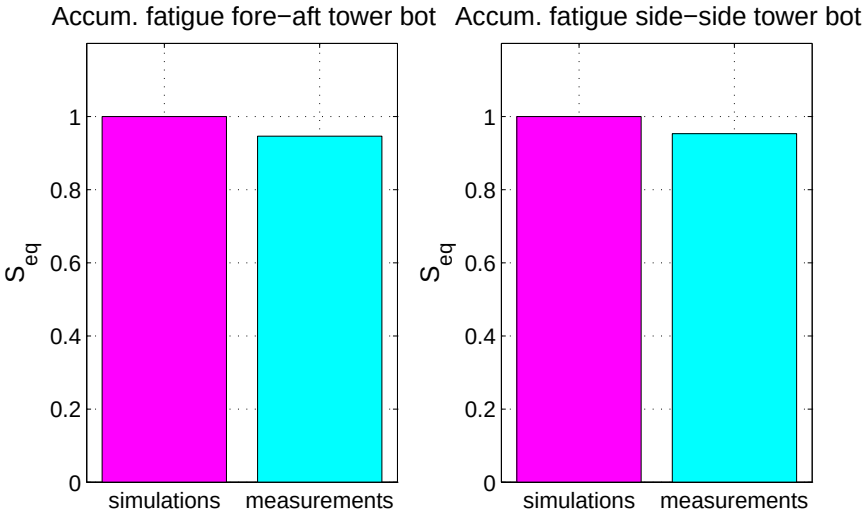

Figure 12.4: The total accumulated fatigue damage for measurements and simulations normalized with the simulations' fatigue.

The damping in the side-side direction during normal operation for different misalignment angles, estimated with the Enhanced Frequency Domain Decomposition method is presented in Figure 12.6. Due to the low contribution of hydrodynamic damping, the overall damping seems to be invariant to the different misalignment angles. It is on a small extent though affected by the higher wind speed, due to the aerodynamic damping introduced to the side-side vibration from the blade pitching.

Figure 12.7 presents the fatigue damage contribution in the side-side direction at the tower bottom for different damping values as a function of the misalignment angle. The sensitivity of the estimated equivalent load to the misalignment angles decreases with increased additional offshore damping. Due to little aerodynamic damping in the side-side direction, the loading is more influenced by the structural damping and the damping due to soil, waves and tower dampers. The equivalent load from the measured time series is less sensitive to the misalignment angle, due to higher damping in the side-side direction of the full scale wind turbine (Figure 12.2).

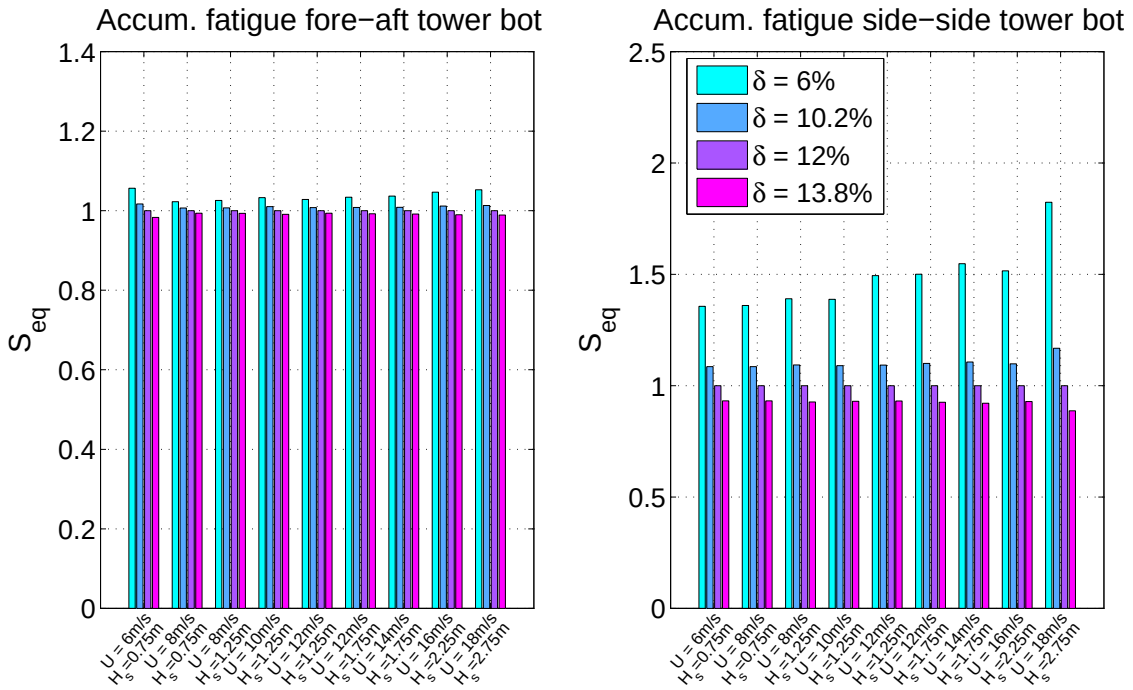

Figure 12.5: The total accumulated fatigue damage from simulations with different values for the additional offshore damping. Normalized with the fatigue from the model tuned to the measured damping.

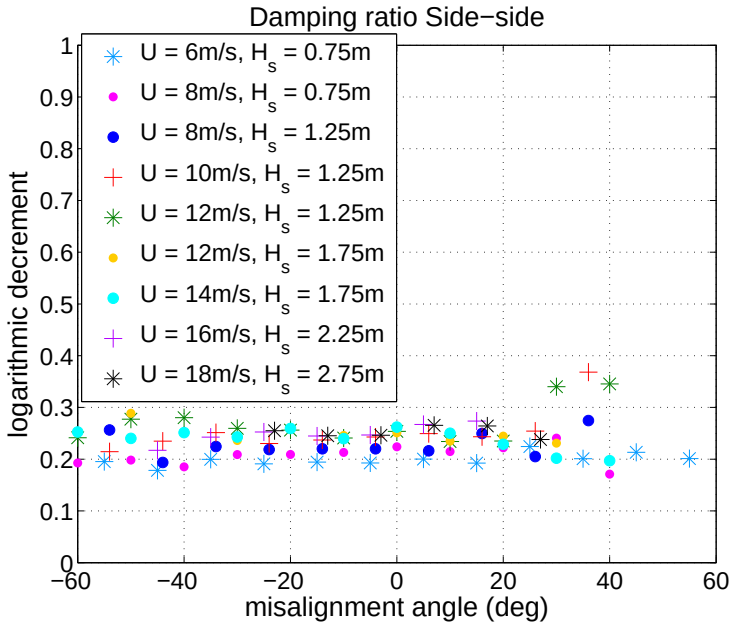

Figure 12.6: Logarithmic decrement in the side-side direction from site-measurements as a function of the misalignment angle for different wind speed - significant wave height conditions.

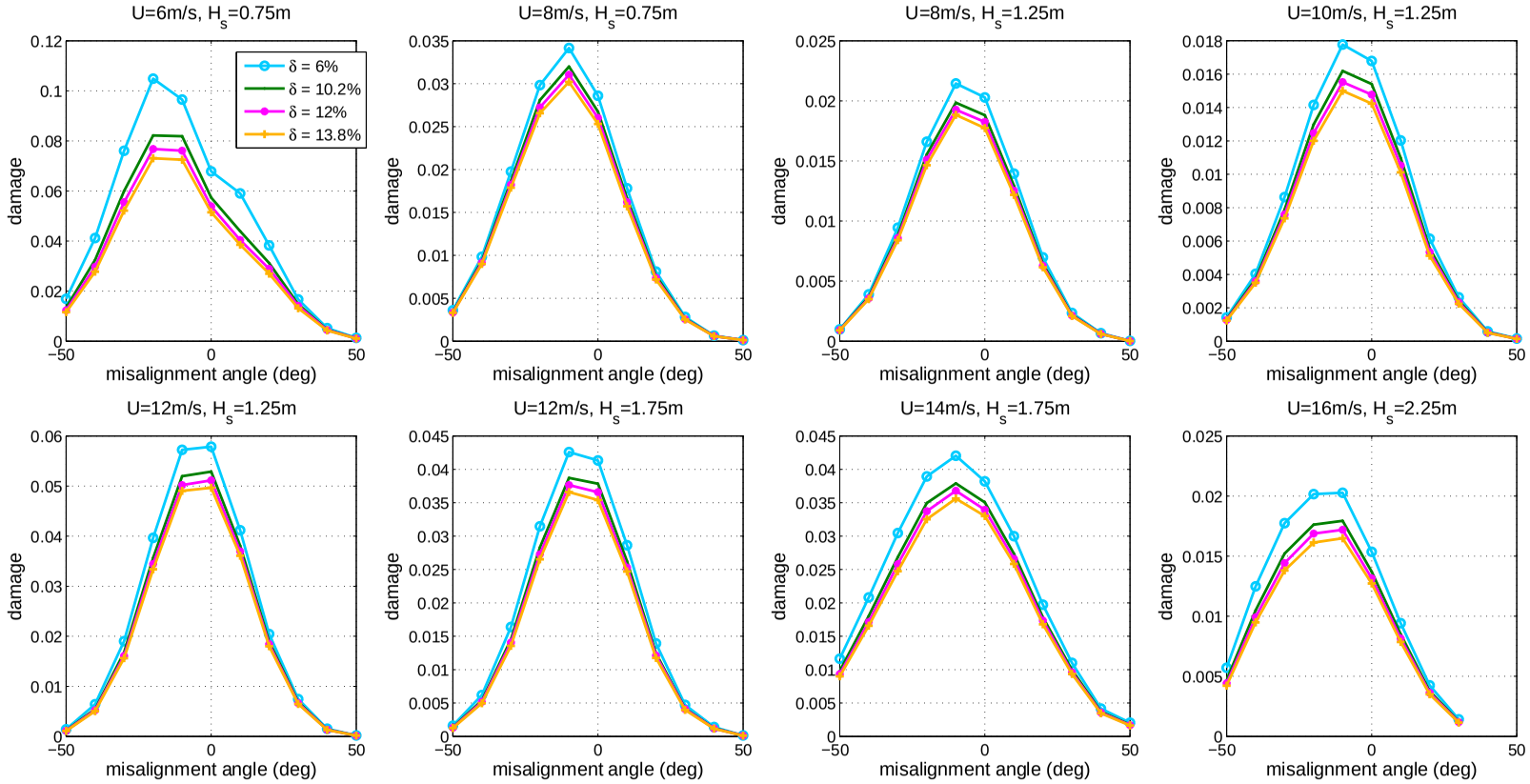

Figure 12.7: Simulated relative damage as a function of the misalignment angles. Results for four different additional offshore damping values (simulations) are presented, normalized with the damage of the reference model at 0^o.

U_{mean} (m/s)	U_{max} (m/s)	TI
28.4	48.2	0.30
29.5	46.4	0.30
27.0	45.8	0.29
28.6	45.5	0.28
26.2	44.8	0.30
29.4	44.4	0.30
28.0	44.2	0.30
27.0	42.7	0.30
24.9	42.5	0.28
26.0	42.4	0.30

Table 12.1: Highest wind speeds observed and respective turbulence intensity.

12.2 Storm

The load response of the structure during a storm and in the case of yaw error is examined in this section. Wind and wave measurements during storms are identified and the highest observed values are compared with the mean wind speed and significant wave height with the 1-year and 50-year return period suggested in the IEC 61400-3 standards [13].

12.2.1 Wind and Wave Measurements

Throughout the two years of the measurement campaign the highest observed wind speeds have been identified. Table 12.1 presents the 10min mean and the maximum values of the 10 highest wind speed measured time series with the respective turbulence intensity. Figure 12.8 portrays the time series of the instantaneous maximum observed wind. The recommended turbulence intensity in the design load cases DLC 6.1-6.3 [17] that correspond to the different storm cases, is $TI = 0.11$. Based on the measurements, the turbulence intensity during storms is almost three times higher than the proposed one. The effect of the rotor can be neglected due to the very slow rotation (idling). However, the nacelle cup-anemometer is usually calibrated for normal operation and not for extreme wind cases. Therefore, further investigation is required to explain this difference. The mean wind speed with 1-year and 50-years return period, implemented in DLC 6.3a and 6.1a (Sections 13.1.1.9, 13.1.1.7) is $U = 38m/s$ and $U = 47.5m/s$ respectively, while the highest observed mean wind speed is almost $30m/s$.

A filtering of the wind speed measurements was necessary for the identification of erroneously high values. Figure 12.9 presents a wind speed time series with a spike due to an electrical error in the instrumentation. Three consecutive time steps running through all the time series are used for the identification of outliers. Cases where the middle point is higher than the average of the other two plus three times the standard deviation of the time series are considered as invalid and excluded from the analysis.

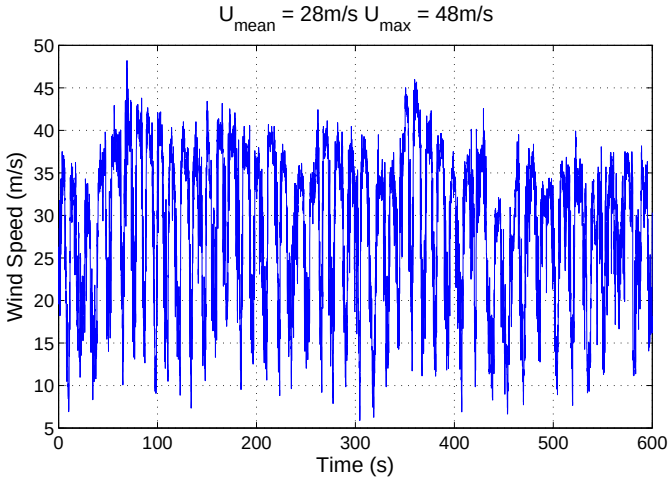

Figure 12.8: Time series of maximum observed wind. $U_{max} = 48m/s$

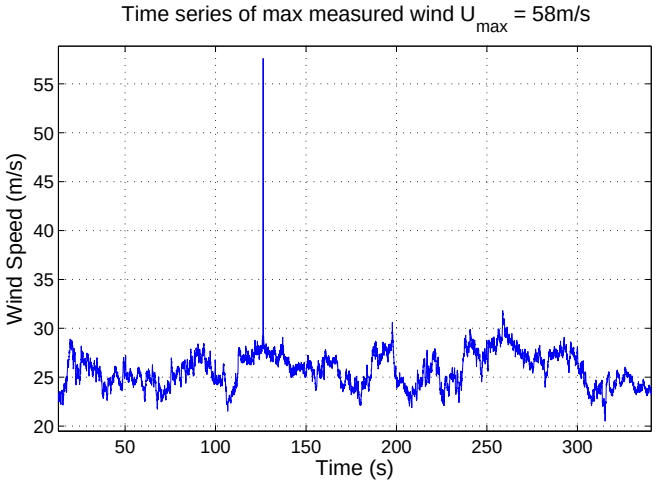

Figure 12.9: Erroneous wind speed measurement time series.

The highest measured surface elevation, during a storm on the site in October 2013, was $H_{max} = 6.4m$ with a significant wave height of $H_s = 3m$. Due to equipment loss, the time series of this measurement are not available. The highest sea surface elevation from the first measurement period (April 2012-October 2012) is $H_{max} = 4.1m$ and it is presented in Figure 12.10a. The significant wave height of this time series is $H_s = 2.8m$. A wave crest as depicted in Figure 12.10b is highly non linear and cannot be reproduced by the irregular linear Airy theory implemented in the simulations. Therefore, for a more detailed analysis of the hydrodynamic loads, a non linear wave model is imperative. Based on the statistical extrapolation of the metocean parameters described in Annex G of the IEC 61400-3 [13], the extreme significant wave height with 1-year and 50-years return period, used in the simulations of the storm cases, is $H_s = 5.74m$ and $H_s = 9.07m$ respectively.

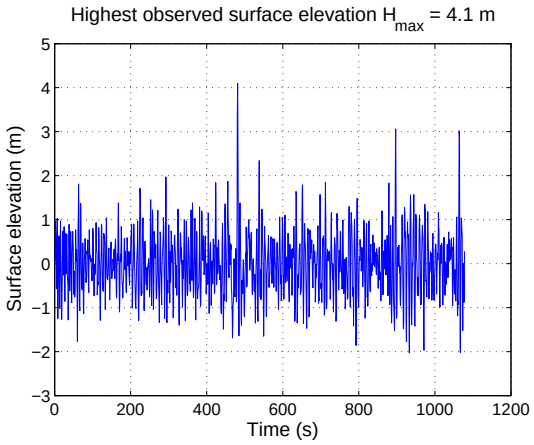

(a) Maximum measured sea surface elevation $H_{max} = 4.1m$. The significant wave height is $H_s = 2.8m$.

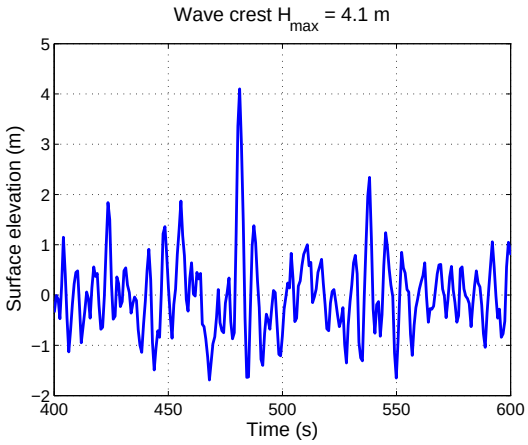

(b) Non linear wave surface elevation.

Figure 12.10: Time series of maximum measured wave surface elevation.

12.2.2 Storm Loads

A yaw error known as a misalignment between the wind direction and the rotor axis introduces a wind component perpendicular to the rotor disk axis. As described in reference [173] this perpendicular component results in an increase of the tangential wind speed at the advancing blade and a decrease of it at the following blade. This difference in the aerodynamic forces on the blades induce excessive vibrations. The effect of the yaw error in the power production has been examined in reference [174].

During the period of the gear box failure, the wind turbine was locked in a specific yaw position. Examining the SCADA data from the surrounding wind turbines, cases of yaw error can be identified. Figures 12.11 and 12.12 present the normalized in-plane blade root and side-side tower bottom bending moments respectively, for various yaw angle errors. In all three cases the wind turbine is idling (pitch angle $\theta = 82^o$) and the mean wind speed is $U = 27m/s$. It can be observed that the amplitude of the in-plane blade root vibrations is increasing with the yaw error. The mean and the extreme of the side-side bending moment at the tower bottom are also increasing with higher yaw error.

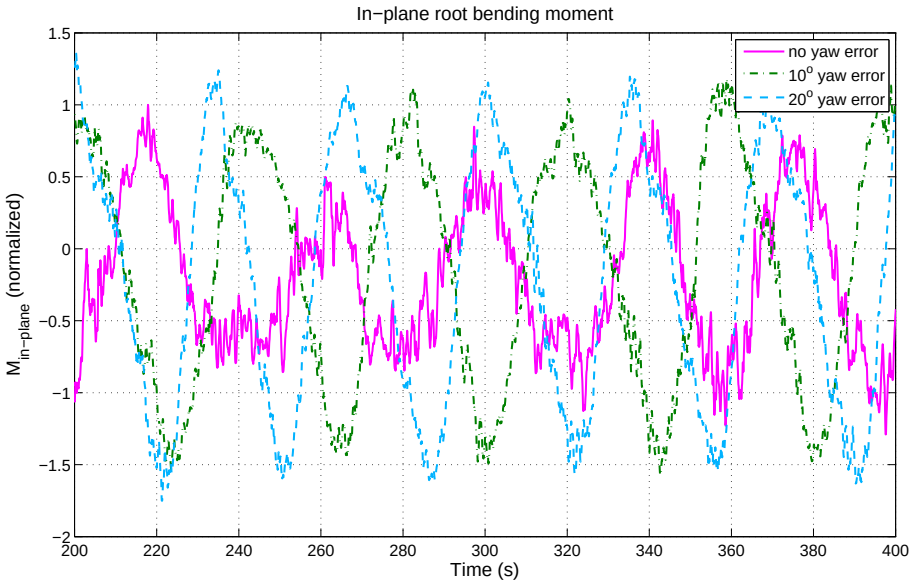

Figure 12.11: In-plane blade root bending moment when the wind turbine is idling ($\theta = 82^o$, $U = 27m/s$). No yaw error (solid pink line), 10^o yaw error (dashed-dotted green line), 20^o yaw error (dashed line). Values normalized with the maximum in-plane moment for the no yaw error case.

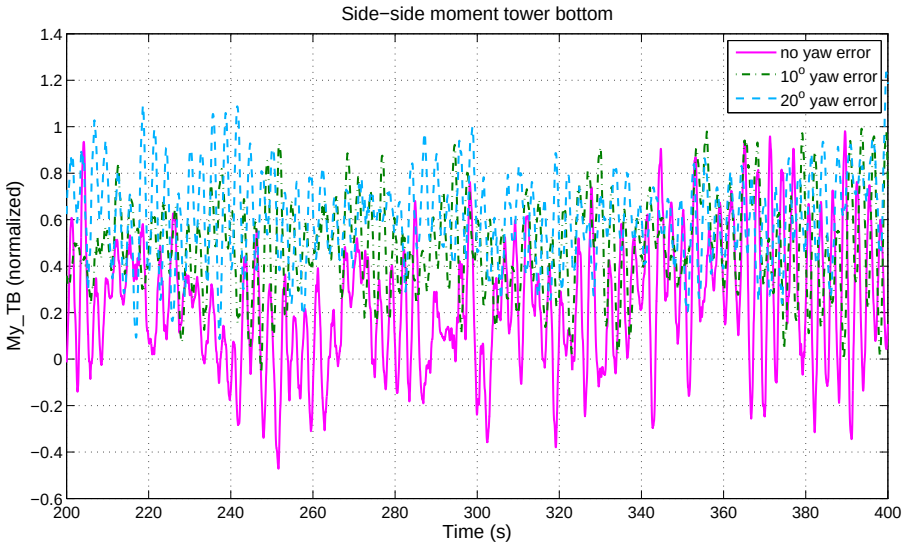

Figure 12.12: Side-side bending moment at the tower bottom when the wind turbine is idling ($\theta = 82^o$, $U = 27m/s$). No yaw error (solid pink line), 10^o yaw error (dashed-dotted green line), 20^o yaw error (dashed line). Values normalized with the maximum side-side bending moment for the no yaw error case.

Chapter 13

Sub-structure/Foundation Design

For the design of an offshore wind turbine's sub-structure/foundation able to withstand various loads, different load cases have to be examined during the design process. In this chapter a preliminary design of the sub-structure/foundation is examined, by implementing in the model the higher additional offshore damping value estimated by the boat incident. Cost savings on the sub-structure due to material reduction are discussed. Since no sensitivity function between the structure's dimensions and the loading is known, the trial and error approach is used, by applying small variations to the initial design. In the way the concept of material saving due to increased damping is proven. For a more detailed design a structural optimization technique should be implemented, but it is outside of the scope of the current thesis.

13.1 Limit State design

"Limit State is a condition beyond which a structure no longer satisfies the design requirements" [11]. For the current design of the sub-structure/foundation the partial safety factors methodology is implemented, where the safety level is obtained by inflating the simulated loads with safety factors, to account for the uncertainties in the loads, the materials and the wind-wave representation. The load safety factors are varying for the different safety classes (a safety class is defined by the consequence of a failure in a component or in the whole structure), while the material factors remain the same. In reference [175] a method using partial safety factors for a more accurate estimation of the fatigue during the design process of a wind turbine is presented.

A component will not fail as long as the design load effect S_d does not exceed the design resistance R_d. The design criterion or design inequality is given by Equation 13.1. The design

load effect is the result of the design load F_d obtained by Equation 13.2, where F_k is the characteristic load derived from the simulations and γ is the partial safety factor.

$$S_d \leq R_d \tag{13.1}$$

$$F_d = \gamma F_k \tag{13.2}$$

According to the IEC 61400-1 standards [17] four analysis should be performed to examine the structural integrity of a wind turbine.

- Analysis of ultimate strength.
- Analysis of fatigue failure.
- Stability analysis.
- Critical deflection analysis.

In the current work the first three types are investigated for the design of the sub-structure/foundation (monopile/pilesand). Due to limited information, for this preliminary study the varying pile thickness is assumed to affect only the fatigue and the load capacity of the structure at the welds, while the bolts remain unchanged. For a more detailed design the fatigue of the bolts and other details on the pile should be investigated. The response of an offshore wind turbine model mounted on a monopile foundation is obtained from simulations, based on design load cases prescribed in IEC 61400-3 [13]. The different load cases simulated for the design of the sub-structure/foundation and their conditions are analyzed in the following Section 13.1.1.

13.1.1 Design Load Cases

For a reliable design of the sub-structure/foundation the response from both normal power production and parked conditions should be examined. Different load cases are used for fatigue failure and ultimate strength analysis. For the current design analysis a total of 25000 simulations were performed for all the different sub-structure/foundation configurations. In the case of turbulent wind, 12 turbulence seeds of 600s per mean wind speed are generated. Irregular Airy waves combined with the Wheeler stretching are used for the generation of the wave field. Due to the position of the examined wind turbine in the Walney farm, 80% of the time it stands in the wake. Therefore, for the design of the sub-structure/foundation an effective turbulence intensity I_{eff} is implemented in the simulations, as described in section 7.1.1.2.

13.1.1.1 DLC 1.2

DLC 1.2 is the only case considered for *fatigue analysis*. The loads acting on the system from a normal turbulence model (NTM, turbulence intensity given by Equation A.3a) and a normal sea state (NSS) during power production are analyzed. The joint wind-wave probability distribution as described in Section 5.1.1 and wind-wave misalignment cases are included in the analysis. Wind speeds from 4m/s (U_{in}) to 25m/s (U_{out}) are considered and simulations with 12 turbulence seeds of 600s per mean wind speed and misalignment angle are performed. A yaw error of $\pm 8^o$ is accounted for in the analysis. Due to very low current velocities, the influence of the current was neglected in the fatigue analysis [53].

13.1.1.2 DLC 1.3

The *ultimate loading* from the extreme turbulence model (ETM, turbulence intensity given by Equation A.3b) combined with the normal sea state is examined in DLC 1.3. Wind speeds from U_{in} to U_{out} are considered with $I_{ref} = 0.14$ (wind turbine class B). A single value of significant wave height, defined from the metocean data (Figure 5.2), is assigned to each mean wind speed. A normal current model (NCM) as described in Section 5.1 is included in the analysis, with current velocity at the mean water level $U_0 = 0.5m/s$.

13.1.1.3 DLC 1.4

Steady wind speeds with an extreme coherent gust (ECD) and direction change, combined with normal sea state and a normal current model can be critical events for *ultimate loading* on the structure. The wind speeds examined are U_{rated} and $U_{rated} \pm 2$ and the corresponding significant wave heights are the same as DLC 1.3. The gust has a magnitude of $U_{cg} = 15m/s$, with a rise time of $T = 10s$. The expressions for the wind speed at hub height during T and the direction change θ_g are given in IEC 61400-1 [17].

13.1.1.4 DLC 1.5

Design load case 1.5 is also considered for *ultimate load analysis*, where extreme shear is present in the wind, combined with normal sea state (NSS) and current model (NCM), similar to the previous case. In IEC 61400-1 [17] the transient shear, occurring in a time interval of $T = 12s$ is separated in two components, vertical and horizontal. The expression for the transient shear is given in IEC 61400-1 [17].

13.1.1.5 DLC 1.6a-b

The *ultimate loading* resulting from normal turbulence model and severe sea state conditions (SSS) or severe wave height (SWH) with 50-years return period, is studied in DLC 1.6. All the wind speeds from 4m/s (U_{in}) to 25m/s (U_{out}) are considered and a normal current model is added in the simulations. Wind and waves are co-directional.

DLC 1.6a. The significant wave height of the SSS is estimated from the distribution of the H_s conditional to the mean wind speed by extrapolation of site measurements using the Inverse First Order Reliability Method (IFORM) [13]. The wind speed is separated in bins of 1m/s and a normal distribution is fitted to the corresponding significant wave heights [13]. The joint wind-wave distribution is represented through two uncorrelated standard normally distributed variables with the use of the Rosenblatt transformation (Equation 13.3), where U_1, U_2 are the two uncorrelated variables, Φ is the standard normal cumulative distribution function, F_U is the marginal CDF of the wind speed and F_{H_s} is the CDF of the significant wave height conditional to the mean wind speed.

$$\begin{aligned} U &= F_U^{-1}\left[\Phi(U_1)\right] \\ H_s &= F_{H_s}^{-1}\left[\Phi(U_2)|V\right] \end{aligned} \tag{13.3}$$

The significant wave height for the severe sea state is estimated by specifying a target probability (50-years return period in the current case) from the equation $U_1^2 + U_2^2 = \beta^2$. β is the target probability and is given by $\Phi(\beta) = 1 - 1/N$, where N is the number of independent sea states in 50 years, which for a 3-hour sea state results in $\beta = 4.35$. $H_{s,SSS}$ is then given by Equation 13.4, where μ and σ are the mean and standard deviation of H_s conditional to U. For higher wind speeds, where the amount of measurements are fewer and the fitting of a distribution cannot be examined, the unconditional extreme significant wave height $H_{s,50}$ is used as a conservative value for the $H_{s,SSS}$ [13].

$$H_{s,SSS} = \mu_{H_s}(U) + \beta\sigma_{H_s}(U) \tag{13.4}$$

DLC 1.6b. The severe wave height is an extreme wave height in the SSS, represented as a deterministic design wave with the use of the stream function. Assuming a Rayleigh distribution of the $H_{s,SSS}$ (an assumption that holds for narrow banded sea elevation, as was shown in Section 5.1 that is the case in this site), the H_{SWH} conditional to the wind speed is given by Equation 13.5.

$$H_{SWH}(U) \approx 1.86 H_{s,SSS}(U) \tag{13.5}$$

The wave peak period T_p is calculated by the expression $T_p = 3.96\sqrt{H_s}$ and is within the

range given by Equation 13.6, where g is the acceleration due to gravity.

$$11.1\sqrt{\frac{H_s}{g}} \leq T_p \leq 14.3\sqrt{\frac{H_s}{g}} \tag{13.6}$$

13.1.1.6 DLC 2.3

The event of an extreme operating gust (EOG) along with a fault in the electrical system is examined in DLC 2.3 as an abnormal case for *ultimate strength analysis*. The wind speeds examined are U_{rated}, $U_{rated} \pm 2m/s$ and U_{out}. The wind conditions are combined with normal sea states (NSS), with an expected significant wave height per mean wind speed as described in Section 13.1.1.2 and a normal current model. The wind speed is steady and the magnitude of the gust is given in IEC 61400-1 [17]. The fault at the electrical system is occurring at the time that the gust reaches the maximum magnitude.

13.1.1.7 DLC 6.1a-b-c

In the following three design cases the loading on the structure in parked conditions (idling) is examined for an *ultimate strength analysis*. DLC 6.1 is analyzing the response during idling with extreme wind and wave models. The wind-wave misalignment is investigated in all cases.

DLC 6.1a. An extreme wind model (EWM) with turbulent field is combined with an extreme sea state (ESS) with a recurrence period of 50 years. The wind speed at hub height is given by $U_{hub} = k_1 U_{ref} = 0.95 \cdot 50 = 47.5m/s$ for a class I wind turbine (average wind speed on the site is almost 10m/s, so $U_{ref} = 5 \cdot U_{ave}$). The turbulence intensity is equal to 0.11 and a yaw error of $\pm 8^o$ is considered. The extreme significant wave height H_{s50} with a 50-year return period is estimated through extrapolation of site specific measurements. A Gumbel distribution is fitted to the measured data as presented in Figure 13.1. The fitting of the Gumbel distribution to the data is examined both graphically from the histogram and by comparison of the mean and standard deviation of the sample with the estimated values from the distribution.

The target probability for the 50-year return period P_f is given by Equation 13.7, where t is the time duration of each measurement (30min in the case of the wave buoy) and R the return period (50 years). When the cumulative probability $f(x)$ is transformed to $-ln(-ln(F(x)))$, the distribution appears to be linear. The H_{s50} is then calculated from the intersection of the distribution with the target probability through Equation 13.8, where P_w is the probability of the maximum observed significant wave height and σ_e and μ_e the scale and location parameters of the Gumbel distribution respectively. The significant wave height of the extreme sea state is then given by $H_s = k_2 H_{s50} = 1.09 \cdot 8.32 = 9.07m$, with a peak period $T_p = 11.92s$. An extreme current model (ECM) is also included in the simulations. The current velocity at the mean water level with 50-years return period is estimated through extrapolation of the

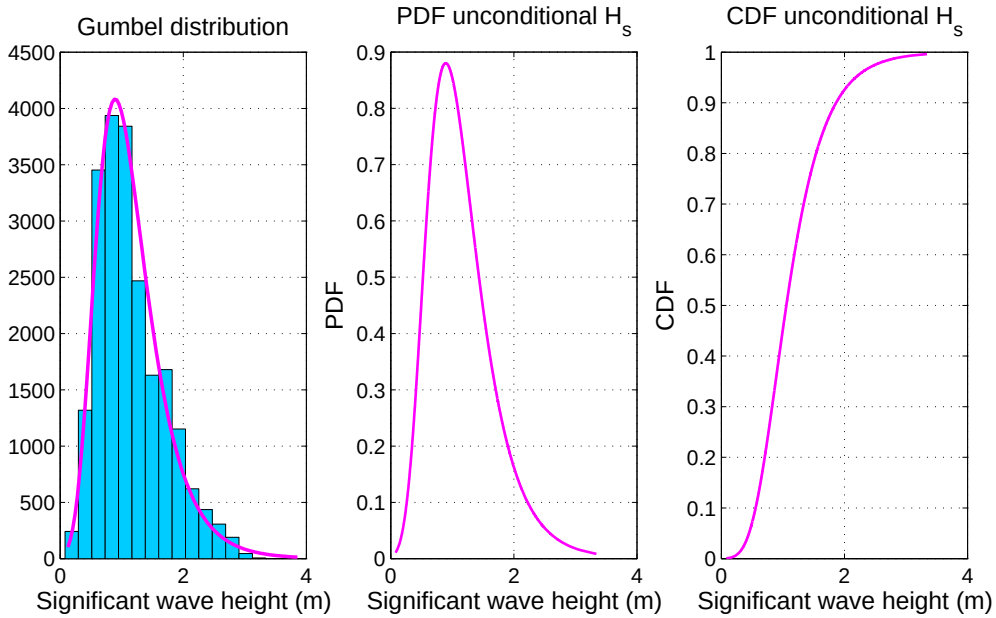

Figure 13.1: a) Histogram of significant wave height along with the fitted Gumbel distribution. b) Probability Density Function of H_s. c) Cumulative Density Function of H_s.

measured data, in the same manner as for the significant wave height. The calculated velocity is $U_0 = 1.3m/s$.

$$P_f = 1 - exp\left(\frac{-t}{R}\right) \tag{13.7}$$

$$H_{s50} = -\sigma_e ln(-ln(1 - P_f/P_w)) + \mu_e \tag{13.8}$$

DLC 6.1b. A steady wind speed with a magnitude of $U_{e50} = 1.4U_{ref} = 70m/s$ at hub height, combined with a deterministic wave with reduced wave height (RWH) $H_{red50} = 1.3H_{s50} = 10.82m$ and 50-years return period is examined in DLC 6.1b. The peak period is equal to $T_p = 3.96\sqrt{H_{red50}} = 13.02s$, respecting the range given by Equation 13.6. A yaw error of $\pm 15^o$ is considered in the analysis.

DLC 6.1c. The steady reduced wind model (RWM) with a wind speed of $V_{red50} = 1.1V_{ref} = 55m/s$ at hub height is taken together with the deterministic wave with extreme wave height (EWH) $H_{50} = 1.86H_{s50} = 15.47m$ and recurrence period of 50 years. A yaw error of $\pm 15^o$ is accounted for in the simulations. Due to the site's actual depth of 26m, the calculated significant wave height leads to breaking waves, the examination of which is outside of the scope of the current work.

13.1.1.8 DLC 6.2a-b

In the following two load cases a loss of electrical power is occurring simultaneously with the storm (stand-still). The extreme wind and wave conditions are the same as the ones described in DLC 6.1a and 6.1b. The effect of a yaw error from $0 - 180^o$ is investigated. The loss of the grid is applied through the implementation of a brake to the low speed shaft. Based on the downscaled values from the 5MW reference wind turbine [68] the time to full braking is 0.51s and the maximum deployed torque to the low speed shaft is 2044kNm.

13.1.1.9 DLC 6.3a-b

The extreme weather conditions with 1-year return period are examined in DLC 6.3 for *ultimate strength analysis*.

DLC 6.3a. The extreme wind model (EWM) with mean wind speed at hub height equal to $U_{hub} = k_1 U_1 = k_1 0.8 U_{ref} = 38m/s$ is combined with the extreme sea state with significant wave height $H_s = k_2 H_{s1} = 1.09 \cdot 5.27 = 5.74m$. The significant wave height H_{s1} is calculated though extrapolation of the measured data, following the same procedure as described in DLC 6.1a with 1 year return period. The peak period is equal to $T_p = 9.5s$. The turbulence intensity is equal to 0.11 and an extreme yaw misalignment of $\pm 20^o$ is assumed.

DLC 6.3b. A steady wind model with wind speed $U_{hub} = U_{e1} = 0.8 \cdot 1.4 U_{ref} = 56m/s$ and deterministic sea state with reduced wave height $H_{red1} = 1.3 H_{s1} = 6.86m$ and period $T = 10.37s$ is examined in DLC 6.3b. An extreme yaw misalignment of $\pm 30^o$ is considered in the simulations.

13.1.2 Ultimate Limit State (ULS)

"The Ultimate Limit State (ULS) is associated with the maximum load-carrying resistance" [11]. Equation 13.9 should be satisfied for structural reliability during extreme operating loads. f_k is a characteristic value of the material property associated with the material resistance. For a normal design situation the load partial safety factor is $\gamma_f = 1.35$ and for an abnormal $\gamma_f = 1.1$. The general partial safety factor for materials γ_m takes values higher or equal to 1.1 and the safety factor for consequences of failure γ_n depends on the safety class of the examined component varying from 0.9 to 1.3.

$$\gamma_f F_k \leq \frac{1}{\gamma_m \gamma_n} f_k \tag{13.9}$$

The stress on each section can be calculated from the characteristic load F_k obtained from the simulations of the design load cases. The axial, circumferential and shear stresses (σ_χ , σ_θ and τ respectively, Equation 13.10) are combined to obtain the maximum stress on each cross

section. The circumferential stress $\sigma_{\theta,water}$ on the monopile is approximated as the pressure introduced from the difference in the water loads. The uniform circumferential stress on the pile because of the soil $\sigma_{\theta,soil}$ is given by the active soil pressure, where $K_a = tan^2(45^o + \phi/2)$, ϕ is the friction angle, s_u is the undrained shear strength of the soil and γ' is the submerged unit weight. The pile deflection induces a non uniform stress distribution around the section as described in Section 13.1.3.3, which is not represented by the active soil pressure. A more detailed design of the structure would require an accurate 3D modeling of the soil, but such a model is outside of the scope of the present work. F_x, F_y, F_z, M_x, M_y and M_z are the forces and moments on each section as defined in Figure 13.2, A is the cross section area ($A = \pi/4\left(D_{out}^2 - D_{in}^2\right)$), I the moment of inertia of the monopile section, t_{th} the wall thickness, $A_o = \pi R_{mid}^2$, Q the static moment of area obtained from Equation 13.11 and x, y the distance of each point from the pile axis where the stress is evaluated. The sections in consideration are thin walled circular tubes and the stress is assumed to be constant through the thickness and thus only evaluated at the middle of the cross section. Therefore the third Cauchy stress component is equal to zero. Applying the von Mises yield criterion (Equation 13.12) the maximum stress σ_v , also called von Mises stress is compared with the yield limit of the material f_y. The stresses are evaluated every $\phi_s = 5^o$ at each time step and the maximum of each section is obtained. The von Mises stress for each design load case has to be less than f_y to ensure deformation in the elastic regime and the validity of the superposition of the cycles for the fatigue analysis.

$$\begin{aligned}
\sigma_\chi &= \frac{F_z}{A} + \frac{M_x}{I} R_{mid} \cdot cos\phi_s + \frac{M_y}{I} R_{mid} \cdot sin\phi_s \\
\sigma_{\theta,water} &= \frac{\rho \cdot g \cdot z \cdot R_{mid}}{t_{th}} \qquad \sigma_{\theta,soil} = \frac{(K_a \cdot \gamma' \cdot z - 2\sqrt{K_a} \cdot s_u) R_{mid}}{t_{th}} \\
\tau &= \frac{M_z}{t_{th} 2A_o} + \frac{F_x Q}{I \cdot t_{th}} + \frac{F_y Q}{I \cdot t_{th}}
\end{aligned} \tag{13.10}$$

$$Q = \int y \mathrm{d}A = 2R_{mid} \cdot sin\phi_s \tag{13.11}$$

$$\sigma_v = \sqrt{\sigma_\chi^2 + \sigma_\theta^2 + (\sigma_\chi - \sigma_\theta)^2 + 3\tau^2} \leq f_y \tag{13.12}$$

The shear stress caused by the tapering of the pile τ_{taper} can be neglected due to the low coning angle. τ_{taper} is given by Equation 13.13, where $\beta_{taper} = 5^o$ is the coning angle [176]. The tapering shear stress is 8.8% of the normal stress.

$$\tau_{taper} = -\sigma_\chi \cdot tan(\beta_{taper}) \xrightarrow{\beta_{taper} = 5^o} \tau_{taper} = -0.088 \cdot \sigma_\chi \tag{13.13}$$

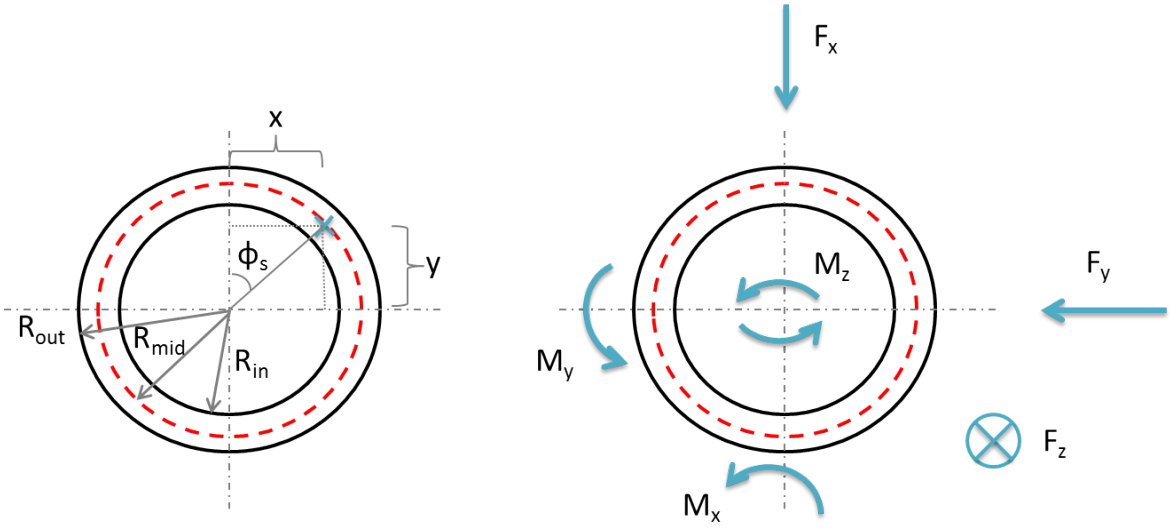

Figure 13.2: Definition of forces and moments on a cross section used for the calculation of the normal and shear stress. F_x is the force in the side-side direction, F_y the force in the fore-aft direction, F_z the axial force along the pile caused by the turbine weight, M_x the bending moment in the fore-aft direction, M_y the bending moment in the side-side direction and M_z the torsion.

13.1.3 Stability Analysis

"Requirements for the elements of the cross section not fulfilling requirements to cross section type 3 need to be checked for local buckling" [11]. The diameter to thickness ratio D/t_{th} of the pile is calculated and the limits from table 5.2 of the Eurocode 3, part 1-1 [177] are used for the classification of the structure. Buckling of circular cylindrical shells under pure bending is reported in references [178, 179]. In reference [180] buckling design rules for thin walled structures in soil are proposed. Buckling should not occur in any component under the characteristic load [17]. The partial safety factors are the same as specified for the ultimate limit state analysis ($\gamma_f = 1.35$ for normal situation and $\gamma_f = 1.1$ for abnormal, $\gamma_m \geq 1.1$ and $0.9 \leq \gamma_n \leq 1.3$).

13.1.3.1 Local Buckling

The ratio in all sections of the examined sub-structure/foundation is above the limit $D/t_{th} > 90\epsilon^2$ (table 5.2 of the Eurocode 3 part 1-1), where $\epsilon = \sqrt{235/f_y}$. Therefore, the structure belongs to class 4 and has to be verified against buckling according to Eurocode 3, part 1-6 [181].

The Eurocode 3 proposes that for the assessment of shell buckling (limit state buckling design) the meridional (axial) σ_χ, the shear τ and the circumferential σ_θ buckling stresses should be considered. The calculation of the stresses on the cross section is given by Equation

13.10. The boundary conditions of the different sections can be described as BC 1 (clamped) at both edges, as specified in the Eurocode 3 and therefore all the following expressions are valid for the examined cases.

The buckling resistance necessary for the limit state buckling design is given by Equation 13.14, where $\sigma_{x,Rd}$ is the meridional buckling resistance, $\sigma_{\theta,Rd}$ the circumferential buckling resistance, τ_{Rd} the shear buckling resistance, χ_k, χ_θ and χ_t the buckling reduction factors and f_y the yield limit.

$$\sigma_{\chi,Rd} = \frac{\chi_k \cdot f_y}{\gamma_m}, \quad \sigma_{\theta,Rd} = \frac{\chi_\theta \cdot f_y}{\gamma_m}, \quad \tau_{Rd} = \frac{\chi_t \cdot f_y}{\sqrt{3}\gamma_m} \tag{13.14}$$

The examined pile is characterized as a truncated conical shell (Figure 13.3). An equivalent cylinder can substitute the conical shell for the assessment of the buckling resistance as described in Annex D of the Eurocode 3, Part 1-6 [181].

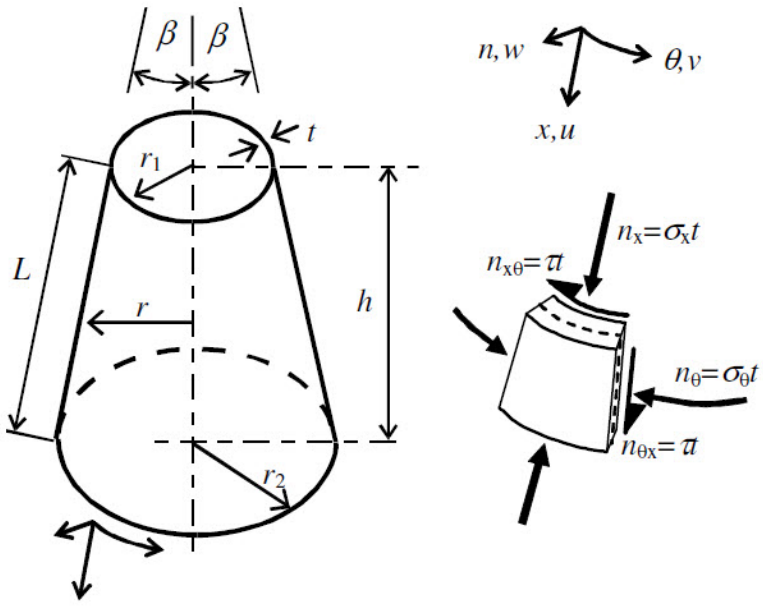

Figure 13.3: Conical shell geometry and stresses. Figure from reference [181].

The equivalent cylinder length for the meridional and the circumferential stress is equal to $l_e = L$. For the shear stress the equivalent length is equal to the height of the cone, but due to the small conical angle $l_e = L$. The equivalent cylinder radius used in the calculation

of the three stresses is given by Equation 13.15.

$$r_{e,\chi} = \frac{r}{cos\beta}, \qquad r_{e,\theta} = \frac{r_1 + r_2}{2cos\beta},$$
$$r_{e,\tau} = \left[1 + \sqrt{\frac{1 + r_2}{2r_1}} - \sqrt{\frac{2r_1}{1 + r_2}}\right] r_1 \cdot cos\beta \tag{13.15}$$

For the calculation of the parameters necessary for the estimation of the buckling stresses, the length of the shell segment needs to be specified from the dimensionless parameter ω_l (Equation 13.16). The expression for the buckling reduction factor χ as a function of the relative slenderness of the shell $\bar{\lambda}$ is given in Annex D of the Eurocode 3, part 1-6 [181].

$$\omega_l = \frac{l_e}{\sqrt{r_e t_{th}}} \tag{13.16}$$

The relative slenderness of the shell for different stress loading is given by Equation 13.17.

$$\bar{\lambda}_\chi = \sqrt{f_y/\sigma_{\chi,Rc}}, \quad \bar{\lambda}_\theta = \sqrt{f_y/\sigma_{\theta,Rc}}, \quad \bar{\lambda}_\tau = \sqrt{f_y/\left(\tau_{Rc}\sqrt{3}\right)} \tag{13.17}$$

The critical buckling stresses $\sigma_{\chi,Rc}$, $\sigma_{\theta,Rc}$, and τ_{Rc} are given in Annex D of the Eurocode 3 as a function of the dimensionless parameter ω.

The interaction of the maximum of each stress should satisfy Equation 13.18 to ensure buckling strength, where k_χ, k_i, k_θ and k_τ are the buckling interaction parameters specified also in Annex D of the Eurocode 3.

$$\left(\frac{\sigma_\chi}{\sigma_{\chi,Rd}}\right)^{k_\chi} - k_i \left(\frac{\sigma_\chi}{\sigma_{\chi,Rd}}\right)\left(\frac{\sigma_\theta}{\sigma_{\theta,Rd}}\right) + \left(\frac{\sigma_\theta}{\sigma_{\theta,Rd}}\right)^{k_\theta} + \left(\frac{\tau}{\tau_{Rd}}\right)^{k_\tau} \leq 1 \tag{13.18}$$

13.1.3.2 Global Buckling

With the assumption of ideally straight members (no imperfections), the critical axial load for global buckling is calculated. An analytical solution given in reference [182] is used. An equivalent cylinder with the same length as the sub-structure and bending stiffness equal to the average of the stiffness at the monopile top and bottom is considered. The verification of this assumption is performed by estimating the critical axial load of a cylinder and a cone with the same boundary conditions (clamped-free). The difference of the calculated critical load between the two cases is 7%. Therefore, the equivalent cylinder will be used for the calculation of the critical buckling load.

In the examined case the boundary condition at the monopile bottom is not clamped, due to the soil flexibility. A hinge with a rotational stiffness calculated from the solution of the Winkler beam is considered. By applying a moment $M_{applied}$ at the pilesand top and calculating the rotation θ_{rot} of the section, the rotational stiffness is given by $\bar{c_a} = M_{applied}/\theta_{rot}$. The critical buckling N_{cr} load is then calculated by the root of Equation 13.19, where EI is the monopile bending stiffness [182].

$$N_{cr} \cdot tan\left(l\sqrt{\frac{N_{cr}}{EI}}\right) - \bar{c}_a \cdot \sqrt{\frac{N_{cr}}{EI}} = 0 \tag{13.19}$$

13.1.3.3 Soil Pile Interaction

The currently implemented p-y curve in most aero-elastic codes accounts only for local reaction, where the soil is simulated as uncoupled springs. Global effects due to the pile deformation are not taken into consideration. The stiffness of the soil springs is based on the soil properties and it is independent of the pile diameter. Such an assumption might hold for slender piles, but it might be ambiguous for large diameter piles. In reference [183] the effect of the small-strain soil stiffness on the first natural frequency of the structure is discussed. Higher measured natural frequencies than the design values are attributed to the soil-pile interaction model. In the same study a 3D finite element model is applied to estimate the initial soil stiffness at small strains.

Due to the pile deformation, pressure imbalance is created around the structure as shown in Figure 13.4a (difference between passive-active earth pressure). Larger pile deflections might create an opening in the soil-pile interaction, reducing the pressure to 0 on one side (Figure 13.4c). Therefore, radial pressure distribution is no longer uniform, leading to ovalization of the plane (Figure 13.4b). The 3D arching of the soil also changes the in-plane pressure distribution on the pile. The soil-pile interface that is responsible for the shear stress is not taken into account in the p-y model. Its modeling is complex and it depends on the soil type, the roughness of the pile, the depth and the installation method.

The doubtful p-y curve for large diameter piles, the incomplete soil data, the unknown interface properties of the soil-pile connection, the unknown in-plane deformation and the non-linearity of the soil render its modeling complex. Accurate estimation of the soil-pile interaction will require a detailed 3D finite element model of the soil, which is outside of the scope of the present study. Therefore, for the sake of simplicity the p-y curve will be used in the analysis. Any assumptions for the soil properties necessary for the design of the foundation is a rough estimation and they are used only for this preliminary design of the structure.

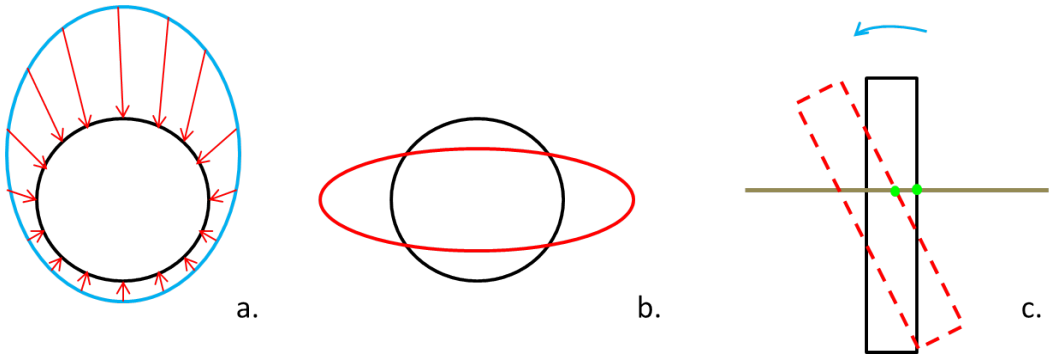

Figure 13.4: a) In-plane pressure imbalance around the pilesand section because of pile deflection. b) Ovalization of the plane due to non-uniform radial pressure distribution. c) Opening in the soil-pile interaction because of large pile deflections.

13.1.4 Fatigue Limit State (FLS)

"The Fatigue Limit State is related to failure due to cumulative damage effect of cyclic loading" [11]. A component is expected to fail when the accumulated damage exceeds 1. The expected damage is given by Equation 13.20. n_{jk} is the expected number of lifetime cycles for the j^{th} wind speed and k^{th} load range (Equation 13.21) and $N(\gamma, S_k)$ is the number of cycles that lead to failure for a specific load range. γ is the product of all three partial safety factors ($\gamma = \gamma_f \gamma_m \gamma_n$). The partial safety factor γ_f can be equal to 1 for both normal and abnormal situations. For materials like steel γ_m can be taken as 1.1, when the survival probability is 97.7%. The safety factor for consequences of failure γ_n varies from 1 to 1.3. The load spectrum F_{ST} is obtained from the histogram of load range-cycles (S-N) by Rainflow counting the time series. P_j is the fraction of time the wind speed is in bin j.

$$E(D) = \sum_{j,k} \frac{n_{jk}}{N(\gamma, S_k)} \leq 1 \tag{13.20}$$

$$n_{jk} = \left(\frac{Lifetime}{T}\right) P_j \left(N_j F_{ST}(S_k | V_j, T)\right) \tag{13.21}$$

A bi-linear S-N curve for piles in seawater given in the DNV guidelines [172] is chosen, to perform a fatigue analysis to the sub-structure/foundation with 25 years target lifetime for the estimation of the equivalent load S_{Leq} as described in Appendix B. The reference number of cycles is $N_{ref} = 10^6$, which corresponds to the number of cycles for 25 years. The welding of the different sections is considered as the most critical detail for the fatigue analysis. From the DNV guidelines [172] the S-N curve **D** (table A-9 Hollow Sections) in seawater is chosen as the one describing better the structure under consideration (Figure 13.5). In every cross section the stress is calculated from Equation 13.10a every 5^o and the exact position of the maximum stress is identified.

The number of cycles from the S-N curve that corresponds to the equivalent accumulated

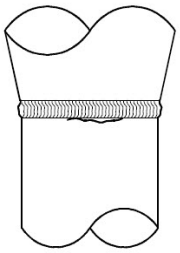

Figure 13.5: Detail describing the welding on the monopile. S-N curve D: "Circumferential butt welds between tubular and conical sections, weld made from both sides" [172].

load for the different examined cases is compared with N_{ref} to assess the lifetime of the structure.

13.2 Structural Analysis of the Sub-structure/ Foundation Design

In the following sections the results of the fatigue, ultimate and stability analysis of the sub-structure/foundation are presented. The partial safety factors described previously are applied to the obtained loads from the simulations. Firstly, the baseline design is tested against fatigue and extreme loads and then the effect of the measured environmental conditions on the lifetime of the structure is examined. The higher estimated additional offshore damping from the boat incident is implemented in the model and the wall thickness of the structure is decreased. The welds connecting the different sections are assumed to be the critical points. For a more detailed analysis other details on the structure like the bolts, as well as load cases accounting for transportation and installation should be examined.

13.2.1 Baseline Design

The baseline design is defined as the sub-structure/foundation design using the external conditions as specified in the IEC 61400-3 [13] and the commonly used damping of $\delta = 6\%$. The design, the wind and the metocean conditions were provided by DONG Energy from measurements on the site during the planning phase.

Figures 13.6 and 13.7 present the maximum von Mises stress for each design load case at the different sections along the sub-structure and the foundation. The solid blue line corresponds to the yield limit of the material. The stresses and the yield limit are normalized with the maximum at each section. During normal operation the design case resulting in the highest stress for all the sections is DLC 1.3, as it was anticipated due to the extreme turbulence model implemented in this case. The highest extreme load is for DLC 6.1b, where a steady

wind with magnitude 70m/s is applied. For all the load cases the von Mises stress is well below the yield limit. The design of the sub-structure/foundation is therefore not driven by the ultimate loads.

Figure 13.8 depicts the stresses along the monopile and the pilesand for DLC 1.3, normalized with the maximum stress of each component. Even though the highest moment on the sub-structure is observed at the bottom, due to the over-dimensionalization of this section the largest von Mises stress is detected a few meters below the monopile top. On the pilesand the stresses follow the moment distribution, with the maximum stress at 5m below the seabed.

Figure 13.9 presents the extreme axial simulated loads $F_{z,max}$ for every design load case at the monopile bottom, normalized with the maximum simulated load. The solid line represents the critical axial load from the analytical solution of Equation 13.19 that causes global buckling on the system. The extreme axial loads are below the critical value for all the cases.

The stresses contributing to the local buckling are combined through Equation 13.18 to verify the buckling strength of the monopile and the pilesand. Figures 13.10 and 13.11 present the interaction of the meridional, the circumferential and the shear stress at the different sections of the sub-structure/foundation. For every design load case the combination of the stresses is below 1, therefore the buckling strength verification is fulfilled.

The monopile/pilesand was designed for 25 years lifetime. The chosen S-N curve from the DNV guidelines for piles in seawater [172] based on the welding detail is D and the $N_{ref} = 10^6$ (Figure 13.12), which corresponds to the total number of cycles during the wind turbine lifetime. The highest accumulated fatigue of the baseline structure is $S_{eq} = 83MPa$ and appears 5m below the seabed.

The design of the sub-structure/foundation seems to be driven by the fatigue of the structure rather than the ultimate loading or the stability. Therefore in the following two sections that the dimensions of the structure remain unchanged, only the fatigue will be examined.

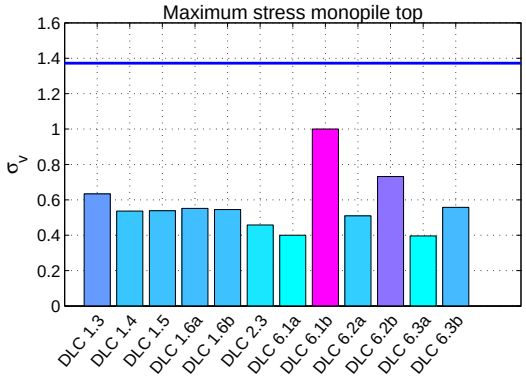

(a) Ultimate stress at monopile top.

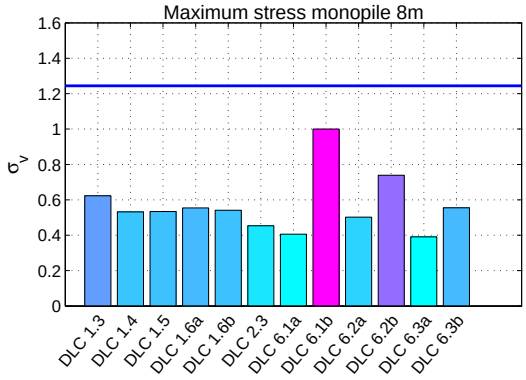

(b) Ultimate stress at 8m below the monopile top.

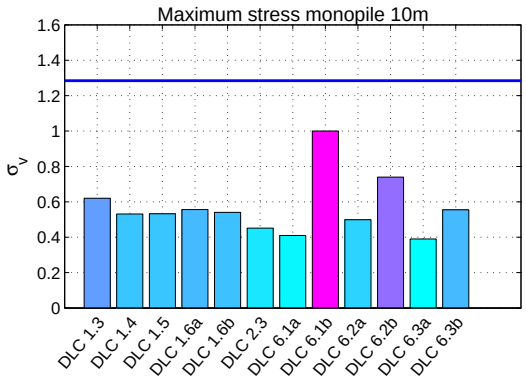

(c) Ultimate stress at 10m below the monopile top.

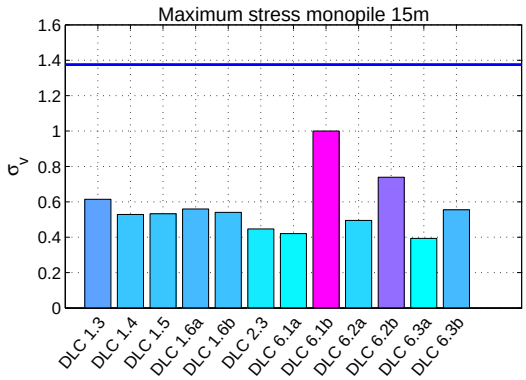

(d) Ultimate stress at 15m below the monopile top.

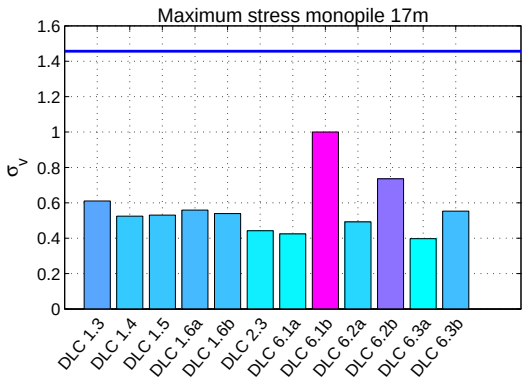

(e) Ultimate stress at 17m below the monopile top.

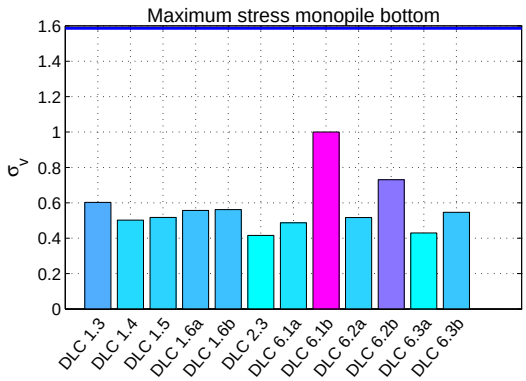

(f) Ultimate stress at monopile bottom.

Figure 13.6: Ultimate stress loads (von Mises stress) on the monopile sections for each design load case. The solid blue line represents the yield limit. All the stresses are normalized with the observed maximum stress on each section.

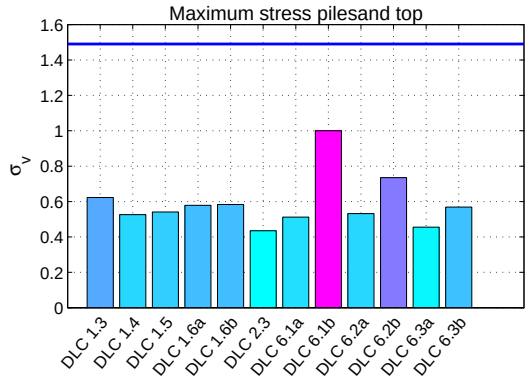

(a) Ultimate stress at pilesand top.

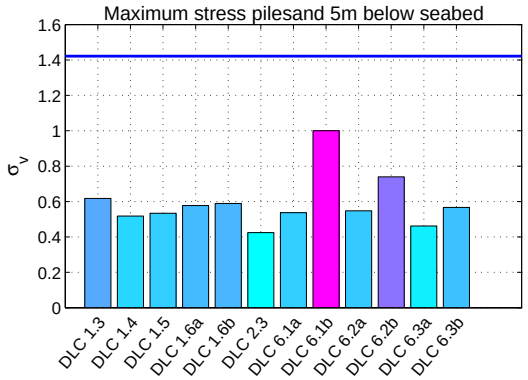

(b) Ultimate stress at 5m below the seabed.

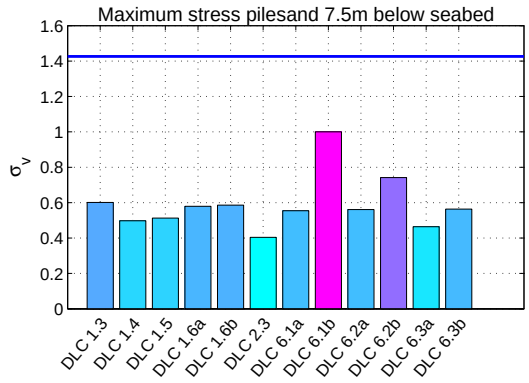

(c) Ultimate stress at 7.5m below the seabed.

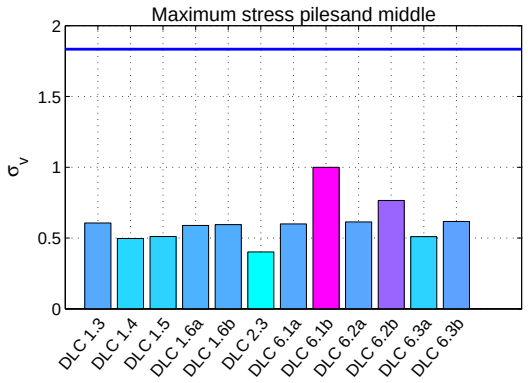

(d) Ultimate stress at 11.5m below the seabed.

Figure 13.7: Ultimate stress loads (von Mises stress) on the pilesand sections for each design load case. The solid blue line represents the yield limit. All the stresses are normalized with the observed maximum stress on each section.

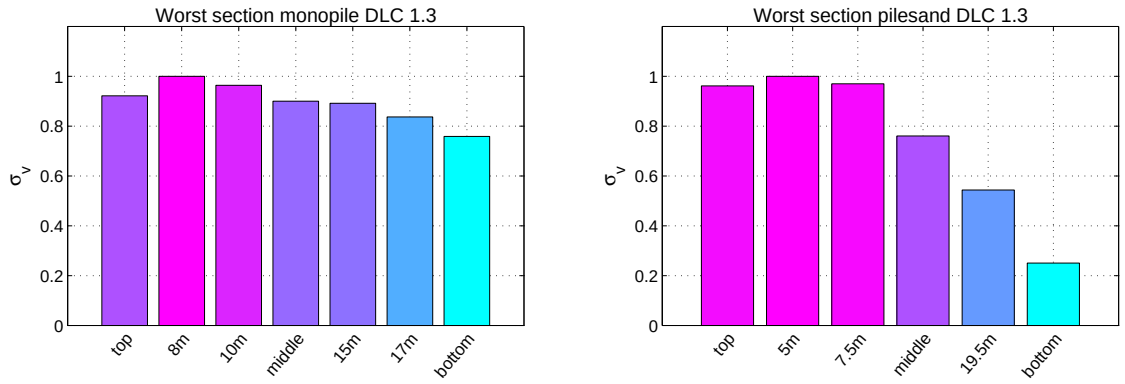

(a) Ultimate stress at different sections along the monopile.

(b) Ultimate stress at different sections along the pilesand.

Figure 13.8: Worst sub-structure/foundation section for DLC 1.3. The stresses are normalized with the maximum stress of each component.

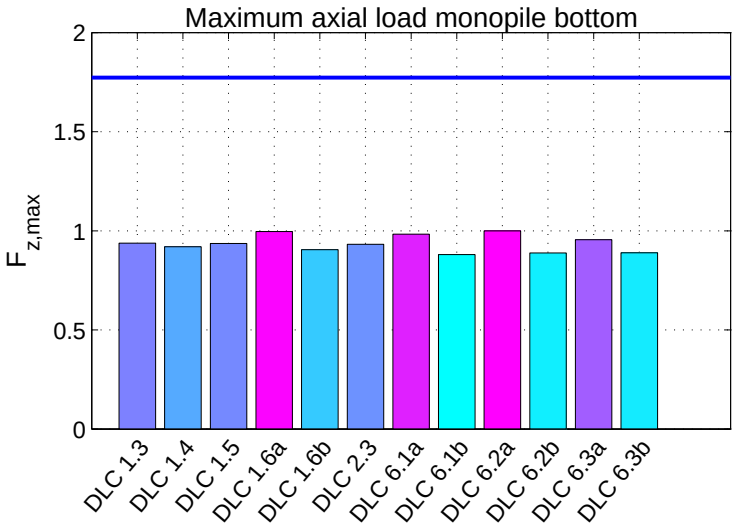

Figure 13.9: Maximum axial load at the monopile bottom for all design load cases, normalized with the maximum simulated load. The solid blue line corresponds to the critical load obtained from Equation 13.19 that leads to global buckling of the sub-structure.

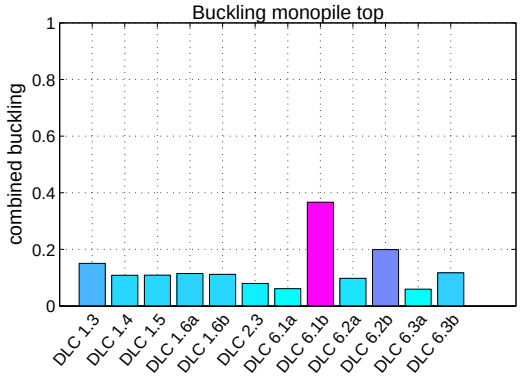

(a) Combined stresses at monopile top.

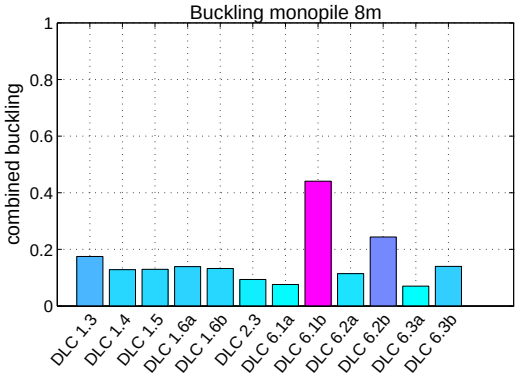

(b) Combined stresses at 8m below the monopile top.

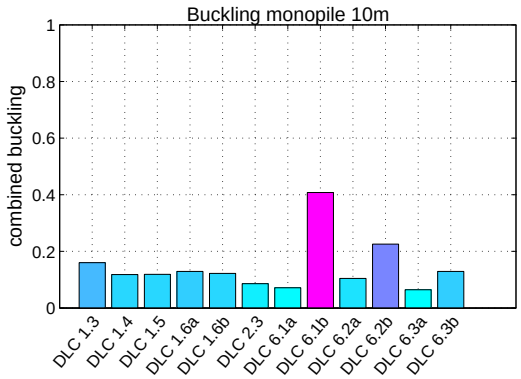

(c) Combined stresses at 10m below the monopile top.

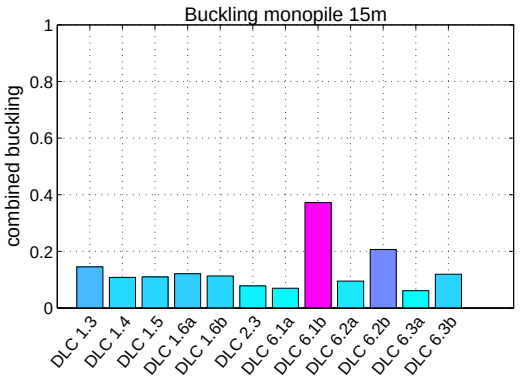

(d) Combined stresses at 15m below the monopile top.

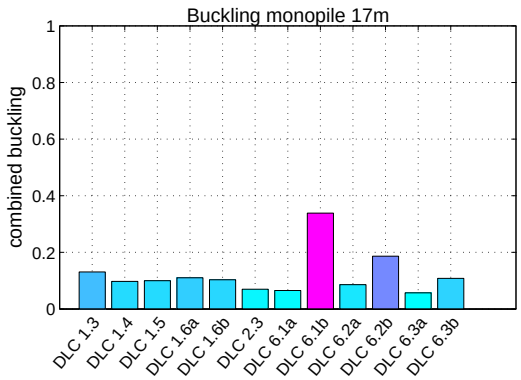

(e) Combined stresses at 17m below the monopile top.

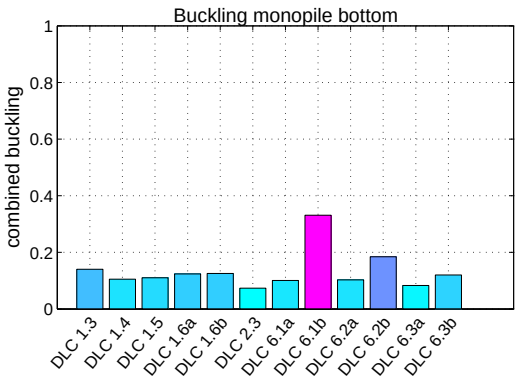

(f) Combined stresses at monopile bottom.

Figure 13.10: Combined meridional, circumferential and shear stress for local buckling strength verification of the sub-structure. In the y axis the result from Equation 13.18 is presented.

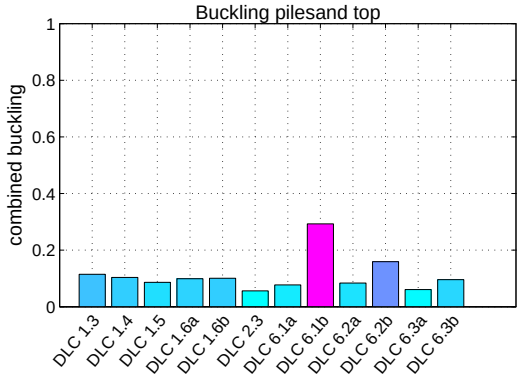

(a) Combined stresses at pilesand top.

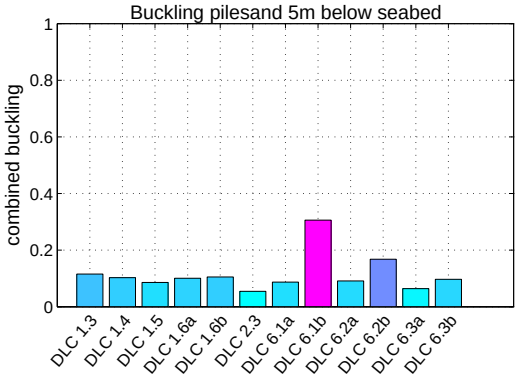

(b) Combined stresses at 5m below the seabed.

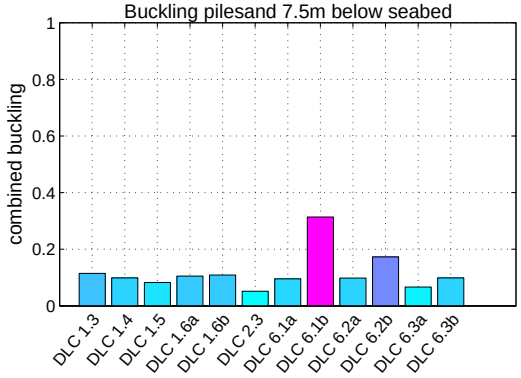

(c) Combined stresses at 7.5m below the seabed.

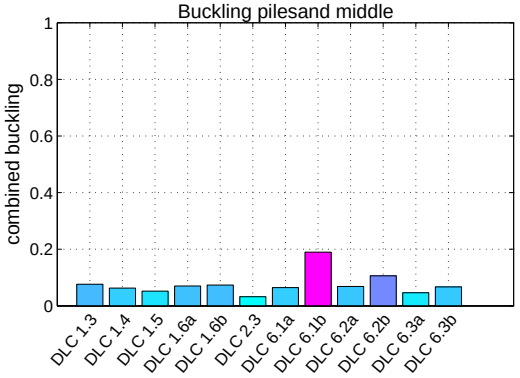

(d) Combined stresses at 11.5m below the seabed.

Figure 13.11: Combined meridional, circumferential and shear stress for local buckling strength verification of the foundation. In the y axis the result from Equation 13.18 is presented.

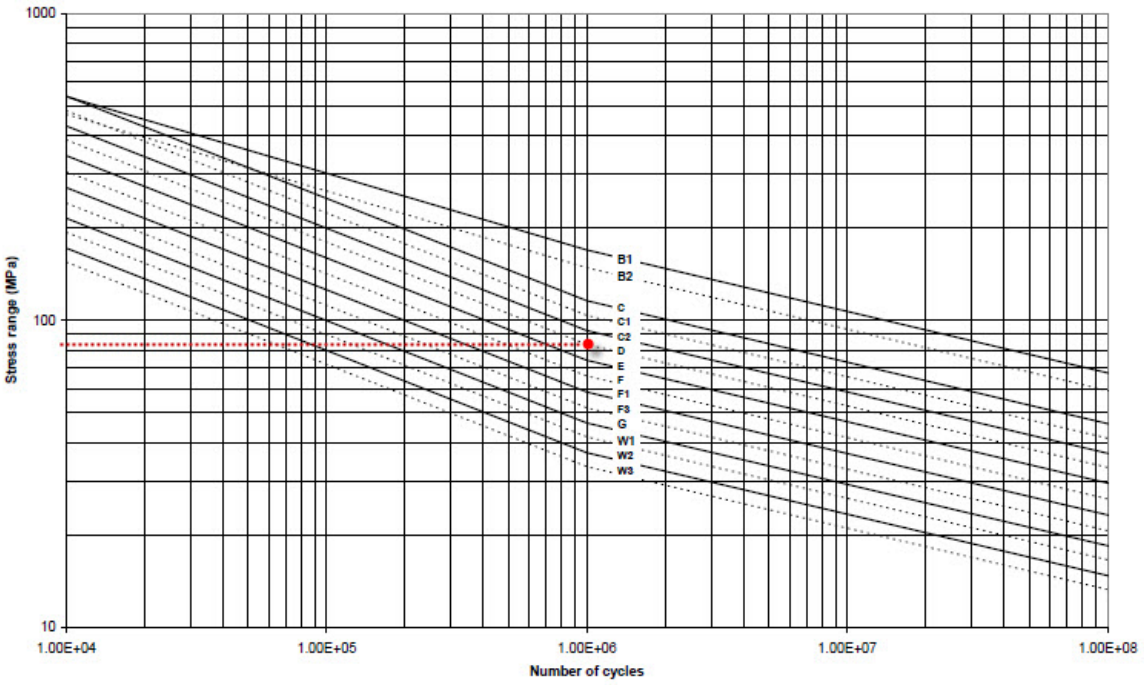

Figure 13.12: S-N curves for structures in seawater. Curve D is chosen for the fatigue analysis of the monopile/pilesand. Figure adapted from reference [172].

13.2.2 Baseline Design-Measured Environmental Conditions

In this section the effect of the measured wind and wave conditions, on the structure's lifetime is examined. A yaw error of $\pm 8^o$ is included in the simulations, to account for changes in the wind direction not captured by the yaw system. Figure 13.13 presents the accumulated fatigue at the most critical section of the monopile and the pilesand, namely 8m below the monopile top and 5m below the seabed respectively. The design of the sub-structure/foundation in both cases (first two bars in the figure) is the same, with only difference the external conditions applied in the simulations. The fatigue of the "baseline design" is obtained from DLC 1.2, where the wind and wave conditions are based on site measurements from the planning phase. The implemented turbulence intensity is the effective turbulence as described in the IEC 61400-1 [17] and presented in Section 7.1.1.2. The accumulated equivalent load of the bar with the caption "measured wind-wave" is also obtained from DLC 1.2 but the long term joint wind-wave probability (Section 5.1.1) and the effective turbulence intensity applied in the simulations are based on the measurements after the installation of the wind farm.

The number of cycles for the accumulated fatigue of the baseline design with the measured environmental conditions, obtained from Figure 13.12 is $N = 2.8 \cdot 10^6$, which corresponds to 2.8 times higher lifetime than the original design. The lower turbulence intensity experienced in the wind farm than the one applied in the design phase (conservative TI from the standards to cover various sites worldwide) and the uncertainty in the long term joint wind-wave probability based on limited measurements might be the reasons for this discrepancy.

13.2.3 Design with Higher Damping

In the simulations of the previous two sections the additional offshore damping implemented in the system is $\delta = 6\%$. In the following two sections the damping of the model is tuned to the measured additional offshore damping from the boat incident $\delta = 12\%$ (Section 11.1) to examine its effect on the accumulated fatigue and the total lifetime of the structure. The baseline design is then modified and the new structure is tested for fatigue, ultimate and stability strength.

13.2.3.1 Baseline Design with Higher Damping

The additional offshore damping of the model is tuned to the estimated damping from the boat incident ($\zeta \simeq 2\%$, $\delta = 12\%$). The wind and wave conditions applied in the simulations are the measured ones. Yaw error of $\pm 8^o$ is included in the analysis. The number of cycles for the equivalent load of this configuration is $N = 3 \cdot 10^6$ (Figure 13.13). The damping seems to play a significant role in the fatigue of the structure. Twice higher additional offshore damping results in 1.1 higher lifetime (comparing the two cases with the same measured environmental conditions "measured wind-wave" and "higher damping").

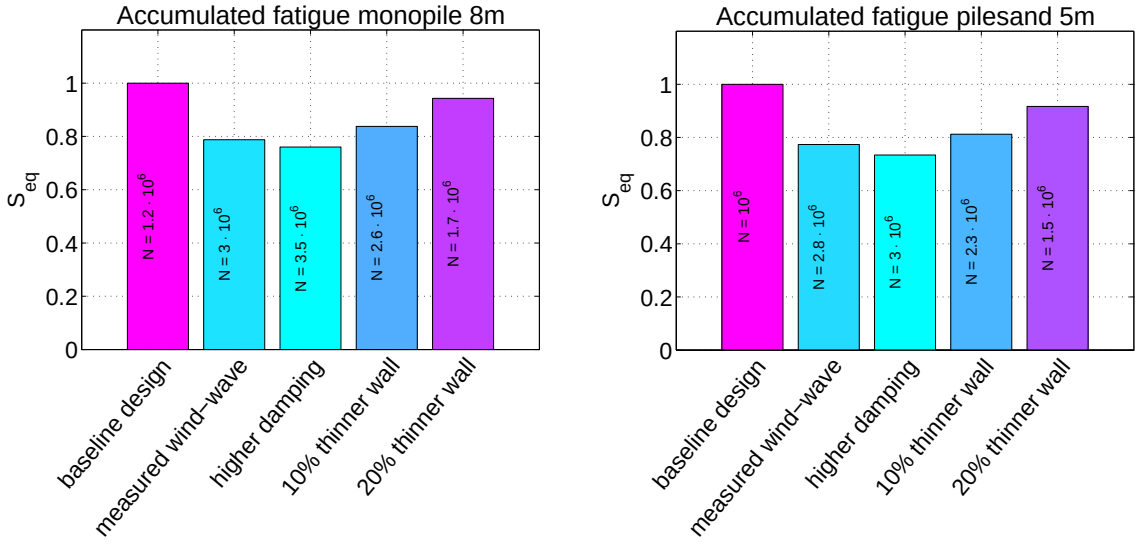

(a) Accumulated fatigue 8m below the monopile top for the different sub-structure/foundation models.

(b) Accumulated fatigue 5m below the seabed for the different sub-structure/foundation models.

Figure 13.13: Accumulated fatigue on the most critical section on the monopile and the pilesand for the different configurations. The presented data are normalized with the equivalent load of the baseline design.

13.2.3.2 Modified Design with Higher Damping

Based on the findings of the previous sections, that the extreme loads are well beyond the limits and that the fatigue (driving case) is decreased when higher damping is available on the system, modifications on the structure are applied. The aim of the modified design is material savings, leading to cost reduction. For the sake of simplicity, the effect of one parameter variation will be examined on the structure. The wall thickness of the monopile/pilesand is reduced uniformly along all sections by 10% and 20%, reducing the total weight of the sub-structure/foundation by 60 tons and 120 tons respectively. The differences in the first and second natural frequencies because of the changes in the mass are less than 5% compared to the baseline design. The natural frequencies are within the boundaries of wave frequency and blade passing. Since the design has been modified, all limit state analysis should be performed to ensure the structural integrity of the system.

Figures 13.14 and 13.15 present the von Mises stresses on the welds of the monopile and the pilesand sections for the baseline and the modified designs (10%, 20% thinner walls). The presented data are normalized with the maximum simulated stress of the baseline design. For the modified designs with the higher damping a small increase on the ultimate loads can be observed. For all cases the extreme loads are still below the yield limit. For the most critical monopile section (8m below the monopile top) DLC 6.1b results in an extreme load almost

equal to the yield limit for the 20% reduced thickness design. Even though the loads on the pilesand seem to be below the limits, the results should be interpreted with caution due to the simplifications of the soil model. A 3D finite element soil model, required for a detailed analysis of the foundation, might result in different stresses due to soil-pile interaction.

The comparison of the combined stresses for the verification of the buckling strength is presented in Figure 13.16 for the monopile and Figure 13.17 for the pilesand. An increase of the combined stress can be observed for the modified models, but the value is always below 1, ensuring the local buckling resistance of the structure.

Figure 13.18 depicts the maximum axial load from all the design load cases for the baseline and the modified designs. The horizontal solid lines represent the critical axial loads that lead to global buckling for every configuration. All the values are normalized with the maximum simulated load for the baseline design. A small decrease of the axial load for the reduced wall thickness designs is observed, due to the reduced weight of the structure.

The maximum stresses are increased because of the modified geometry of the structure, but they always remain below the limits. The fatigue is the driving design factor as was shown in Section 13.2.1 and is mainly affected by the net damping of the system. Reduced thickness of 10% and 20% and increased damping result in 2.3 and 1.5 times higher lifetime respectively compared to the baseline design (Figure 13.13 comparison between bars with caption "baseline design", "10% thinner wall" and "20% thinner wall"). Consequently, the higher measured damping can lead to material savings, if it is implemented during the design phase. In the examined case up to 1% of the whole structure's weight can be saved.

The common price of the steel (hot rolled steel plates with high thickness) used in the manufacturing of the monopiles for offshore wind turbines, ranges between 680-750 €/MT. 20% reduced wall thickness (120 tons) leads to cost savings from 81600-90000€ per wind turbine. For a wind farm like Walney 1 with 51 wind turbines, the cost saving is 4161600-4590000€. The steel prices were provided by ThyssenKrupp [184], Dansteel [185] and Oakley Steel [186]. Therefore, appropriate damping values, based on site measurements, implemented during the design of the sub-structure/foundation of an offshore wind turbine, can lead to significant cost savings.

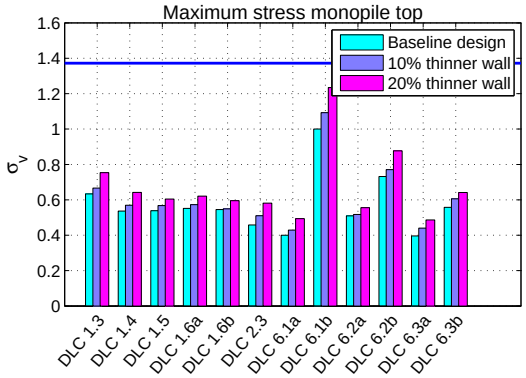

(a) Ultimate stress comparison at monopile top.

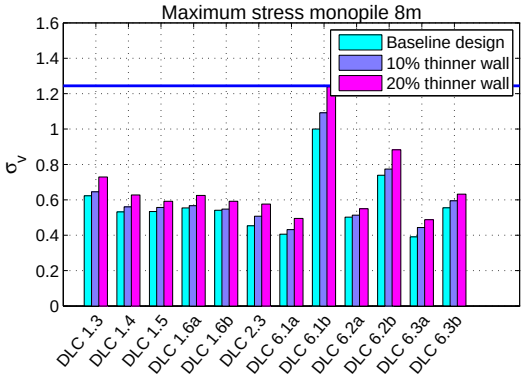

(b) Ultimate stress comparison at 8m below the monopile top.

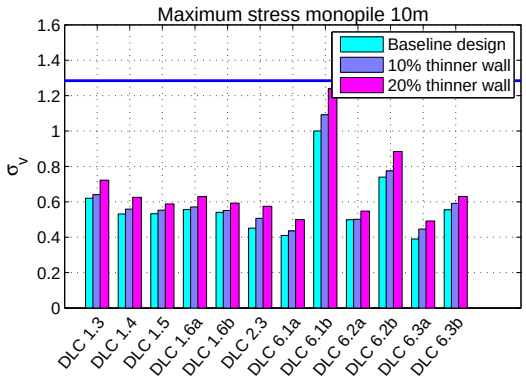

(c) Ultimate stress comparison at 10m below the monopile top.

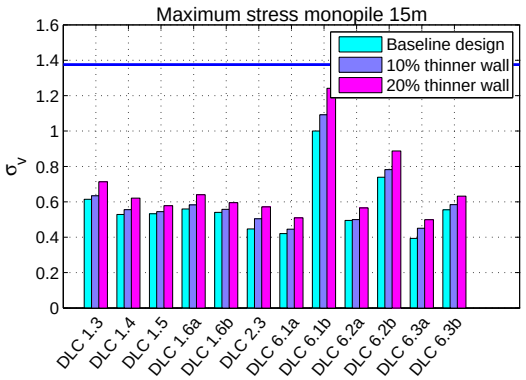

(d) Ultimate stress comparison at 15m below the monopile top.

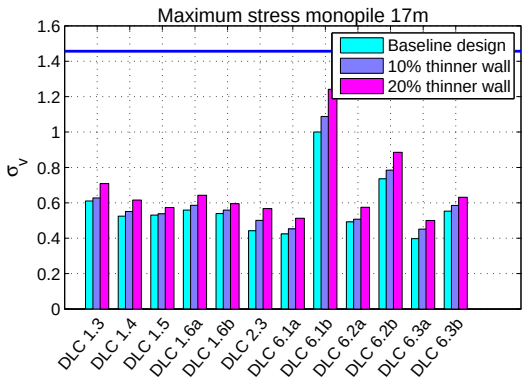

(e) Ultimate stress comparison at 17m below the monopile top.

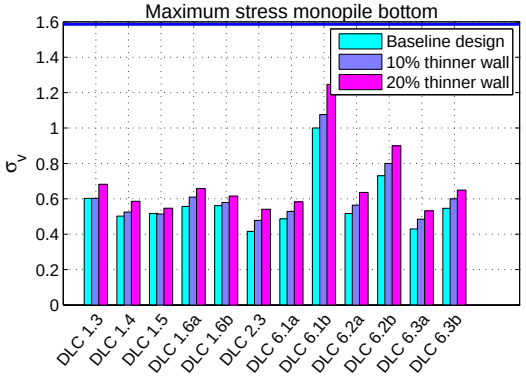

(f) Ultimate stress comparison at monopile bottom.

Figure 13.14: Ultimate stress loads comparison between the baseline design and the sub-structure with the reduced thickness. Von Mises stress calculated on the monopile sections for each design load case normalized with the maximum stress. The solid blue line represents the yield limit normalized with the observed maximum stress of the baseline design.

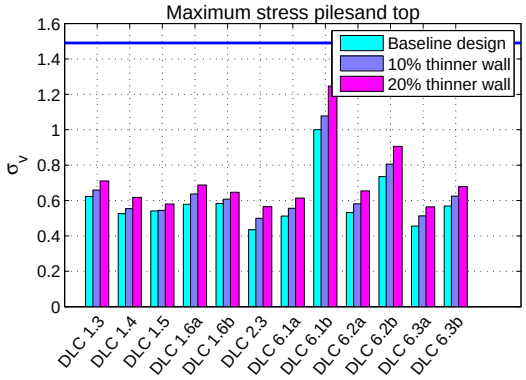

(a) Ultimate stress comparison at pilesand top.

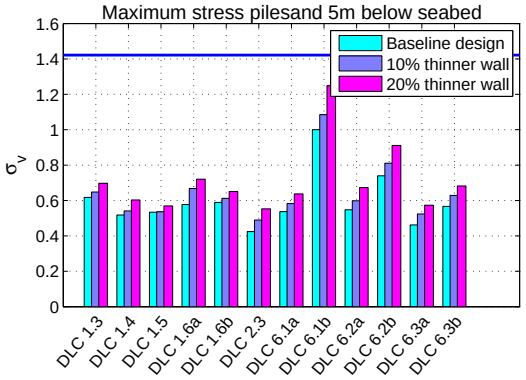

(b) Ultimate stress comparison at 5m below the seabed.

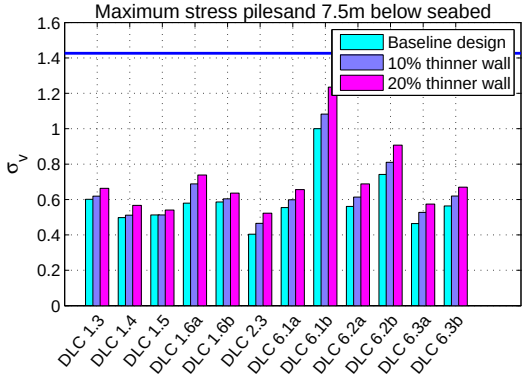

(c) Ultimate stress comparison at 7.5m below the seabed.

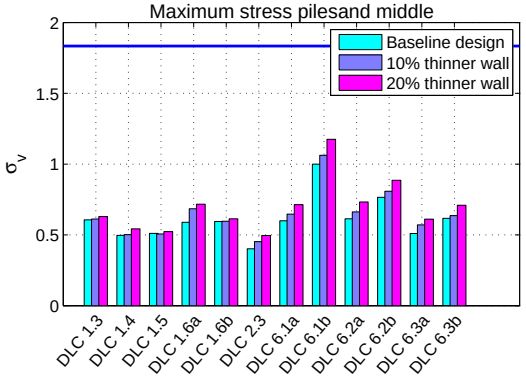

(d) Ultimate stress comparison at 11.5m below the seabed.

Figure 13.15: Ultimate stress loads comparison between the baseline design and the foundation with the reduced thickness. Von Mises stress calculated on the pilesand sections for each design load case normalized with the maximum stress. The solid blue line represents the yield limit normalized with the observed maximum stress of the baseline design.

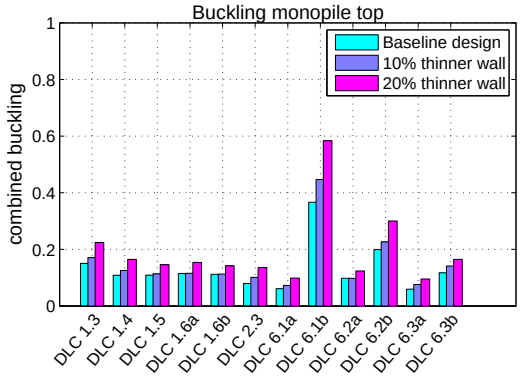

(a) Combined stresses comparison at monopile top.

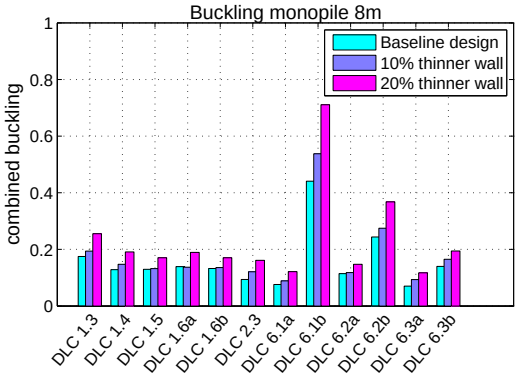

(b) Combined stresses comparison at 8m below the monopile top.

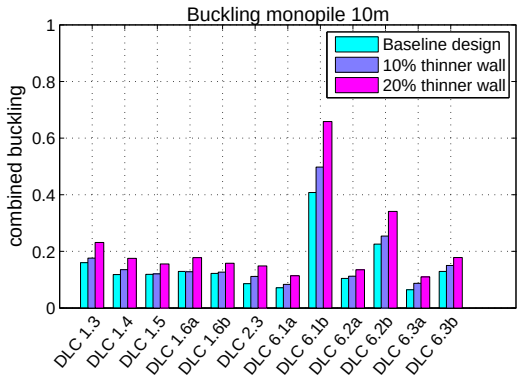

(c) Combined stresses comparison at 10m below the monopile top.

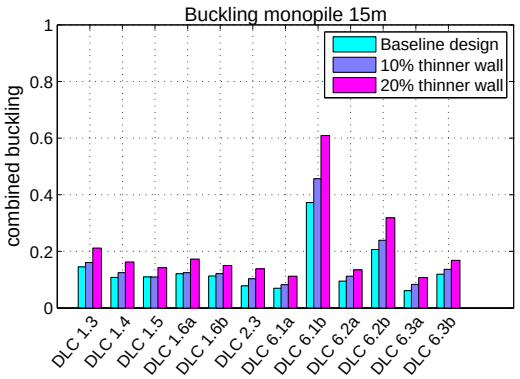

(d) Combined stresses comparison at 15m below the monopile top.

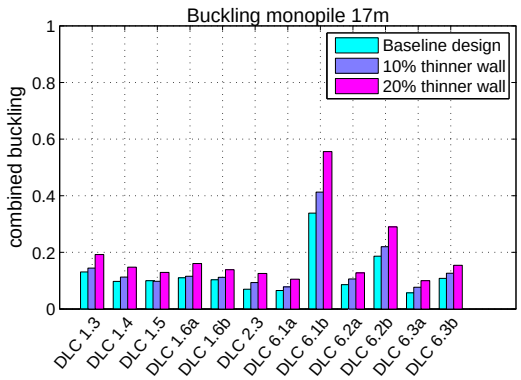

(e) Combined stresses comparison at 17m below the monopile top.

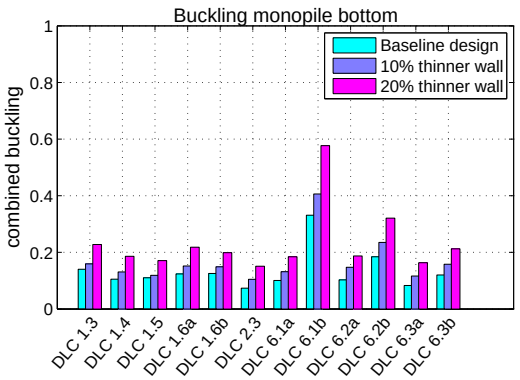

(f) Combined stresses comparison at monopile bottom.

Figure 13.16: Combined meridional, circumferential and shear stress for local buckling strength verification of the sub-structure. Comparison between the baseline design and the sub-structure with the reduced thickness. In the y axis the result from Equation 13.18 is presented.

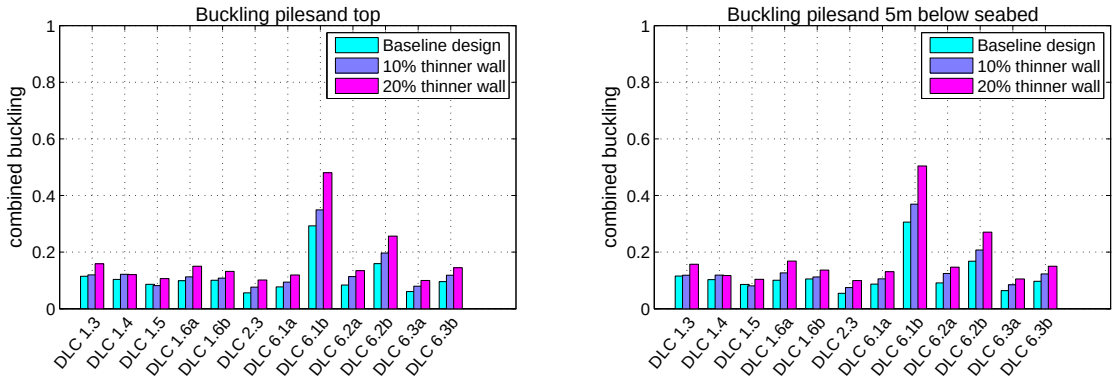

(a) Combined stresses comparison at pilesand top.

(b) Combined stresses comparison at 5m below the seabed.

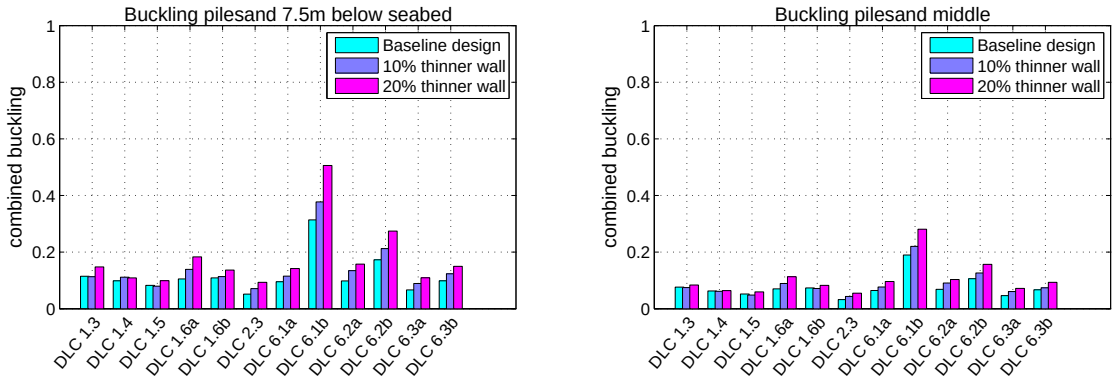

(c) Combined stresses comparison at 7.5m below the seabed.

(d) Combined stresses comparison at 11.5m below the seabed.

Figure 13.17: Combined meridional, circumferential and shear stress for local buckling strength verification of the foundation. Comparison between the baseline design and the pilesand with the reduced thickness. In the y axis the result from Equation 13.18 is presented.

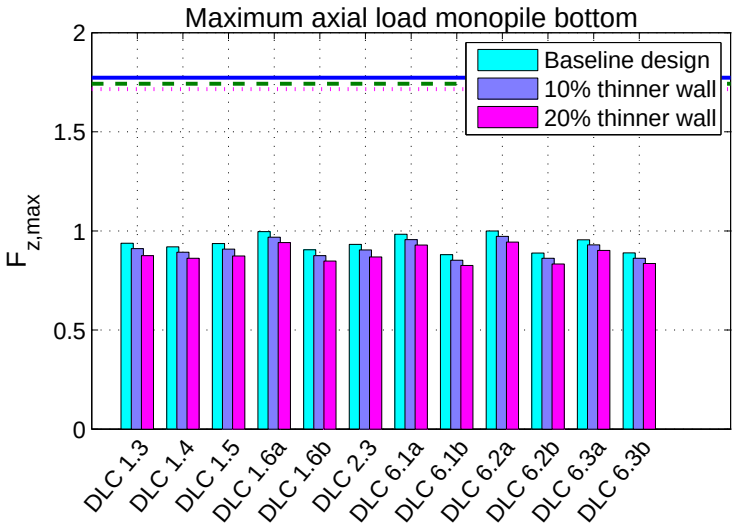

Figure 13.18: Comparison of maximum axial load at the monopile bottom between the baseline design and the sub-structure with the reduced thickness for all design load cases, normalized with the maximum simulated load. The solid lines correspond to the critical load obtained from Equation 13.19 for all the designs.

Chapter 14

Conclusions

Offshore wind energy has become the main target of the wind industry over the last years. Offshore wind turbines are continuously growing in size, increasing at the same time the challenges due to more severe operational conditions and rendering the accurate prediction of their response even more important. The design of the support structure requires a great effort, due to site dependency and its considerable influence upon the wind turbine loading.

For enhanced component reliability and thus cost reduction it is imperative to reduce the uncertainties in the design of offshore wind turbines, by gaining a better understanding of the driving design cases. The aim of this thesis has been the accurate prediction of the response of a fixed bottom offshore wind turbine and the investigation of the effect of damping on the fatigue of the structure and the sub-structure/foundation design for increased component reliability.

A 3 bladed 3.6MW pitch regulated-variable speed Siemens offshore wind turbine installed at the Walney Offshore Wind farm 1 in the Irish sea, has been fully instrumented for load measurements. Wind and wave measurements were provided by a nacelle mounted cup-anemometer and a wave buoy respectively. The additional offshore damping of the structure has been estimated from the impulse response caused by a boat impact. The measurements have been used for the validation of an offshore wind turbine model on a monopile foundation built in the aero-servo-hydro-elastic code HAWC2. Variations in the design of the sub-structure/foundation have been examined for possible material savings.

Measurements calibration

The calibration of the measured data is a crucial step before the post-processing of the results. The turbulence intensity has been estimated from a nacelle mounted cup-anemometer.

Due to conservative readings because of the rotor wake effect, a correction factor has been applied, based on the differences between the simulated and the measured load spectra. The effective turbulence intensity has been calculated applying the Frandsen's wake model and the wind direction probability. The wave properties (significant wave height, peak period and wave direction) were provided by a wave buoy installed close to the instrumented wind turbine.

A gravity based calibration procedure for the different components is described. Various issues like data synchronization and data availability are discussed. The problems encountered during this measurement campaign are important lessons for future studies. Large amount of money is spent on instrumentation and setting up of measurement campaigns, without always ensuring the final quality of the data. Therefore, it is recommended that calibration tests are performed regularly (yaw and low speed idle tests) to avoid drifts due to temperature changes. The synchronization and the overlap of the different systems should be examined before the beginning of the measurement period. Cases of boat impacts on the support structure should be recorded for the estimation of the support structure net damping.

Model set-up and validation

The 3 bladed 3.6MW pitch regulated-variable speed offshore wind turbine on a monopile foundation modeled in the aero-servo-hydro-elastic tool HAWC2 [3] was validated against bending strain measurements from the support structure and the blades of a full scale wind turbine. The model was built by down-scaling the NREL 5MW reference offshore wind turbine and modifying the mass and stiffness distributions to match the characteristics provided by the manufacturer. The model was tuned to match the additional offshore damping and the standstill natural frequencies of the actual turbine. The ultimate and the fatigue loads obtained from the measurements and the simulations and their uncertainties are compared. The accurate representation of damping in the model seemed to have a pronounced effect on the prediction of the loads on the structure. The predicted loads show similar behavior with the measured bending moments. Discrepancies between measurements and simulations are due to differences in the aerodynamic blade profiles, erroneous cup-anemometer readings and uncertainties in the soil modeling.

The wind turbulence intensity, the wave parameters and the soil model are based on site measurements. The simulation of the wind turbulence is based on the Mann wind turbulence model (IEC 61400-1 [17]). A JONSWAP spectral model is derived from the wave buoy measurements and the irregular wave theory combined with the wheeler stretching is implemented in HAWC2 to account for hydrodynamic loads. For the lateral loading of the pile the p-y method is employed [11].

Damping Estimation

The modal damping of a full scale offshore wind turbine on a monopile foundation was estimated both in standstill and in normal operation. An exponential curve was fitted to the relative maxima of the decaying response after the application of an impulse, for the estimation

of the additional offshore damping. The result was used to verify the corresponding estimation given by the auto-correlation function, which is further developed to predict damping under normal operation. A mean value of the total standstill damping $\zeta = 1.9\%$ (logarithmic decrement $\delta = 12.2\%$) is identified. The finding is in agreement with previous studies, where higher additional offshore damping than the currently used is reported. Exact values of net support structure damping are site dependent due to the influence of the soil damping on the structure's response. The damping of the first two modes of the structure was estimated under ambient excitation. The output-only Enhanced Frequency Domain Decomposition (EFDD) method was applied to the response time series. The damping in the fore aft (FA) vibration mode has a scatter of 8.1% around a mean logarithmic decrement of $\delta = 65\%$ and in the side-side (SS) 6.7% around $\delta = 30\%$. The beating phenomenon on the auto-correlation function and the harmonics render the identification of the side-side modal damping less reliable. Their effect is less pronounced in the fore-aft direction due to the aerodynamic damping dominating this mode. However, the accuracy of the damping estimation should always be examined with caution, due to bias errors introduced by the application of the FFT to the time series.

The damping in normal operation was compared with the identified damping from the model turbine. Results of the damping in the fore-aft direction showed good agreement between measurements and simulations for all mean wind speeds. The presence of a tower damper in the real wind turbine, which is not taken into account in the model and the uncertainties in the soil model are responsible for the discrepancies in the damping estimation of the side-side vibration mode.

Response under various operational conditions

The side-side tower-bottom fatigue of a 3.6MW offshore wind turbine is estimated from measurements on the Walney 1 offshore wind farm. The joint wind-wave distribution and the wind and wave direction distribution based on 6 months of measurements are included in the analysis. The implementation of the joint wind-wave probability scaled to 25 years lifetime, showed that the largest contributors to the accumulated fatigue damage on the sub-structure is from the most probable combinations of wind speed, significant wave height, and misalignment angle; rather than those combination which resulted in the highest 1Hz equivalent loads. Simulations with HAWC2 show good agreement with the measurements in the estimation of the equivalent load for each wind-wave combination and the accumulated fatigue throughout the whole lifetime of the structure.

The side-side fatigue loads at the tower bottom were shown to be extremely sensitive to the damping applied in the HAWC2 model; especially in the case of wind-wave misalignment. Increasing values of the additional offshore damping (to $\delta = 12\%$) result in a reduction in the side-side accumulated fatigue of up to 46%, compared to simulations with a damping value of $\delta = 6\%$ (a typical value used for design of the sub-structure). Additionally, at a typical design damping of 6%, the simulated side-side fatigue loads are very sensitive to the wind-wave misalignment angle; however, this sensitivity decreased when higher damping values were applied. Therefore, an accurate choice of this damping value is necessary in order to accurately predict the side-side fatigue loads on the sub-structure.

On the other hand, the measured side-side fatigue loads were shown to be relatively insensitive to the misalignment angle. The damping in the side-side direction estimated from the measurements during normal operation also seems to be insensitive to the misalignment angle. Additionally, the damping value estimated from the measurements of 12% was significantly higher than the typical design damping of 6%. These findings indicate that there may be significantly more additional offshore damping than is typically considered in the design of wind turbine sub-structures.

Since the side-side fatigue loads are highly sensitive to the choice of damping, the use of a conservative damping value in the wind farm design phase may result in significant overprediction of the lifetime side-side fatigue loads. These overpredicted loads may result in a significantly overdesigned sub-structure. Choice of an appropriate damping value can therefore result in significant material and cost savings during the design of offshore wind turbine sub-structures.

In the case of a yaw error during a storm, the amplitudes of the measured in plane blade root and tower bottom side-side measured bending moments are increasing.

Sub-structure/Foundation design

The design of the sub-structure/foundation has been modified to examine the possibility of material savings, based on the findings of the higher damping available in the system. For the sake of simplicity for this preliminary design the thickness of the structure is decreased uniformly. Limitations due to uknown design details and simplifications in the soil model are discussed.

For the calculation of the loads during the design process, various design load cases (normal operation and extreme events), prescribed in the IEC 61400-3 standards [13], are tested to examine all possible wind-wave combinations that the offshore wind turbine will be subject during its lifetime. For the study of the monopile/pilesand design a total of 25000 simulations were performed in HAWC2. The stresses at the sections along the sub-structure/foundation are computed and a fatigue, an ultimate and a stability analysis are performed to investigate the structural integrity of the system. The von Mises criterion and the buckling strength verification specified in the Eurocode 3 [181] are applied for the examination of the ultimate limit state and the stability respectively. The Rainflow counting technique combined with the Miner's rule are used for the calculation of the accumulated fatigue load. The joint wind-wave distribution of the probability is accounted for in the analysis.

The design of the sub-structure/foundation is driven by the fatigue. Reduction in the wall thickness up to 20% and implementation of the higher measured damping ($\zeta = 1.9\%$) resulted in 1.5 higher lifetime than the baseline design (37 years). The thickness reduction results in saving 120 tons of steel and approximately 81600-90000€ per wind turbine, based on the current steel plate prices, as provided by the specialized steel mills (ThyssenKrupp, Dansteel) and steel trading companies (Oakley Steel). However, the uncertainty introduced to the fatigue by the estimation of the joint wind-wave probability based on limited measurements and the uncertainty of the soil model should be taken into account in a more detailed analysis.

The extreme loads are below the yield limit and the buckling stability is verified. Therefore, material savings due to higher implemented damping are possible.

14.1 Future Work

Specific details in the modeling of the environment (wind, waves, soil) and the wind turbine, necessary for the implementation in real projects, were outside of the scope of the current thesis. For the presentation of the results several assumptions have been made. For a more specific and thorough analysis, more structural details and further developments of the currently applied tools are necessary. Non linear waves should be applied in the simulations for accurate calculation of hydrodynamic loads on the support structure.

Considering the damping estimation during normal operation, the elimination of the harmonics before the identification process is required. The implementation of a tower damper in the simulations will provide a better estimation of the damping in the side-side direction. Various methods of damping estimation (ex. SSI) should be applied for the verification of the accuracy of the results.

A detailed sub-structure/foundation design calls for a more thorough analysis of the fatigue of the structure, knowing the exact manufacturing details (ex. welds, bolts). A 3D finite element soil model is imperative for the representation of the soil-pile interaction and the reliable estimation of the loads on the pilesand. Investigation of the soil damping on the fatigue of the system could lead to reduction of the uncertainties in the design of the structure. Taking into account the higher available damping in the system, an optimization algorithm and a cost function are required for the calculation of the optimum wall thickness.

References

[1] European Wind Energy Association et al. Eu energy policy to 2050: Achieving 80-95% emissions reductions, 2011.

[2] Germanischer Lloyd WindEnergie GmbH. Guideline for the Certification of Offshore Wind Turbines. In *Technical Report*. Hamburg, Germany, 2005.

[3] T. J. Larsen and A. M. Hansen. *How 2 HAWC2, the user's manual*. Denmark. Forskningscenter Risø. Risø National Laboratory, 2007.

[4] R. Brincker, C. Ventura, and P. Andersen. Damping estimation by frequency domain decomposition. In *19th International Modal Analysis Conference*, pages 698–703, 2001.

[5] N. J. Jacobsen, P. Andersen, and R. Brincker. Using enhanced frequency domain decomposition as a robust technique to harmonic excitation in operational modal analysis. In *Proceedings of ISMA2006: International Conference on Noise & Vibration Engineering*, pages 18–20, 2006.

[6] E. Morgan, M. Lackner, R. M. Vogel, and L. G. Baise. Probability distributions for offshore wind speeds. In *Energy Conversion and Management*, volume 52, pages 15–26, 2011.

[7] B. M. Sumer and F. Jorgen. *Hydrodynamic around Cylindrical Structures*. World Scientific, 2006.

[8] Sir G. B. Airy. Tides and waves. In *Encycl. Metrop.*, volume 192, 1845.

[9] J.D. Wheeler et al. Method for calculating forces produced by irregular waves. In *Journal of Petroleum Technology*, volume 22, pages 359–367. Society of Petroleum Engineers, 1970.

[10] O. T. Gudmestad. Measured and predicted deep water wave kinematics in regular and irregular seas. In *Marine Structures*, volume 6, pages 1–73. Elsevier, 1993.

[11] DNV. Design of Offshore Wind Turbine Structures. In *Offshore Standard DNV-OS-J101*. 2012.

[12] E.J. Norton. Wind and wave misalignment effects on fatigue loading. Technical Report 10084, Garrad Hassan, 2003. IEC Working Group 3 (Wind Turbine Offshore Standard).

[13] International Electrotechnical Commission (IEC). IEC 61400-3, Wind Turbines Part 3: Design Requirements for offshore wind turbines. In *International Standard*. 2009.

[14] Y. Hasegava, J. Murata, H. Imamura, K. Karikomi, and N. Yonezawa. Aerodynamic loads calculation of a horizontal axis wind turbine rotor in combined inflow condition. In *European Wind Energy Conference and Exhibition EWEC*, London, UK, 2004.

[15] T. Burton, N. Jenkins, D. Sharpe, and E. Bossanyi. *Wind energy handbook*. John Wiley & Sons, 2011.

[16] B. Ernst and J. R. Seume. Investigation of site-specific wind field parameters and their effect on loads of offshore wind turbines. In *Energies*, volume 5, pages 3835–3855. Molecular Diversity Preservation International, 2012.

[17] International Electrotechnical Commission (IEC). IEC 61400-1, Wind Turbines Part 1: Design Requirements. In *International Standard*. 2005.

[18] A. H. Monahan. The probability distribution of sea surface wind speeds. part i: Theory and seawinds observations. In *Journal of climate*, volume 19, pages 497–520, 2006.

[19] M. Courtney, R. Wagner, and P. Lindelöw. Testing and comparison of lidars for profile and turbulence measurements in wind energy. In *IOP Conference Series: Earth and Environmental Science*, volume 1, page 012021. IOP Publishing, 2008.

[20] R. Wagner, T. Friis Pedersen, M. Courtney, J. Gottschall, I. Antoniou, R. Møller, S. Markilde Pedersen, T. Velociter, M. Bardon, N. Le, et al. Power performance measured using a nacelle lidar. In *European Wind Energy Conference and Exhibition EWEC*, 2011.

[21] R. Wagner and S. Davoust. Nacelle lidar for power curve measurement, avedøre campaign. In *Technical Report, DTU Wind Energy*. Roskilde, Denmark, 2013.

[22] C. Devriendt, P. J. Jordaens, G. De Sitter, and P Guillaume. Damping Estimation of an Offshore Wind Turbine on a Monopile Foundation. In *IET Renewable Power Generation*, volume 7, pages 401–412. The Institution of Engineering and Technology, 2013.

[23] N. Haritos. Introduction to the analysis and design of offshore structures–an overview. In *EJSE, Special*, 2007.

[24] M. S. Longuet-Higgins. On the Statistical Distribution of the Heights of Sea Waves. In *Journal of Marine Research*, volume 11, pages 245–266, 1952.

[25] J. A. Battjes and H. W. Groenendijk. Wave height distributions on shallow foreshores. In *Coastal engineering*, volume 40, pages 161–182. Elsevier, 2000.

[26] S. Mai, J. Wilhelmi, and U. Barjenbruch. Wave height distributions in shallow waters. In *Coastal Engineering*, page 2, 2010.

[27] W. H. Michel. Sea spectra revisited. In *Marine Technology*, volume 36, pages 211–227, 1999.

[28] H. E. Krogstad and Arntsen Ø. A. Sea state parameters and engineering wave spectra. `http://folk.ntnu.no/oivarn/hercules_ntnu/LWTcourse/partB/3seastate/3%20SEA%20STATE%20PARAMETERS%20AND%20ENGINEERING%20WAVE%20SPECTRA.htm`.

[29] K. Johannessen, T. S. Meling, and S. Haver. Joint Distribution for Wind and Waves in the Northern North Sea. In *International Offshore and Polar Engineering Conference*, Stavanger, Norway, 2001.

[30] P. Agarwal and L. Manuel. The influence of the joint wind-wave environment on offshore wind turbine support structure loads. In *Journal of solar energy engineering*, volume 130, pages 030301–1. American Society of Mechanical Engineers, 2008.

[31] F. Cai and G. R. Eiksund. The Influences of Clay Properties on Wind Turbine Tower. In *International Offshore and Polar Engineering, ISOPE*, Anchorage, Alaska, USA, 2013.

[32] L. Andersen and M. A. Liingaard. Lumped-parameter models for wind turbine footings on layered ground. Technical report, Aalborg University. Department of Civil Engineering, 2007.

[33] M. Wang, Y. Zhao, W. Du, Y. He, and R. Jiang. Derivation and Validation of Soil-Pile-Interaction Models for Offshore Wind Turbines. In *International Offshore and Polar Engineering, ISOPE*, Anchorage, Alaska, USA, 2013.

[34] M. B. Zaaijer. Foundation models for the dynamic response of offshore wind turbines. In *Marine Renewable Energy Conference MAREC*, Newcastle, UK, 2002.

[35] E. Bush and Manuel L. Foundation Models for Offshore Wind Turbines. In *47th Aerospace Science Meeting including the New Horizons Forum and Aerospace Exposition*, Orlando, Florida, 2009.

[36] M. B. Zaaijer. Foundation modelling to assess dynamic behaviour of offshore wind turbines. In *Applied Ocean Research*, volume 28, pages 45–57, 2006.

[37] A. Stahlmann. Numerical and Experimental Modeling of Scour at Foundation Structures for Offshore Wind Turbines. In *International Offshore and Polar Engineering, ISOPE*, Anchorage, Alaska, USA, 2013.

[38] M. B. Zaaijer. Comparison of monopile, tripod, suction bucket and gravity base design for 6MW turbine. In *Offshore Windenergy in Mediterranean and Other European Seas, OWEMES*, Naples, Italy, 2003.

[39] J.H. Vugts, J. van der Tempel, and E.A. Schrama. Hydrodynamic loading on monotower support structures for preliminary design. In *Proceedings of Special Topic Conference on Offshore Wind Energy*, 2001.

[40] M.C. (editor) Ferguson, M. Kuhn, G. J. W. van Bussel, W. A. A. M. Bierbooms, T. T. Cockerill, B. Goransson, L. A. Harland, J. H. Vugts, and R. Hes. A Typical Design Solution for an Offshore Wind Energy Conversion System. In *Opti-OWECS Final Report Vol. 4*. Delft, Netherlands, 1998.

[41] G. Moe and R. Verley. Hydrodynamic damping of offshore structures in waves and currents. In *Offshore Technology Conference*, 1980.

[42] G. Najafian, R.G. Tickell, R. Burrows, and J.R. Bishop. The UK Christchurch Bay compliant cylinder project: analysis and interpretation of morison wave force and response data. In *Applied Ocean Research*, volume 22, pages 129–153. Elsevier, 2000.

[43] A. R. Henderson, M. B. Zaaijer, and T. R. Camp. Hydrodynamic Loading on Offshore Wind Turbines. In *Offshore Windenergy in Mediterranean and Other European Seas, OWEMES*, Naples, Italy, 2003.

[44] S. K. Chakrabarti. Hydrodynamics of Offshore Structures. In *WIT Press*, volume ISBN 0-905451-66-X, 1987.

[45] R. G. Dean. Stream Function Representation of Non Linear Ocean Waves. In *Geophysics*, volume 70, No. 18, pages 4561–4572, 1965.

[46] S. Schløer. *Fatigue and extreme wave loads on bottom fixed offshore wind turbines. Effects from fully nonlinear wave forcing on the structural dynamics.* PhD thesis, Technical University of Denmark, 2013.

[47] P. Agarwal and L. Manuel. Extrem Loads for an Offshore Wind Turbine using Statistical Extrapolation from Limited Field Data. In *Wind Energy*, volume 11, pages 673–684, 2008.

[48] W. Bierbooms. Investigation of Spatial Gusts with Extreme Rise Time on the Extreme Loads of Pitch-regulated Wind Turbines. In *Wind Energy*, volume 8, pages 17–34, 2005.

[49] A. Natarajan and D. R. Verlest. Outlier robustness for wind turbine extrapolated extreme loads. In *Wind Energy*, volume 15, pages 679–697, 2011.

[50] K. Freudenreich and K. Argyriadis. The load level of modern wind turbines according to iec 61400-1. In *Journal of Physics: Conference Series*, volume 75, page 012075. IOP Publishing, 2007.

[51] A. Natarajan, W. E. Holley, R. Penmatsa, and B. C. Brahmanapalli. Identification of contemporaneous component loading for extrapolated primary loads in wind turbines. In *Wind Energy*, volume 11, pages 577–587. Wiley Online Library, 2008.

[52] J. C. Marin, A. Barroso, F. Paris, and J. Canas. Study of fatigue damage in wind turbine blades. In *Engineering Failure Analysis*, volume 16, pages 656–668, 2009.

[53] D. Veldkamp. *A Probabilistic Approach to Wind Turbine Fatigue Design.* PhD thesis, Technical University of Delft, 2006.

[54] X. Munduate and F. N. Coton. Identification of dynamic of dynamic stall regions on horizontal axis wind turbines. In *19th ASME wind energy symposium*, Reno, Nevada, 2000.

[55] T. Wang. An examination of two tower-shadow modelling strategies for downwind wind turbines. In *ASME wind energy symposium*, Reno, Nevada, 1998.

[56] R. R. Pedersen, S. R. K. Nielsen, and P. Thoft-Christensen. Stochastic analysis of the influence of tower shadow on fatigue life of wind turbine blade. In *Structural Safety*, volume 35, pages 63–71, 2012.

[57] A. Sathe and W. Bierbooms. Influence of different wind profiles due to varying atmospheric stability on the fatigue life of wind turbines. In *The Science of Making Torque from Wind*, Lyngby, Denmark, 2007.

[58] R. J. Barthelmie, G. C. Larsen, L. Fransen, S. T. amd Folkerts, K. Rados, S. C. Pryor, B. Lange, and G. Schepers. Comparison of wake model simulations with offshore wind turbine wake profiles measured by sodar. In *Journal of Atmospheric and Oceanic Technology*, volume 23, pages 888–901, 2005.

[59] J. A. Dahlberg, M. Poppen, and S. E. Thor. Wind farm load spectra based on measurements in: P.H. Madsen, P. lundsager (Eds). In *Proc. EWEA Special Topic Conf. 92: The Potential of Wind Farms*, Herning, Denmark, 1992.

[60] K. Thomsen, H. Bindner, and T. Friis Pedersen. Fatigue loads on a pitch regulated wind turbine operating in a coastal wind turbine array. Roskilde, Denmark, 1994. Risoe National Lab. Meteorology and Wind Energy.

[61] S. T. Frandsen. Turbulence and turbulence-generated fatigue loading in wind turbine clusters. In *Report riso-r-1188(en)*. Riso National Laboratory, Roskilde, Denmark, 2005.

[62] J. Berg, J. Mann, and M. Nielsen. Introduction to micro meteorology for wind energy. DTU Wind Energy, 2012.

[63] K. Thomsen and P. Sørensen. Fatigue loads for wind turbines operating in wakes. In *Journal of Wind Engineering and Industrial Aerodynamics*, volume 80, pages 121–136. Elsevier, 1999.

[64] S. Frandsen and M. L. Thogersen. Integrated fatigue loading for wind turbines in wind farms by combining ambient turbulence and wakes. In *Wind Engineering*, volume 23, pages 327–340. [London] Multi-Science Pub. Co., 1977-, 1999.

[65] K. Thomsen and H. A. Madsen. A new simulation method for turbines in wake applied to extreme response during operation. In *Wind Energy*, volume 8, pages 35–47. Wiley Online Library, 2005.

[66] N. Sezer-Uzol and O. Uzol. Effect of steady and transient wind shear on the wake structure and performance of a horizontal axis wind turbine rotor. In *Wind Energy*. Wiley Online Library, 2009.

[67] A. M. S. Hwas and R. Katebi. Wind turbine control using pi pitch angle controller. In *IFAC Conference on Advances in PID Control PID'12*, 2012.

[68] J. Jonkman, S. Butterfield, W. Musial, and G. Scott. Definition of a 5-mw reference wind turbine for offshore system development. In *Technical Report NREL/TP-500-38060*. National Renewable Energy Laboratory, 2009.

[69] M. Hansen, A. Hansen, T. J. Larsen, S. Oye, P. Sorensen, and P. Fuglsang. Control design for a pitch-regulated, variable speed wind turbine. In *Technical Report Riso - R-1500 (EN)*. Riso National Laboratory, Roskilde, Denmark, 2005.

[70] M. H. Hansen and L. C. Henriksen. Basic DTU Wind Energy controller. In *Technical Report, DTU Wind Energy*. Roskilde, Denmark, 2013.

[71] E. A. Bossanyi. Wind Turbine Control for Load Reduction. In *Wind Energy*, volume 6, pages 229–244, 2003.

[72] D. W. Lobitz and P. S. Veers. Load mitigation with bending/twist-coupled blades on rotors using modern control strategies. In *Wind Energy*, volume 6, pages 105–117. Wiley Online Library, 2003.

[73] S. Johnson, C. van Dam, and D. Berg. Active Load Control Techniques for Wind Turbines. In *Technical Report*. Sandia National Laboratories, Albuquerque, New Mexico, 2008.

[74] L. Zhang and Y. Tamura. Damping estimation of engineering structures with ambient response measurements. In *Proceeding of the 21st IMAC*, 2003.

[75] A. K. Chopra. *Dynamics of structures: theory and applications to earthquake engineering*, volume 2. Prentice Hall Englewood Cliffs, NJ, 1995.

[76] S. Krenk. Dynamics of Structures. Technical report, Technical University of Denmark, Department of Mechanical Engineering, 2013.

[77] I. Chowdhury and S. P. Dasgupta. Computation of rayleigh damping coefficients for large systems. In *The Electronic Journal of Geotechnical Engineering*, volume 8, 2003.

[78] B. Schmidt. Overall Damping for Piled Offshore Support Structures. In *GL Wind, Guideline for the Certification of Offshore Wind Turbines*. 2005.

[79] C. Devriendt, P. J. Jordaens, G. De Sitter, and P Guillaume. Damping Estimation of an Offshore Wind Turbine on a Monopile Foundation. In *European Wind Energy Conference, EWEA*, Copenhagen, Denmark, 2012.

[80] M. F. Cook. Damping estimation, response prediction and fatigue calculation of an operational single pile platform. Master's thesis, Massachusetts Institute of Technology and Woods Hole Oceanographic Institution, 1982.

[81] N. J. Tarp-Johansen, L. Andersen, Christensen E. D., C. Morch, B. Kallesoe, and S. Frandsen. Comparing Sources of Damping of Cross-Wind Motion. In *European Wind Energy Conference EOW*, Stockholm, Sweden, 2009.

[82] M. Damgaard, J. KF Andersen, L. B. Ibsen, and L. V. Andersen. Natural frequency and damping estimation of an offshore wind turbine structure. In *International Offshore and Polar Engineering Conference, ISOPE*, Rhodes, Greece, 2012.

[83] D. J. Cerda Salzmann and J. van der Tempel. Aerodynamic Damping in the Design of Support Structures for Offshore Wind Turbines. In *Copenhagen Offshore Wind Conference*, Copenhagen, Denmark, 2005.

[84] A. Cunha, E. Caetano, F. Magalhães, and C. Moutinho. From input-output to output-only modal identification of civil engineering structures. In *1st International Operational Modal Analysis Conference (IOMAC)*, pages 11–27. Copenhagen, Denmark, 2005.

[85] P. Andersen, R. Brincker, B. Peeters, G. De Roeck, L. Hermans, and C. Krämer. Comparison of system identification methods using ambient bridge test data. In *Proc. of the 17th International Modal Analysis Conference, Kissimee, Florida*, pages 7–10, 1999.

[86] D. F. Pilkey and D. J. Inman. A survey of damping matrix identification. In *Proceddings-Spie the International Society For Optical Engineering*, volume 1, pages 104–110. Spie International Society For Optical Engineering, 1998.

[87] G.H. James, T.G. Carne, and P.S. Veers. Damping measurements using operational data. In *Journal of solar energy engineering*, volume 118. Sandia National Laboratory, 1996.

[88] G.H. James, T. G. Carne, and R. L. Mayes. Modal parameter extraction from large operating structures using ambient excitation. In *Proceddings-Spie the International Society For Optical Engineering*, pages 77–83. Spie International Society For Optical, 1996.

[89] T. G. Carrie and A. R. Nord. Modal testing of a rotating wind turbine. In *Proc Sixth Biennial Wind Energy Conf and Workshop*, pages 825–34, 1983.

[90] F. Magalhães. *Operational Modal Analysis for testing and monitoring of bridges and special structures.* PhD thesis, University of Porto, Faculty of Engineering, 2012.

[91] B. Cauberghe. *Applied frequency-domain system identification in the field of experimental and operational modal analysis.* PhD thesis, Vakgroep Werktuigkunde, Faculteit Toegepaste Wetenschappen, 2004.

[92] P. Verboven. *Frequency-domain system identification for modal analysis.* PhD thesis, Vrije Universiteit Brussel, Brussels, 2002.

[93] J. J. Thomsen. *Vibrations and stability: advanced theory, analysis, and tools.* Springer Verlag, 2003.

[94] W. Gawronski. *Advanced structural dynamics and active control of structures.* Springer Verlag, 2004.

[95] S. Adhikari. *Damping Models for Structural Vibration.* PhD thesis, Cambridge University, Engineering Department, 2000.

[96] R.E. Spears and S.R. Jensen. Approach for selection of rayleigh damping parameters used for time history analysis. In *Proceedings of PVP*, pages 17–24, 2009.

[97] J. F. Hall. Problems encountered from the use (or misuse) of rayleigh damping. In *Earthquake engineering & structural dynamics*, volume 35, pages 525–545. Wiley Online Library, 2006.

[98] D. F. Pilkey and D. J. Inman. An iterative approach to viscous damping matrix identification. In *Proceddings-Spie the International Society For Optical Engineering*, pages 1152–1157. Spie International Society For Optical Engineering, 1997.

[99] C. Minas and D.J. Inman. Identification of a nonproportional damping matrix from incomplete modal information. In *Journal of vibration, acoustics, stress, and reliability in design*, volume 113, pages 219–224. American Society of Mechanical Engineers, 1991.

[100] L. Starek and D.J. Inman. A symmetric inverse vibration problem for nonproportional underdamped systems. In *Journal of applied mechanics*, volume 64, pages 601–605. American Society of Mechanical Engineers, 1997.

[101] S. Adhikari and J. Woodhouse. Identification of damping: part 1, viscous damping. In *Journal of Sound and Vibration*, volume 243, pages 43–61. Elsevier, 2001.

[102] M.J. Roemer and D.J. Mook. Mass, stiffness, and damping matrix identification-an integrated approach. In *ASME Transactions Journal of Vibration Acoustics*, volume 114, pages 358–363, 1992.

[103] J. Fabunmi, P. Chang, and J. Vorwald. Damping matrix identification using the spectral basis technique. In *Journal of Vibration Acoustics Stress and Reliability in Design*, volume 110, page 332, 1988.

[104] S.Y. Chen, M.S. Ju, and Y.G. Tsuei. Estimation of mass, stiffness and damping matrices from frequency response functions. In *Journal of vibration and acoustics*, volume 118, pages 78–82. American Society of Mechanical Engineers, 1996.

[105] J. Fang and G.J. Lyons. Material damping of free hanging pipes: Theoretical and experimental studies. In *Journal of sound and vibration*, volume 172, pages 371–389. Elsevier, 1994.

[106] M. Dalenbring. Damping function estimation based on measured vibration frequency responses and finite-element displacement modes. In *Mechanical systems and signal processing*, volume 13, pages 547–569. Elsevier, 1999.

[107] S. Adhikari and J. Woodhouse. Identification of damping: part 2, non-viscous damping. In *Journal of Sound and Vibration*, volume 243, pages 63–88. Elsevier, 2001.

[108] A. J. Felber. *Development of a hybrid bridge evaluation system.* PhD thesis, University of British Columbia, 1993.

[109] J. Rodrigues, R. Brincker, and P. Andersen. Improvement of frequency domain output-only modal identification from the application of the random decrement technique. In *Proc. 23rd Int. Modal Analysis Conference, Deaborn, MI*, 2004.

[110] C. W. de Silva and W. E. Seemann. Vibration: Fundamentals and practice. In *Applied Mechanics Reviews - Including Supplement*, volume 53, page B41, 2000.

[111] G. A. Papagiannopoulos and G. D. Hatzigeorgiou. On the use of the half-power bandwidth method to estimate damping in building structures. In *Soil Dynamics and Earthquake Engineering*, volume 31, pages 1075–1079. Elsevier, 2011.

[112] J. Wang, D. Lü, F. Jin, and C. Zhang. Accuracy of the half-power bandwidth method with a third-order correction for estimating damping in multi-dof systems. In *Earthquake Engineering and Engineering Vibration*, volume 12, pages 33–38. Springer, 2013.

[113] R. Brincker, L. Zhang, and P. Andersen. Modal identification from ambient responses using frequency domain decomposition. In *Proceedings of I 8th International Modal Analysis Conference*, pages 625–630, 2000.

[114] R. Brincker, L. Zhang, and P. Andersen. Output-only modal analysis by frequency domain decomposition. In *Proceedings of the International Seminar on Modal Analysis*, volume 2, pages 717–724. KU Leuven, 2001.

[115] S. Gade, N. Møller, H. Herlufsen, and H. Konstantin-Hansen. Frequency domain techniques for operational modal analysis. In *Proceedings 1st IOMAC Conference*, pages 26–27, 2005.

[116] R. Brincker, S. Krenk, P. H. Kirkegaard, and A. Rytter. Identification of dynamical properties from correlation function estimates, 1992.

[117] J. C. Asmussen. *Modal analysis based on the random decrement technique: application to civil engineering structures.* PhD thesis, unknown, 1997.

[118] R. Shirzadeh, C. Devriendt, M. A. Bidakhvidi, and P. Guillame. Experimental and computational damping estimation of an offshore wind turbine on a monopile foundation. In *Journal of Wind Engineering and Industrial Aerodynamics*, volume 120, pages 96–106. Elsevier, 2013.

[119] M. Damgaard, L. B. Ibsen, L. V. Andersen, and JK.F. Andersen. Cross-wind modal properties of offshore wind turbines identified by full scale testing. In *Journal of Wind Engineering and Industrial Aerodynamics*, volume 116, pages 94–108. Elsevier, 2013.

[120] W. G. Versteijlen, A. Metrikine, J. S. Hoving, E. H. Smidt, and W. E. De Vries. Estimation of the vibration decrement of an offshore wind turbine support structure caused by its interaction with soil. Master's thesis, Technical University of Delft, 2011.

[121] R. Osgood, G. Bir, H. Mutha, B. Peeters, M. Luczak, and G. Sablon. Full-scale modal wind turbine tests: comparing shaker excitation with wind excitation. In *Structural Dynamics and Renewable Energy, Volume 1*, pages 113–124. Springer, 2011.

[122] F. Magalhães, Á. Cunha, E. Caetano, and R. Brincker. Damping estimation using free decays and ambient vibration tests. In *Mechanical Systems and Signal Processing*, volume 24, pages 1274–1290. Elsevier, 2010.

[123] P. Van Overschee and B. De Moor. *Subspace Identification for Linear Systems.* Kluwer Academic Publishers, 1996.

[124] M.H. Hansen, K. Thomsen, P. Fuglsang, and T. Knudsen. Two methods for estimating aeroelastic damping of operational wind turbine modes from experiments. In *Wind Energy*, volume 9, pages 179–191. Wiley Online Library, 2006.

[125] J. Bogunović Jakobsen and E. Hjorth-Hansen. Determination of the aerodynamic derivatives by a system identification method. In *Journal of wind engineering and industrial aerodynamics*, volume 57, pages 295–305. Elsevier, 1995.

[126] Ch. Hoen, T. Moan, and S. Remseth. System identification of structures exposed to environmental loads. In *Proceedings of Eurodyn '93*, pages 835–845, 1993.

[127] C. Hoen. *System identification of structures excited by stochastic load processes.* PhD thesis, The Norwegian Institute of Technology, NTH, Trondheim, 1991.

[128] J. Bogunović Jakobsen. *Fluctuating wind load and response of a line-like engineering structure with emphasis on motion-induced wind forces.* PhD thesis, The Norwegian Institute of Technology, NTH, Trondheim, 1995.

[129] P. Van Overschee and B. De Moor. Subspace algorithms for the stochastic identification problem. In *Automatica*, volume 29, pages 649–660. Elsevier, 1993.

[130] P. Van Overschee and B. De Moor. N4sid: Subspace algorithms for the identification of combined deterministic-stochastic systems. In *Automatica*, volume 30, pages 75–93. Elsevier, 1994.

[131] M. Viberg. Subspace-based methods for the identification of linear time-invariant systems. In *Automatica*, volume 31, pages 1835–1851. Elsevier, 1995.

[132] P. Van Overschee and B. De Moor. A unifying theorem for three subspace system identification algorithms. In *Automatica*, volume 31, pages 1853–1864. Elsevier, 1995.

[133] B. Peeters and G. De Roeck. Reference-based stochastic subspace identification for output-only modal analysis. In *Mechanical systems and signal processing*, volume 13, pages 855–878. Elsevier, 1999.

[134] P. Trnka and V. Havlena. Integrating prior information into subspace identification methods. In *Control Applications, 2007. CCA 2007. IEEE International Conference on*, pages 1161–1166. IEEE, 2007.

[135] P. Trnka and V. Havlena. Subspace identification method incorporating prior information. In *Decision and Control, 2007 46th IEEE Conference on*, pages 4968–4973. IEEE, 2007.

[136] L. H. Kaasa. Design of an experimental setup for measurements of the aerodynamic properties of bridge decks. Master's thesis, Norwegian University of Science and Technology, NTNU, Trondheim, 2012.

[137] V. Boonyapinyo and T. Janesupasaeree. Data-driven stochastic subspace identification of flutter derivatives of bridge decks. In *Journal of Wind Engineering and Industrial Aerodynamics*, volume 98, pages 784–799. Elsevier, 2010.

[138] L. Lennart. *System identification: theory for the user,* 2^{nd} *ed.* PTR Prentice Hall, Upper Saddle River, NJ, 1999.

[139] D. Tcherniak, S. Chauhan, M. Rossetti, I. Font, J. Basurko, and O. Salgado. Output-only modal analysis on operating wind turbines: application to simulated data. In *Proceedings of European Wind Energy Conference, Warsaw, Poland*, 2010.

[140] D. Tcherniak, S. Chauhan, and M. H. Hansen. Applicability limits of operational modal analysis to operational wind turbines. In *Structural Dynamics and Renewable Energy, Volume 1*, pages 317–327. Springer, 2011.

[141] A. Agneni, G. Coppotelli, and C. Grappasonni. A method for the harmonic removal in operational modal analysis of rotating blades. In *Mechanical Systems and Signal Processing*, volume 27, pages 604–618. Elsevier, 2012.

[142] B. Peeters, B. Cornelis, K. Janssens, and H. Van der Auweraer. Removing disturbing harmonics in operational modal analysis. In *Proceedings of International Operational Modal Analysis Conference, Copenhagen, Denmark*, 2007.

[143] R. Pintelon, B. Peeters, and P. Guillaume. Continuous-time operational modal analysis in the presence of harmonic disturbances. In *Mechanical Systems and Signal Processing*, volume 22, pages 1017–1035. Elsevier, 2008.

[144] N. J. Jacobsen. Separating structural modes and harmonic components in operational modal analysis. In *Proceedings IMAC XXIV Conference*, 2006.

[145] C. Devriendt, T. De Troyer, G. De Sitter, and P. Guillaume. Automated operational modal analysis using transmissibility functions. In *Proceedings of the International Conference on Noise and Vibration Engineering ISMA*, pages 2457–2470, 2008.

[146] R. Wagner, A. Sathe, A. Mioullet, and M. Courtney. Turbulence measurement with a two-beam nacelle lidar. In *European Wind Energy Conference and Exhibition EWEC*, 2013.

[147] P. Chaviaropoulos. Similarity Rules for W/T Up-Scaling. In *UPWIND Project*. CRES, 2006.

[148] P. Federici. Impact of wave conditions on the extreme and fatigue loads of a wind turbine monopile foundation in moderately deep waters. Master's thesis, Technical University of Denmark, Lyngby, Denmark, 2012.

[149] J.S. Bendat and A.G. Piersol. *Engineering applications of correlation and spectral analysis*. John Wiley, 1980.

[150] H.F. Veldkamp and J. Van Der Tempel. Influence of wave modelling on the prediction of fatigue for offshore wind turbines. In *Wind Energy*, volume 8, pages 49–65. Wiley Online Library, 2005.

[151] J. Slootweg, S. de Haan, H. Polinder, and W. Kling. General Model for Representing Variable Speed Wind Turbines in Power System Dynamics Simulations. In *Transactions on Power Systems*, volume 18, 2003.

[152] J. Van Der Tempel. *Design of Support Structures for Offshore Wind Turbines*. PhD thesis, TU Delft, 2006.

[153] J. Jonkman and W. Musial. Offshore code comparison collaboration (oc3) for iea task 23 offshore wind technology and deployment. In *Contract*, volume 303, pages 275–3000, 2010.

[154] W. Popko, F. Vorpahl, A. Zuga, M. Kohlmeier, J. Jonkman, A. Robertson, T. J. Larsen, A. Yde, K. Sætertrø, K. M. Okstad, et al. Offshore code comparison collaboration continuation (oc4), phase i–results of coupled simulations of an offshore wind turbine

with jacket support structure. In *22nd International Society of Offshore and Polar Engineers Conference. Rhodes, Greece*, 2012.

[155] T. J. Larsen, H. A. Madsen, G. C. Larsen, and K. S. Hansen. Validation of the dynamic wake meander model for loads and power production in the egmond aan zee wind farm. In *Wind Energy*, volume 16, pages 605–624. Wiley Online Library, 2013.

[156] D. Todd Griffith and T. G. Carne. Experimental Uncertainty Quantification of Modal Test Data. In *25th International Modal Analysis Conference*, Orlando, FL, USA, 2001.

[157] D. Todd Griffith, M. Casias, G. Smith, J. Paquette, and T. Simmermacher. Experimental Uncertainty Quantification of a Class of Wind Turbine Blades. In *Technical Report*. Sandia National Laboratories, Albuquerque, New Mexico, 2006.

[158] ISO/IEC. Uncertainty of measurement- part3: Guide of the expression of uncertainty in measurement. In *Guide 98-3*. Geneva, Switzerland, 2008.

[159] M. A. Lackner, A. L. Rogers, and J. F. Manwell. Uncertainty analysis in wind resource assessment and wind energy production estimation. In *45th AIAA Aerospace Sciences Meeting and Exhibit, AIAA-2007-1222*, 2007.

[160] M. C. Brower. Uncertainty in wind resource assessment. In *Wind Resource Assessment: A Practical Guide to Developing a Wind Project*, pages 220–232. Wiley Online Library, 2012.

[161] E. G. de las Heras, R. Gutiérrez, E. Azagra, and J. D. Sørensen. Assessment of wind turbine for site-specific conditions using probabilistic methods. In *European Wind Energy Association 2013 Annual Event*, 2013.

[162] EA Laboratory Committee. Evaluation of the Uncertainty of Measurement in Calibration. European co-operation for Accredidation, 2013.

[163] International Electrotechnical Commission (IEC). IEC 61400-12-2, Wind Turbines Part 12-2: Power Performance of Electricity Producing Wind Turbines based on Nacelle Anemometry. In *International Standard*. 2013.

[164] Joint Committee for Guides in Metrology. Evaluation of measurement data-Guide to the expression of uncertainty in measurement. JCGM 100:2008, 2008.

[165] S. L. R. Ellison, M. Rosslein, A. Williams, et al. Quantifying uncertainty in analytical measurement, third edition. Eurachem, 2012.

[166] R. J. Allemang. The modal assurance criterion–twenty years of use and abuse. In *Sound and Vibration*, volume 37, pages 14–23, 2003.

[167] M. Pastor, M. Binda, and T. Harčarik. Modal assurance criterion. In *Procedia Engineering*, volume 48, pages 543–548. Elsevier, 2012.

[168] C. Koukoura, A. Natarajan, and A. Vesth. Identification of support structure damping of a full scale offshore wind turbine in normal operation. In *submitted to Renewable energy*. Elsevier, 2013.

[169] T. Fischer, P. Rainey, E. Bossanyi, and M. Kühn. Study on control concepts suitable for mitigation of loads from misaligned wind and waves on offshore wind turbines supported on monopiles. In *Wind Engineering*, volume 35, pages 561–574. Multi-Science, 2011.

[170] E.J. Norton and D.C. Quarton. Recommendations for design of offshore wind turbines (RECOFF). Technical report, 2003.

[171] M. B. van der Meulen, T. Ashuri, G. J. W. van Bussel, and D. P. Molenaar. Influence of nonlinear irregular waves on the fatigue loads of an offshore wind turbine. *The Science of Making Torque from Wind, Oldenburg, Germany*, pages 1–10, 2012.

[172] DNV. Fatigue design of offshore steel structures. In *DNV Recommended Practice DNV-RP-C203*. 2012.

[173] J. F. Manwell, J. G. McGowan, and A. L. Rogers. *Wind Energy Explained - Theory Design and Application*. Wiley Online Library, 2010.

[174] R. Fadaeinedjad, G. Moschopoulos, and M. Moallem. The impact of tower shadow, yaw error, and wind shears on power quality in a wind–diesel system. In *Energy Conversion, IEEE Transactions on*, volume 24, pages 102–111. IEEE, 2009.

[175] D. Veldkamp. A probabilistic evaluation of wind turbine fatigue design rules. In *Wind Energy*, volume 11, pages 655–672. Wiley Online Library, 2008.

[176] C. Petersen. *Stahlbau. Grundlagen der Berechnungund baulichen Ausbildung von Stahlbauten*. Vieweg, 2001.

[177] DIN EN 1993-1-1. Eurocode 3: Design of steel structures. In *Deutsches Institut für Normung*, 2005.

[178] P. Seide and V. I. Weingarten. On the buckling of circular cylindrical shells under pure bending. In *Journal of Applied Mechanics*, volume 28, pages 112–116. American Society of Mechanical Engineers, 1961.

[179] L. Chen, C. Doerich, and J. M. Rotter. A study of cylindrical shells under global bending in the elastic-plastic range. In *Steel Construction*, volume 1, pages 59–65. Wiley Online Library, 2008.

[180] A. Hübner. *Tubular Piles-Buckling Design in a Complex Situation*. PhD thesis, Universität Fridericiana zu Karlsruhe, 2007.

[181] DIN EN 1993-1-6. Eurocode 3: Design of steel structures. In *Deutsches Institut für Normung*, 2007.

[182] Klaus-Jürgen Schneider and Klaus Berner. *Bautabellen für Ingenieure: mit Berechnungshinweisen und Beispielen;[mit CD-ROM: Stabwerksprogramm sowie inhaltliche Darstellung der Eurocodes 1, 2, 3, 5 und 6]*. Werner, 2002.

[183] W.G. Versteijlen, K.N. van Dalen, A.V. Metrikine, and L. Hamre. Assessing the small-strain soil stiffness for offshore wind turbines based on in situ seismic measurements. In *Journal of Physics: Conference Series*, volume 524, page 012088. IOP Publishing, 2014.

[184] DanSteel. Nlmk dansteel a/s. http://www.thyssenkrupp.com/.

[185] Thyssen Krupp. Thyssen krupp ag. http://www.dansteel.dk.

[186] Oakley Steel. Oakley steel products co. http://www.oakleysteel.com.

Appendix A

Appendix A

A.1 Wind

For the calculation of the offshore turbulence intensity the 90^{th} percentile of the standard deviation from the scatter data is used (Equation A.1).

$$\sigma_{90} = \frac{U_{hub}}{ln(z_{hub}/z_0)} + 1.28 \cdot 1.44 \cdot I_{15} \tag{A.1}$$

I_{15} is the expected turbulence intensity at 15m/s wind speed depending on the wind turbine class, U_{hub} the mean wind speed at hub height and z_0 is the surface roughness length, calculated iteratively by Equation A.2 as proposed in IEC 61400-3 [13] for site specific offshore wind turbine design. $A_C = 0.011$ is the Charnock parameter for open sea, $\kappa = 0.4$ is the von Karman parameter and g is the acceleration due to gravity.

$$z_0 = \frac{A_C}{g}\left[\frac{\kappa \cdot U_{hub}}{ln(z_{hub}/z_0)}\right]^2 \tag{A.2}$$

Equation A.3 shows the turbulence intensity for the load cases DLC1.1 and DLC 1.3 as given by the IEC 61400-1 standard [17], where U_{ave} is average wind speed on the site at hub height, I_{ref} is the expected value of the turbulence intensity at 15m/s (here equal to 0.14

turbine class B), $b = 5.6m/s$ and $c = 2m/s$

$$TI_{1.1} = \frac{I_{ref}(0.75U_{hub} + b)}{U_{hub}}, \tag{A.3}$$

$$TI_{1.3} = \frac{cI_{ref}\left(0.072\left(\frac{U_{ave}}{c} + 3\right)\left(\frac{U_{hub}}{c} - 4\right) + 10\right)}{U_{hub}}$$

An effective turbulence intensity I_{eff} to account for the wake effect inside a wind farm is given by Equation A.4.

$$I_{eff} = \left[\int_0^{2\pi} p(\theta|U_{hub}) I_{wake}^m(\theta|U_{hub}) \mathrm{d}\theta\right]^{1/m} \tag{A.4}$$

Where p is the probability density function of wind direction θ, I_{wake} the combined turbulence intensity of the ambient and the wake flow, U_{hub} the mean wind speed at hub height and m the Wöhler exponent for the considered material. The exponent of the most sensitive material should be used for the verification of the safety of the entire wind turbine [62]. In the case of limited information about the wind direction (wind rose) a uniform distribution can be considered. Based on Frandsen's wake model the wake turbulence is given by Equation A.5.

$$I_{wake} = \sqrt{I_{added}^2 + I_{ambient}^2} \tag{A.5}$$

The added turbulence intensity I_{added} is given by Equation A.6.

$$I_{added}^2 = \frac{1}{\left(1.5 + 0.8d_t/\sqrt{C_T(U)}\right)^2} \tag{A.6}$$

d_t is the distance from a neighboring turbine normalized by the rotor diameter and C_T is the mean thrust coefficient depending on the wind velocity U. By applying these formulas no reduction in the wind speed inside the farm needs to be assumed.

When uniform wind direction is assumed, Equation A.7 can be used for the calculation of the effective turbulence intensity. σ is the ambient turbulence standard deviation, σ_T is the maximum center-wake hub height turbulence standard deviation, d_t is the distance to the neighboring wind turbine, N is the number of the neighboring turbines and $p_w = 0.06$.

$$I_{eff} = \frac{1}{U_{hub}}\left[(1 - Np_w)\hat{\sigma}^m + p_w \sum_{i=1}^{N} \hat{\sigma_T}^m(d_t)\right]^{1/m} \tag{A.7}$$

Weibull Distribution

The Weibull distribution is often used to describe the wind speed distribution. The probability density function (PDF) $f(U;\beta_w,\alpha_w)$ and the cumulative distribution function (CDF) $F(U;\beta_w,\alpha_w)$ are given by Equations A.8 and A.9 respectively.

$$f(U;\beta_w,\alpha_w) = \frac{\beta_w U^{\beta_w-1}}{\alpha_w^{\beta_w}} exp\left[-\left(\frac{U}{\alpha_w}\right)_w^{\beta}\right] \tag{A.8}$$

$$F(U;\beta_w,\alpha_w) = 1 - exp\left[-\left(\frac{U}{\alpha_w}\right)_w^{\beta}\right] \tag{A.9}$$

The shape parameter β_w is calculated using the maximum-likelihood estimation and solving Equation A.10 iteratively. Where U is the mean wind speed and n is the number of observations.

$$\frac{\sum_{i=1}^{n}\left(U_i^{\hat{\beta_w}} lnU_i\right)}{\sum_{i=1}^{n} U_i^{\hat{\beta_w}}} - \frac{1}{\hat{\beta_w}} - \frac{1}{n}\sum_{i=1}^{n} lnU_i = 0 \tag{A.10}$$

After estimating the shape parameter β_w, the scale parameter α_w is given by Equation A.11.

$$\hat{\alpha_w} = \left(\frac{1}{n}\sum_{i=1}^{n} U_i^{\hat{\beta_w}} lnU_i\right)^{\frac{1}{\hat{\beta_w}}} \tag{A.11}$$

Rayleigh Distribution

The Rayleigh distribution is a specific case of the Weibull distribution with one parameter ($\beta = 2$). The PDF and the CDF are given by Equations A.12 and A.13 respectively.

$$f(U;b) = \frac{U}{b^2} exp\left(-\frac{1}{2}\frac{U^2}{b^2}\right) \tag{A.12}$$

$$F(U;b) = 1 - exp\left(-\frac{1}{2}\frac{U^2}{b^2}\right) \tag{A.13}$$

The scale parameter b is calculated using the maximum-likelihood estimation (Equation A.14).

$$\hat{b} = \sqrt{\frac{1}{2n}\sum_{i=1}^{n} U_i^2} \tag{A.14}$$

A.2 Waves

The wave surface elevation η , the particle velocity u and acceleration $\dot{u_w}$ of an Airy wave of amplitude $H/2$ at any time t and horizontal position x , are given by Equation A.15, where k_w is the wave number $k_w = 2\pi/L$, ω is the frequency of the wave and d is the water depth. The main characteristics of the regular waves are presented in Figure A.1.

$$\begin{aligned} &\eta = \tfrac{H}{2}\cos(\omega t - k_w x), \\ &u_w = H\omega\frac{\cosh(\eta + d)}{\sinh kd}\cos(k_w x - \omega t), \quad \dot{u_w} = H\omega^2\frac{\cosh(\eta + d)}{\sinh kd} sin(k_w x - \omega t) \end{aligned} \tag{A.15}$$

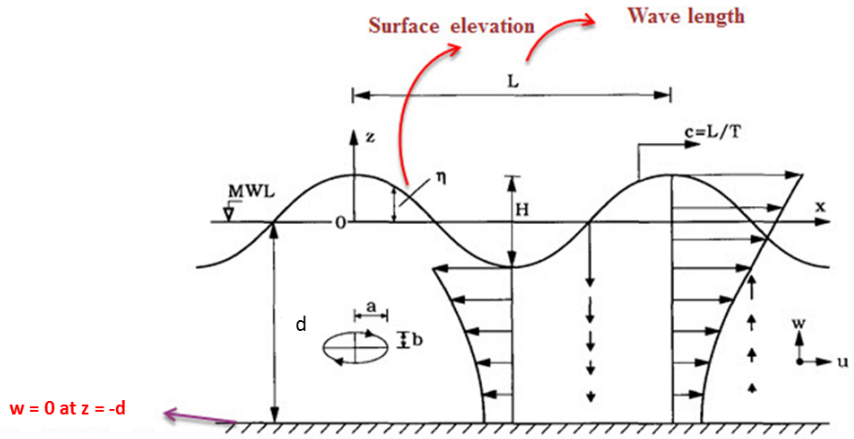

Figure A.1: Regular linear waves. Figure from reference [7]

The Pierson-Moskowitz (Equation A.16) and the JONSWAP (Equation A.17) are the wave spectra used to describe the wave distribution of the Norht Sea. The JONSWAP Spectrum is an extension of the Pierson-Moskowitz.

$$S^{+}(\omega) = \frac{8.1}{10^3}\frac{g^2}{\omega^5}e^{-0.032\left(g/H^{1/3}\omega^{-2}\right)^2} \tag{A.16}$$

$$S(f) = \alpha_j \cdot \frac{g^2}{(2\pi)^4} f^5 exp\left(-\frac{5}{4}\left(\frac{f}{f_0}\right)^4\right)\gamma^{exp\left(-0.5\left(\frac{f-f_0}{\sigma f_0}\right)^2\right)} \tag{A.17}$$

f_0 is the peak frequency, g the gravity acceleration, α_j is given by Equation A.18 and σ by Equation A.19. A well described sea state is one that has most of its energy around the peak frequency f_0. The above mentioned spectra does not take into account higher order peaks.

$$\alpha_j = 5\frac{H_s^2 f_0^4}{g^2}\left(1 - 0.287log(\gamma)\right)\pi^4 \tag{A.18}$$

$$\sigma = \begin{cases} 0.07 & \text{for } f \leq f_0 \\ 0.09 & \text{for } f > f_0 \end{cases} \tag{A.19}$$

The γ parameter of the spectrum is given by Equation A.20 as proposed in reference [11], where T_p is the peak period in seconds and H_s is the significant wave height in meters. For $\gamma = 1$ the JONSWAP spectrum is equal to the Pierson-Moskowitz spectrum.

$$\gamma = \begin{cases} 5 & \text{for } \frac{T_p}{\sqrt{H_s}} \leq 3.6 \\ exp\left(5.75 - 1.15\frac{T_p}{\sqrt{H_s}}\right) & \text{for } 3.6 < \frac{T_p}{\sqrt{H_s}} \leq 5 \\ 1 & \text{for } 5 < \frac{T_p}{\sqrt{H_s}} \end{cases} \tag{A.20}$$

A.3 Soil

The p-y curve used to describe the soil-pile interaction can be generated from Equation A.21 for sand and Equations A.23 and A.24 for clay:

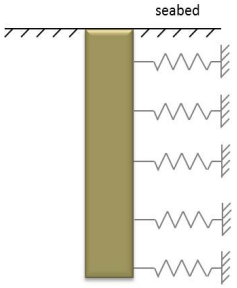

Figure A.2: Distributed springs model.

$$p = Ap_u \tanh\left(\frac{k_s X}{Ap_u} y\right) \tag{A.21}$$

X is the depth of penetration, k_s is the initial modulus of subgrade reaction, A takes the value of 0.9 for cyclic loading and p_u is the static ultimate resistance (Equation A.22).

$$p_u = \begin{cases} (C_1 X + C_2 D)\,\gamma' X & \text{for } 0 < X \leq X_R \\ C_3 D \gamma' X & \text{for } X > X_R \end{cases} \tag{A.22}$$

The coefficients C_1, C_2 and C_3 depend on the friction angle ϕ, X_R is a transition depth, D is the pile diameter and γ' is the submerged unit weight of soil.

For cyclic loading and $X \leq X_R$

$$p = \begin{cases} \frac{p_u}{2}(\frac{y}{y_c})^1/3 & \text{for } y \leq 3y_c \\ 0.72p_u \left(1 - \left(1 - \frac{X}{X_R}\right)\frac{y - 3y_c}{12y_c}\right) & \text{for } 3y_c < y \leq 15y_c \\ 0.72p_u \frac{X}{X_R} & \text{for } y > 15y_c \end{cases} \tag{A.23}$$

For cyclic loading and $X > X_R$

$$p = \begin{cases} \frac{p_u}{2}(\frac{y}{y_c})^1/3 & \text{for } y \leq 3y_c \\ 0.73p_u & \text{for } y > 3y_c \end{cases} \tag{A.24}$$

Here $y_c = 2.5\epsilon_c D$, where ϵ_c is the strain which occurs at one half of the maximum stress. The static ultimate resistance p_u in the case of clay is given by Equation A.25

$$p_u = \begin{cases} (3s_u + \gamma' X)\,D + J s_u X & \text{for } 0 < X \leq X_R \\ 9 s_u D & \text{for } X > X_R \end{cases} \tag{A.25}$$

s_u is the undrained shear strength of the soil and J is a dimensionless empirical constant with a range between 0.25 and 0.5. For a more detailed analysis of the p-y model with distributed springs reference is made to the DNV guidelines [11].

Appendix B

Appendix B

B.1 Fatigue

The 1Hz equivalent load, associated to a number of equivalent cycles is given by Equation B.1a, where N is the number of cycles related to stress range S, m is the Wöhler exponent depending on the material and n_s the number of stress ranges that the stress ranges are separated.

$$S_{eq} = \left(\frac{\sum_{i=1}^{n_s} N_i S_i^m}{n_{eq}} \right)^{1/m} \tag{B.1}$$

The lifetime equivalent load S_{Leq} can be extrapolated by summing up the fatigue loads for all the load cases and using the joint wind-wave probability distribution as weighting function, as in Equation B.2, where f_{U,H_s} is the joint wind-wave probability distribution and N_{eq} is the equivalent number of cycles over the lifetime of the wind turbine, (usually equal to 25 years).

$$S_{Leq} = \left(\frac{\int S_{eq}(u)^m N f_{U,H_s} N_{eq} \mathrm{d}u}{N_{eq}} \right)^{1/m} \tag{B.2}$$

This dissertation is submitted in partial fulfillment of the requirements for the degree of Doctor in Philosophy in Engineering at the Technical University of Denmark. The work was conducted at the Wind Turbines Section (VIM) of the Department of Wind Energy and has been part of the EUDP project titled, “Offshore wind turbine reliability through complete loads measurements”, project no. 64010-0123.

Principal supervisor: Senior Scientist Anand Natarajan, Technical University of Denmark
Co-supervisor: Senior Scientist Kim Branner, Technical University of Denmark
Examiners: Senior Scientist Kurt S. Hansen, Technical University of Denmark
Principal Engineer Ervin Bossanyi, Garrad Hassan
Professor Lars Bo Ibsen, University of Aalborg

Technical University of Denmark
Frederiksborgvej 399
Building 118
4000 Roskilde
Denmark
Telephone: (+45) 46775085
www.vindenergi.dtu.dk

ISBN 978-87-92896-88-9